UNIVERSITAT POLITÈCNICA
DE CATALUNYA
BARCELONATECH

New insights on the fundamentals and modeling of the external sulfate attack in concrete structures

by

Tai Ikumi Montserrat

ADVERTIMENT La consulta d'aquesta tesi queda condicionada a l'acceptació de les següents condicions d'ús: La difusió d'aquesta tesi per mitjà del repositori institucional UPCommons (http://upcommons.upc.edu/tesis) i el repositori cooperatiu TDX (http://www.tdx.cat/) ha estat autoritzada pels titulars dels drets de propietat intel·lectual **únicament per a usos privats** emmarcats en activitats d'investigació i docència. No s'autoritza la seva reproducció amb finalitats de lucre ni la seva difusió i posada a disposició des d'un lloc aliè al servei UPCommons o TDX. No s'autoritza la presentació del seu contingut en una finestra o marc aliè a UPCommons (*framing*). Aquesta reserva de drets afecta tant al resum de presentació de la tesi com als seus continguts. En la utilització o cita de parts de la tesi és obligat indicar el nom de la persona autora.

ADVERTENCIA La consulta de esta tesis queda condicionada a la aceptación de las siguientes condiciones de uso: La difusión de esta tesis por medio del repositorio institucional UPCommons (http://upcommons.upc.edu/tesis) y el repositorio cooperativo TDR (http://www.tdx.cat/?locale-attribute=es) ha sido autorizada por los titulares de los derechos de propiedad intelectual **únicamente para usos privados enmarcados** en actividades de investigación y docencia. No se autoriza su reproducción con finalidades de lucro ni su difusión y puesta a disposición desde un sitio ajeno al servicio UPCommons No se autoriza la presentación de su contenido en una ventana o marco ajeno a UPCommons (*framing*). Esta reserva de derechos afecta tanto al resumen de presentación de la tesis como a sus contenidos. En la utilización o cita de partes de la tesis es obligado indicar el nombre de la persona autora.

WARNING On having consulted this thesis you're accepting the following use conditions: Spreading this thesis by the institutional repository UPCommons (http://upcommons.upc.edu/tesis) and the cooperative repository TDX (http://www.tdx.cat/?locale-attribute=en) has been authorized by the titular of the intellectual property rights **only for private uses** placed in investigation and teaching activities. Reproduction with lucrative aims is not authorized neither its spreading nor availability from a site foreign to the UPCommons service. Introducing its content in a window or frame foreign to the UPCommons service is not authorized (framing). These rights affect to the presentation summary of the thesis as well as to its contents. In the using or citation of parts of the thesis it's obliged to indicate the name of the author.

New insights on the fundamentals and modeling of the external sulfate attack in concrete structures

Thesis by publications

Doctoral Thesis by:
Tai Ikumi Montserrat

Directed by:
Sergio Henrique Pialarissi Cavalaro
Ignacio Segura Pérez

Barcelona, September 2017

Universitat Politècnica de Catalunya
Departament d'Enginyeria Civil i Ambiental

DOCTORAL THESIS

Acta de calificación de tesis doctoral

Curso académico: 2016 - 2017

Nombre y apellidos	TAI IKUMI MONTSERRAT
Programa de doctorado	INGENIERÍA DE LA CONSTRUCCIÓN
Unidad estructural responsable del programa	DEPARTAMENTO DE INGENIERÍA CIVIL Y AMBIENTAL

Resolución del Tribunal

Reunido el Tribunal designado a tal efecto, el doctorando / la doctoranda expone el tema de su tesis doctoral titulada

"*New insights on the fundamentals and modeling of the external sulfate attack in concrete structures*".

Acabada la lectura y después de dar respuesta a las cuestiones formuladas por los miembros titulares del tribunal, éste otorga la calificación:

☐ NO APTO ☐ APROBADO ☐ NOTABLE ☐ SOBRESALIENTE

(Nombre, apellidos y firma) Presidente/a	(Nombre, apellidos y firma) Secretario/a	
(Nombre, apellidos y firma) Vocal	(Nombre, apellidos y firma) Vocal	(Nombre, apellidos y firma) Vocal

_____, _____ de _____ de _____.

El resultado del escrutinio de los votos emitidos por los miembros titulares del tribunal, efectuado por la Escuela de Doctorado, a instancia de la Comisión de Doctorado de la UPC, otorga la MENCIÓN CUM LAUDE:

☐ SÍ ☐ NO

(Nombre, apellidos y firma) Presidente de la Comisión Permanente de la Escuela de Doctorado	(Nombre, apellidos y firma) Secretario de la Comisión Permanente de la Escuela de Doctorado

Barcelona a _____ de _____ de _____.

“*Nothing behind me,*

everything ahead of me,

as is ever so on the road”

- Jack Kerouac

ACKNOWLEDGMENTS

Siempre he pensado que casi todo lo que soy, lo he aprendido de mis padres y del rugby. Mis padres me han ensañado a distinguir lo que importa de lo que no importa y el rugby me ha ayudado a superar mis miedos, a tener confianza en mí mismo.

Una vez finalizado el doctorado, tengo que añadir un punto más. Sergio y Nacho, de vosotros he aprendido que en esta vida vale la pena esforzarse. Que no hay que conformarse con las cosas "suficientemente buenas" y que únicamente con el esfuerzo podré encontrar la belleza en aquello que hago. Ahora que lo entiendo, me doy cuenta de lo mucho que lo necesitaba. Muchas gracias. Se me hace difícil pensar en Sergio y Nacho sin recordar a Albert y Antonio. A pesar de no ser mis tutores directos, he aprendido mucho de vosotros. Agradezco mucho la actitud que siempre habéis tenido hacia mí y todas las oportunidades que me habéis brindado. Junto con Eva, habéis conseguido crear un ambiente en la oficina que me hace sonreír al entrar.

Chris and Simon, I usually protect myself from people. However, with you guys I never felt this need. I think it was the way you listen what helped me talk. Thank you Chris for always being there for me, I really enjoyed our honest chats about anything, everything or nothing. Simon, thanks for sharing with me your biggest treasure. I hope one day my book will look as ugly and old as the one you have.

Quiero agradecer al personal del LTE por haberme apoyado en las campañas experimentales. En especial a Jordi y Robert. No sólo habéis mostrado siempre una disponibilidad total a ayudarme sino que siempre habéis intentado mejorar mi trabajo, enseñándome técnicas y métodos que desconocía, contribuyendo así de forma muy activa a esta tesis.

La experiencia del doctorado puede ser más o menos traumática dependiendo de la gente que te rodea. El día a día en la universidad lo he compartido con muchos compañeros, todos distintos pero necesarios para mí. A todos con los que he coincidido les quiero dar las gracias. El doctorado no hubiese sido lo mismo sin las conversaciones sinceras, los descansos al sol, el humor negro, las bromas inoportunas, discusiones sobre política, religión, teorías conspirativas o simplemente criticando a nuestros supervisores sin descanso. Si las alegrías y miserias compartidas durante el doctorado unen, compartir el master y el doctorado lo hace mucho más. Edu, Carlos, Tina, Anna, Rubén y Razmik, a pesar de mis empeños por mantener a la gente alejada, a vosotros siempre os he sentido muy cerca. Renan, ya sabes lo que pienso de ti, me pareces de las pocas personas que conozco que conseguirá vivir su vida sin hacer daño a nadie. Más allá de tu amistad, quiero agradecerte tu ayuda y paciencia en las clases de química que nos dabas en el despacho. También quiero aprovechar este espacio para pedir perdón. A veces cierro mis puertas y no dejo entrar a nadie. Algunas veces no me he portado bien y quiero que sepáis que me arrepiento. Intentaré mejorar!

Albert, Dídac, Laba, Pakareu, Mora, Xus, Pol, Vic y Xavi, a vosaltres no us demano perdó, ja que sé que us sentiríeu insultats si ho fes. Com més gent conec, com més em moc, més aprecio la vostra amistat.

A la meva família, no sé com donar les gràcies. Vosaltres sou jo.

SUMMARY

The external sulfate attack (ESA) is a complex degradation process typically compromising the durability of underground foundations, nuclear or industrial waste containments and tunnel linings exposed to sulfate solutions. The structures affected usually remain covered its entire service life, which compromises the detection of this phenomenon before severe material degradation has occurred. Once diagnosed, the large size and criticality of the typical structures affected greatly limit the efficiency of the remedial actions. Consequently, monitoring of the evolution of the structural behavior is often the only applicable measure.

This scenario places the development of reliable tools to assist the design of sulfate-resisting concrete structures and assess the risk of ESA in existing properties as key challenges for structural durability. The present thesis aims to advance knowledge in this field by presenting important contributions in three different research lines: numerical modeling of the ESA, role of porosity during the attack and the relevance of reproducing field-like conditions on ESA assessments.

Advances on the ESA numerical modelization led to the development of a chemo-transport-mechanical model and a simplified assessment methodology. The former simulates the effects of ionic transport, chemical reactions, degradation mechanisms and the mechanical response of the structure. The validations performed indicate that the model captures the importance of the location of the ettringite formed within the pore network and provides a fair quantification of the overall expansions. The simplified assessment methodology evaluates the risk of failure during the ESA based on the aggressiveness of the media, the reactivity and mechanical properties of the material and the geometric characteristics and service life of the element under attack, without resorting to complex iterative algorithms. Unlike current design guidelines, the application of this simplified procedure allows the definition of flexible and optimized precautionary measures for each application.

The second research line involved an extensive experimental program that led to the formulation of a conceptual model to explain the role of porosity during the ESA. The results obtained indicate that high durability against the attack might be achieved by limiting the penetration of sulfates or increasing the capacity of the matrix to accommodate expansive products. Both approaches correspond to opposing pore characteristics of the matrix: the former is usually associated with low porosities while the latter requires matrices with high porosities. These results question the common perception that high porosities are always negative for ESA durability and open up the possibility to design sulfate-resisting materials by increasing the capacity of the matrix to accommodate expansive phases.

The third research line evaluates the influence of early sulfate exposure and the effects of confinement on the ESA by two experimental programs. The first study suggests that the delayed exposition to sulfates commonly adopted in accelerated laboratory tests might lead to imprecise damage estimations for structures cast in situ. In these cases, it is recommended to expose the samples to sulfates shortly after casting. The second study suggests that assessing sulfate resistance on specimens in free-expanding conditions might not be representative of the behavior of real structures where the attack is developed in combination with confining conditions. Results indicate that compressive stresses generated by confinement interact with the normal development of the attack by limiting or delaying the appearance of micro-cracks and reducing the amount of ettringite crystals exerting expansive pressures.

RESUMEN

El ataque sulfático externo (ASE) es un proceso de degradación complejo que afecta principalmente la durabilidad de estructuras de cimentación, contenedores de residuos nucleares o industriales y revestimientos de túneles. Dichas estructuras suelen permanecer enterradas toda su vida útil, lo que compromete la detección del fenómeno antes de que se hayan desarrollado altos niveles de degradación. Una vez detectado, el tamaño e importancia estratégica de las estructuras afectadas limitan las opciones de reparación y su eficacia. Debido a ello, habitualmente la única acción posible consiste en la monitorización de la evolución del comportamiento estructural.

Este escenario sitúa el desarrollo de herramientas para el diseño de estructuras resistentes a sulfatos y la evaluación del fenómeno en propiedades existentes como desafíos clave para la durabilidad de estructuras enterradas. Esta tesis doctoral aspira a profundizar el conocimiento en torno a esta temática mediante contribuciones relevantes en tres líneas de investigación: la modelización numérica del ASE, el rol de la porosidad durante el ataque y la relevancia de reproducir condiciones de campo en la evaluación del ASE.

Avances en el campo de la modelización numérica han dado lugar a un modelo avanzado y una metodología de evaluación simplificada del ASE. El primero se basa en la simulación de procesos de transporte iónico, reacciones químicas, mecanismos de degradación y respuesta mecánica de la estructura. Las validaciones realizadas indican que el modelo refleja la importancia de la localización de la etringita dentro de la red porosa y proporciona estimaciones ajustadas de las expansiones generadas. La metodología de evaluación simplificada mide el riesgo de fallo estructural basándose en la agresividad del medio, la reactividad y propiedades mecánicas del material y las características geométricas y vida útil del elemento atacado, sin recurrir a algoritmos iterativos. A diferencia de las guías de diseño actuales, su aplicación permite la definición de medidas preventivas ajustadas a cada aplicación.

La segunda línea de investigación ha dado lugar a un modelo conceptual que explica el rol de la porosidad durante el ASE. Los resultados obtenidos indican que se pueden alcanzar altas resistencias al ataque mediante la limitación de la penetración de sulfatos en la estructura o incrementando la capacidad de la matriz de acomodar fases expansivas. Los dos enfoques se corresponden a características porosas opuestas de la matriz. La primera se suele asociar a bajas porosidades mientras que la segunda se maximiza en porosidades altas. Los resultados obtenidos cuestionan la idea de que porosidades altas siempre son negativas para la durabilidad ante el ASE y abre la posibilidad de diseñar materiales resistentes a sulfatos incrementando la capacidad de acomodar fases expansivas.

La tercera línea de investigación evalúa la influencia de la exposición temprana a sulfatos y los efectos del confinamiento en el ASE. Resultados referentes al primer estudio indican que una exposición tardía a los sulfatos como la empleada en la mayoría de ensayos acelerados puede conllevar a estimaciones incorrectas del daño generado en estructuras fabricadas in situ. El segundo estudio, referente a los efectos del confinamiento, sugiere que el uso de probetas en condiciones de expansión libre puede no ser adecuado para reproducir los efectos del ASE en estructuras donde el ataque se desarrolla en condiciones confinadas. Las tensiones de compresión generadas interactúan con el desarrollo normal del ataque limitando o retardando la aparición de micro-fisuras y reduciendo la cantidad de cristales de etringita creciendo en condiciones confinadas y por ende, ejerciendo presiones expansivas.

TABLE OF CONTENTS

1. GENERAL INTRODUCTION

This chapter is divided in two main parts. The first part introduces preliminary notions on the external sulfate attack (ESA) and provides a brief description of the different processes involved during the attack. The second part presents the theoretical framework needed to understand the importance of the objectives defined in this work, based on a critical review of the different numerical and experimental ESA assessment methods available. The topics addressed in this thesis are introduced in the discussion of the limitations of each method.

Contents

1.1. PREFACE

The external sulfate attack (ESA) is a complex degradation process compromising the durability of cement-based materials exposed to sulfate solutions [1,2]. The different processes involved (transport, chemical reactions, degradation mechanisms and mechanical response) are depicted in Figure 1.1 through a schematic representation of a group of end bearing piles before and after the attack.

ESA is triggered by the penetration of sulfate ions from underground waters in contact with soluble sulfate salts or industrial or nuclear wastes into the pore network of the material. Mass fluxes between the external aqueous media and the reactive cementitious material alter the equilibrium state of the system, promoting chemical reactions to restore minimum internal energy. The chemical reactions triggered vary depending on the sulfate salt present in the external media. The main salts associated to the ESA are sodium sulfate (Na_2SO_4), calcium sulfate ($CaSO_4$) and magnesium sulfate ($MgSO_4$). The low solubility of $CaSO_4$ (about 100 times smaller than the solubility of Na_2SO_4 or $MgSO_4$) reduces the maximum sulfate concentration in solution to about 1.5 g/l, which greatly limits the deleterious effects caused by this form of attack. On the other hand, the damage generated by Na_2SO_4 and $MgSO_4$ solutions might be much more significant due to the potentially high sulfate concentrations (132 and 230 g/l for Na_2SO_4 and $MgSO_4$, respectively). For this reason, most of the research on ESA has been focused on Na_2SO_4 and $MgSO_4$ solutions.

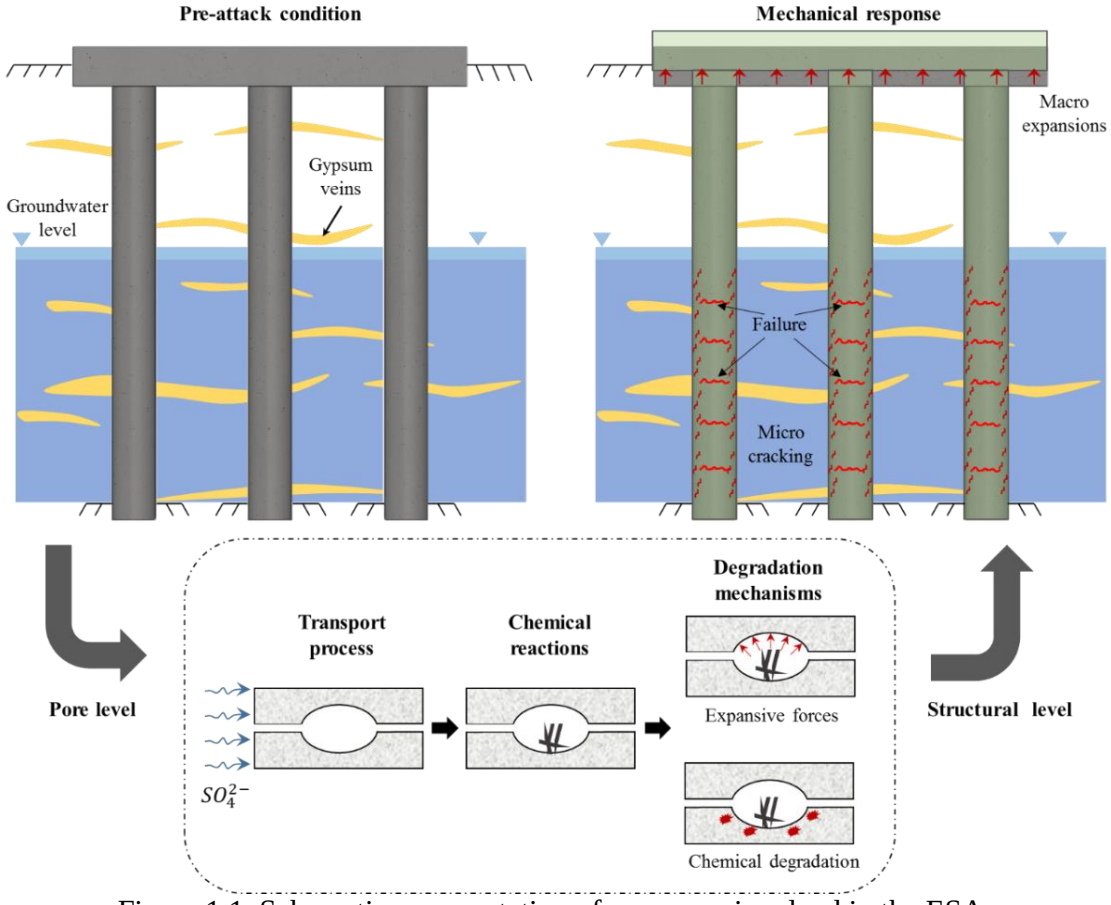

Figure 1.1. Schematic representation of processes involved in the ESA.

The cation of the sulfate salt (Na^+ or Mg^{2+}) plays an important role in the definition of the chemical reactions and the damage mechanism associated to the attack. ESA caused by sodium sulfate is characterized by ettringite and gypsum formation in such a quantity that

the material sustains physical damage. Moreover, sulfate ingress triggers a series of chemical reactions that involves dissolution of soluble calcium bearing phases (mainly portlandite) for ettringite and gypsum precipitation. The dissolution of portlandite might have important effects on the overall strength of the material. Even though some researchers suggest that sodium ions in solution could modify the solubility of the silicate phases and alter the morphology of the C-S-H gel [3,4], it is generally accepted that the presence of sodium from the sulfate salt does not significantly alter the development of the attack. A review of the chemical reactions related to sodium sulfate solutions can be found in [1,5,6].

ESA caused by magnesium sulfate follows a completely different damage mechanism, which is strongly influenced by the presence of magnesium ions in solution from the sulfate salt. The formation of magnesium hydroxide lower the pH of the pore solution, which promotes the transformation of the C-S-H gel into a M-S-H phase without binding properties. This transformation causes softening and disintegration of the matrix and the formation of gypsum and brucite. A review of the chemical reactions related to magnesium sulfate environments can be found elsewhere [7].

This thesis only addresses ESA caused by sodium sulfate solutions. The chemical reactions trigger a series of degradation mechanisms that are responsible for the "visible" consequences of the attack (macroscopic expansions, cracking and spalling or delamination of the hardened material). The driving forces that explain those phenomena are found at the pore scale of the material in the form of chemical damage and expansive forces (Figure 1.1).

Chemical damage is usually associated to the degradation caused by the deterioration of mechanical properties in the cementitious matrix of the hardened concrete. Gypsum and ettringite formation requires calcium, which is mainly obtained by the dissolution of calcium hydroxide due to its high solubility. However, at late stages of the attack or under shortage of portlandite availability calcium might be obtained from C-S-H gel. The C-S-H phase is the main responsible of strength and stiffness in the cementitious matrix and its dissolution might cause a mechanical strength loss and microcrack formation.

On the other hand, it is well established that the precipitation of expansive phases generates macroscopic expansions and subsequent stress-induced cracking and spalling [1]. Several mechanisms have been suggested in the literature to explain how the precipitation/dissolution processes are converted into actual expansions. The two theories that currently stand as the most discussed are the volume increase and crystallization pressure. The former assumes that the expansions observed are the result of the additional volume generated by the expansive products precipitated during the attack. The latter theory states that expansions are caused by the crystallization pressure exerted on the pore walls due to the formation of ettringite in confined conditions. A comprehensive review of the suggested theories can be found in [1,8].

As indicated in Figure 1.1, the degradation processes described take place at the pore scale of the material. If ESA was an internal attack that affects uniformly all the structure, the local response of the material would be representative of the macroscopic behavior of the element. This scenario is depicted in Figure 1.2, where local expansions (ε_{local}) are directly translated into macroscopic expansions (ε_{macro}) without generating any stress.

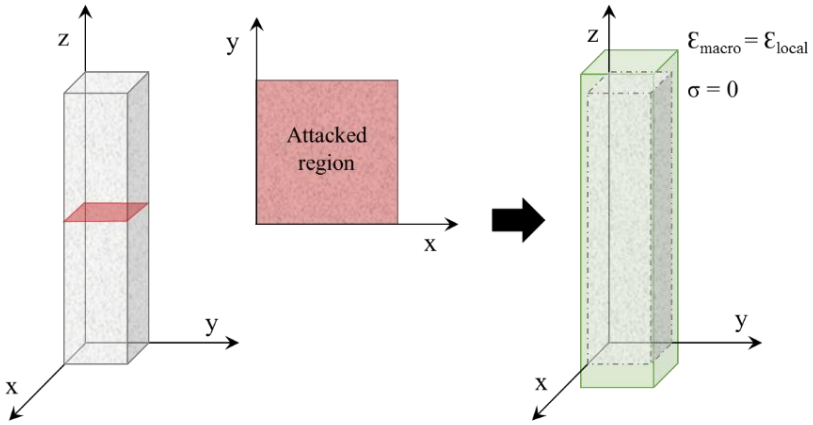

Figure 1.2. Schematic representation of the mechanical response of a uniformly attacked element.

However, the degradation caused by ESA progresses gradually from the external surface towards the inner layers of the material, as sulfate ions penetrate and react with compounds from the hydrated cement paste. Consequently, a multi-layered pattern is formed with an external damaged layer and an internal sound core (Figure 1.3). In this case, the expansive forces generated at the pore level within the attacked region cannot be fully released by deformations since the sound core of the element acts as a restriction to maintain compatibility. Because of that, the macroscopic expansions developed are usually considerably lower than the local expansions generated. Moreover, the mechanical interaction between sound and damage regions generates an auto-balanced tension state, leading to microcracking in the attacked region due to compressive stresses and possible mechanical failures outside the zone directly affected by the sulfate penetration.

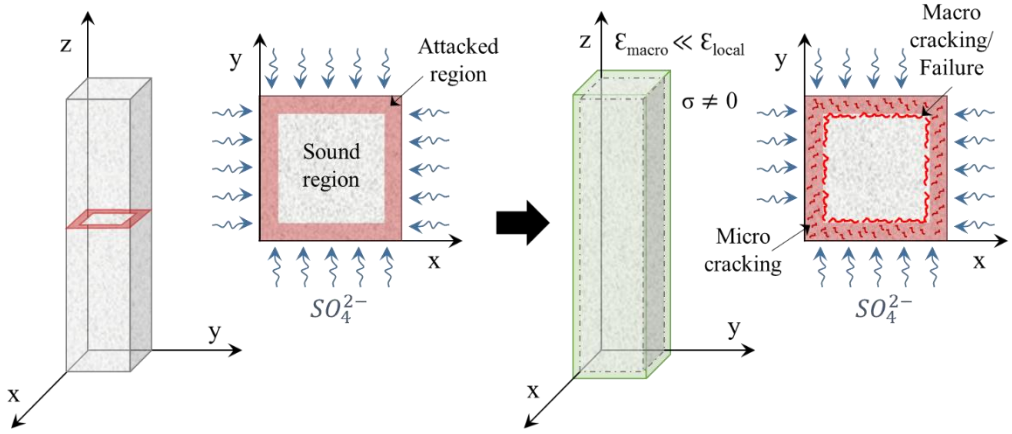

Figure 1.3. Schematic representation of the mechanical response of an element exposed to ESA.

The description of the fundamental mechanisms associated to the ESA highlights the complexity of this phenomenon and identifies the necessary conditions for the attack to develop: an external source of sulfate ions, a reactive cement-based matrix and a liquid phase connecting the external aqueous media with the hydrated compounds of the cement paste [6]. These requirements define the typical structures affected by the ESA, which include underground foundations, nuclear or industrial waste containments and tunnel linings.

The majority of these structures remain covered during its entire service life, which compromises the early diagnostic of the attack that may only be detected after severe material

degradation has occurred. Additionally, once the attacked is diagnosed, the large size and criticality of the typical structures affected greatly limits the efficiency of the remedial actions applicable. Indeed, in the majority of cases once a concrete deterioration process is detected, the only possible action is of the palliative nature, through a monitoring of the structural behavior.

This scenario establishes the development of reliable tools to assist the design of sulfate-resisting concrete structures and assess the risk of ESA in existing properties as key challenges for structural durability. Despite the large body of research performed during the last decades in this direction, current design guidelines prescribe precautionary measures based on over-simplified assessments of the attack, which often leads to unnecessary protective measures. The cost overruns associated to the needless use of sulfate-resisting cement or other remedial actions together with the urge to develop reliable prediction models have prompted the industry to seek ways to optimize the design and assessment of structures exposed to the ESA.

The present thesis was originated in this context. The collaboration with the industry and the access to real structures allowed the identification of key needs to advance knowledge in this field. The specific topics addressed in the thesis reach a wide variety of areas, but all ultimately aim to examine and improve the current design and assessment methods related to the ESA. The research significance and the conceptual framework of all the topics covered are discussed in the following section by a critical discussion on the limitations of current assessment methods and design guidelines.

1.2. ASSESSMENT OF THE EXTERNAL SULFATE ATTACK

The existing tools for the design of sulfate-resisting structures and assessment of the ESA are gathered in three main groups: prescriptive approaches and simplified analytical relations, advanced numerical models and accelerated test methods.

1.2.1. Prescriptive approaches and simplified analytical relations

This section reviews the main simplified empirical and mechanistic relations to assess the ESA and the design guidelines to obtain sulfate-resisting concrete structures. The empirical relations include analytical models based on direct observations, measurements or extensive experimental data records while the mechanistic relations are those procedures based on a simplified understanding of the attack mechanisms. The review and critical discussion on design guidelines are solely focused on how current building codes and standards assess the potential aggressiveness of the ESA, not on the selection or validity of the precautionary measures prescribed. Performance tests to classify the cement resistance are reviewed in section 1.2.3.

Building codes and standards

Most building codes and standards consider that the potential damage generated by the ESA can be solely predicted by the aggressiveness of media surrounding the structure (EN 206:2013+A1:2016 [9], ACI 318-08 [10], EHE-08 [11]). Structures are classified into different exposure classes based on the sulfate concentration of the soil or water. Depending on the classification obtained, a set of requirements are prescribed to withstand the environmental actions. These are given in terms of limiting values for concrete dosage (cement type, max. water/cement ratio and min. cement content) and established concrete

properties (min. compressive strength). The reasoning behind these recommendations is to obtain a dense, workable concrete with low reactivity to sulfates able to withstand the internal stresses caused by the expansions. According to this approach, a concrete structure exposed to sulfates is considered durable if it complies with all the requirements associated to its exposure class. If one of these requirements is not fulfilled, the durability of the structure might not be guaranteed.

The UK national provision BS 8500-1 [12] and the BRE Special Digest 1 [13] present a more accurate approach to assess the aggressiveness of the attack and select the precautionary measures. In this case, the aggressiveness of the media is assessed by the sulfate concentration, type (natural or brownfield) and acidity (pH) of soil and mobility of groundwater (static or mobile). From the characteristics of the media and the intended working life, the quality of concrete (max. w/c ratio, min. cement content and type of cement) and additional protective measures (enhanced concrete quality, surface protection, sacrificial layer, address drainage of site or controlled permeability formwork) are prescribed. Additionally, the size of the structure is briefly considered by recommendations regarding minimum section thickness and relaxation of the requirements in large elements where certain amount of surface damage is tolerated. The criticality of the structure is also indirectly addressed by increasing the intended working life from 50 to 100 years in structures where the consequences of failure are relatively serious.

Empirical and simplified mechanistic relations

Several empirical and simplified mechanistic relations have been developed to quantify the deleterious effects experienced by concrete or mortar elements exposed to the ESA. Most of these works were developed during the ‘80s and ‘90s based on accelerated laboratory tests performed with small-scale specimens within a framework of a limited understanding of the mechanisms associated with the attack and poor computational capabilities. In general, early models were developed to predict the penetration of the sulfate degradation depth [14–16] and later evolved towards the estimation of the evolution of expansions [17–19].

Unlike most building codes and standards, in the majority of empirical and simplified mechanistic relations the reactivity of the material, properties related to the transport process and time are considered as input parameters for the assessment of the attack. The reactivity of the material is usually introduced as the C_3A content of the cement [15–17,19]. Additionally, the model from J.R. Clifton & J.M. Pommersheim [19] takes into account the cement content to assess the reactivity based on the aluminate content per unit volume of concrete, which might be more appropriate. The empirical model from P.J. Monteiro & K.E. Kurtis also considers the C_3S and C_4AF content in the cement [18].

The importance of the transport process is addressed by the consideration of the water/cement ratio, porosity, diffusion coefficient of sulfates or a combination of those. Time is computed either as a degree of reaction and hydration [19], formed ettringite [14] or/and explicitly as time [14–18]. Except for the model proposed by A. Atkinson & J.A. Hearne [14], all models reviewed ignored the mechanical aspect of the attack. A. Atkinson & J.A. Hearne proposed a mathematical relation based on a more mechanistic point of view to predict the degradation or spalling depth [14]. In this case, the fracture energy, the Young modulus and the Poisson’s ratio of concrete are considered as input parameters. However, the predictions made were not accurate, with a large divergence between measured and calculated results.

Limitations

The majority of building codes and standards do not consider the size or the required service life during the selection of the precautionary measures to design sulfate-resisting structures. This approach supports the idea that ESA is mainly a chemical attack, as most of the recommendations included are focused on reducing the penetration of sulfates or the reactivity of the material. However, as described in section 1.1 the region directly affected by sulfate penetration is usually restricted to a few centimeters close to the external surface. The sound region, which in most real structures constitutes a larger area, contributes to reduce the damage caused by the attack. Therefore, ignoring the mechanical aspect of the attack might lead to unrealistic assessments. Notice that with the existing framework, codes might prescribe the same precautionary measures for massive elements of temporary structures and slender elements of structures with long working lives. This may lead to unjustified penalizing measures and cost overruns due to the unnecessary use of sulfate resistant cement.

The procedures included in BS 8500-1 [12] and the BRE Special Digest 1 [13] represent a great improvement on the traditional approach adopted by the codes, as it recognizes the importance of time and size for a realistic selection of the precautionary measures. However, the influence of these parameters are introduced in terms of broad recommendations that might not respond to the actual performance of the structure but to qualitative trends usually associated to the ESA. Most of these problems are inherent to the use of prescriptive approaches based on limiting values to classify the aggressiveness of the attack or the geometrical characteristics of the structure. The limited framework provided by this approach does not allow an optimum selection of precautionary measures for each attacked structure.

The main drawbacks associated with empirical models are their limited applicability, as these are only valid for elements subjected to the same conditions used in the tests (usually small specimens in highly aggressive environments). Amongst the simplified mechanistic models reviewed, none considered simultaneously parameters related to the aggressiveness of the media and the reactivity and transport properties of the material. Moreover, none of the models developed considered the size of the structure. Consequently, the macro-structural mechanical effects caused by the interaction between damaged and undamaged regions are completely ignored. This could be justified in the case of the model from A. Atkinson & J.A. Hearne [14] since it aimed to predict the degradation rate or depth, where the effects of undamaged regions could be disregarded as a simplification. However, it is hard to justify the absence of mechanical considerations in models that aim to predict the evolution of expansions.

Based on the literature review, the use of current empirical or simplified mechanistic relations as a tool to assess the deleterious effects of field structures exposed to ESA seems questionable, as reliable predictions of the long-term performance might not be attained. The limitations of the models described and the complexity of the task is indirectly acknowledged by the lack of recent attempts to develop simplified models to assess the ESA. Since the early 2000, the efforts have shift towards more comprehensive numerical models that take into account the transport of ions, the chemical reaction and the microstructural damage through several differential equations, whose solution commonly require iterative procedures. However, the complexity of the equations involved and the high computational cost for their solution may not be accessible to practitioners and certainly are not compatible with the philosophy of most design codes.

Simplified methodologies for the assessment of the potential damage caused by the ESA must be further developed to incorporate parameters representative of all main processes involved during the attack. The specific conditions found in each application and the expected service life of the structure should be explicitly considered to obtain reliable assessments. The development of such optimized procedures without resorting to complex iterative calculations is definitely a challenge for the scientific community and is widely claimed by the industry.

1.2.2. Advanced models for ESA assessment

Advanced numerical models based on complex iterative algorithms are at present the most sophisticated tools for ESA assessment. Even though ESA could be basically decomposed into four main processes (ionic transport, chemical reactions, degradation mechanisms and the mechanical response of the structure), advanced models were traditionally focused on the simulation of a specific phenomenon within the overall problem. This approach led to the development of models that assessed the deleterious effects of ESA based solely on a simulation of the ionic transport process or/and the chemical reactions triggered by the attack. Nowadays, these models are able to predict accurately the phase composition of the system through chemical equilibrium calculations that takes into account the aggressiveness of the media and the reactivity and transport properties of the matrix. The most well-known chemo-transport ESA models might be the ones presented by Y. Maltais [20], E. Samson & J. Marchand [21] and B. Lothenbach [22].

Even though the utility of these models is beyond question, such approaches are not able to provide realistic assessments in large elements where the area affected by the attack comprises only a small fraction of the overall structure or at late stages of the attack when the damage developed is significant. This limitation has been recognized by several researchers and since the early 2000s advanced numerical models that aim to provide reliable assessments based on the simulation of the four processes involved in the ESA are available (e.g. [23–30]).

The consideration of the mechanical effects in the simulations have traditionally been associated to simplified transport and chemical approaches. Consequently, the majority of comprehensive ESA models only consider the diffusion of sulfates (single-ionic models) in saturated conditions and the chemical reactions are simulated by simplified chemical kinetic laws, e.g. [23,25,26]. Some models have introduced more comprehensive approaches to simulate the ionic transport process by also considering other species [27–30] and/or the advection mechanism associated to unsaturated conditions [27,28,31–33]. However, only the chemo-transport-mechanical ESA models from F. Schmidt-Döhl & F.S. Rostásy [27,28] and B. Bary [30] include chemical equilibrium calculations.

Practically all chemo-transport-mechanical models assume that the only source of degradation are the expansive forces generated at the pore network [23,25,26,29,30]. The two main approaches used to quantify the expansive forces are the volume increase and the crystallization pressure theory. So far, the volume increase approach has persisted in numerical modeling as it has been successful at reproducing experimental macroscopic expansions [23,25,26,33]. This theory quantifies the forces generated during the attack by the volume increase associated to the formation of expansive phases. Expansive products are defined as those phases that take up more space than the volume used by the reactants consumed for its formation. Usually, the numerical expression described in Eq. (1.1)

proposed by J.R. Clifton & J.M. Pommersheim [19] is adopted to quantify an expansion factor (v). Values of v for the common reactions associated to the ESA can be found in [19,34].

$$v = \frac{\sum solid\ product\ volumes - \sum solid\ reactant\ volumes}{\sum solid\ reactant\ volumes} \quad (1.1)$$

As indicated by Eq. (1.1), only the volume occupied by solid reactants and products are considered. This assumes that the aqueous species consumed during the reaction (e.g. water molecules) are instantly replaced by new molecules entering the system from an external source. Linear expansions (ε_l) at the pore level might be simply estimated by multiplying the expansion factor (v), the molar volume (V_m) and the concentration of solid reactants consumed (CA^r), as described in Eq. (1.2).

$$\varepsilon_l = (1 + vV_m CA^r)^{1/3} - 1 \quad (1.2)$$

Models based on this approach usually consider that not all aluminate reacted generates expansions, as the pore network is able to accommodate a certain amount of expansive product without exerting any pressure to the pore walls [23,25,26]. A pressure on the surrounding walls may be only exerted if the crystals become too large and/or too numerous to fit into the available space. Consequently, the equation previously described to estimate local linear expansions (Eq. (1.2)) is modified to capture this phenomenon (Eq. (1.3)) [23]. This equation quantifies the capacity to accommodate expansive product by the fraction (f) of the concrete initial connected porosity (φ_0) that has to be filled prior expansion starts.

$$\varepsilon_l = \text{Max.}\{[(1 + vV_m CA^r - f\varphi_0)^{1/3} - 1], 0\} \quad (1.3)$$

Microcracking has been traditionally accounted by a macroscopic damage variable based on continuum damage mechanics. The early approach presented by R. Tixier & B. Mobasher [23] has been widely implemented and served as a basis for most of the models developed. However, approaches based on continuum damage mechanics have important limitations when it comes to predict crack patterns or the spalling effects. The model presented by A.E. Idiart et al. represents an important contribution in this field [26]. The main feature of this model is the nonlinear fracture mechanics-based crack propagation procedure, which considers the effect of cracking explicitly in the degradation process. For that, zero-thickness interface elements are introduced in all the aggregate–matrix contacts and also in predetermined locations within the matrix. Currently, this might be the only model able to capture accurately the main crack patterns.

Limitations

The literature review features models with high degrees of sophistication regarding the modelization of the transport mechanism, chemical reactions and the mechanical response of the material. The modelization of these processes have been studied during many decades for a wide variety of areas (e.g. transport of contaminants in soils or the thermodynamic modeling of geochemical systems), which has promoted the development of ESA models based on the same principles. On the other hand, investigations on the simulation of the expansive forces generated during the attack are rare. Consequently, notwithstanding recent progress, the modeling of the degradation mechanisms currently presents significant limitations.

Eq. (1.3) states that the expansive forces generated at the pore level are the result of the addition of two opposing phenomena: volume increase from ettringite formation ($vV_{\mathrm{m}}\,CA^{r}$) and the buffer capacity of the pore network ($f\varphi_0$). The consideration of the overall initial porosity and a unique buffer coefficient assumes that all complexity of the concrete porosimetry can be reduced to a single pore where all expansive products precipitate in. This is equivalent to saying that the precipitation and expansion occur evenly in all pores regardless of their size, as the amount of expansive products precipitated in each pore is proportional to its volume. A schematic representation of the simplifications assumed by Eq. (1.3) are shown in Figure 1.4.

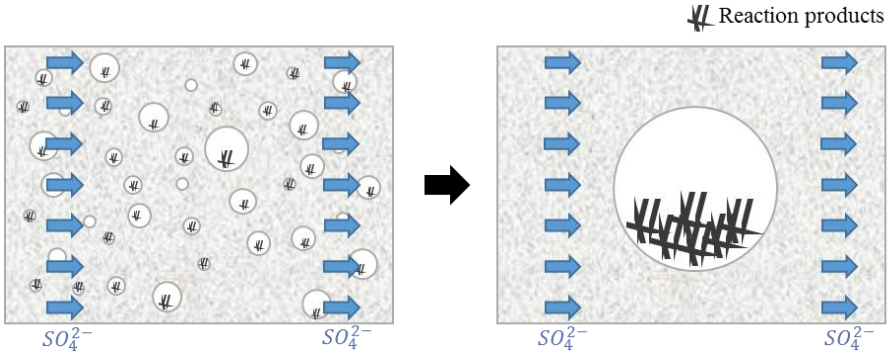

Fig. 1.4. Schematic representation of the simplification on concrete porosimetry and deposition patterns.

The direct consequence of this simplification is the inability of the model to compute expansive pressures before the volume of ettringite formed ($vV_{\mathrm{m}}\,CA^{r}$) fills the entire buffered volume ($f\varphi_0$). Because of that, the model cannot capture pressures generated during the early stages of the attack. Figure 1.5 quantifies the relevance of this phenomenon by depicting separately the contribution of the volume increase and buffer capacity terms in the Eq. (1.3) for two different porosities (φ_0 =0.07 and 0.15). The dotted lines illustrate the buffer term for different buffer coefficients (f) while the blue shaded regions correspond to the volume increase term for cements with varying reactivity and aluminate consumed. Figure 1.5 assumes that all aluminates are in the form of monosulfate prior to its reaction to form ettringite. Other values adopted for the calculations are: cement content=350 kg/m^3, v=0.54 [19] and V_m=309 cm^3/mol.

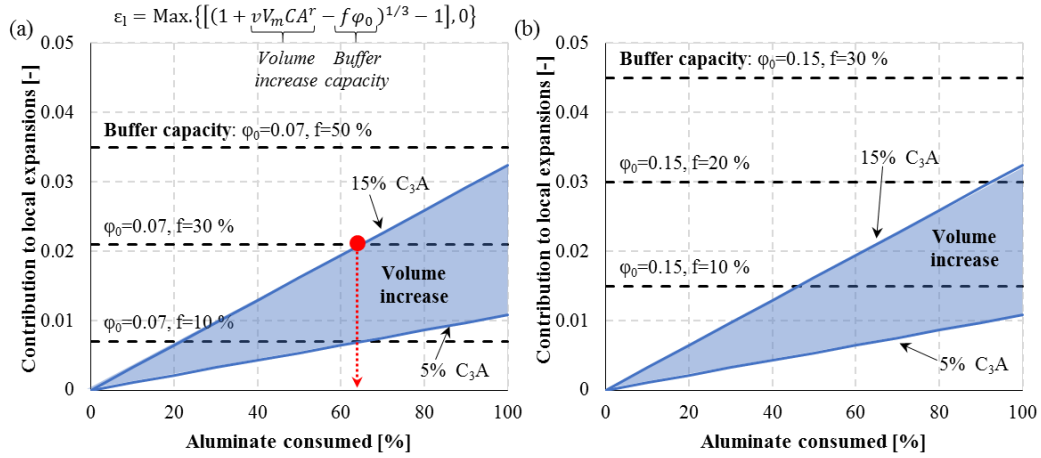

Fig. 1.5. Relative weight of the buffer and volume increase term in Eq. (1.6): (a) φ_0 =0.07 and (b) φ_0 =0.15.

Figure 1.5 shows that during the early stages of the attack (low aluminate consumed), the buffer term is generally above the volume increase term, regardless of the reactivity of the cement used. As more ettringite is formed, the contribution of the volume increase term increases until it equals the buffer capacity of the matrix, which represents the time threshold for expansion onset. This instant is depicted with a red dot in Figure 1.5a for highly reactive matrices (15 % C_3A) with a buffer capacity of the 30 % of the initial porosity. In these circumstances, the model would not compute expansions at the pore level until the 65 % of the local aluminate is consumed. From there, the expansive forces estimated increase linearly with the aluminate reacted.

Notice that if the buffer capacity considered is set above the 50 % of the porosity (φ_0 =0.07), the volume increase term would not exceed the buffer term even after the conversion of all aluminate into ettringite. This scenario is reached for f > 22 % in matrices with φ_0 =0.15 (Figure 1.5b). In these situations, the model would not compute expansions throughout the attack, which is not realistic. Actually, ettringite precipitation occurs simultaneously in a wide variety of pore ranges, depending on the availability of reactants and the pressure conditions inside the pores. Ettringite formed in small pores might generate expansive forces before ettringite precipitated in larger pores, due to its lower capacity to accommodate expansive products. In light of the above, methodologies to compute expansions at the pore level should be further developed to account for the different strain contributions from ettringite precipitated in different pore sizes.

Figure 1.5 also highlights the critical relative weight attributed to the capacity of the matrix to accommodate expansive phases. However, such critical role does not come from an accurate understanding of this phenomenon as its importance has never been comprehensively assessed. In fact, solid experimental evidences and explanations regarding the mere existence of a buffer capacity of the matrix are rare and inconclusive. Consequently, scientists adopt different values of f arbitrarily, often treating this variable as a fitting parameter.

The early works of A. Atkinson & J.A. Hearne [14] and J.R. Clifton & J.M. Pommersheim [19] assumed that only 5 % of the volume of ettringite formed caused expansions. Additionally, J.R. Clifton & J.M. Pommersheim [19] considered that expansion occurs only when the reaction products fill the entire volume of capillary porosity (f=100 %). More recently, R. Tixier & B. Mobasher fixed this parameter in a range between 5 % - 40 % of the initial porosity [23]. Other authors M. Basista & W. Weglewski [25] and Y. Yu et al. [35] arbitrarily assumed it to be 50 and 36 %, respectively. As can be deduced by Figure 1.5, discrepancies of these ranges in such an important parameter greatly compromise the reliability of the assessments obtained. Therefore, the limitations of the current approach are not only related to partial computational methodologies but also to a lack of understanding of the expansion mechanism and the overall role of porosity during the attack.

Following this line of thought, the use of Eq. (1.3) has another relevant implication. Eq. (1.3) states that an increase of porosity leads to lower expansive pressures, which is justified by the greater capacity of matrices with high porosity to accommodate expansive products. This idea suggests the possibility to obtain sulfate-resisting materials by maximizing the porosity. However, it is generally accepted that materials with low permeability show a better durability against sulfates than the corresponding samples with higher permeability. Although permeability and porosity are not synonyms, in general the decrease of permeability is accompanied by a consequent decrease in the porosity of the

matrix. Therefore, the accepted knowledge on ESA dictates that an increase of porosity could never lead to an increase of durability against sulfates. An improved understanding on the role of porosity during the attack may clarify this apparent controversy and possibly lead to explore new strategies to develop sulfate-resisting materials by using the buffer capacity as the main resisting mechanism.

1.2.3. Accelerated test methods

The complexity and slow development of the ESA have interfered with the adoption of a single performance test method to evaluate the deleterious effects of the attack. During the last decades, several experimental test methods have been developed to assess different aspects related to the ESA resistance. In general, the vast majority of methods incorporate accelerated tests to reproduce the whole life of the specimen in a reasonable time. The acceleration of the attack is usually achieved by increasing the sulfate concentration in solution and using slender specimens with large surface area/volume ratios. However, other strategies used to accelerate the attack include high w/c ratios to obtain a higher permeability of the material, continuous wetting drying cycles to promote sulfate penetration and crystallization damage or the addition of gypsum to the cement paste to directly introduce the sulfates into the concrete matrix [36].

Discord amongst experimental test methods also rises on the way of quantifying the degree of degradation. Even though the most established methodologies use expansion measurements on free-expanding conditions [37,38], some researchers propose the use of other criteria such as the decrease in compressive strength or the visual degradation [36]. A recent comprehensive review of the test methods available can be found in [36].

Currently, the only performance-based test method recognized by building codes to assess sulfate resistance is the ASTM standard C1012 [37]. ACI 318-08 [10] allows its use to evaluate the sulfate resistance of concrete mixtures with varying combinations of supplementary cementitious materials. Since its main purpose is the qualification of binders, only the chemical aspect of the attack is considered. Procedures included in the ASTM C1012 define mortar prisms of 25.4 x 25.4 x 285 mm cured in non-aggressive conditions until a strength of 20 MPa is reached prior to immersion in a 50 g/l sodium sulfate solution at 23 ºC [37]. Sulfate resistance is evaluated based on linear expansion measurements. The expansion test limits are 0.10 % at 6 months for moderate exposure conditions, 0.05 % at 6 months or 0.10 % at 12 months for severe exposure conditions and 0.10 % at 18 months for very severe conditions. A detailed guidance on qualification of mixtures using ASTM C1012 is given in ACI 201.2R guide to durability [39].

Limitations

The set of testing conditions prescribed by experimental test methods to assess ESA resistance are formulated to accelerate the attack mechanism and simplify the experimental set-up. Some of the conditions adopted greatly differ from the real conditions found in practice. This situation raise concern on whether the results obtained are representative of the conditions found in field.

Currently, it is fairly well understood the implications assumed by adopting most of the testing conditions commonly prescribed. Studies dealing with the influence of the testing temperature (e.g. [36]), variable pH in the aggressive solution (e.g. [40,41]) or high sulfate concentrations (e.g. [42,43]) on the mechanism of the ESA are available. Research performed

on the influence of other testing conditions is reviewed in the recent RILEM state of the art report from TC 211 [36]. However, the effects associated with the use of non-aggressive curing periods before sulfate exposure and the use of specimens in free-expanding conditions have drawn little attention.

The majority of test methods prescribe curing periods in non-aggressive conditions prior to sulfate exposure. This practice is adopted to allow blended materials to react and reach a minimum strength before the test. However, this conditions are not found in the majority of field structures. As described in section 1.1, ESA is especially relevant in underground structures like foundations, tunnels or waste containers. Due to their size, these are usually built in situ, hence being exposed to sulfates since casting. The delayed exposure of specimens to sulfates is now established as a common practice in almost all experimental studies related to the ESA. The typical age of exposure is 28 days (e.g. [44–48]) for mortars but pre-curing periods may be extended up to 90 days when mineral admixtures are used [49]. This practice indirectly assumes that ESA in field conditions does not induce significant alterations in the material during the first 28 or 90 days of exposure, which might be supported by the common perception that ESA is a slow process. However, further research is needed to verify the hypothesis and fully understand the effects associated to this practice.

On the other hand, test methods usually evaluate sulfate resistance based on length change measurements of specimens in free-expanding conditions, thus assuming the absence of mechanical actions during the attack. However, typical elements such as foundations or retaining walls experience the attack under the combined presence of a variety of stresses due to interactions between different elements of the structure and the soil. Figure 1.6a illustrates this situation with a group of end bearing piles joined at the top by a pile cap subjected to constant external compressive loads (F_{ext}).

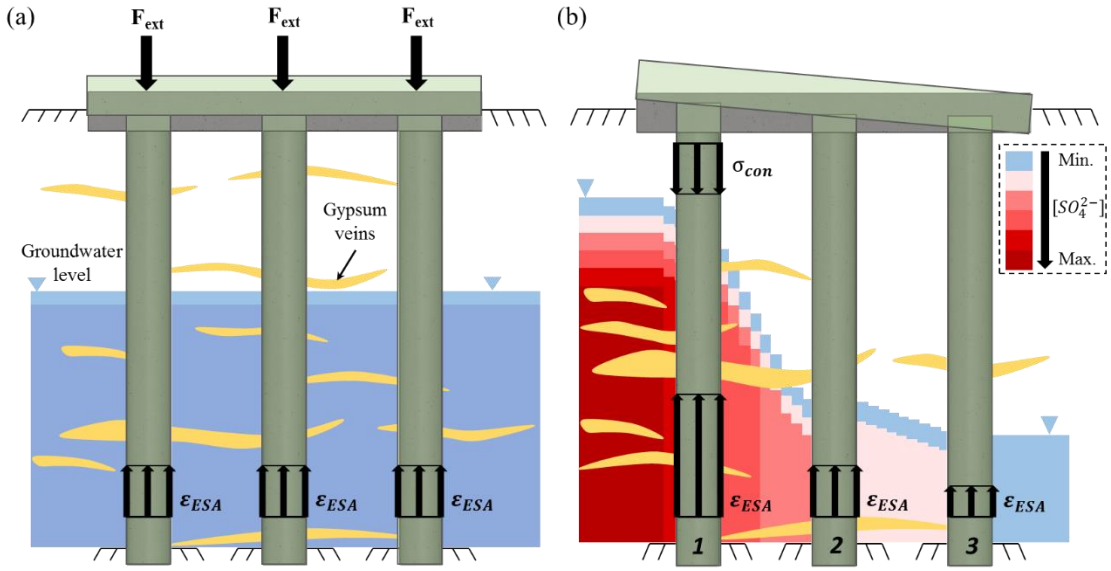

Figure 1.6. Schematic representation of a group of end bearing piles under (a) External loading and (b) Confinement effects.

The coupled action of constant external loads and ESA has been addressed during the last decades. Most studies report that the combined action of sulfate attack and compressive loading results in favorable effects on the durability against the attack for low stress levels. However, compressive stresses accelerate the sulfate attack when the stress is set above a certain threshold value, estimated between the 30-60 % of the ultimate compressive strength

[50–52]. This acceleration is attributed to the generation of microcracks that promotes sulfate penetration [50–52]. In general, studies report similar conclusions for flexural loading applied together with sulfate exposure. In this case, the negative effects are observed especially on the face subjected to tensile stresses when the loading exceeded 40-60 % of the maximum flexural load [53,54].

In all studies presented above, the load was applied from exposure and remained constant until the end of the test. Although this configuration might simulate the effects of underground water, rocks, overlaying soil or dead loads from the superstructure, it does not represent the effects of confinement that might appear in indeterminate structures under different expansion rates. In this case, the load rises as a consequence of the expansions generated by the ESA, thus increasing gradually along the attack. Figure 1.6b illustrates this situation. Due to the heterogenic characteristics of the groundwater level and the distribution of gypsum veins in the soil, the expansive forces generated by the attack (ε_{ESA}) evolve at different rates at each pile. However, highly indeterminate structures act as a single entity prior to failure. Consequently, the least affected elements (pile 2 and 3) restraint the expansions and confine the concrete of pile 1 by applying an increasing compressive load (σ_{con}) in the whole section.

Understanding how stresses generated by confinement interact with the ESA is not only relevant in highly indeterminate structures such as the one represented in Figure 1.6b. In field conditions, ESA frequently only affects a small external fraction of the cross section. In these conditions, the sound core of the element restraints the expansions and confines the external layers in order to ensure equilibrium and compatibility of strains in the cross section. Consequently, the attack in large single elements might also develop under high confining conditions. Unfortunately, the potential effects of stresses generated by confinement remain practically unexplored and are systematically ignored during the assessment of the ESA. Its understanding could lead to more realistic assessments of the attack and contribute to explain the large difference between the damage developed in small-scale free-expanding laboratory specimens and the one observed in real structures.

REFERENCES

[1] J. Marchand, I. Odler, J.P. and Skalny, Sulfate attack on concrete, Spon Press, Taylor & Francis Group, New York, 2002.

[2] A. Neville, The confused world of sulfate attack on concrete, Cem. Concr. Res. 34 (2004) 1275–1296. doi:10.1016/j.cemconres.2004.04.004.

[3] S. Kumar, C.V.S. Kameswara Rao, Effect of sulfates on the setting time of cement and strength of concrete, Cem. Concr. Res. 24 (1994) 1237–1244. doi:10.1016/0008-8846(94)90108-2.

[4] B. Mota, T. Matschei, K. Scrivener, The influence of sodium salts and gypsum on alite hydration, Cem. Concr. Res. 75 (2015) 53–65. doi:10.1016/j.cemconres.2015.04.015.

[5] S. Sarkar, S. Mahadevan, J.C.L. Meeussen, H. van der Sloot, D.S. Kosson, Numerical simulation of cementitious materials degradation under external sulfate attack, Cem. Concr. Compos. 32 (2010) 241–252. doi:10.1016/j.cemconcomp.2009.12.005.

[6] M. Collepardi, A state-of-the-art review on delayed ettringite attack on concrete, Cem. Concr. Compos. 25 (2003) 401–407. doi:10.1016/S0958-9465(02)00080-X.

[7] O.S. Baghabra Al-Amoudi, Attack on plain and blended cements exposed to aggressive sulfate environments, Cem. Concr. Compos. 24 (2002) 305–316. doi:10.1016/S0958-9465(01)00082-8.

[8] W. Kunther, B. Lothenbach, K.L. Scrivener, On the relevance of volume increase for the length changes of mortar bars in sulfate solutions, Cem. Concr. Res. 46 (2013) 23–29. doi:10.1016/j.cemconres.2013.01.002.

[9] BS EN 206, BSI Standards Publication Concrete — Specification , performance , production and conformity, 2013.

[10] ACI Committee 318, Building Code Requirements for Structural Concrete (ACI 318-08) and Commentary, 2008. doi:10.1016/0262-5075(85)90032-6.

[11] Code on Structural Concrete EHE-08, 2008.

[12] BS 8500-1:2015 Complementary British Standard to BS EN 206 Part 1 : Method of specifying and guidance for the specifier, 2015.

[13] BRE construction Division Special Digest 1, Concrete in aggressive ground, 2005.

[14] A. Atkinson, J.A. Hearne, Mechanistic Model for the Durability of Concrete Barriers Exposed to Sulphate-Bearing Groundwaters, MRS Proc. 176 (1989) 149. doi:10.1557/PROC-176-149.

[15] A. Atkinson, D.J. Goult, J.A. Hearne, The influence of wasteform permeability on the release of radionuclides from a repository, Nucl. Chem. Waste Manag. 5 (1985) 203–214. doi:10.1016/0191-815X(85)90079-8.

[16] R. Shuman, V.C. Rogers, R.A. Shaw, The barrier code for predicting long-term concrete performance, Waste Manag. 89 (1989) 701–705.

[17] K.E. Kurtis, P.J.M. Monteiro, S.M. Madanat, Empirical Models to Predict Concrete Expansion Caused by Sulfate Attack, ACI Mater. J. 97 (2000) 156–161. doi:10.14359/818.

[18] P.J.M. Monteiro, K.E. Kurtis, Experimental asymptotic analysis of expansion of concrete exposed to sulfate attack, ACI Mater. J. 105 (2008) 62–71.

[19] J.R. Clifton, J.M. Pommersheim, Sulfate attack of cementitious materials: Volumetric relations and expansions, NISTIR 5390, Natl. Inst. Stand. Technol. (1994) 22.

[20] Y. Maltais, E. Samson, J. Marchand, Predicting the durability of Portland cement systems in aggressive environments - Laboratory validation, Cem. Concr. Res. 34 (2004) 1579–1589. doi:10.1016/j.cemconres.2004.03.029.

[21] E. Samson, J. Marchand, Modeling the transport of ions in unsaturated cement-based materials, Comput. Struct. 85 (2007) 1740–1756. doi:10.1016/j.compstruc.2007.04.008.

[22] B. Lothenbach, B. Bary, P. Le Bescop, T. Schmidt, N. Leterrier, Sulfate ingress in Portland cement, Cem. Concr. Res. 40 (2010) 1211–1225. doi:10.1016/j.cemconres.2010.04.004.

[23] R. Tixier, B. Mobasher, Modeling of Damage in Cement-Based Materials Subjected to External Sulfate Attack. I: Formulation, J. Mater. Civ. Eng. 15 (2003) 305–313. doi:10.1061/(ASCE)0899-1561(2003)15:4(305).

[24] R. Tixier, B. Mobasher, Modeling of Damage in Cement-Based Materials Subjected

to External Sulfate Attack. II: Comparison with Experiments, J. Mater. Civ. Eng. 15 (2003) 314–322. doi:10.1061/(ASCE)0899-1561(2003)15:4(314).

[25] M. Basista, W. Weglewski, Chemically Assisted Damage of Concrete: A Model of Expansion Under External Sulfate Attack, Int. J. Damage Mech. 18 (2009) 155–175. doi:10.1177/1056789508097540.

[26] A.E. Idiart, C.M. López, I. Carol, Chemo-mechanical analysis of concrete cracking and degradation due to external sulfate attack: A meso-scale model, Cem. Concr. Compos. 33 (2011) 411–423. doi:10.1016/j.cemconcomp.2010.12.001.

[27] F. Schmidt-Döhl, F.S. Rostásy, A model for the calculation of combined chemical reactions and transport processes and its application to the corrosion of mineral-building materials Part I. Simulation model, Cem. Concr. Res. 29 (1999) 1039–1045. doi:10.1016/S0008-8846(99)00087-3.

[28] F. Schmidt-Döhl, F.S. Rostásy, A model for the calculation of combined chemical reactions and transport processes and its application to the corrosion of mineral-building materials Part II. Experimental verification, Cem. Concr. Res. 29 (1999) 1047–1053. doi:10.1016/S0008-8846(99)00094-0.

[29] B. Bary, Simplified coupled chemo-mechanical modeling of cement pastes behavior subjected to combined leaching and external sulfate attack, Int. J. Numer. Anal. Methods Geomech. 32 (2008) 1791–1816. doi:10.1002/nag.696.

[30] B. Bary, N. Leterrier, E. Deville, P. Le Bescop, Coupled chemo-transport-mechanical modelling and numerical simulation of external sulfate attack in mortar, Cem. Concr. Compos. 49 (2014) 70–83. doi:10.1016/j.cemconcomp.2013.12.010.

[31] E. Rigo, F. Schmidt-Döhl, M. Krauß, H. Budelmann, Transreac: A model for the calculation of combined chemical reactions and transport processes and its extension to a probabilistic model, Cem. Concr. Res. 35 (2005) 1734–1740. doi:10.1016/j.cemconres.2004.10.004.

[32] M.A. Shazali, M.H. Baluch, A.H. Al-Gadhib, Predicting Residual Strength in Unsaturated Concrete Exposed to Sulfate Attack, J. Mater. Civ. Eng. 18 (2006) 343–354. doi:10.1061/(ASCE)0899-1561(2006)18:3(343).

[33] N. Cefis, C. Comi, Chemo-mechanical modelling of the external sulfate attack in concrete, Cem. Concr. Res. 93 (2017) 57–70. doi:10.1016/j.cemconres.2016.12.003.

[34] S. Sarkar, S. Mahadevan, J.C.L. Meeussen, H. van der Sloot, D.S. Kosson, Numerical simulation of cementitious materials degradation under external sulfate attack, Cem. Concr. Compos. 32 (2010) 241–252. doi:10.1016/j.cemconcomp.2009.12.005.

[35] Y. Yu, Y.X. Zhang, A. Khennane, Numerical modelling of degradation of cement-based materials under leaching and external sulfate attack, Comput. Struct. 158 (2015) 1–14. doi:10.1016/j.compstruc.2015.05.030.

[36] M. Alexander, A. Bertron, N. De Belie, Performance of Cement-Based Materials in Aggressive Aqueous Environments, Springer, 2013. doi:10.1007/978-94-007-5413-3.

[37] ASTM C1012/C1012M-15, Standard test method for length change of hydraulic-cement mortars exposed to a sulfate solution, (2015). doi:10.1520/C1012.

[38] ASTM C452, Standard Test Method for Potential Expansion of Portland-Cement Mortars Exposed to Sulfate, (2002). doi:10.1520/C0452.

[39] ACI Committee 201, 201.2R-16 Guide to durable concrete, 2016. https://www.concrete.org/store/productdetail.aspx?ItemID=201216 (accessed July 20, 2017).

[40] P.K. Mehta, H.H. Haynes, Durability of Concrete in Seawater, J. Struct. Div. 101 (1975) 1679–1686. http://cedb.asce.org/CEDBsearch/record.jsp?dockey=0006150 (accessed July 20, 2017).

[41] P.W. Brown, An evaluation of the sulfate resistance of cements in a controlled environment, Cem. Concr. Res. 11 (1981) 719–727. doi:10.1016/0008-8846(81)90030-2.

[42] M.D. Cohen, B. Mather, Sulfate Attack on Concrete: Research Needs, ACI Mater. J. 88 (1991) 62–69. doi:10.14359/2382.

[43] F.P. Glasser, The thermodynamics of attack on Portland cement with special reference to sulfate, concrete in aggressive aqueous environments, performance, testing and modeling., in: M. Alexander, A. Bertron (Eds.), Concr. Aggress. Aqueous Environ., Toulouse, 2009: pp. 3–17.

[44] J. Stroh, B. Meng, F. Emmerling, Monitoring of sulphate attack on hardened cement paste studied by synchrotron XRD, Solid State Sci. 48 (2015) 278–285. doi:10.1016/j.solidstatesciences.2015.08.006.

[45] I. Sirisawat, W. Saengsoy, L. Baingam, P. Krammart, S. Tangtermsirikul, Durability and testing of mortar with interground fly ash and limestone cements in sulfate solutions, Constr. Build. Mater. 64 (2014) 39–46. doi:10.1016/j.conbuildmat.2014.04.083.

[46] M. Zhang, J. Chen, Y. Lv, D. Wang, J. Ye, Study on the expansion of concrete under attack of sulfate and sulfate-chloride ions, Constr. Build. Mater. 39 (2013) 26–32. doi:10.1016/j.conbuildmat.2012.05.003.

[47] W. Müllauer, R.E. Beddoe, D. Heinz, Sulfate attack expansion mechanisms, Cem. Concr. Res. 52 (2013) 208–215. doi:10.1016/j.cemconres.2013.07.005.

[48] T. Aye, C.T. Oguchi, Resistance of plain and blended cement mortars exposed to severe sulfate attacks, Constr. Build. Mater. 25 (2011) 2988–2996. doi:10.1016/j.conbuildmat.2010.11.106.

[49] C. Yu, W. Sun, K. Scrivener, Degradation mechanism of slag blended mortars immersed in sodium sulfate solution, Cem. Concr. Res. 72 (2015) 37–47. doi:10.1016/j.cemconres.2015.02.015.

[50] W.G. Piasta, Z. Sawicz, J. Piasta, Sulfate durability of concretes under constant sustained load, Cem. Concr. Res. 19 (1989) 216–227. doi:10.1016/0008-8846(89)90086-0.

[51] U. Schneider, W. Piasta, The behaviour of concrete under Na2S04 solution attack and sustained compression or bending, Mag. Concr. Res. 43 (157) (1991) 281–289. http://www.icevirtuallibrary.com/doi/abs/10.1680/macr.1991.43.157.281 (accessed July 20, 2017).

[52] H. Xu, Y. Zhao, L. Cui, B. Xu, Sulphate attack resistance of high-performance concrete under compressive loading, J. Zhejiang Univ. Sci. A. 14 (2013) 459–468. doi:10.1631/jzus.A1300067.

[53] R. Gao, Q. Li, S. Zhao, Concrete Deterioration Mechanisms under Combined Sulfate

Attack and Flexural Loading, J. Mater. Civ. Eng. 25 (2012) 462. doi:10.1061/(ASCE)MT.1943-5533.0000538.

[54] J. Gao, Z. Yu, L. Song, T. Wang, S. Wei, Durability of concrete exposed to sulfate attack under flexural loading and drying-wetting cycles, Constr. Build. Mater. 39 (2013) 33–38. doi:10.1016/j.conbuildmat.2012.05.033.

2. OBJECTIVES, PUBLICATIONS AND STRUCTURE

This chapter describes the general and specific objectives of this thesis, formulated from the discussion presented in Chapter 1. Additionally, it includes the list of publications derived from this work and the structure of the document.

Contents

2.1. GENERAL OBJECTIVE

The objective of the thesis is to examine and improve current numerical and experimental ESA assessment methods. For that, this work seeks to advance knowledge on the numerical modeling of the ESA, shed light on the fundamental mechanisms related to the pore network that determine sulfate resistance and examine the representativeness of typical conditions adopted in accelerated test methods.

2.2. SPECIFIC OBJECTIVES

The specific objectives are grouped within the three main areas of contribution of the thesis.

i. Numerical modeling of the ESA

- Develop a comprehensive model for ESA assessment taking into account the chemical reactions, ionic transport, degradation mechanisms and the mechanical response.

- Propose a numerical approach to capture the early expansions caused by ESA and the different strain contributions from ettringite growing in different pore sizes.

- Propose a direct and intuitive approach to capture the effects of cracking on the diffusion coefficient of sulfates.

- Develop a simplified methodology for ESA assessment that explicitly accounts for the specific conditions found in each application (the aggressiveness of the media, reactivity and mechanical properties of the material and geometrical characteristics of the element under attack).

- Propose a set of simplified equations to estimate the penetration of sulfates.

- Propose a set of simplified equations to assess the risk of failure associated to the ESA.

ii. Role of porosity in the ESA

- Understand the mechanisms defined by the pore network that contribute to the durability against the ESA.

- Understand the influence of porosity on the precipitation patterns of expansive phases.

- Examine the validity and limitations of the volume increase approach commonly adopted in the numerical models to simulate the expansive forces generated during the attack.

- Explore new approaches to design sulfate-resisting materials based on promoting the capacity of the pore network to accommodate expansive phases.

iii. Effects of field-like conditions on ESA assessment

- Evaluate if ESA assessments on specimens in free-expanding conditions can be representative of typical field conditions.

- Understand how confining stresses interact with the normal development of the ESA.

- Evaluate the impact of sulfate exposure shortly after casting on the pore network development during the first 28 and 90 days of curing.

2.3. LIST OF PUBLICATIONS

The publications derived from this thesis are listed below. The area of contribution that each paper addresses is specified in brackets. The publications are grouped into published and submitted papers.

Published papers

JOURNAL PAPER I (*i. Numerical modeling of the ESA*)

Alternative methodology to consider damage and expansions in external sulfate attack modeling, T. Ikumi, S.H.P. Cavalaro, I. Segura, A. Aguado, Cement and Concrete Research 63 (2014) 105-116. Impact factor: 4.1, Q1. DOI: 10.1016/j.cemconres.2014.05.011.

JOURNAL PAPER II (*i. Numerical modeling of the ESA*)

Simplified methodology to evaluate the external sulfate attack in concrete structures, T. Ikumi, S.H.P. Cavalaro, I. Segura, A. de la Fuente, A. Aguado, Materials & Design 89 (2016) 1147-1160. Impact factor: 3.6, Q1. DOI: 10.1016/j.matdes.2015.10.084.

JOURNAL PAPER III (*ii. Role of porosity in the ESA + iii. Effects of field-like conditions on ESA assessment*)

Influence of early sulfate exposure in the pore network development of mortars, T. Ikumi, I. Segura, S.H.P. Cavalaro, Construction and Building Materials 143 (2017) 33-47. Impact factor: 2.4, Q1. DOI: 10.1016/j.conbuildmat.2017.03.081.

CONFERENCE PAPER I (*i. Numerical modeling of the ESA*)

Simplified model to assess the durability of elements subjected to external sulfate attack: Influence of shape and size of the elements, T. Ikumi, S. Cavalaro, I. Segura, A. de la Fuente, A. Aguado. In: Baroghel-Bouny V., Martins I., Menéndez E. (eds) Proceedings of the workshop External Sulfate Attack, Portugal (2017) 131-142. ISBN: 9789724922973.

Submitted papers

JOURNAL PAPER IV (*ii. Role of porosity in the ESA*)

The role of porosity in external sulfate attack, T. Ikumi, S.H.P. Cavalaro, I. Segura, submitted to Cement and Concrete Research in Nov. 2016.

JOURNAL PAPER V (*iii. Effects of field-like conditions on ESA assessment*)

Effects of confinement in mortars exposed to external sulfate attack, T. Ikumi, I. Segura, S.H.P. Cavalaro, submitted to Cement and Concrete Research in Jan. 2017.

2.4. STRUCTURE OF THE DOCUMENT

This document aims to present and discuss the contributions derived from the compilation of papers written during the PhD. For that, this document is divided in 5 chapters. Their content is summarized below:

Chapter 1 includes a brief description of the fundamental mechanisms associated to the ESA and presents the theoretical framework needed to understand the relevance of the topics addressed in this thesis.

Chapter 2 describes the general and specific objectives of the thesis, the list of publications derived indicating the areas of contribution of each paper and the structure of the document.

Chapter 3 reproduces a full version of the published publications.

Chapter 4 reproduces a full version of the publications under revision or pending publication.

Chapter 5 presents a general discussion of the contributions made. The discussion is divided in three parts corresponding to the main areas addressed in the thesis: Numerical modeling of ESA, role of porosity in the ESA and effects of field-like conditions in the ESA assessment. Finally, general and specific conclusions are summarized.

A separate bibliography is included for chapters 1 and 5. Each paper included in Chapter 3 and 4 follows its own numbering of sections, figures, equations and references.

3. PUBLICATIONS: PUBLISHED PAPERS

This chapter reproduces the published journal and conference papers derived from this thesis. Each paper follows its own numbering of sections, figures, equations and references.

Contents

3.1. JOURNAL PAPER I. ALTERNATIVE METHODOLOGY TO CONSIDER DAMAGE AND EXPANSIONS IN EXTERNAL SULFATE ATTACK MODELING

Published in Cement and Concrete Research 63 (2014) 105-116.

Tai Ikumi[a,*], Sergio H.P. Cavalaro[a], Ignacio Segura[a] and Antonio Aguado[a]

[a] Department of Construction Engineering, Universitat Politècnica de Catalunya Barcelona Tech, Jordi Girona 1-3, C1, E-08034 Barcelona, Spain

* Corresponding author: Tai Ikumi Montserrat. Department of Construction Engineering, Universitat Politècnica de Catalunya Barcelona Tech, Jordi Girona 1-3, C1, E-08034 Barcelona, Spain. Email address: tai.ikumi@upc.edu,
Tel: +34 93 401 6507 Fax: +34 93 401 1036

Abstract

A diffusion – reaction numerical model is proposed to simulate the response of concrete exposed to external sulfate attack. Diffusion properties are modified based on the strain reached and the ratio of porosity filled by ettringite. A direct and intuitive approach is proposed for the consideration of the diffusion in a cracked porous media based on the constitutive law of the material. A methodology to compute expansions based on a more realistic consideration of the concrete porosimetry is presented, by which it is possible to distinguish different strain contributions from different pore sizes. The described approach also allows the consideration of different capacities to accommodate expansive product for each pore size considered and the faster filling rate existent in small pores. Critical parameters of the numerical model developed are recognized and established. Expansions obtained by the new model are in good agreement with experimental data published in the literature.

Keywords: Sulfate Attack (C), Concrete (E), Durability (C), Modeling (E), Pore Size Distribution (B)

1- INTRODUCTION

Durability of concrete has become a major issue in structural engineering over the last decades. In 2012, it was estimated that 51.2% of the annual investment in the construction field in EU27 countries (excluding Cyprus, Greece, Luxembourg and Malta) plus Norway and Switzerland, was dedicated to Renovation and Maintenance (R&M), turning concrete durability into a key aspect in the industry [1]. Within this framework, restoring and management systems of existing structures gain prominence, where numerical modelization of degradation phenomena plays an essential role. It is important to highlight that in many cases, once a concrete deterioration process is detected in built structures, the only possible action is of the palliative nature, through a monitoring of the structural behavior. For this, the development of prediction models about the future evolution become crucial.

Degradation of concrete exposed to sulfate solutions has been of concern since the early years of the 19th century [2]. The importance of the external sulfate attack in the concrete degradation processes is usually related to the need of assessing the durability of underground nuclear waste containments, tunnel linings and dams, which may be sometimes in contact with sulfate-rich soils [3-6]. The relative significance of this phenomenon has been questioned over the last decade and, according to Neville [7], the opinion that sulfate attack is not a widespread problem in concrete structures is expressed even by those who have published extensively on the topic. The fact that there are few reported cases of structures in service damaged by sulfates in the soil or in groundwater is supported by several authors [7,8]. Despite all these opinions, most of them based on indisputable facts, now the rate of published papers dealing with the sulfate attack is greater than ever, reflecting a growing interest in the scientific community. This growing interest may be explained by the considerable controversy still existing on basic topics within the sulfate attack phenomenon and the deterioration mechanisms involved, such as the expansion mechanism and the gypsum role on the expansion process [7]. On the other hand, despite structural failures due to sulfate attack are rare, in structures that requires high stability due to a small displacement tolerance, the expansive nature of the sulfate attack should be carefully assessed.

Traditionally, due to the high level of complexity of the external sulfate attack, where transport, chemical and physical processes between sulfate ions and the hydrated compounds of the cement paste are involved [9,10], unilateral efforts have been made into different specific fields to model a specific phenomenon within the overall problem. However, during the last years, a number of advanced comprehensive models have been developed [3,4,11,12], even considering a full tenso-deformational mechanical analysis through a mesostructural representation of the material, able to simulate not only crack formation and propagation, but also its influence on the diffusion-driven process [4].

Every possible mechanical framework that may be developed is based on the expansions obtained through the numerical model. Most of the models referred above [3,4,11] obtain the expansions using a simplified expression described by Tixier & Mobasher [11]. In this expression, the pores capacity to accommodate ettringite is represented by a single buffer coefficient (f). This coefficient is linearly applied to the overall ettringite formation and the overall porosity is considered without differentiating the size of the pores. By this consideration, all the buffer capacity of the matrix has to be filled before the expansions start to be computed. In this way, the early expansions caused by precipitation of ettringite in the small pores, where the capacity to accommodate ettringite is very limited, are neglected. As the expansions computed are the base of any future mechanical consideration, it is believed

that this simplified expression is in contradiction with the sophisticated mechanical framework included in the advanced models. From this situation, the need to explore new ways to compute expansions, according to the degree of complexity and precision incorporated, is highlighted.

The objective of the present work is to present a diffusion – reaction model where a simplified approach of the chemical processes involved in external sulfate attack and the mechanical processes related to ettringite formation in the pores are considered. It is mainly based on the original proposal of Tixier & Mobasher [11], which has been significantly modified by describing a new expression for the diffusion in a cracked porous media and through a new expression to compute the expansions. This new expression is based on a more realistic consideration of the porosimetry of concrete and on the introduction of a new ettringite formation rate ($\mathcal{F}$), which quantifies and distributes ettringite precipitation. By this approach, it is able to distinguish the different strain contributions from different pore sizes. In Figure 1, a schematic diagram of the different processes considered in this model is depicted. Critical parameters of the numerical model developed will be recognized and established. Finally, expansions obtained by the new model will be compared to experimental data by Brown [13] and Ferraris et al. [14].

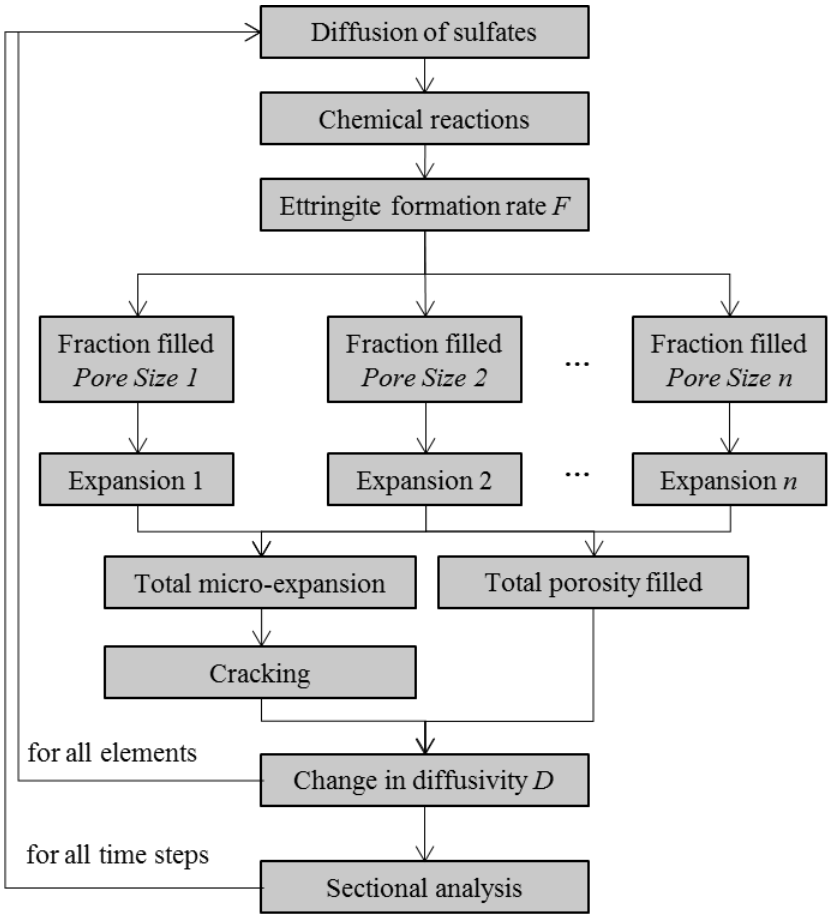

Fig. 1. Processes considered in the model.

2- DESCRIPTION OF THE CHEMO – TRANSPORT MODEL

2.1- CHEMICAL REACTIONS CONSIDERED

In this model, it is considered that the deterioration process related to external sulfate attack is caused by the potential volume expansions associated to the chemical reactions of sulfate ions with the unreacted hydration compounds of the cement paste. Eqs. (1)-(4) describe the series of reactions considered to take place when the sulfate ions penetrate a cement based structure. This process is initiated by the reaction of sulfate ions (SO_4^{2-}) with calcium hydroxide (CH) to form gypsum ($C\bar{S}H_2$) (Eq. (1)).

$$CH + SO_4^{2-} \rightarrow C\bar{S}H_2 + 2OH^- \tag{1}$$

Gypsum formation is considered as an intermediate phase that later may react with the aluminate phases to form secondary ettringite ($C_6A\bar{S}_3H_{32}$) [11,15,16,17]. Three calcium aluminates phases are considered as described in Eqs. (2)-(4): tricalcium aluminate (C_3A), tetracalcium aluminate (C_4AH_{13}) and monosulfate ($C_4A\bar{S}H_{12}$). Note that no direct reactions between the sulfate solution ions and aluminate phases are contemplated, since it is assumed that all ingressing sulfates react first with calcium hydroxide to form gypsum.

$$C_3A + 3C\bar{S}H_2 + 26H \rightarrow C_6A\bar{S}_3H_{32} \tag{2}$$

$$C_4AH_{13} + 3C\bar{S}H_2 + 14H \rightarrow C_6A\bar{S}_3H_{32} + CH \tag{3}$$

$$C_4A\bar{S}H_{12} + 2C\bar{S}H_2 + 16H \rightarrow C_6A\bar{S}_3H_{32} \tag{4}$$

It is assumed that the expansions are caused only by the formation of secondary ettringite. The role of gypsum in the expansion mechanism is still far from clear [7], so in this study, the expansive nature of gypsum formation is not considered. As previously proposed by Tixier & Mobasher [11], and afterwards used by other researchers [4,17], Eqs. (2)-(4) are lumped in a single expression to simplify the numerical treatment (Eq. (5)). It should be noticed that by this simplification, one single chemical reaction rate will be used to define the kinetics of the reactions between the three calcium aluminates reactive phases and the gypsum formed.

$$CA + qC\bar{S}H_2 \rightarrow C_6A\bar{S}_3H_{32} \tag{5}$$

In Eq. (5), CA refers to the equivalent calcium aluminates (see Eq. (6)) and q represents the stoichiometric weighted coeficcient of the sulfate phase (see Eq. (7)).

$$CA = \gamma_1 C_3A + \gamma_2 C_4AH_{13} + \gamma_3 C_4A\bar{S}H_{12} \tag{6}$$

$$q = 3\gamma_1 + 3\gamma_2 + 2\gamma_3 \tag{7}$$

In Eqs. (6)-(7), the coefficients γ_i used are defined as the proportion of each aluminate phase to the total aluminate content.

2.2- DIFFUSION – REACTION MODEL

The deterioration processes defined by the chemical reactions take place depending on the availability of sulfate ions and calcium aluminates. Its concentrations are computed, for each time and space considered in the discretization of the structure, through a diffusion-reaction model based on the Fick's second law. It takes into account the diffusion of sulfate ions under a concentration gradient and its depletion due to gypsum formation.

Depending on the geometry of the structure under study, different formulations of the diffusion-reaction model are provided in Table 1. In this work, diffusion flux is classified as approximately unidirectional (typical in large elements with one dimension much smaller than the other two) and radial (typical in elements with small circular cross section, i.e. elements with two dimensions much smaller than the other one), where an intensification of the ingressing sulfate ions flux is produced as they progress towards inner layers. As underground and founding constructions are the most likely to be subjected to the external sulfate attack, in Table 1 it is also included the most representative underground structural typologies for both cases, although it is equally applicable to other typologies.

Table 1. Diffusion – Reaction model formulation.

Diffusion Flux	Representative Structural Typologies	Formulation	
One-dimensional	Diaphragm walls or tunnels	$\frac{\partial C_{SO}}{\partial t} = \frac{\partial}{\partial x}\left[D\frac{\partial C_{SO}}{\partial x}\right] - kC_{CA}C_{SO}$	(8)
Radial	Piles	$\frac{\partial C_{SO}}{\partial t} = D\left(\frac{\partial^2 C_{SO}}{\partial R^2} + \frac{1}{R}\frac{\partial C_{SO}}{\partial R}\right) - kC_{CA}C_{SO}$	(9)

One additional equation is also considered in both cases (Eq. (10)) to account for the calcium aluminates depletion to form ettringite.

$$\frac{\partial C_{CA}}{\partial t} = -\frac{kC_{CA}C_{SO}}{q} \tag{10}$$

Eqs. (8)-(10) denote C_{SO} as sulfate concentration in the aggressive soil, C_{CA} as aluminate concentration, D as the effective diffusion coefficient, k as the lumped rate of take-up sulfates and R as the radius of the structure. The formulation used in the subsequent simulations is the one corresponding to radial diffusion fluxes, as the experimental results used to validate the present model were obtained from mortar bars with one dimension considerably larger than the other two.

2.3- DIFFUSION COEFFICIENT OF SULFATE IONS

Due to the chemical reactions triggered by the migration of sulfate ions throughout the capillary pores of concrete, the effective diffusivity of sulfate ions is highly dependent on the current stage of the degradation process. In this work, the diffusion coefficient is assumed to be dependent on the pore filling effect and on the damage state of the concrete matrix due to the expansive nature of ettringite. In this way, two parallel effects are computed for the calculation of the effective diffusion coefficient for each time and space considered: a decrease in diffusivity due to pore filling by ettringite and an increase of diffusivity due to cracking and spalling phenomena.

2.3.1- Pore filling effect

The effective diffusivity of sulfate ions through concrete is decreased by the precipitation of ettringite in the pore system, as it constrains the transport paths for the ions diffusion. Different proposals may be found in the literature to consider the pore filling effect [4,18,19]. In this work, the hyperbolic function proposed by Idiart et al. [4] has been adopted, which yields comparable trends to the relationship proposed by Samson & Marchand [19] and has the advantage to explicitly depend on the initial porosity (φ_0). The diffusion coefficient is calculated according to Eq. (11).

$$D = D_{min} + (D_0 - D_{min}) \cdot \frac{e^{-\beta_D} \cdot \frac{\varphi}{\varphi_0}}{1 + (e^{-\beta_D} - 1)\frac{\varphi}{\varphi_0}} \tag{11}$$

To simplify the mathematical representation of the diffusion phenomenon it is assumed that the system is saturated and all pores are accessible. In Eq. (11), φ represents the updated porosity value, calculated by the Eq. (12). The term β_D is a shape factor, adjusted in 1.5 as proposed by Idiart [16]. The initial capillary porosity is calculated by Powers model. Note that the hyperbolic function is defined within two limit values of the diffusion coefficient: D_0, representing the initial diffusivity (when $\frac{\varphi}{\varphi_0} = 1$) and D_{min}, representing the minimum diffusivity yield when all the pore system is filled by ettringite (when $\frac{\varphi}{\varphi_0} = 0$).

$$\varphi = Max[\varphi_0 - \alpha_s CA^{react}, 0] \tag{12}$$

In Eq. (12), the term $\alpha_s CA^{react}$ represents the porosity filled by ettringite formation, which, due to the chemical reactions considered, is computed by the calcium aluminates reacted. The parameter α_s, which corresponds to a converting factor to obtain the volumetric expansion from the amount of aluminates reacted, is defined in Eq. (17).

2.3.2- Cracking effect

The volumetric expansion caused by ettringite formation can lead to cracking and spalling of the cementitious matrix when the stress produced by the expansions reaches the tensile strength of the material. This process increases the diffusivity of sulfate ions through the concrete matrix, as easier paths towards the inner layers may be found.

Traditionally, the increase in diffusivity due to cracking was related to a damage parameter (*w*) defined by an isotropic damage model based on continuum damage mechanics [3,11,15]. In this work, a more direct and intuitive approach is presented, based on the idea that the loss of concrete strength is directly related to the cracking state of concrete, and hence, to the increase in diffusivity. It is important to remark that special types of failure could occur in elements with large or singular geometries subjected to large deformations. Such failures are related with the stress distribution inside the elements generated to maintain the strain compatibility and might occur outside the zone directly affected by the expansion. The simplified model proposed in this study do not account for this phenomenon, even though it is capable of simulating the repercussion of the damage in the diffusion mechanism in zones affected by the expansions. Despite that, the model should be valid as long as these special types of failure do not occur or if their influence on the diffusion mechanism remains small. In cases these conditions may not be guaranteed, more advanced simulation should be performed, for instance with coupled FEM.

This approach is based on the constitutive law of the material, depending on the elastic and the inelastic strain that may be present. The former corresponds to the elastic deformation of the material (ε^e), and the latter corresponds to the contribution of cracking (ε^c). In one dimension, the strain decomposition is represented by Eq. (13).

$$\varepsilon = \varepsilon^e + \varepsilon^c \tag{13}$$

To represent this behavior, a rheological model composed by an elastic spring that introduces the elastic strain (ε^e) is coupled with a unit representing the contribution of the crack (ε^c) [20]. As shown in Figure 2, both unities transmit the same stress since they are coupled in series.

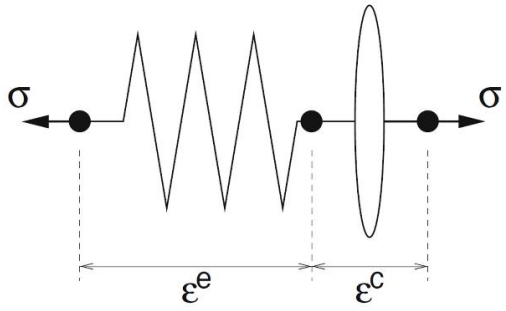

Fig. 2. Rheological model of strain decomposition [20].

To be able to distinguish the elastic and inelastic contribution of the total strain, a simplified constitutive law of the material has to be defined. In Figure 3, the simplified constitutive law chosen is depicted and the nomenclature used in the subsequent definition of this new proposal is defined.

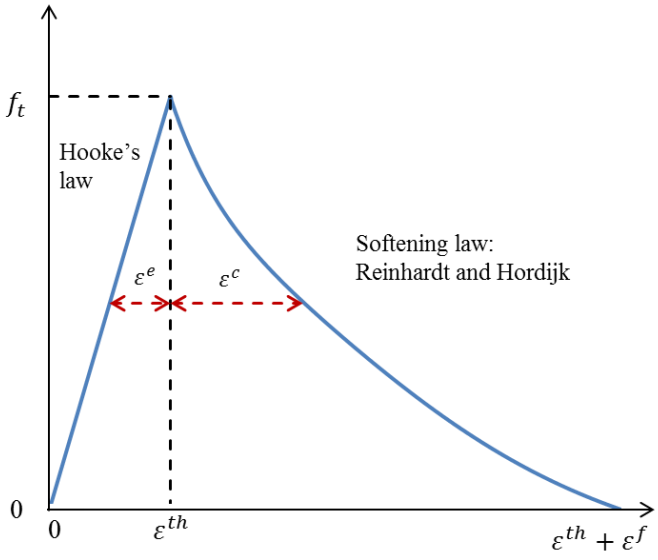

Fig. 3. Material simplified constitutive law.

The ascending branch is defined by a linear elastic response of the concrete, based on Hook's law, until ε^{th} is reached. In this region, only the elastic behavior is observed since the material is practically undamaged. When the stress reaches the tensile strength of the material (f_t), the crack formation is initiated. After crack initiation, the softening non-linear law considered is the one proposed by Reinhardt and Hordijk [21] (Eq. 14).

$$\sigma = f^c(\varepsilon^c) \equiv f_t \left\{ \left[1 + \left(\frac{c_1 \varepsilon^c}{\varepsilon^f} \right)^3 \right] exp\left(-\frac{c_2 \varepsilon^c}{\varepsilon^f} \right) - exp^{-c_2}(1 + c_1^3) \frac{\varepsilon^c}{\varepsilon^f} \right\} \quad (14)$$

As may be seen in Eq. (14), the softening law is completely defined by the material's uniaxial tensile strength (f_t) and the strain at which the crack becomes stress-free (ε^f). The physical significance of the strain ε^f corresponds to a material where the strength loss is total, so the sulfate ions diffusivity reach the maximum value. The reference parameter for the definition of the exponential softening law is the fracture energy G_F, which represents the amount of energy released after cracking occurs. This is equivalent to the area below the stress-strain curve for a strain bigger than ε^{th}. In the present model, the value of G_F may be estimated through Eq. (15), obtained through the integration of Eq. (14) depending on a characteristic cracking length (l_{ch}) [21]. For the simulations performed in this paper, the value of c_1 and c_2 were defined respectively as 3 and 6.93, in accordance with the recommendation from Hordijk [21]. This entails fracture energy equal to 0.159 kN/m for a characteristic length of 26 mm.

$$\begin{aligned} G_F = \int_0^{\varepsilon^f} l_{ch}\, \sigma d\varepsilon \\ = l_{ch} f_t \varepsilon^f \left\{ \frac{1}{c_2} \left[1 + 6 \left(\frac{c_1}{c_2} \right)^3 \right] \right. \\ \left. - \left[\frac{1}{c_2} + {c_1}^3 \left(\frac{1}{c_2} + \frac{3}{{c_2}^2} + \frac{6}{{c_2}^3} + \frac{6}{{c_2}^4} \right) + \frac{1}{2}(1 + {c_1}^3) \right] exp(-c_2) \right\} \end{aligned} \quad (15)$$

From a given linear strain, it is possible to distinguish the elastic and inelastic contributions of the total strain measured through the material constitutive law defined in Figure 3. As the degree of concrete strength loss (i.e. the degree of cracking) is defined by the inelastic contribution, only this part of the total strain causes the formation of cracks that modify the diffusivity. Therefore, to consider the influence of cracking on sulfates diffusivity, a relation between inelastic strains and diffusion coefficient must be defined.

In this regard, according to the strain level reached, uncracked, cracked and fully cracked regions are defined (Figure 4). The uncracked region covers the domain where the inelastic strain is equal to zero since the tensile strength of the material has not been reached and only elastic strain is observed. In this domain the diffusivity is not increased. On the other hand, in the cracked zone, the strain reached is high enough to develop inelastic contributions. Consequently, the diffusivity is increased by the cracking until a maximum diffusivity value is reached (D_{max}). This maximum value, corresponds to the strain where the concrete strength loss is total. As this new proposal is based on the idea that concrete strength loss is directly related to the cracking state of the material, the slope of this curve will be defined by the tangent of the softening curve defined in the material constitutive law (see Figure 3). Once the maximum diffusivity value is reached, it will remain constant for further deformations.

In the literature, no agreement was found in the definition of the upper bound (D_{max}) of the function depicted in Figure 4, representing the diffusivity of sulfate ions in a medium that has lost all its capability to carry stresses. Since few experimental studies may be found on the diffusion of sulfate ions through cracked concrete specimens, results from chloride migration test are commonly used to quantify this parameter. Although in this case more results are available, different increase factor of chloride diffusivity are suggested. Gerard & Marchand [22] quantify the increase factor from 2 to 10, whereas Sahmaran et al. [23] assessed increasing factors of 200 for a crack width of 400 μm. According to the results of

Djerbi et al. [24], Idiart et al. [4] proposed that in a completely cracked medium, the diffusion coefficient tends to reach the diffusivity in free solution.

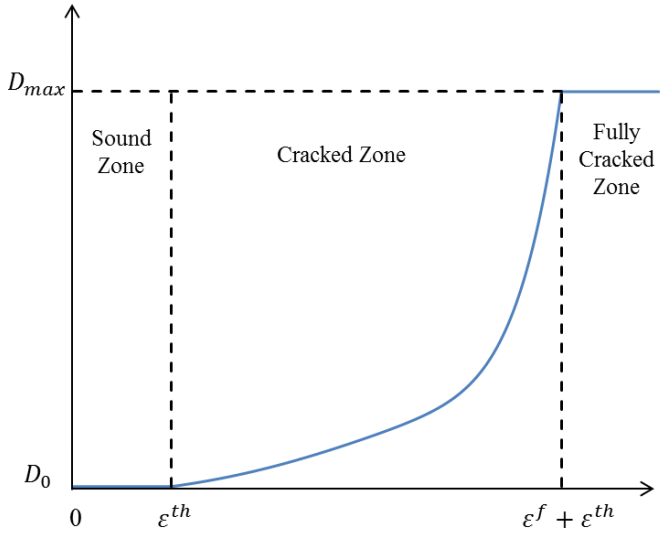

Fig. 4. Increase of diffusivity according to the strain level reached.

The value adopted in this paper for the upper bond diffusivity (D_{max}) is the free solution diffusivity, which Gerard & Marchand [22] quantified as 10^{-9} m^2/s. Although the authors acknowledge that the ions are able to move freely only within cracks, given the lack of agreement in the quantification of an upper bound for the diffusion coefficient, it was decided to fix this value at the diffusivity in free solution. Notice that other considerations based on reliable experimental results may also be used in the model if appropriate.

3- MODELING VOLUMETRIC EXPANSIONS

Amongst the several mechanisms that have been suggested in the literature to explain how the precipitation of ettringite leads to expansion, two theories stand as the most discussed [25]. In the first of them, expansion are a result of the additional volume generated by ettringite formation (e.g. [3,11,17,26]). In the second of them, expansions are caused by the crystallization pressure exerted on the pore walls due to the formation of ettringite from supersaturated solution within small pores (e.g. [25,27]). The latter theory is supported by recent publications [25,28,29], placing this approach as the most plausible theory [29]. Nevertheless, the use of the volume increase approach has persisted in the literature even though it lacks an explanation for the force needed to cause the expansions. The reason may be found in the inherent difficulties associated to the modelization of the crystallization pressure theory, where pores cannot be treated as independent elements and interconnectivity between them must be taken into account during the crystallization process.

Due to the need of simplifying the computational modelization, the first approach is used here, assuming that the volumetric strain is the result of the volume change associated with the chemical reactions. A new way to compute expansions is presented, by which it is possible to obtain the different strain contributions provided by each pore size. This new proposal is more representative of the real situation and is able to reflect some important effects described by the crystallization pressure theory since it takes into account the greater contribution of the small pores in the overall expansion. In fact, the new model proposed opens up the possibility of combining both theories given that the crystallization pressure

may be used as an indirect qualitative reference to define the buffer sulfate concentration depending on the pore size.

Expansions are defined by the previously mentioned chemical reactions considered in the model. In this work, ettringite is considered as the only reaction product governing the expansions of the structure. As mentioned before, the possible expansion due to gypsum formation is neglected. The additional volume generated by the reaction products is calculated by using stoichiometric constants [26]. As described in Eq. (5), ettringite formation is directly defined by the calcium aluminates reacted, thus the volumetric strain can be calculated by the amount of calcium aluminates reacted. According to the three aluminate phases considered in the present model, the additional volume can be calculated as indicated in Eq. (16).

$$\frac{\Delta V}{V} = \sum_{1}^{3} \frac{\Delta V_i}{V_i} \frac{M_i}{\rho_i} \frac{C_i}{\sum_1^3 C_i} \cdot CA^{react} \tag{16}$$

The term $\Delta V_i/V_i$ is the volumetric change of each reaction in Eqs. (2)-(4), whose values are listed in Table 2. The weight of each aluminate phase is quantified by the term $C_i/\sum_1^3 C_i$, where C_i correponds to the total concentration of each aluminate phase considered. The term M_i/ρ_i corresponds to the molar volume of each aluminate phase and CA^{react} is the total concentration of calcium aluminates reacted to form ettringite. According to the notation previously used to define the decrease of diffusivity due to pore filling (Eq. (12)), α_s can be expressed as in Eq. (17).

$$\alpha_s = \sum_{1}^{3} \frac{\Delta V_i}{V_i} \frac{M_i}{\rho_i} \frac{C_i}{\sum_1^3 C_i} \tag{17}$$

Table 2. Values of volume change for each reaction.

Chemical Reaction	$\Delta V_i/V_i$
Eq. (2)	1.31 [26]
Eq. (3)	0.48 [30]
Eq. (4)	0.55 [26]

Whether expansion actually occurs or not, will depend on the capacity of the pore structure to accommodate ettringite as well as on the capacity of the matrix to resist expansive stresses [11,26,31]. All recent models based on the additional volume generated approach use the expression presented by Tixier & Mobasher (Eq. 18) [11].

$$\varepsilon_v = \frac{\Delta V}{V} - f\varphi_0 \tag{18}$$

The second term ($f\varphi_0$) represents the fraction of the concrete initial porosity that has to be filled prior expansion starts, usually fixed in a range between 5%-40% [11]. Note that the buffer coefficient is linearly applied to the overall ettringite formation and the overall porosity is considered without differentiating the size of the pores. This is equivalent to say that in the precipitation process, the amount of ettringite inside each pore is proportional to its volume. This situation is represented in Figure 5, where all the complexity of the concrete porosimetry is reduced to a single pore, where all ettringite precipitates in. Consequently, it is indirectly assumed that the expansion occurs simultaneously in all pores, regardless of their size. However, this contradicts the observation from Scherer [27], which showed an inverse

relationship between the pressure exerted and the size of the pore. Therefore, crystals growing in small pores, with a low capability to accommodate ettringite, are more likely to generate important pressures to the pore wall.

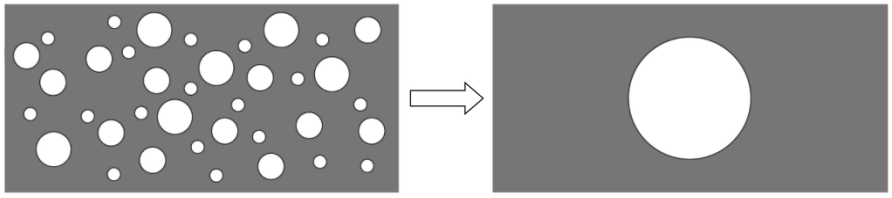

Fig. 5. Schematic representation of the simplification made on concrete porosimetry.

To account for these phenomena, a new simplified approach is presented. It considers an ettringite formation rate ($\mathcal{F}$) which quantifies and distributes the ettringite within the different pore sizes considered in the discretization of the concrete porosimetry. The formation rate $\mathcal{F}$ is defined in Eq. (19) as a constant parameter within each cell and time step considered.

$$\mathcal{F} = \frac{Q_T}{S_T} \tag{19}$$

The term Q_T is the volume of ettringite precipitated, described in Eq. (20). The term S_T is the total pores surface, described in Eq. (21). In Figure 6, a schematic representation of those parameters is depicted.

$$Q_T = \frac{\Delta V}{V} V_{cell} \tag{20}$$

$$S_T = \sum_{i=1}^{n} S_i = \sum_{i=1}^{n} n_i 4\pi R_i^2 \tag{21}$$

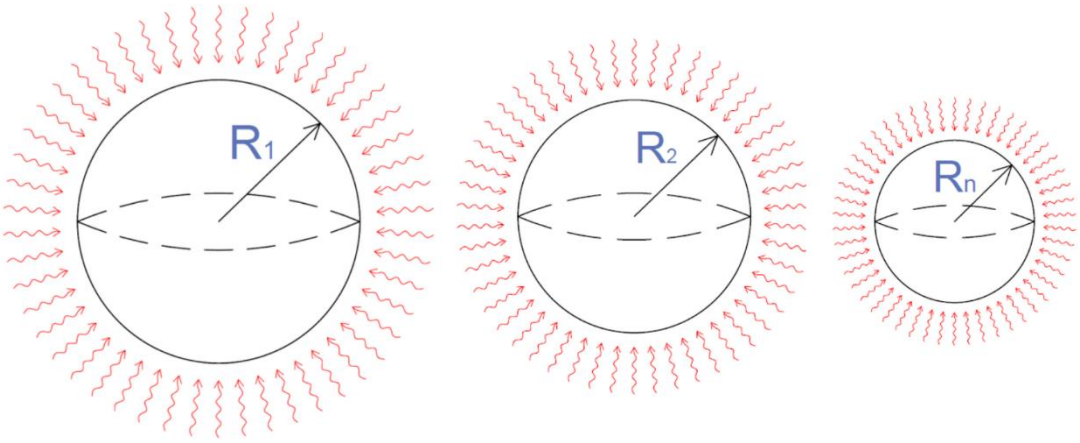

Fig. 6. Representation of the different pore sizes under the incidence of the ettringite formation rate $\mathcal{F}$.

The term R_i is the radio of the pore size *i* and V_{cell} corresponds to the total volume of the cell under consideration. The term n_i is the number of pores of each pore size, as described in Eq. (22).

$$n_i = \frac{V_{cell}\varphi_0 X_\mathrm{i}}{4/3\pi R_i^3} \tag{22}$$

As can be seen in Eq. (22), pores are considered to have a round shape. The only parameter not yet defined is X_i, which represents the pore ratio of each size. Both parameters R_i and X_i can be defined by a pore size distribution diagram, commonly obtained through mercury intrusion porosimetry (MIP). From the porosimetry distribution, the curve obtained can be discretised into a finite number of pore sizes. Once the discretization is defined, X_i is obtained through a simple area ratio as defined in Eq. (23). The equivalent radius R_i is estimated as the mean radius for each pore size considered.

$$X_i = \frac{A_\mathrm{i}}{A_T} \tag{23}$$

This procedure is represented in Figure 7, which depicts the porosimetry distribution of a CEM I 42.5 R/SR concrete, with a simple discretization of the pores into three pore sizes according to the capillary pore classes defined by Mindess [32]. Each $\mathrm{X_i}$ can be obtained by a simple area ratio between the colored areas.

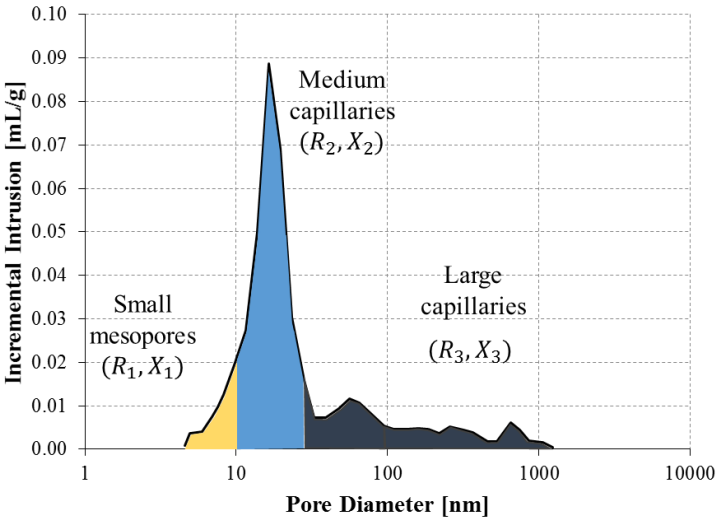

Fig. 7. Example of the pore size discretization.

Once the formation rate term $\mathcal{F}$ is defined, the criteria by which the amount of ettringite formed is distributed within the different pore sizes is assessed. The crystallization process of ettringite is a complex dynamic phenomenon where the effects of the interconnectivity of the pore network play an essential role. However, due to the simplifying assumptions adopted for computational modelization, these effects are not taken into account explicitly such as in the crystallization theory. From Eq. (19), the volume of ettringite precipitated in each pore of size i can be defined as the ettringite formation rate $\mathcal{F}$ present in the cell multiplied by the corresponding internal surface of the pore S_i. Therefore, as described in Eq. (24), pores with bigger surface, will receive more volume of ettringite.

$$Q_i = \mathcal{F} S_i \tag{24}$$

However, the initiation of the expansion is not related with the total amount of ettringite but with the proportion of the pore that is filled. Concerning the numerical model, the amount of ettringite precipitated in each pore size is not relevant. That is why the above mentioned equation is divided by its corresponding pore volume V_i.

$$\frac{Q_i}{V_i} = \mathcal{F}\frac{S_i}{V_i} \tag{25}$$

In Eq. (25), Q_i/V_i is the pore volume ratio filled by ettringite. Through this expression, it can be seen that small pores, with a high S_i/V_i ratio, are filled faster than bigger pores. Hence, despite small pores receive a lower amount of ettringite compared to bigger pores (Eq. (24)), they are filled faster, due to its higher S_i/V_i ratio (Eq. (25)).

Finally, the volumetric expansion (ε_v), is obtained by considering the contribution to the volumetric expansion of each pore size (ε_i):

$$\varepsilon_i = Max\left[\frac{Q_i}{V_i} - f_i, 0\right]\frac{V_i}{\sum V_i} \tag{26}$$

$$\varepsilon_v = \varepsilon_1 + \varepsilon_2 + \cdots + \varepsilon_n \tag{27}$$

It should be noted that through the new equation to compute expansions (Eq. 26), it is possible to define a different buffer coefficient (f_i) for each pore size. Therefore, it is able to consider the lower capability of small pores to accommodate ettringite without exerting pressure to the pore walls. However, in the model proposed in this paper, the influence of the interconnectivity of the pore network in the pressure stability and in the ettringite precipitation is not taken into account explicitly such as in the crystallization theory. This effect is simulated indirectly by means of a minimum sulfate concentration required for expansion, which varies with the pore size.

This new proposal, based on the simplified approach that considers expansions as the result of the additional volume generated by ettringite formation, is not only applicable to the external sulfate attack phenomenon, but to every single deterioration process associated to the precipitation of expansive reaction products within the pore network.

4- PARAMETRIC STUDY

In order to detect the critical parameters of the numerical model developed, a parametric analysis was conducted in which five parameters were considered. As shown in Figure 8, the influence of each parameter is evaluated by the aluminates depletion profile. The advance of the reaction front is evaluated at three different points to define its amplitude. This provides information regarding which is the governing process: the diffusion or the chemical reaction.

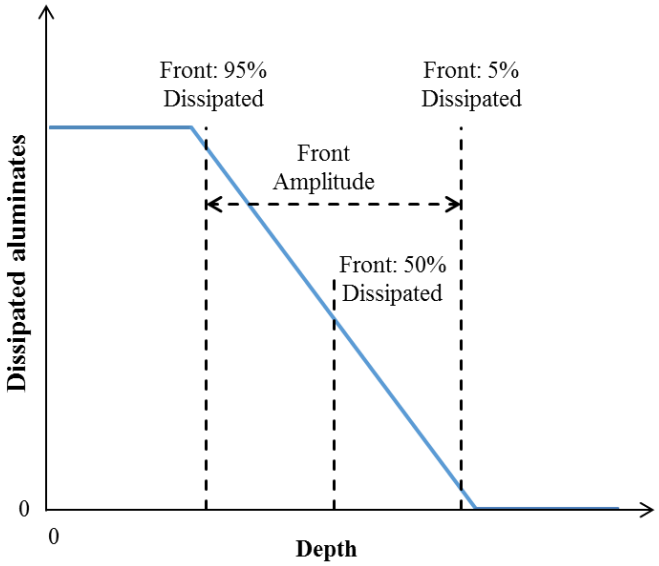

Fig. 8. Definition of the criteria used to evaluate the influence of the parameters.

The parameters considered and its ranging values are listed on Table 3. The ranges were defined according to realistic values found in the literature. The parameter under study is varied within a range defined by the maximum and minimum values while the other parameters are fixed in its reference values. Total time simulated is fixed at 5 years. The porosimetry distribution used in this study is based on the MIP results obtained by Abdelkader for a 28 days concrete CEM I 42.5 R/SR [33]. The curve is discretized in 4 pore sizes and the corresponding pore ratios are obtained through Eq. (23). In Table 4, values of X_{i} and R_i used during the simulations are listed. The buffer coefficients (f_i) are fixed at the same value in all pore sizes considered for each simulation.

Table 3. Range of parameters: preliminary parametric study.

	k [$\mathrm{m^3/mol \cdot s}$]	f_i	D_0 [$\mathrm{m^2/s}$]	C_{CA} [$\mathrm{mol/m^3}$]	C_{SO} [$\mathrm{mol/m^3}$]
Reference	10^{-8}	0.15	10^{-12}	130	50
Minimum	10^{-9}	0.05	10^{-13}	60	10
Maximum	10^{-7}	0.40	10^{-11}	190	100

Table 4. Discretization of the porosimetry distribution.

X_1 [%]	X_2 [%]	X_3 [%]	X_4 [%]	R_1 [nm]	R_2 [nm]	R_3 [nm]	R_4 [nm]
8	10	22	60	3.5	6	10	100

More than 75 simulations were carried out in the parametric study in order to detect which parameters influence more the response of the model. According to the criteria defined to evaluate the influence of the different parameters considered, the reaction front variation is evaluated. To quantify it, the variation of the curve which corresponds to the 50% reacted is assessed within the range under study. Table 5 shows the ranked list that has resulted from this analysis. The sulfate concentration in the aggressive soil (C_{SO}) and the lumped rate of take-up sulfates (k), resulted to be the most influencing parameters on the reaction front. On the other hand, changes in the initial diffusivity (D_0) and calcium aluminates concentration (C_{CA}) do not affect significantly the reaction front.

Table 5. Ranking of parameters resulted from the preliminary parametric study.

Order	Parameter	Reaction Front Variation
1	Sulfates concentration, C_{SO}	4.35 cm
2	Lumped rate of sulfates take-up, k	2.92 cm
3	Buffer coefficient, f_i	2.04 cm
4	Initial diffusion coefficient, D_0	1.19 cm
5	Aluminates concentration, C_{CA}	1.15 cm

Figure 9a shows the variation of the reaction front for different values of the sulfate concentration (C_{SO}). A uniform increase in the reaction front is depicted when the sulfate concentration increases within the range defined. Regarding the front amplitude, it can be seen that it remains constant during the whole range under study. This behavior means that variations in the sulfate concentration do not modify the weight of the two processes involved (diffusion and chemical reactions). In Figure 9b, the influence of the lumped rate of take-up sulfates (k) is evaluated. In this case, the reaction front shows an important increment for values between the minimum (10^{-9} m^3/mol·s) and the reference (10^{-8} m^3/mol·s). This important increment is related to crack initiation, which results into an amplification of the effective diffusivity. For values above the reference, the increment in the reaction front is more moderate and tends to stabilize. As expected, the front amplitude shows a high influence on the lumped rate k. For low values of k, the front amplitude increases considerably, showing that the diffusion process is gaining prominence in comparison to the chemical reaction process. While for high values of k, the front amplitude is considerably reduced. This reduction can be explained by the fact that with an increase of the reaction rate, a higher number of diffusive sulfate ions are involved in chemical reactions as they progress towards inner layers, so they are no longer available for the diffusion process.

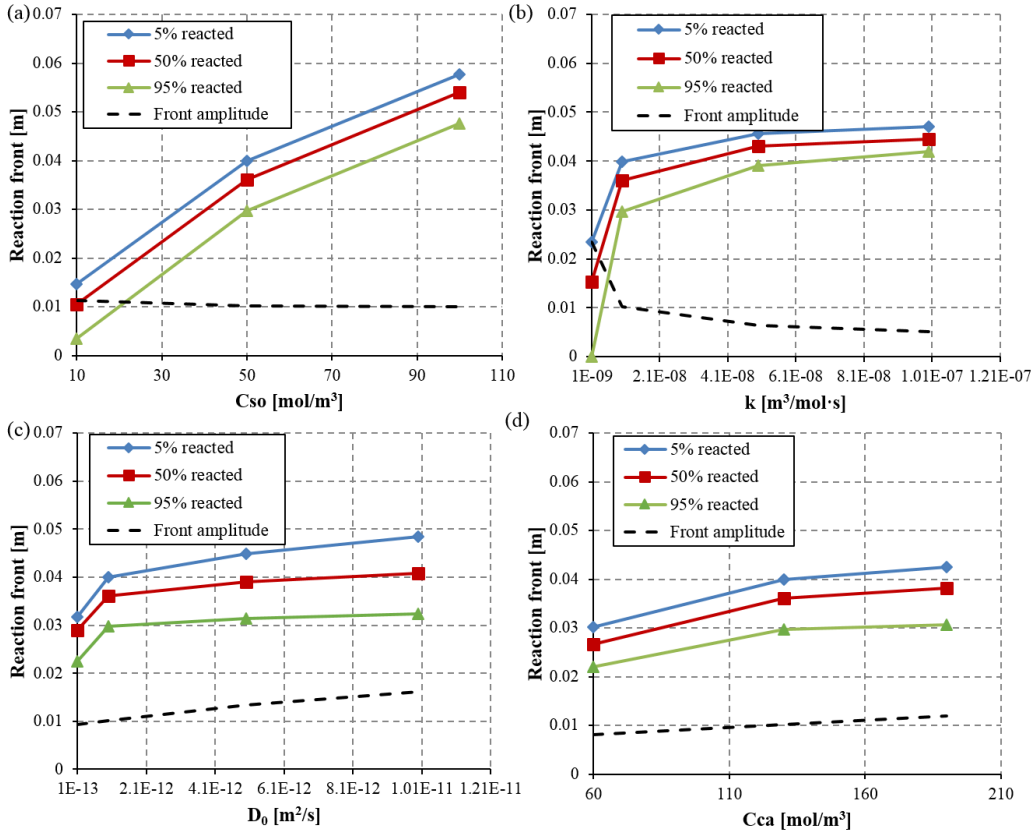

Fig. 9. Influence on the reaction front of: (a) C_{SO}, (b) k, (c) D_0 and (d) C_{CA}.

The influence of the initial diffusivity (D_0) on the reaction front is depicted in Figure 9c. It can be seen that variations in diffusivity between 10^{-13} m^2/s to 10^{-11} m^2/s do not affect significantly the penetration of the reaction front. It is important to note that the influence gain prominence when the 5% reacted front, which is the most representative of the diffusion process, is evaluated. However, the 95% reacted front, more representative of the chemical reaction process, is barely affected by the initial diffusivity. As a result, the front amplitude shows an important increase within the range under study. Reflecting the fact that this parameter has more influence on the diffusion process rather than on the chemical one.

In Figure 9d the influence of calcium aluminates concentration (C_{CA}) is represented. This parameter showed the smallest influence on the reaction front amongst all the parameters considered. It should be remembered that in this study, the influence on the expansions profile, where the aluminates concentration is a key parameter, is not evaluated. Surprisingly, the front amplitude shows a slight increment with the increase of calcium aluminates. This fact means that the increase on the reaction front when the aluminates concentration increases is caused, to a greater extend, by the diffusion process.

Finally, the buffer coefficient (f_i) is evaluated. This parameter is placed in a different set of figures because in this case, the results obtained by the consideration of different pore sizes are also compared to the ones obtained by the traditional approach, which does not differentiate the size of the pores. In Figure 10a the influence on the reaction front is depicted. As expected, the reaction front decreases as the buffer capacity increases, since more ettringite can be accommodated in the pores. However, the uniform slope of this tendency was not so expected. To understand this behavior, in Figure 10b the results obtained are compared to the traditional unified buffer coefficient approach. For clarity, only the curves corresponding to the 50% reacted front are depicted in both cases. It can be seen that by considering different pore sizes, the reaction front always reaches higher values. Therefore, the influence of the buffer coefficient is considerably reduced. This behavior may be explained by the fact that through the consideration of different pore sizes, expansions start to compute earlier, as small pores have a limited capacity to accommodate ettringite crystals. This expansions will trigger the increase in diffusivity due to cracking since earlier stages, so the reaction front will penetrate more into inner layers. As can be seen in Figure 10b, the differences between the two approaches are more relevant for high values of the buffer capacity.

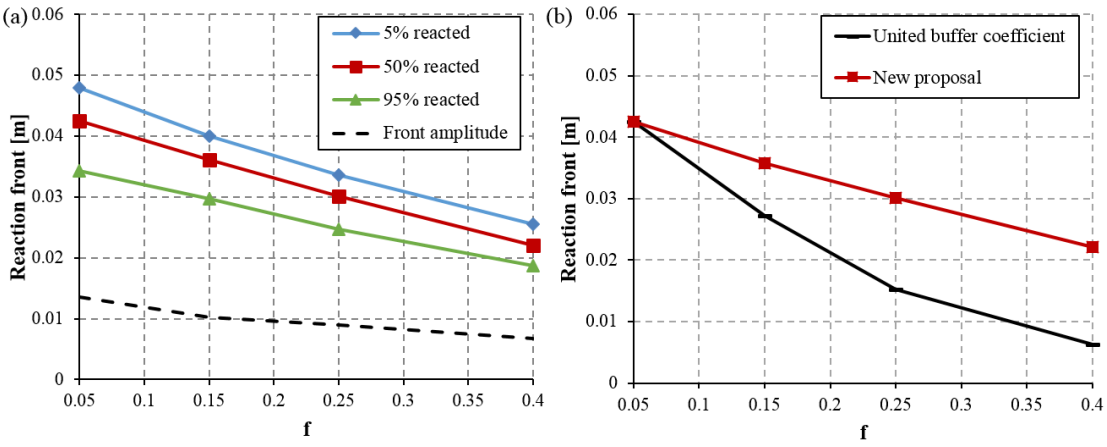

Fig. 10. (a) Influence of f_i on the reaction front, (b) Comparison with the traditional approach.

5- VALIDATION

Experimental results by Brown [13] and Ferraris et al. [14] are used to validate the expansions obtained through the model developed in this paper. The potential expansion calculated with the models proposed here are the direct result of the external sulfate attack. However, depending on the boundary conditions and on the size of the specimen, this expansion attributed to the chemical reactions may be reduced due to the compatibility of strain of adjacent elements that compose the cross section. In other words, the mechanical behavior of the element affects the resulting macroscopic expansion experienced by the cross section. In order to validate the model developed to predict the potential expansion due to the chemical reactions using experimental data from the literature, the mechanical behavior has to be considered. In this context, the macroscopic expansions of the simulated specimens are obtained through a typical sectional analysis, which considers that plane sections remain plane after the deformation (due to compatibility of strain).

Since the diffusion process is much slower than the chemical reactions, the external sulfate attack is initially limited to a region close to the external surface of the specimen. Consequently, two zones may be defined in the cross section: a more external layer affected by the attack and an inner core that has not been yet affected by it. Due to the compatibility of strains, the inner core contributes to stiffen the specimen or structural element, hence restraining the expansions experienced by the external layer. This situation is simulated through Eq. (28), which provides the resultant strain ($\Delta\varepsilon_{\mathrm{section}}$) observed at the instant $\mathrm{t_{n+1}}$.

$$\Delta\varepsilon_{section}(t_{n+1}) = \frac{\int_{Area} E(t_n, x) \cdot \Delta\varepsilon_{exp}(t_{n+1}, t_n, x) dArea}{\int_{Area} E(t_n, x) dArea} \tag{28}$$

In this equation, the term $E(\mathrm{t_n}, \mathrm{x})$ represents the elastic modulus of the material at a certain time and $\Delta\varepsilon_{exp}$ corresponds to the expansion increment resulting from the external sulfate attack in the time step and position calculated with the model proposed in this work. It is important to remark that the term *Area* indicated in Eq. (28) stands for the total cross section of the specimen, not only the directly affected by the reaction. Notice that the integral in the numerator includes the term $\Delta\varepsilon_{exp}$, which will be 0 for zones without expansion due to the external sulfate attack. These zones, however, contribute for the integral in the denominator. Consequently, $\Delta\varepsilon_{section}$ will be smaller than the maximum $\Delta\varepsilon_{exp}$ estimated at a certain time. For the assessment of the stress level, the difference between the total strain and the non-mechanical strain (i.e. $\Delta\varepsilon_{exp}$) is considered according with equation Eq. (29). As expected, $\Delta\sigma_c$ will assume negative values in zones highly affected by the attack, indicating the presence of compressive stresses. On the contrary, in zones from the inner core not affected by the expansion ($\Delta\varepsilon_{exp}$=0), the term $\Delta\sigma_c$ will be positive, indicating the existence of tensile stresses.

$$\Delta\sigma_c(t_{n+1}, x) = E(t_n, x) \cdot \left[\Delta\varepsilon_{section}(t_{n+1}, x) - \Delta\varepsilon_{exp}(t_{n+1}, x)\right] \tag{29}$$

It is also necessary to take into account that a very high stress is generated by the external sulfate attack in a small region close to the surface of the sample, since the diffusion process is much slower than the chemical reactions. This tends to produce a layered damage of the sample, which has been described by many authors that tested mortar prisms exposed to an external sulfate attack. To account for this in the mechanical model, a simplified

consideration of the damage was introduced. Damage in the compressed zone of the specimens is modelled through a degradation of the elastic modulus, initiating a plastic behavior of the material for stresses higher than 80% of the compressive strength.

Notice that the mechanical model used consider several simplifications. In fact, more advanced mechanical models should be selected for the analysis of complex elements or structures subjected to cracking and nonlinearities. In this context, the new approach proposed to estimate the potential strain due to the chemical reactions represents the main contribution of this work since it could be implemented in other types of mechanical models.

5.1- VALIDATION BASED ON EXPERIMENTAL RESULTS BY BROWN

In 1981, Brown performed a series of experimental tests to investigate how a controlled environment accelerates the rate of sulfate attack [13]. The linear expansions were measured for mortar bars immersed in a 352 mmol of sulfates/liter solution while maintaining the solution pH at 10. Mortar bars were cast at w/c=0.6 using a high C_3A, 14%, type I cement. Lacking the experimental value for the lumped rate of take-up of sulfates and the fraction of the pore that can be filled without causing expansions, for the time being, k and f_i are considered as fitting parameters of the model. No information regarding the porosimetry distribution was available, so realistic values for the mortar used were adopted. The values of the main parameters for fitting the data are shown in Table 6. Other parameters used in the computations were: C_{so}=35.2 mol/m^3, $D_0=1\cdot10^{-12}$ m^2/s, $D_{min}=D_0/10$ [22], $D_{max}= 1000D_0$ [16], ε_f=0.005, c_1=3 [21], c_2=6.93[21], f_t=2.89 N/mm^2, f_c=25 N/mm^2, E_{28}=28000 N/mm^2, w/c=0.6, β_D=1.5 [16], q=3, R_1=8 nm, R_2=15 nm, R_3=30 nm, R_4=50 nm, R_5=0.1 μm and $\Delta V/V \cdot m$=0.000170 m^3/mol (for monosulfate). The number of space intervals and time steps considered were 50 and 50 s, respectively.

Table 6. Parameters used to fit experimental data of Brown.

k [m^3/mol·s]	C_{CA} [mol/m^3]	X_1 [%]	X_2 [%]	X_3 [%]	X_4 [%]	X_5 [%]	f_1	f_2	f_3	f_4	f_5
$1.5\cdot10^{-7}$	244	10	12	17	51	10	0.12	0.13	0.15	0.25	0.35

The experimental results were contrasted with the outputs of the model developed and compared with the evolution of longitudinal expansions obtained by the model of Tixier & Mobasher [34]. As may be seen in Figure 11, the shape of the curve provided by the model from the authors is not able to fit accurately the experimental data. The reason for this may be found into the consideration of the buffer effect from the porosity and the influence of the mechanical behavior. By considering a single buffer coefficient applied to the overall porosity, all ettringite formed during early stages of the simulation is neglected since it is absorbed by the pores. Consequently, a null expansion is estimated initially. However, once this buffer capacity is filled, the additional ettringite precipitated leads to an increase of internal stress and expansion. After a critical tensile stress is reached, failure occurs and part of the stress is redistributed, producing an extra expansion. From this point on, an abrupt increase of strains is observed as a result of a combination of a chemical phenomenon (the additional formation of ettringite) and a mechanical phenomenon (release of stress due to cracking). This combined effect may explain the sudden increase in the estimations provided by Tixier and Mobasher [34] in Figure 11. On the contrary, the estimations provided by the model developed here show a much better fit throughout the 60 days of the simulation. This is the result of the new approach proposed for the buffer capacity of different pore sizes.

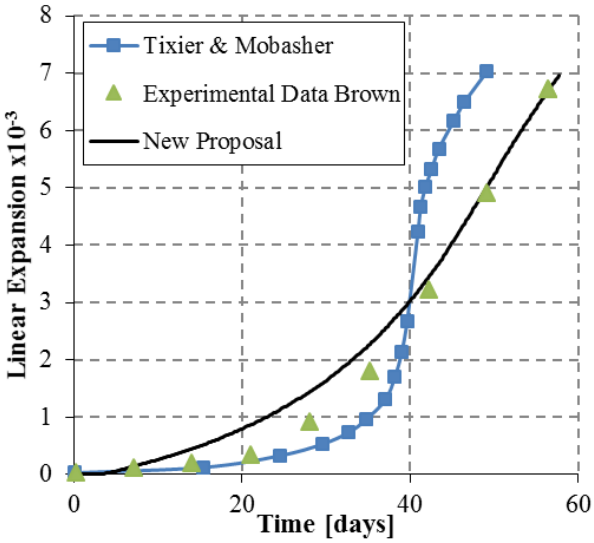

Fig. 11. Validation of present model with data by Brown.

Figure 12a shows the fraction filled at the end of the simulation for each pore size considered. As expected, as the pore size decreases the pore fraction filled increases, being the *Pore Size 1*, corresponding to the smallest radio R_1= 8 nm, the one that has resulted in a higher fraction filled. In Figure 12b, the contribution of each pore size into the total volumetric expansion is represented. As the strains are calculated by the pore fraction filled (Eq. 26), the contribution from small pores to the overall expansion could be larger than that from large pores. In the current simulation, pores of radio 50 nm and 100 nm do not contribute to the expansions. This fact reflects the phenomenon described by the crystallization pressure theory, in which crystals growing in small pores (of order of tens of nanometers) are more likely to generate significant expansive pressure [29]. In a recent publication by Müllauer [35], it was quantified that the formation of ettringite in small pores (10 to 50 nm) generates a stress of about 8MPa that exceeds the tensile strength of the binder matrix and is responsible for damage. The same author suggests that bigger pores are not able to generate enough crystallization pressure to exceed the tensile strength of the matrix. Although the model developed here reproduces this behavior, the results cannot be quantitatively compared to the ones obtained through a crystallization pressure model since the expansions are computed solely from the additional volume generated.

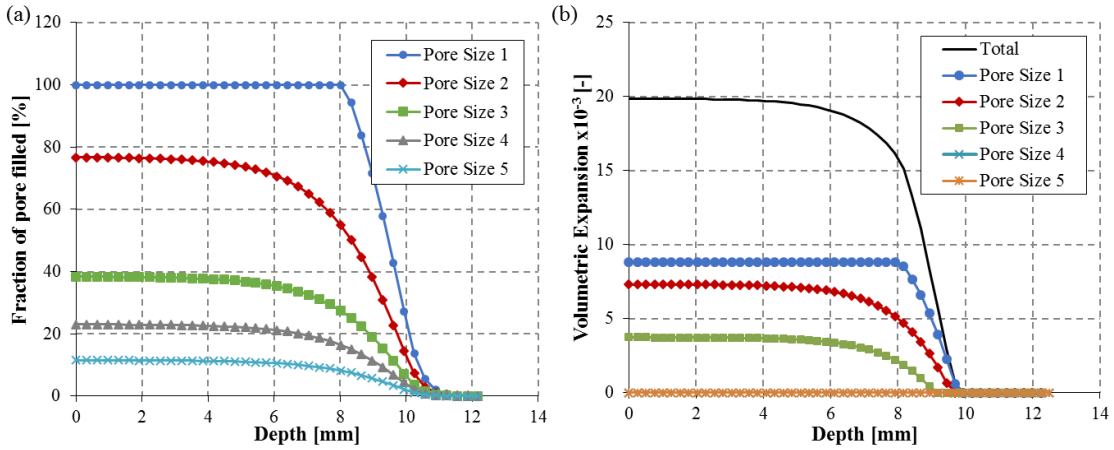

Fig. 12. (a) Pore fraction filled at the end of the simulation, (b) Volumetric strain contribution of each pore size at the end of the simulation.

5.2- VALIDATION BASED ON EXPERIMENTAL RESULTS BY FERRARIS ET AL.

Additional validation of the expansion profile is performed using experimental data from Ferraris et al. [14]. Mortar prisms 25 mm x 25 mm x 276 mm were immersed in 5% solution of sodium sulfate. The pH of the solution was maintained at 7 until disintegration of the specimen occurred. The tests used a cement with a C_3A content at 12.8% and a w/c ratio of 0.485. Changes in length of each specimen were monitored. No information regarding the porosimetry distribution was available, so realistic values for the mortar used were adopted. For consistency, same pore sizes as in the validation based on the experimental results by Brown are considered. As in the previous validation, no experimental values for the parameters k and f_i are provided. This scenario forces to consider k and f_i as fitting parameters of the model. The values of the main parameters for fitting the data are shown in Table 7. Other parameters used in the computations were: C_{so}=35.2 mol/m^3, D_0=1·10^{-12} m^2/s, D_{min}= D_0/10 [22], D_{max}= 1000D_0 [16], ε_f=0.005, c_1=3 [21], c_2=6.93[21], f_t=2.89 N/mm^2, f_c=25 N/mm^2, E_{28}=28000 N/mm^2, w/c=0.485, β_D=1.5 [16], q=3, R_1=8 nm, R_2=15 nm, R_3=30 nm, R_4=50 nm, R_5=0.1 μm and $\Delta V/V \cdot m$=0.000170 m^3/mol. The number of space intervals and time steps considered were 40 and 75 s, respectively.

Table 7. Parameters used to fit experimental data of Ferraris et al.

k [m^3/mol·s]	C_{CA} [mol/m^3]	X_1 [%]	X_2 [%]	X_3 [%]	X_4 [%]	X_5 [%]	f_1	f_2	f_3	f_4	f_5
6·10^{-8}	223	5	10	30	45	10	0.15	0.20	0.22	0.23	0.35

In Figure 13, the longitudinal expansions obtained by the model developed in the present study are compared with the expansions obtained by Tixier & Mobasher [34] and experimental measurements from Ferraris et al. [14]. The prediction provided by the model of Tixier & Mobasher presents a good fit until the late stage of the simulation, where the last point measured during the experimental campaign is not fitted by the model. The prediction provided by the approach presented in this paper shows a good fit throughout the 120 days of the simulation.

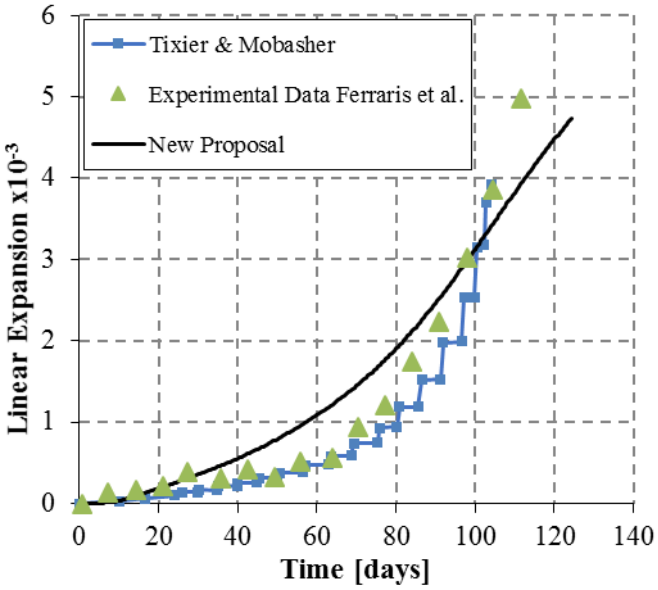

Fig. 13. Validation of present model with data by Ferraris et al.

The pore fraction filled at the end of the simulation, and the contribution of each pore size into the volumetric expansion are depicted in Figure 14a and 14b, respectively. As in the previous validation, as the pore size decreases the pore fraction filled increases, according to the higher surface/volume ratio present in small pores. Filled percentages reached 100 % for the smallest pore, and almost 12 % for the biggest one at the end of the simulation. The behavior depicted in Figure 14b, where pores from 8 nm to 30 nm contribute to the total strain, is in accordance with the phenomenon described by the crystallization pressure theory [29,35].

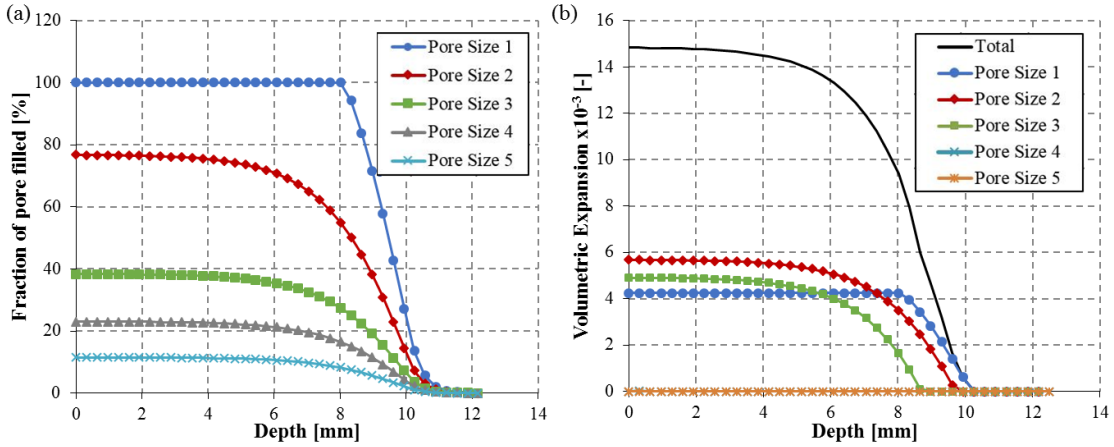

Fig. 14. (a) Pore fraction filled at the end of the simulation, (b) Volumetric strain contribution of each pore size at the end of the simulation.

6- CONCLUSIONS

The following conclusions may be derived from the present study.

(1)- A new expression for the consideration of the diffusion in a cracked porous media has been proposed based on the constitutive law of the material. It allows a more direct and intuitive approach since it does not require the definition of any damage parameter such as the one used by isotropic damage models based on continuum damage mechanics. In this case, the damage is considered indirectly, thus making the estimations simpler.

(2)- A new approach to compute expansions is presented, based on a more realistic consideration of the concrete porosimetry. The described approach allows the consideration of different filling rates and capacities to accommodate expansive product for each pore size considered. These features, already considered in models based on crystallization pressure theory, were not possible to be considered in models based on the simplified theory of the volume increase approach until now. The authors believe that through this path, it will be possible to consistently model the expectable effects of the crystallization pressure theory through the simplified volume increase approach.

(3)- Referring to the parametric analysis, the sulfate concentration in the aggressive soil and the lumped rate of take-up sulfates, resulted to be the most influencing parameters on the reaction front. On the other hand, changes in the initial diffusivity and calcium aluminates concentration do not affect significantly the reaction front.

(4)- Expansions obtained by the new model are in good agreement with experimental data by Brown [13] and Ferraris et al. [14], suggesting that the proposed model is able to

predict its behavior. As described by the crystallization pressure theory, a bigger contribution of small pores into the total strain is observed in the simulations [29]. More advanced mechanical models capable of accounting for the failure of the specimens should be selected for the analysis of more complex elements or structures.

ACKNOWLEDGMENTS

Support from the Spanish Ministry of Economy and Competitiveness through research project BIA2010-20913-C02-02 is greatly acknowledged. Dr. I. Segura is supported by the postdoctoral Juan de la Cierva program of the Spanish Ministry of Economy and Competitiveness.

REFERENCES

[1] EUROCONSTRUCT Conference, VTT, Buildecon. Construction in Europe breakdown in 2012.

[2] O.S. Baghabra Al-Amoudi, Attack on plain and blended cements exposed to aggressive sulfate environments, Cem. Concr. Compos. 24 (2002) 305–316.

[3] S. Sarkar, S. Mahadevan, J.C.L. Meeussen, H. van der Sloot, D.S. Kosson, Numerical simulation of cementitious materials degradation under external sulfate attack, Cem. Concr. Compos. 32 (2010) 241–252.

[4] A.E. Idiart, C.M. López, I. Carol, Chemo-mechanical analysis of concrete cracking and degradation due to external sulfate attack: A meso-scale model,» Cem. Concr. Compos. 33 (2011) 411–423.

[5] C. Ayora, S. Chinchón, A. Aguado, F. Guirado, Weathering of iron sulfides and concrete alteration: Thermodynamic model and observation in dams from central Pyrenees, Spain, Cem. Concr. Res. 28 (9) (1998) 1223–1235.

[6] A. Campos, Análisis numérico de presas de hormigón bajo acciones expansivas, Phd Thesis, Universitat Politécnica de Catalunya, Barcelona, 2012.

[7] A. Neville, The confused world of sulfate attack on concrete, Cem. Concr. Res. 34 (2004) 1275–1296.

[8] P.K. Mehta, Sulfate attack on concrete—a critical review, Mater. Sci. Concr. III, Am. Ceram. Soc., Westerville, 1992, pp. 105-130.

[9] J.P. Skalny, I. Odler, J. Marchand, Sulfate Attack on Concrete, Spon, London, 2001.

[10] M. Collepardi, A state-of-the-art review on delayed ettringite attack on concrete, Cem. Concr. Compos. 25 (2003) 401–407.

[11] R. Tixier, B. Mobasher, Modeling of Damage in Cement-Based Materials Subjected to External Sulfate Attack. I: Formulation, J. Mater. Civ. Eng. 15 (2003) 305–313.

[12] B. Bary, Simplified coupled chemo-mechanical modeling of cement pastes behavior subjected to combined leaching and external sulfate attack, Int. J. Numer. Anal. Meth. Geomech. 32 (2008) 1791–1816.

[13] P.W. Brown, An evaluation of the sulfate resistance of cements in a controlled environment, Cem. Concr. Res. 11 (1981) 719–727.

[14] C.F. Ferraris, J.R. Clifton, P.E. Stutzman and E.J. Garboczi, Mechanisms of degradation of portland cement-based systems by sulfate attack, in: K.L. Scrivener and J.F. Young (Eds), Mechanisms of chemical degradation of cement-based systems, E&FN Spon, London, 1997, pp. 185–192.

[15] M. Basista, W. Weglewski, Chemically assisted damage of concrete: a model of expansion under sulfate attack, Int. J. Damage Mech. 18 (2008) 155–175.

[16] A.E. Idiart, Coupled analysis of degradation processes in concrete specimens at the meso-level, PhD Thesis, Universitat Politécnica de Catalunya, Barcelona, 2009.

[17] X.B. Zuo, W. Sun, C. Yu, Numerical investigation on expansive volume strain in concrete subjected to sulfate attack, Constr. Build. Mater. 36 (2012) 404–410.

[18] P.N. Gospodinov, R.F. Kazandjiev, T.A. Partalin, M.K. Mironova, Diffusion of sulfate ions into cement stone regarding simultaneous chemical reactions and resulting effects, Cem. Concr. Res. 29 (1999) 1591–1596.

[19] E. Samson, J. Marchand, Modeling the transport of ions in unsaturated cement based materials, Comput. Struct. 85 (2007) 1740–56.

[20] M. Jirásek, Damage and Smeared Crack Models, in: G. Hofstetter and G. Meschke (Eds.), Numerical Modeling of Concrete Cracking, CISM, Udine, 2011, pp. 1–49.

[21] D.A. Hordijk, Local Approach to Fatigue of Concrete, Phd Thesis, Delft University of Technology, Delft, 1991.

[22] B. Gérard, J. Marchand, Influence of cracking on the diffusion properties of cement-based materials. Part I: Influence of continuous cracks on the steady-state regime, Cem. Concr. Res. 30 (2000) 37–43.

[23] M. Sahmaran, M. Li, and V.C. Li, Transport Properties of Engineered Cementitious Composites under Chloride Exposure, ACI Mater. J., V. 104, No. 6, (2007) 303–310.

[24] A. Djerbi, S. Bonnet, A. Khelidj, V. Baroghel-bouny, Influence of traversing crack on chloride diffusion into concrete, Cem. Concr. Res. 38 (2008) 877–883.

[25] W. Kunther, B. Lothenbach, K. Scrivener, On the relevance of volume increase for the length changes of mortar bars in sulfate solutions, Cem. Concr. Res. 46 (2013) 23–29.

[26] J.R. Clifton, J.M. Pommersheim, Sulfate attack of cementitious materials: volumetric relations and expansions, NISTIR 5390, Building and Fire Research Laboratory, Gaithersburg (MD), 1994.

[27] G.W. Scherer, Crystallization in pores, Cem. Concr. Res. 29 (1999) 1347–1358.

[28] W. Kunther, B. Lothenbach, K. Scrivener, Influence of bicarbonate ions on the deterioration of mortar bars under sulfate attack, Cem. Concr. Res. 44 (2013) 77–86.

[29] C. Yu, K. Scrivener, Mechanism of expansion of mortars immersed in sodium sulphate solution, Cem. Concr. Res. 43 (2013) 105–111.

[30] J.G.Wang, Sulfate attack on hardened cement paste, Cem. Concr. Res. 24 (1994) 735–42.

[31] I. Oliveira, S.H.P. Cavalaro, A. Aguado, New kinetic model to quantify the internal sulfate attack in concrete, Cem. Concr. Res. 43 (2013) 95–104.

[32] S. Mindess, J. F. Young and D. Darwin, Concrete, Englewood. Cliffs. New Jersey. Prentice Hall, 2002.

[33] S.M. Abdelkader, Influencia de la composición de distintos hormigones en los mecanismos de transporte de iones agresivos procedentes de medios marinos, PhD thesis, Universidad Politécnica de Madrid, Madrid, 2010.

[34] R. Tixier and B. Mobasher, Modeling of damage in cementbased materials subjected to external sulfate attack. II: Comparison with experiments, J. Mater. Civ. Eng. 15 (2003) 314–322.

[35] W. Müllauer, R. E. Beddoe, D. Heinz, Sulfate attack expansion mechanisms, Cem. Concr. Res. 52 (2013) 208–215.

3.2. JOURNAL PAPER II. SIMPLIFIED METHODOLOGY TO EVALUATE THE EXTERNAL SULFATE ATTACK IN CONCRETE STRUCTURES

Published in Materials & Design 89 (2016) 1147-1160.

Tai Ikumi[a], Sergio H.P. Cavalaro[a,*], Ignacio Segura[a], Albert de la Fuente[a], Antonio Aguado[a]

[a] Department of Construction Engineering, Universitat Politècnica de Catalunya Barcelona Tech, Jordi Girona 1-3, C1, E-08034 Barcelona, Spain

* Corresponding author: Sergio H. P. Cavalaro. Department of Construction Engineering, Universitat Politècnica de Catalunya Barcelona Tech, Jordi Girona 1-3, C1, E-08034 Barcelona, Spain. Email address: sergio.pialarissi@upc.edu, Tel: +34 93 401 6507 Fax: +34 93 401 1036

Abstract

The external sulfate attack is a degradation process that causes expansion and cracking in concrete structures. Due to the absence of simplified methodologies to predict the potential damage, codes specify that sulfate resistant cement should be used whenever the surrounding sulfate concentration surpasses a predefined limit. This may lead to penalizing measures as the size of the element or the mechanical properties of the concrete used are not considered. In the present work, an alternative approach is proposed. A simplified chemo-mechanical methodology is deducted to assess the potential damage in concrete elements exposed to sulfate rich environments. Equations to estimate the penetration of sulfates are derived from a numerical model taking into account sulfate consumption, acceleration of the penetration induced by cracking and decrease in diffusivity caused by pore filling. Failure modes associated to this phenomenon are analyzed and a set of equations to assess the risk of failure are deducted. Finally, a parametric study with different geometries of elements and surrounding sulfate contents is performed. The results show that the criterion included in codes might be modified depending on the characteristics of the structure.

Keywords: Concrete; Durability; External sulfate attack; Diffusion; Failure

1.- INTRODUCTION

The external sulfate attack (ESA) is a complex phenomenon in which chemical reactions, ionic transport and mechanical damage interact with each other, leading to expansions and degradation in concrete structures [1-4]. The degradation progresses as sulfate ions from the outside penetrate the element and react with compounds from the hydrated cement paste. As a result, a multi-layered pattern is formed with an external damaged layer and an internal sound core [5]. The mechanical interactions between these zones play a major role in determining the damage induced by the attack.

The ESA has special relevance in underground or foundation structures in contact with sulfate-rich soils. Such structures remain covered during most of their service life, which compromises the early diagnostic of the attack that may only be detected after severe material degradation has occurred. The existing tools to account for potential damage caused by ESA in real structures may be gathered in three main groups: procedures included in building codes, empirical models and integrated models.

Building codes have traditionally specified precautionary measures to protect concrete against this type of attack. The most common approach is based on the definition of exposure classes regulated by the sulfate content in the media surrounding the structure. Depending on the classification obtained, prescriptions of maximum water/cement ratio, minimum compressive strength and type of cement should be followed to avoid durability problems (e.g. Model Code 2010, BS 8500-1:2006, ACI 201.2R-08, UNE EN 206-1:2008). Notice that the size of the element under study or the mechanical properties of the concrete used are not considered. In fact, through the application of this criterion, practitioners are not able to predict the potential damage of the attack or the compliance of a minimum service life. This may lead to penalizing measures and cost overruns as a result of unnecessary use of sulfate resistant cement in some cases.

Several empirical models have been developed to quantify the spalling depth or the evolution of expansions of concrete elements exposed to ESA. Most of them are based on experience or accelerated laboratory tests performed with small specimens (e.g. [6-8]). The main drawbacks associated with these models are their limited applicability since they are only valid for elements subjected to the same conditions used in the tests. Integrated models take into account the transport of ions, the chemical reaction and the microstructural damage through several differential equations, whose solution commonly require iterative procedures. At present, these models provide the most precise assessment of the ESA. However, the complexity of the equations involved and the high computational cost for their solution may not be accessible to practitioners and certainly are not compatible with the philosophy of most design codes. Besides, the majority of the integrated models from the literature are only capable of predicting the expansion and the damage at a micro-scale level. To estimate the macro-structural response in terms of cracking and failure, advanced structural models should be used, thus compromising even more the straightforward assessment of the attack.

It is evident that a simplified methodology for the assessment of the potential damage caused by the ESA compatible with the philosophy of building codes is still needed. The objective of this paper is to propose this simplified methodology considering both the micro and macro scale effects. First, the latest integrated models from the literature are analyzed. Based on this, the model by Ikumi et al. [9] is selected and used to derive straightforward equations for the reactive-transport phenomenon accounting for the sulfate consumption, the acceleration of the penetration due to micro-cracking and the decrease in diffusivity due to

pore filling. Then, a comprehensive study of the common mechanical failure modes associated with the ESA is presented and a set of simplified equations to assess the failure of the structure are derived. A parametric study is conducted to evaluate the methodology proposed for different geometries under a wide range of realistic field conditions. Based on this study, reference values are proposed for the aluminate content depending on the type and the dimensions of the structure.

The methodology developed here represents a step forward on how to assess the ESA explicitly in the design of concrete structures. It allows a more detailed evaluation of the durability of the structures since the specific conditions and expected service life are considered. As a result, an optimized definition of precautionary measures may be obtained for each application.

2.- INTEGRATED MODELS

Table 1 summarizes some of the integrated models developed during the last decade. This table does not include models that consider ettringite formation through a solid-state mechanism since it is believed that it must occur through solution [10].

Table 1. Integrated models developed during the last decade

Authors	Year	Expansion mechanism	Expansive products
Tixier and Mobasher [11,12]	2003	Volume increase	Ettringite
Bary et al. [13]	2008	Crystallization pressure	Ettringite and gypsum
Sarkar et al. [14]	2010	Volume increase	Ettringite
Idiart et al. [15]	2011	Volume increase	Ettringite
Zuo et al. [16]	2012	Volume increase	Ettringite
Cefis and Comi [17]	2014	Volume increase	Ettringite
Bary et al. [18]	2014	Crystallization pressure/Volume increase	Ettringite
Ikumi et al. [9]	2014	Volume increase	Ettringite
Nie et al. [19]	2015	Volume increase	Ettringite

Controversy still exists on basic topics of the ESA, especially regarding the expansion mechanism and the gypsum role on the expansion process [3,20]. Amongst the several mechanisms suggested to explain how the precipitation of ettringite leads to expansion, mainly two theories have been implemented in comprehensive models: the volume increase and the crystallization theories.

According with the first of them, expansions are a result of the additional volume generated by ettringite formation [11,21]. In this case, the response of the matrix and the expansive stresses are calculated from the imposed volumetric strains. According with the second of them, expansions are caused by the crystallization pressure exerted on the pore walls due to the formation of a supersaturated solution within small pores [22,23]. In this case, the actual driving pressure that will be translated into strains is obtained by different modifications of the Correns equation [24,25]. Even though the latter theory is supported by recent publications [10,26,27], it requires a very complex chemical approach once the evolution of phases in the pore solution has to be monitored during the attack in terms of chemical activities. Moreover, it was shown by [13] that, despite predicting the cracking state with a relatively good accuracy, this theory leads to macroscopic expansions about two orders of magnitude smaller than the found in experimental data. According to Zhang et al. [28], the reason is that the crystallization pressure assessment is based in an elastic approach that does

not account for microcraking and differed deformations (creep), which may play an important role in the final strain measured.

In a recent publication [18], Bary et al. tried to solve this issue by introducing an additional macroscopic bulk strain due to the increase of volume produced by secondary ettringite formation. The authors used the equation derived by Tixier and Mobasher [11] and subsequently used by many other researchers [9,14,15]. By adding this consideration, the expansions are a result of both the additional volume generated by ettringite formation and the crystallization pressure exerted on the pore walls by the supersaturated solution. Free expansions calculated with this approach is similar to the obtained in the test of specimens. Bary et al. also pointed out that the contribution of the crystallization pressure is negligibly small compared to the bulk strain produced by secondary ettringite formation [18], which would indicate that the volume increase is the overriding factor in the macroscopic strain evolution.

Like Bary et al., other studies from the literature [9] also suggest that the volume increase and the crystallization theories may be compatible as they probably represent two different stages of the sulfate attack. When the solubility limit of ettringite is reached due to the ingress of sulfate ions, the system always tend to return to an equilibrium state through ettringite precipitation. When this energy cannot be released by crystal precipitation, it is released in the form of pressure to the pore walls and the subsequent microcracking as described in the crystallization pressure theory. Microcraking decreases the pressure conditions in the pore, thus allowing ettringite to precipitate near the cracks. Therefore, macroscopic free strains increase proportionally to the amount of ettringite precipitated, being the volume increase inherent to this chemical reaction the driving force of the macroscopic strains. In other words, the initiation of the macroscopic strains arises mainly from the action of the crystallization pressure, while the macroscopic free expansions are explained by the volume increase.

Considering that the aim of the present study is to generate simplified models capable of estimating the expansive strain and the failure at a macro-structural level, an integrated model based on the volume increase was selected. This also contributes to a more straightforward approach since a smaller number and simpler input parameters are required to estimate the expansions in the volume increase theory. Therefore, the integrated model by Ikumi et al. [9] was selected as the basis to develop the simplified methodology since it also introduces a more direct and intuitive consideration for the damage assessment and thereby facilitate the definition of the input parameters.

It is important to remark that this model only provides the expansion and the damage at a small-scale level. To evaluate the overall response at a macro-scale level and the failure of the structure, Ikumi et al. [9] and other authors suggest that the expansions estimated should be implemented in finite element models that account for the mechanical response of the structure. This represents an important limitation found in practically all integrated models from the literature, which are unable to provide a straightforward verification of the durability of the structure in terms of global failure.

3.- SIMPLIFIED METHODOLOGY

The methodology proposed in this paper is based on the application of a set of simplified equations to assess the extent of the reactive-transport process and the possible mechanical

structural failure at a given service life. As outlined in Figure 1, the aggressiveness of the media and the reactivity of the material define the input parameters for the simplified reactive-transport equations that provide the maximum sulfate penetration and the maximum expansion in the damaged layer of the element. This information combined with the geometric and mechanical characteristics of the element allows the verification of the most common mechanical failure modes. If no mechanical failure occurs and the serviceability is not compromised, it is considered that the structure will comply with the required service life.

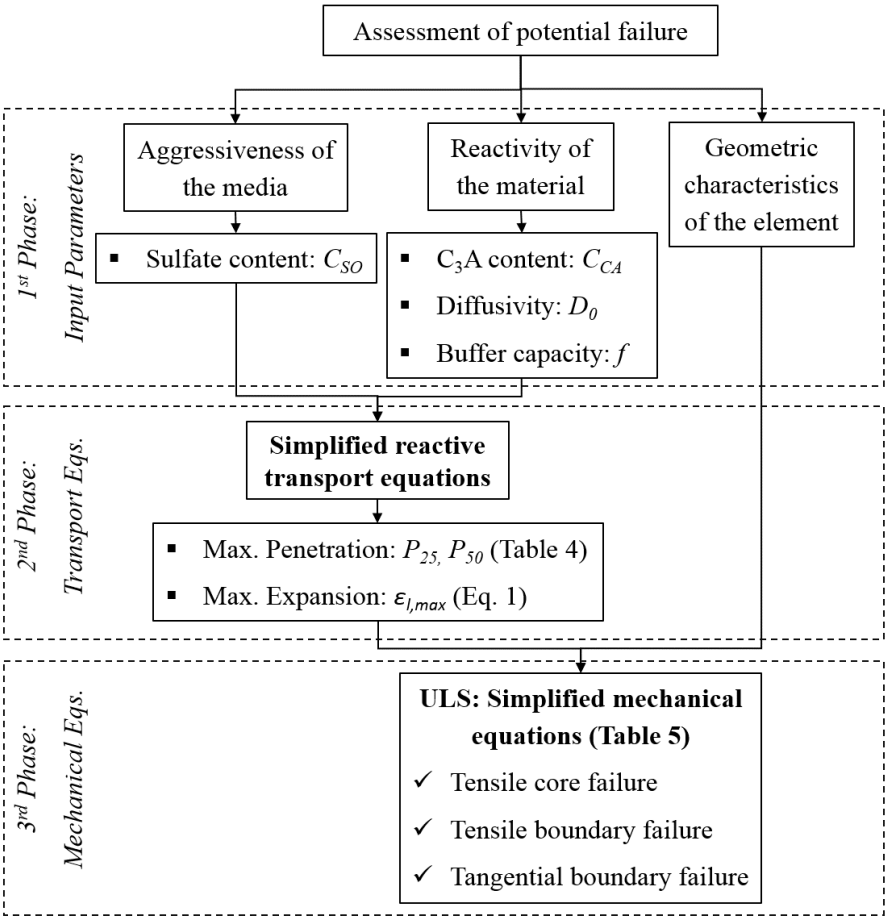

Fig. 1. Outline of the simplified methodology for the durability assessment of the ESA

3.1- SIMPLIFIED REACTIVE-TRANSPORT EQUATIONS

In this section, simplified equations to quantify the maximum penetration of the sulfate front and the maximum linear micro-strains at 25 and 50 years are deduced. As these equations are derived from the model described by Ikumi et al. [9], firstly the main features of the model and the hypothesis adopted here are presented.

3.1.1 Hypothesis adopted based on the integrated model by Ikumi et al. [9]

It is assumed that expansions are caused by the volume increase associated to secondary ettringite formation, being the expansive nature of gypsum disregarded. To simplify the model, all hydrated aluminates are considered in the form of monosulfate ($C_4A\bar{S}H_{12}$) since this should be the predominant aluminate phase in hydrated Portland cement pastes at long ages.

Sulfate and aluminate concentrations are computed through a diffusion-reaction model based on the Fick's second law, which takes into account the ingress of sulfate ions under a concentration gradient and its depletion due to ettringite formation. The effective diffusivity (D) is affected by pore filling, which reduces the paths for additional sulfate diffusion, and micro-cracking and spalling of the cementitious matrix. The latter increases the diffusivity as more paths towards the inner layers may be found.

The upper bound of the diffusivity reached when the material is completely damaged is set to 10^{-10} m^2/s. This value is slightly below the diffusivity of sulfates in free solution, which Gerard and Marchand [29] quantified as 10^{-9} m^2/s for ions able to move freely within cracks. For the simulations performed in this paper, the value of c_1 and c_2 described in [9] were defined respectively as 3 and 6.93, in accordance with the recommendation from [30]. The characteristic cracking length (l_{ch}) is fixed at 26 mm, following the validation by [9].

Expansions at micro scale are calculated by the additional volume generated by the reaction product ($\Delta V/V$) [21]. This calculation gives a 55% volume increase when monosulfate is converted into ettringite. The total linear strain (ε_l) associated with this expansion is computed by multiplying the expansion factor by the amount of monosulfate reacted ($C^{react}_{C_4A\bar{S}H_{12}}$), as described in Eq. 1. The term M/ρ corresponds to the molar volume of monosulfate and $C^{react}_{C_4A\bar{S}H_{12}}$ is expressed as a molar concentration. Notice that the maximum expansive strain ($\varepsilon_{l.max}$) may be calculated with Eq. 1 by assuming that all monosulfate react to form ettringite.

$$\varepsilon_l = \left(1 + \frac{\Delta V}{V}\frac{M}{\rho} C^{react}_{C_4A\bar{S}H_{12}} - f\varphi_0\right)^{1/3} - 1 \qquad (1)$$

Since ettringite precipitates within the pore network, the matrix is able to accommodate a certain amount of expansive product without exerting any pressure to the pore walls [11,14,31]. Consequently, not all aluminate present will generate expansions. The expression presented by Tixier & Mobasher [11] is used to estimate the buffered expansion. This is represented in the second term of Eq. 1, in which φ_0 is the initial porosity of the matrix and f is the fraction of this porosity that may be filled by expansive products before expansions occur. According with Tixier & Mobasher [11], f usually ranges between 0.05 and 0.40.

3.1.2- Intensification effect in radial fluxes

In the majority of underground structures subjected to the ESA, the diffusion flux may be classified as approximately linear - typical in diaphragm walls or tunnels - or radial- typical in piled foundations. Transport processes in radial direction are subjected to flux intensification as sulfate penetrates towards the center of the element, concentrating at a smaller area. Conversely, no intensification occurs in a linear flux.

In a simplified methodology, it is convenient to minimize the number of equations proposed. Therefore, prior to deriving the simplified equations, the sulfate penetration in radial elements is compared with that from linear elements. The aim is to demonstrate that both provide similar results for most real size structures, thus justifying the use of the linear flux formulation for the majority of cases.

The maximum penetration depths obtained through linear and radial flux approximation were compared for radius ranging from 5 to 50 cm. A minimum sulfate content

of 1% of the sulfate concentration in the external surface is defined as a threshold to calculate the penetration depth. Table 2 presents the parameters used in the analysis defined according with the literature. The material used corresponds to a concrete with 350 kg/m^3 of cement that contains 80% clinker and 10.8 % of C_3A. Total time simulated is fixed at 25 years. Space intervals of 0.25 mm and variable time steps were considered to ensure stability and convergence.

Table 2. Parameters used in the preliminary study of the flux intensification effect

k [m^3/mol·s]	D_0 [m^2/s]	C_{SO} [mol/m^{3}water] ([g/l])	C_{CA} [mol/m^{3}concrete] ([%C_3A])	f_{cm} [MPa]	f	φ_o
0 or 10^{-8}	10^{-12}	34.37 (3.3)	112 (10.8)	30	0.05	0.1

Figure 2 shows the penetrations depths obtained in the analysis. When no chemical reaction is considered (k = 0), the radial and the linear flux provide approximately the same penetration depth for radius of more than 20 cm. The flux intensification observed in radial fluxes reduces the entrance of sulfates and decreases slightly the penetration. This is reasonable since the rate of transfer of a substance in accordance with Fick's second law is proportional to the concentration gradient measured along the diffusion direction. Once the differences in concentrations are smaller in radial fluxes due to the intensification effect, smaller penetration depths should be expected.

When sulfate depletion caused by the chemical reaction is considered (k=10^{-8} m^3/mol·s), the penetration depth is reduced approximately by a factor of 8 in both models. This indicates that chemical reactions are the governing process in the initial stages of the transport phenomenon. In this case, the linear flux and the radial flux approaches provide virtually the same results.

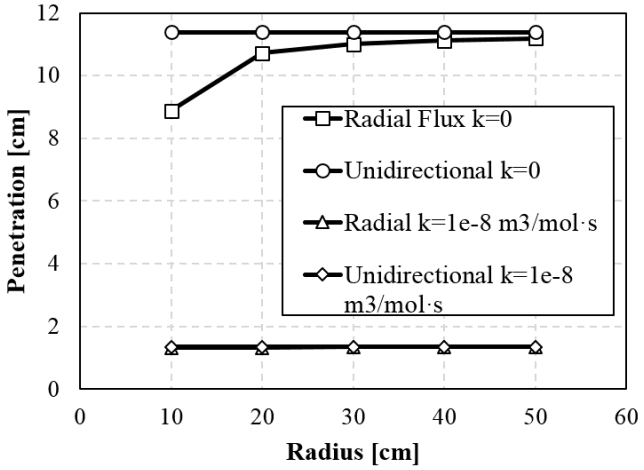

Fig. 2. Flux intensification effect

The analysis performed confirms the small differences between both approaches simulated, especially when the chemical reactions are considered. Moreover, the linear flux approximation provides a prediction of the penetration depth on the safe side given that slightly higher values are obtained. Therefore, in this work a linear flux is adopted for all structural typologies, thus avoiding the definition of two different formulations and the consideration of the element size in the simplified reactive-transport equations.

3.1.3- Definition of input parameters

To derive the simplified transport equations, penetration depths obtained through the model by [9] are fitted to a straightforward numerical formulation. Since several parameters are needed in the model by [9], the first step to obtain simplified equations is to detect which of the parameters are the most relevant. For that, a sensitivity analysis is conducted with the values defined in Table 3, which are based on recommendations from the literature and found in practice. The range defined for the aluminate content (C_{CA}) correspond to a concrete with 350 kg/m^3 of cement that contain 80% of clinker and from 4% to 12% of C_3A. The reference value is equivalent to cement with 8% of C_3A.

Table 3. Ranges of parameters and penetration front variation in sensitivity analysis

Parameter	Minimum	Reference	Maximum	Penetration depth variation [cm]
C_{SO} [mol/m$^3_{water}$] ([g/l])	6.25 (0.6)	34.37 (3.3)	62.5 (6.0)	1.4
D_0 [m^2/s]	10^{-12}	$5{\cdot}10^{-12}$	10^{-11}	1.4
f [-]	0.0	0.1	0.4	0.8
C_{CA} [mol/m$^3_{concrete}$] ([%C_3A])	41 (4)	83 (8)	124 (12)	0.8
φ_o	0.08	0.10	0.14	0.3
f_{cm} [MPa]	20	30	40	0.1

In practice, the kinetics of the reactions (k) and the temperature might affect the penetration of sulfates. However, nowadays no widely accepted test to quantify this parameter is available. Therefore, it does not seem reasonable to leave the selection of k to the final user. For that reason, k is not considered as a variable in this study. Instead, a constant k of 10^{-8} m^3/mol·s was selected for all analyses given that other authors traditionally assume values that range from 10^{-10} to 10^{-6} m^3/mol·s [32].

In the sensitivity analysis, a linear flux was simulated considering the same time steps and mesh size of section 3.1.2. Simulations were performed by varying parameters one by one between the maximum and the minimum values, whereas the other parameters were kept equal to the reference values. This procedure is repeated for all parameters from Table 3. In each case, the difference between the penetration depths estimated with the maximum and the minimum values is calculated and presented in Table 3.

The sulfate content and the initial diffusion coefficient are the most influencing parameters. Conversely, the compressive strength and initial porosity show a smaller influence over the penetration depth. Based on these results, C_{SO}, D_0, f and C_{CA} are considered explicitly as input variables of the simplified reactive-transport equations. On the other hand, f_{cm} and φ_o are assumed constant and equal to their reference values for the estimation of the equations that govern the reactive-transport phenomenon (notice that f_{cm} is a variable in the equations developed in later sections to assess the risk of failure).

3.1.4- Proposal of equations

A new study with the model by Ikumi et al. [9] was conducted to derive the simplified reactive-transport equations. At this time, simulations were performed with multiple combinations of the most influencing parameters with several values within the ranges listed in Table 3. More than 2000 simulations were completed at 25 and 50 years. Once a sufficiently big database of penetration depths was obtained, a nonlinear numerical regression was applied to derive the simplified equations that yield the best fit with the numerical results.

The final formulations obtained to estimate the penetration depth at 25 and 50 years (P_{25} and P_{50}) are presented in Table 4.

Table 4. Simplified reactive-transport equations

Service Life [years]	Simplified reactive transport formulation [cm]	K_{95} [cm]
25	$P_{25} = (7e10D_0 + 0.035C_{SO}) \exp\left(\frac{6.65e11D_0+10.737}{C_{CA}} - \frac{1e-10}{35D_o} f\right)$ (2)	0.65
50	$P_{50} = 1.26P_{25}$ (3)	0.86

The initial diffusivity (D_0) is introduced in m^2/s, whereas the aluminate content (C_{CA}) is expressed in mol per cubic meter of concrete. The sulfate content (C_{SO}) is expressed in mol of sulfate per cubic meter of water. As these equations are deduced from the model described by Ikumi et al. [9], sulfate consumption, acceleration of the penetration due to cracking and decrease of diffusivity due to pore filling are indirectly considered. Figure 3.a and 3.b depict the correlation between the penetration depths obtained through the integrated model by [9] and with Eq. 2 or Eq. 3. Correlation coefficients of 0.91 and 0.90 were obtained, respectively. Notice that both equations are applicable as long as the input parameters remain within the ranges defined in Table 3.

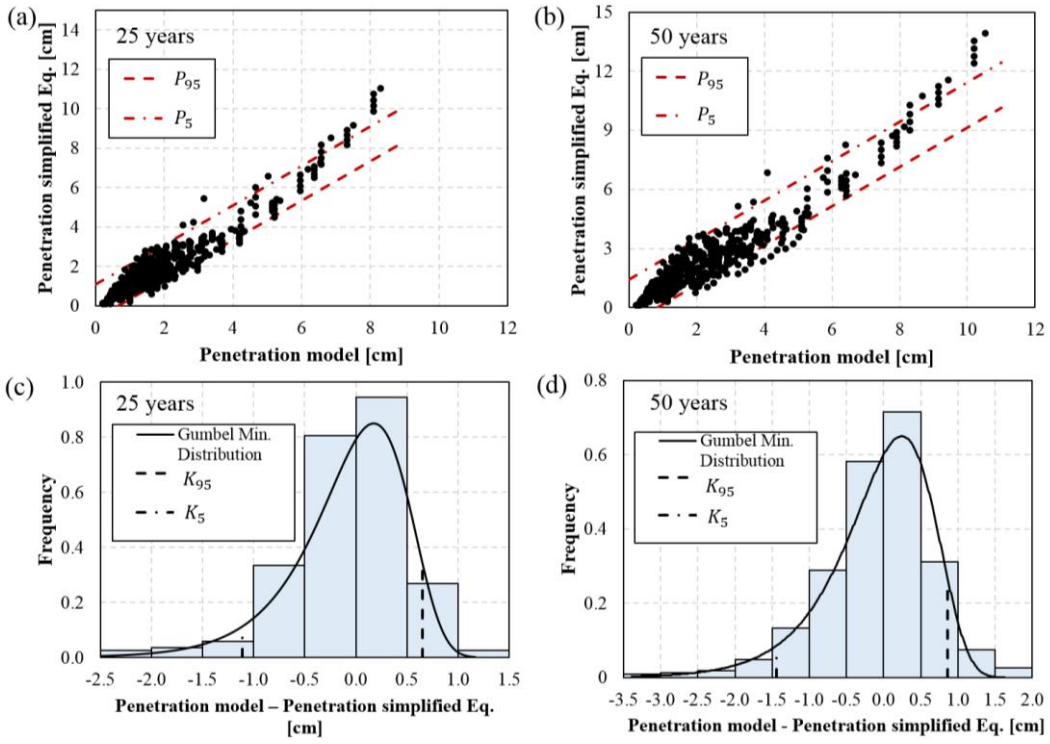

Fig. 3. Correlation between penetration obtained with integrated model and simplified equation (a and b); Gumbel distribution to assess error of estimation (c and d)

Even though the simplified reactive-transport equations provide a fair approximation of the integrated model, in some situations it might be necessary to use estimations on the safe side. Therefore, a statistical analysis was performed in order to assess the error of prediction of Eq. 2 and Eq. 3. As shown in Figures 3.c and 3.d, the frequency of the error of estimation was fit to a Gumbel distribution (minimum extreme value type I). Then, the distribution was used to assess the minimum penetration depth that had to be summed to the obtained with the simplified equations in order to assure a 95% of probability of achieving

values above the calculated with the integrated model by [9]. This additional value (K_{95}) is shown in Table 4 and should be directly added to Eq. 2 and Eq. 3 in case a safer estimation is required.

For the chemical reaction rate (k) considered in the literature, it has been demonstrated that the aluminates of the exterior layers are rapidly consumed by the ingressing sulfates [9]. This means that the maximum expansive strain ($\varepsilon_{l.max}$) is rapidly reached at the surface layers of the element. Once the aluminates are consumed, the sulfates advance at a higher rate to the inner layers, reacting with new aluminates present. Hence, an abrupt variation of the expansion should occur close to the penetration front.

Figure 4 shows in continuous lines the typical strain profiles due to ESA in structures under symmetric (sulfate insource from all sides) or asymmetric sulfate exposure conditions (sulfate insource from only one side). To simplify the structural consideration of the ESA, the strain profile depicted with the red discontinuous line is used instead. It assumes that $\varepsilon_{l.max}$ estimated with Eq. 1 occurs along the whole penetration depth obtained with Eq. 2 or Eq. 3, which is a hypothesis on the safe side.

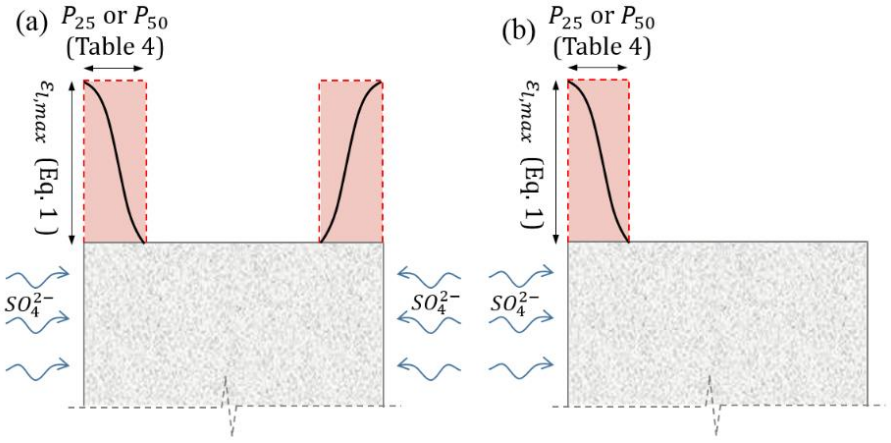

Fig. 4. Strain profiles for symmetric (a) and asymmetric (b) sulfate exposure

3.2- SIMPLIFIED MECHANICAL EQUATIONS

Although expansion due to ettringite formation is concentrated in the surficial layers, strains also appear in the sound core of the element to maintain compatibility. In fact, the sound core acts as a restriction that reduces the expansion calculated with Eq. 1. An auto-balanced tension state is generated, leading to possible mechanical failures outside the zone directly affected by the sulfate penetration and by the attack. Three failures modes are distinguished: tensile failure of the sound core, tangential failure and tensile failure in the boundary between the surficial layers and the sound core.

Micro-cracks in the external layers of the element due to high compressive stresses are usually developed prior to any failure mode. Generally, the micro-cracking is localized, affecting only a few millimeters closer to the surface. Therefore, it is not considered a failure mode as it does not imply the macro-structural failure of the element. The superficial micro-cracking modifies the local mechanical properties and the sulfate diffusion coefficient. This phenomenon is taken into account in the simplified methodology by a degradation of the elastic modulus and an increase in the diffusion coefficient in the zone directly affected by the sulfate penetration. Notice that interactions with other elements in contact with the structure directly under attack (such as external loads or strain constraints in specific

directions) could modify the stresses profile and affect the failure. However, these considerations cannot be included in a simplified methodology as they will vary depending on each study case.

3.2.1- Tensile failure of the sound core

The expansions of the outer layers along the length of the element are restrained due to the stiffness provided by the sound inner core. This causes normal compressive stresses (σ_c) at the surficial layers, while normal tensile stresses (σ_{tc}) appear at the sound inner core. If σ_{tc} reaches the tensile strength of concrete, the inner core might crack, reducing significantly the restrains applied to the external layers. This might produce a release of the restricted strains and an abrupt displacement of the structure. In Figure 5, such situation is represented before and after cracking for elements under symmetric and asymmetric sulfate exposure conditions.

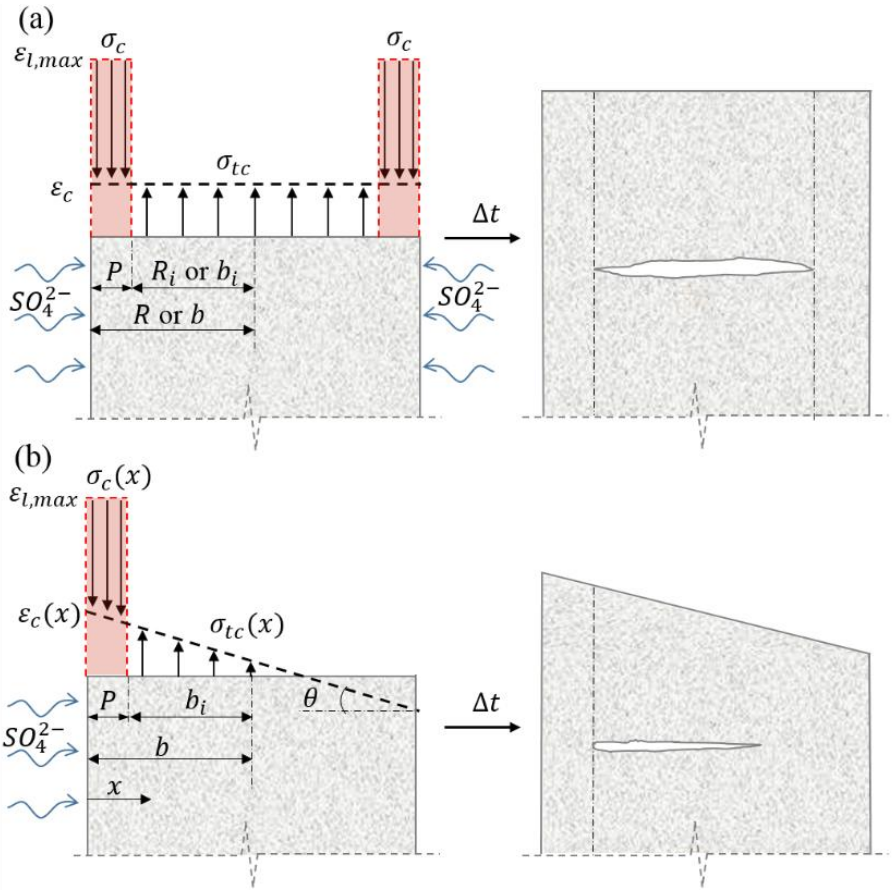

Fig. 5. Normal stress distribution in symmetric (a) and 1 face (b) sulfate exposure.

As an approximation, it is assumed that the Navier-Bernouilli hypothesis applies to the cross-section of the element. This means that the original cross-section (before any expansion occurs) should remain plane after the expansions take place. Consequently, the final strain (ε_c) of the cross-section should follow the profile depicted as a discontinuous line in Figure 5. By imposing equilibrium in a simple sectional analysis (Eq. 4 to 6), it is possible to assess σ_c and σ_{tc}.

$$N = 0 = \int_{Area} E(x) \cdot \left(\varepsilon_c(x) - \varepsilon_l(x)\right) \partial Area \qquad (4)$$

$$M = 0 = \int_{Area} E(x) \cdot \left(\varepsilon_c(x) - \varepsilon_l(x)\right) x \partial Area \quad (5)$$

$$\varepsilon_c(x) = \varepsilon_c(x = 0) + \zeta x \quad (6)$$

The term ζ (<<1) represents the curvature of the cross-section. The stress level is calculated with Eq. 7 by multiplying the elastic modulus of the material (E) and the difference between the total strain (ε_c) and the non-mechanical strain (ε_l).

$$\sigma(x) = E(x) \cdot [\varepsilon_c(x) - \varepsilon_l(x)] \quad (7)$$

The value of E is affected by the damage induced by the ESA, varying along the cross-section. In this sense, the sound core presents an elastic modulus E_0 that should be higher than the elastic modulus E_e of the external layer affected by microcracking. To account for this effect on the structural formulation, E_e is assumed constant along the external layer, whereas E_0 is set constant in the sound core. Even though no consensus exists in the literature on the quantification of the degradation of mechanical properties, most studies suggest that the strength loss for specimens may range between 10-50% [33,34].

Creep deformations were not considered in the simplified methodology proposed here as this implies an iterative calculation that would compromise the straightforwardness of the approach. Notice that creep deformations would reduce the internal stress level of the structural element, allowing the accommodation of part of the expansions. Therefore, disregarding creep effects is a simplification on the safe side since it would lead to the calculation of higher stresses than the expected in reality. However, this assumption also affects the assessment of the displacements and the verification of the serviceability limit state since smaller strain levels than the expected in reality would be obtained with the formulation proposed here. If high precision is required in the assessment of the displacement, differed strains should be taken into account.

By solving Eq. 4 to 6 for different structural typologies and sulfate exposures, Eq. 8 to 10 are obtained to predict the maximum tensile stresses acting at a certain time in the cross-section (see Table 5). In the case of piles, R represents the total radius of the cross-section and R_i is the radius of the sound core given by the difference between R and the penetration depth P calculated with Eq. 2 or 3. In the case of diaphragm walls or tunnels, b represent the half thickness of the element.

Table 5. Simplified equations to predict the maximum stresses due to ESA

Struct. typology	Sulfate exposure	Tensile failure of the sound core	Tangential boundary failure	Tensile boundary failure
Piles (linear elements)	Full	$\sigma_{tc} = \frac{E_0 E_e \varepsilon_l (R^2 - R_i^2)}{E_e(R^2 - R_i^2) + E_0 {R_i}^2}$ (8)	$\tau_b = \frac{E_0 E_e \varepsilon_l (R^2 - R_i^2) R_i \beta_r}{2(E_e(R^2 - R_i^2) + E_0 {R_i}^2)} tanh\left(\frac{\beta_r l}{2}\right)$ (13)	$\sigma_{tb} = \frac{\varepsilon_l E_e P}{R_i}$ (17)
Diaphragm walls or tunnels (surface elements)	2 faces	$\sigma_{tc} = \frac{E_0 E_e \varepsilon_l P}{E_e P + E_0 (\mathrm{b-P})}$ (9)	$\tau_b = \frac{E_0 E_e \varepsilon_l P b_i \beta}{E_e P + E_0 (\mathrm{b-P})} tanh\left(\frac{\beta l}{2}\right)$ (14)	-
	1 face	$\sigma_{tc} = \frac{E_0 \varepsilon_l P (3P^2 - 9Pb + 8b^2)}{4b^3}$ (10)		

All equations included in Table 5 are able to assess mechanical failures at any time, as long as the penetration of sulfates are provided. The different mechanical failure modes considered and the corresponding stresses are treated separately in this paper. Even though a certain interaction might occur, it was assumed that one of the failure modes would happen because of the predominant stress. In case a more accurate prediction of the structural failure is needed, stresses from different mechanisms should be treated in a coupled way and more advanced simulations should be performed, for instance with coupled FEM.

3.2.2- Tangential boundary failure

Experimental studies show that mortar prisms exposed to ESA tend to present a layered spalling of the surface [5,15]. One of the possible mechanisms responsible for this phenomenon is depicted in Figure 6.

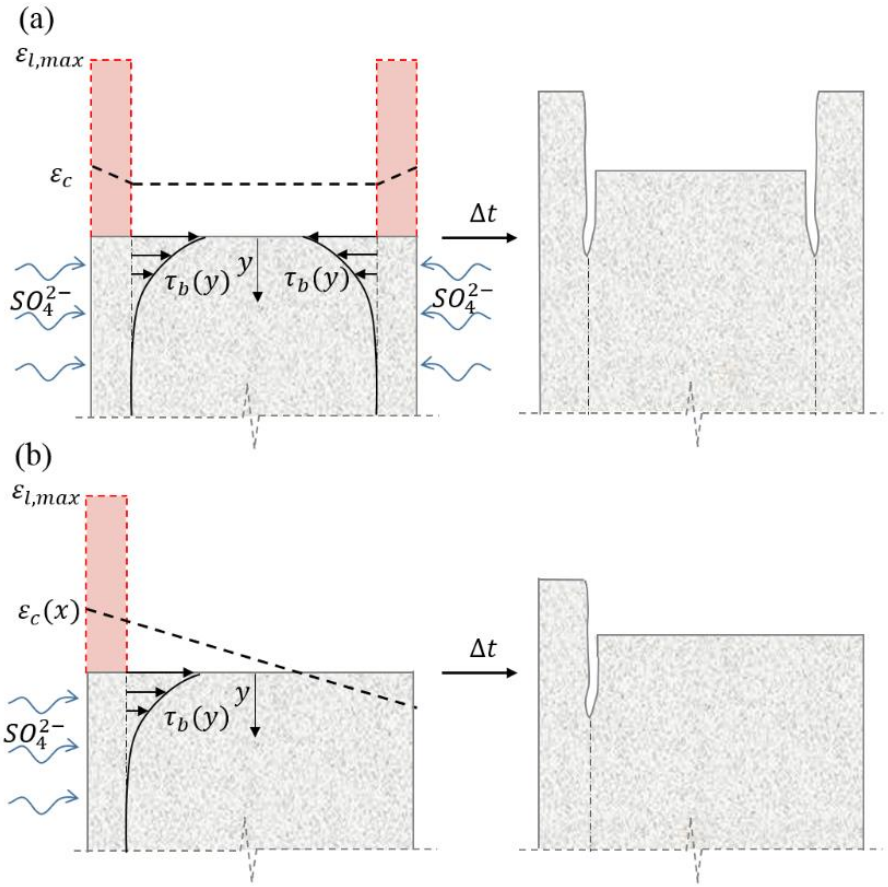

Fig. 6. Tangential stress distribution in symmetric (a) and 1 face (b) sulfate exposure.

Even though at intermediate sections the normal stresses distribution described in section 3.2.1 guarantees the compatibility of the deformation, at the top free cross-section of the element the compatibility has to be achieved through alternative mechanisms since no normal stresses exist. The difference in terms of vertical displacement creates tangential stresses between the surface layers affected by the ESA and the sound core. These should guarantee the compatibility of displacements at the extremities of the element. If the tangential stresses reach the tangential strength of the material, cracks might appear leading to the failure of the structure.

In this study, an analogy with the classical Mixing Theory for short fibers is applied [35-37] in order to deduct the equations to assess the tangential stresses. By imposing

equilibrium and compatibility, Eq. 11 is obtained to estimate the tangential stresses (τ_b) between the sound core and the surface layers at the position *y* along the axis of a pile. In this equation, l is the length of the element, β_r is a coefficient given by Eq. 12 and G is the elastic shear modulus of concrete, which may be estimated from the elastic modulus. The maximum tangential stresses are located at the extremities of the element so that *y* should be substituted by 0 in Eq. 11. This gives Eq. 13 (see Table 5) for the assessment of the maximum tangential stresses in piles.

$$\tau_b(y) = \frac{E_0 \varepsilon_c R_i \beta_r}{2} \frac{sinh\left[\beta\left(\frac{l}{2} - y\right)\right]}{cosh\left(\beta \frac{l}{2}\right)} \tag{11}$$

$$\beta_r = \sqrt{\frac{2G}{E_0 R_i^2 ln\left(\frac{R}{R_i}\right)}} \tag{12}$$

Analogous deductions may be performed for diaphragm walls or tunnels. Eq. 14 is obtained for such elements exposed to sulfates at 2 faces (see Table 5). The parameter β should be calculated according with Eq. 15. The same formulation is also adopted when elements are exposed to the sulfate ingress only in one face. The curvature introduced by the asymmetric load increases the macroscopic strain in the external damaged layer and reduces the compressive stresses in this region. Therefore, the tangential stresses transmitted to the sound core are reduced, leading to an assessment on the safe side.

$$\beta = \sqrt{\frac{G}{E_0 (b - P) P}} \tag{15}$$

It is important to remark l only affects the assessment of the tangential stresses if the length of the element is below a critical value (around 1 m for most structures). For bigger values of l, the maximum tangential stress at the extremities of the element will remain approximately constant. Therefore, the parameter l would not affect the stresses calculated in most structures.

3.2.3- Tensile boundary failure

In linear structures exposed all around to sulfates, the layered spalling may also be caused by a tensile boundary failure. As shown in Figure 7, tensile stresses (σ_{tb}) are induced by the restrictions of the sound core to the expansions experienced by the affected layer in the cross-sectional plane. Cracks appear if the stresses reach the tensile strength of concrete.

Since the penetration depth tends to be significantly smaller than the radius of the element, an analogy with the thin-walled cylinders subjected to internal pressure may be made. The affected external layer would tend to present an expansion $\varepsilon_{l,max}$ due to the ESA. This would generate stresses in the interface with the inner core, which would deform by ε_{ce} along the diameter of the element. The restriction generates compressive stresses at the external surface affected by the ESA equal to $E_e(\varepsilon_{l,max} - \varepsilon_{ce})$.

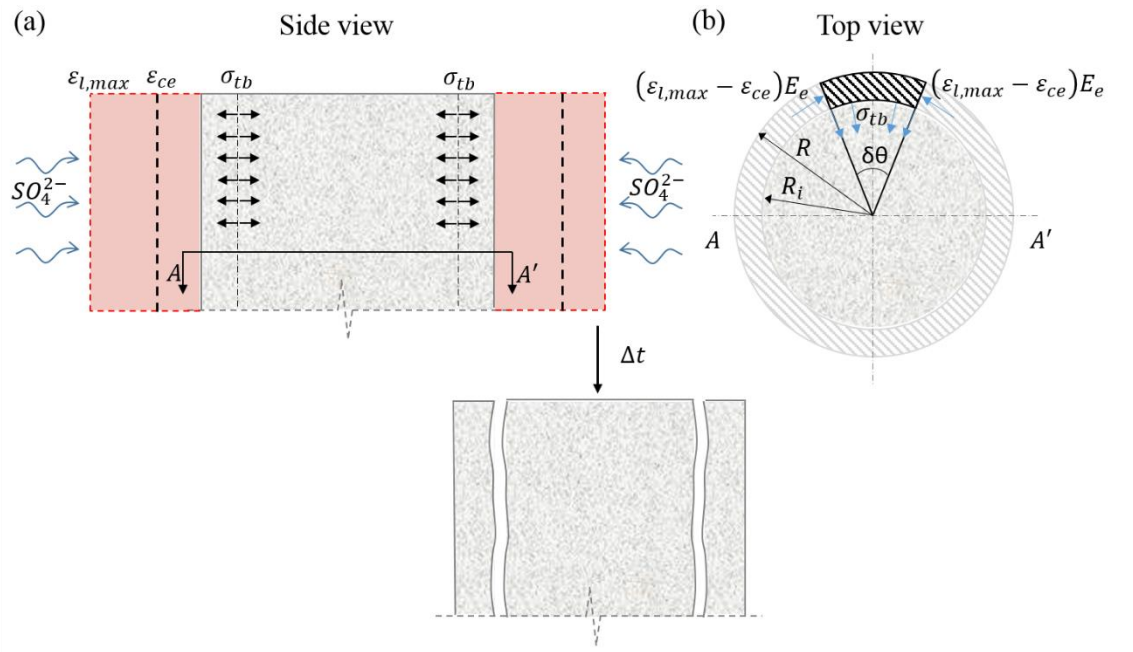

Fig. 7. Side view (a) and top view (b) of tensile stresses due to restrain of expansions in the cross-sectional plane

These compressive stresses should be balanced by the tensile stresses σ_{tb} acting in the interface with the sound core, as shown in Figure 7.b. By imposing equilibrium of the in-plane forces, Eq. 16 is obtained. Maximum tensile stresses occur when the external surface of the element is totally restrained by the sound core, that is, ε_{ce} equals 0. This gives Eq. 17, which should be used for the assessment of σ_{tb} (see Table 5).

$$\sigma_{tb} = \frac{PE_e(\varepsilon_{l.max} - \varepsilon_{ce})}{R_i} \tag{16}$$

4.- PARAMETRIC STUDY

A parametric study is performed to evaluate the results provided by the simplified methodology under a wide range of realistic conditions found in practice. Different sulfate concentrations in the media, aluminate contents and size of elements were evaluated. The results obtained are compared to those calculated with the integrated model by [9] and to the criteria from structural codes.

Table 6 shows the ranges and the reference values assumed for the two parameters considered in the study. All sulfate concentrations (C_{SO}) evaluated correspond to moderately or highly aggressive exposure classes according to UNE EN 206-1. The range defined for the aluminate content (C_{CA}) corresponds to a concrete with 350 kg/m^3 of cement that contains 80% of clinker and from 4% to 12% of C_3A. The reference value is equivalent to cement with 10% of C_3A. Initial diffusivity and the buffer capacity of the matrix are initially fixed at 10^{-12} m^2/s and 0.15, respectively. The length (l) of the structural element is fixed at 5 m, which is above the critical length for the assessment of the tangential stresses. This means that the results derived from the parametric study also apply to elements with bigger values of l. The additional input parameters required in the integrated model by [9] are fixed at the reference values adopted in section 3.1.3.

Table 6. Range of parameters in the parametric study

Parameter	Minimum	Reference	Maximum
C_{SO} [g/l]	0.6	3.0	4.2
C_{CA} [% C_3A]	4	10	12

The compressive strength and the elastic modulus of concrete are fixed at 30 MPa and 28000 MPa, respectively. The elastic modulus was considered the same at the sound core and at the superficial layer affected by ESA. This consideration is on the safe side since it provides higher internal stresses in the equations from Table 5. The tensile strength (f_t) of the material is approximated through the formulation included in the Model Code. The formulation proposed by Kaneko et al. [38] is used to estimate the shear strength, which gives a τ_{max} of 7.1 MPa. This value is in agreement with experimental tests performed by Djazmati [39].

4.1.- INFLUENCE OF *Cso*

Figure 8 shows the penetration depth at 25 and 50 years obtained with the integrated model by Ikumi et al. [9] and with the simplified equations (Eqs. 2 and 3) for different sulfate concentrations. The curves corresponding to the simplified equations with the 95% probability (K_{95}) are depicted in dotted lines. At both ages, the simplified equations derived in this study provide a good fit of the penetration front. The use of K_{95} yields penetration depths above the expected values, ensuring conservative results.

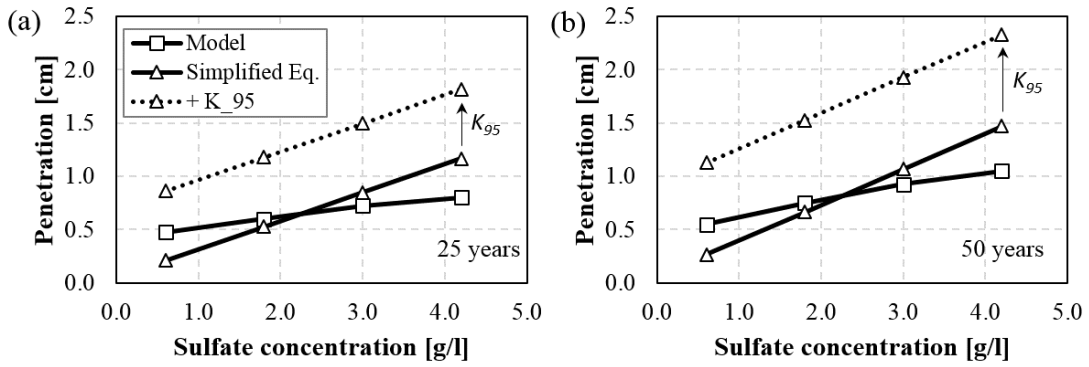

Fig. 8. Penetration depth for different sulfate concentrations

To evaluate the risk of mechanical failure, the maximum linear expansions ($\varepsilon_{l,max}$) are calculated with Eq. 1, assuming that all aluminate react to form ettringite. This gives a $\varepsilon_{l,max}$ of $8.7 \cdot 10^{-4}$. Simplified equations presented in Table 5 for piles under full sulfate exposure are applied to calculate the tensile stress in the sound core (σ_{tc}), the tangential stress (τ_b) and the tensile stress (σ_{tb}) between the damaged and undamaged areas. Only penetration depths obtained through the simplified equation are evaluated. The ratio between each stress and the corresponding strength is calculated through Eqs. 18 to 20 to make the risk of failure comparable for the different modes analyzed. The failure occurs if any of the ratios become bigger than 1.

$$\psi_{Tensile\ core} = {}^{\sigma_{tc}}/_{f_t} \tag{18}$$

$$\psi_{Tangential} = {}^{\tau_b}/_{\tau_{max}} \tag{19}$$

$$\psi_{Tensile\ boundary} = {}^{\sigma_{tb}}/_{f_t} \tag{20}$$

Figure 9 shows the stress/strength ratios at 25 and 50 years for piles with 90 cm, 40cm and 30 cm of diameter under different sulfate exposure conditions. In these figures, the limit of failure is depicted with a discontinuous line.

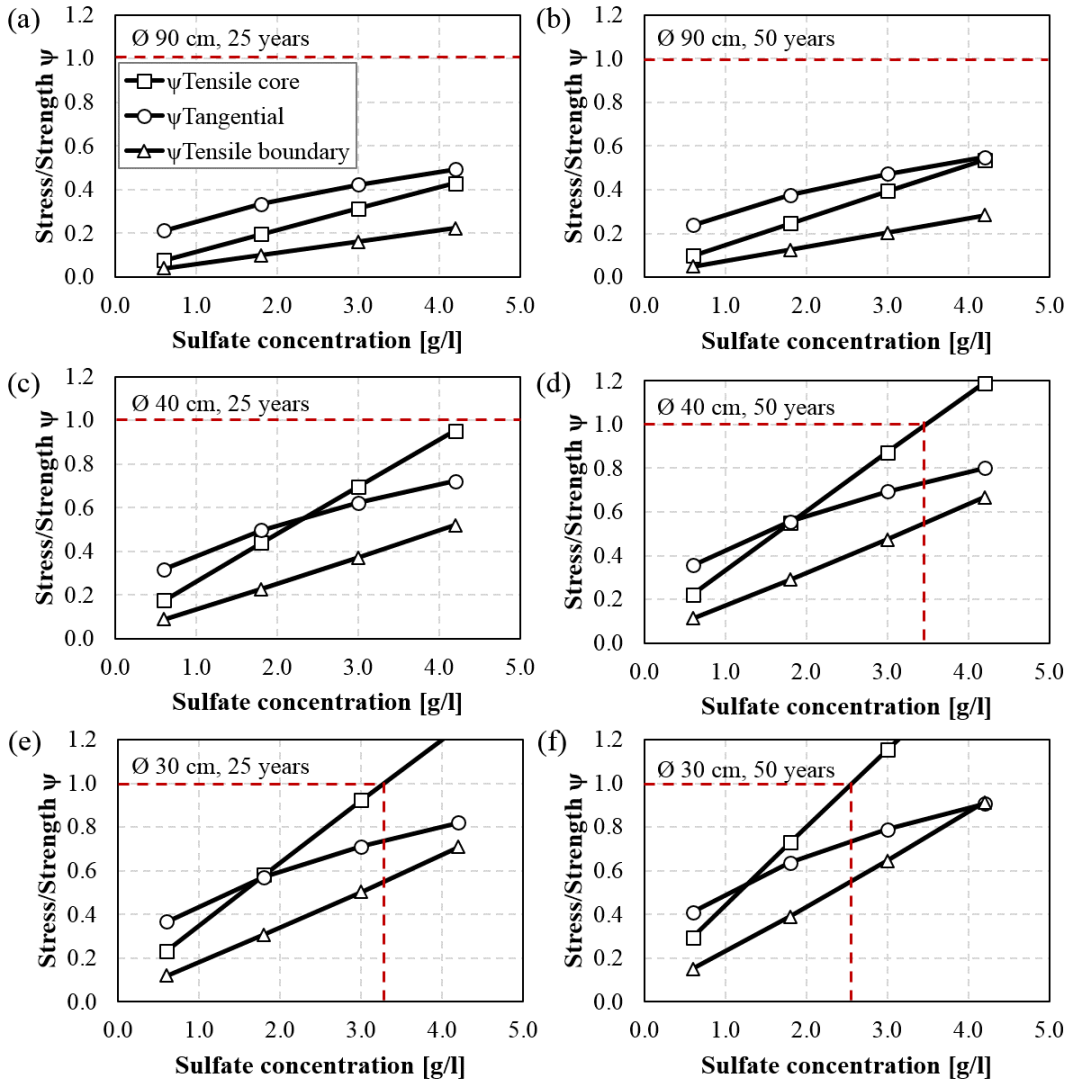

Fig. 9. Stress/strength ratio for different sulfate concentrations

Results for piles with 90 cm of diameter (Figures 9.a and 9.b) indicate no mechanical failure for any sulfate concentration below 4.2 g/l. The highest ratios are found for $\psi_{Tangential}$, followed by $\psi_{Tensile\ core}$ and $\psi_{Tensile\ boundary}$. In piles with 40 cm of diameter, $\psi_{Tangential}$ are the highest for low sulfate exposure conditions, while $\psi_{Tensile\ core}$ become critical in severe sulfate exposure conditions. In fact, a tensile failure of the sound core may occur for sulfate concentrations above 3.4 g/l at 50 years (Figure 9.d). Likewise, for piles with 30 cm of diameter, failure occurs according with the same mechanism for sulfate concentrations above 2.6 g/l and 3.3 g/l at 25 and 50 years, respectively (Figures 9.e and 9.f).

Results suggest that, for low sulfate concentrations, failure is likely to occur due to tangential stresses that causes surface delamination. Conversely, for higher sulfate concentrations, failure is likely to occur due to the tensile stresses at the sound core that causes cracking at the cross-section. This distinction is relevant since delamination of exterior layers

may be accepted as long as it does not compromise the safety of the structure or the protection of the steel rebar. On the contrary, cracking of the cross-section should be taken with care especially in piles subjected to moments or to tensile forces.

Notice that according to the European standard UNE EN 206-1, the 10% C_3A cement used in this parametric study is not allowed for sulfate concentrations above 0.6 g/l, regardless of the size of the pile. The estimations performed indicate that the limit established in the codes may be modified depending on the size of the element, the cement content and the mechanical properties of the concrete used in each application.

4.2.- INFLUENCE OF C_3A CONTENT

Penetration depths predicted with the integrated model by Ikumi et al. [9] and with the simplified equations derived in this work are compared in Figure 10 for different C_3A contents at 25 and 50 years. Again, the simplified equations provide a good fit of the penetration depths at both ages. As described in section 4, the aluminate content has minor influence on the penetration front. However, it is one of the main parameters that define the magnitude of the maximum expansion in Eq. 1.

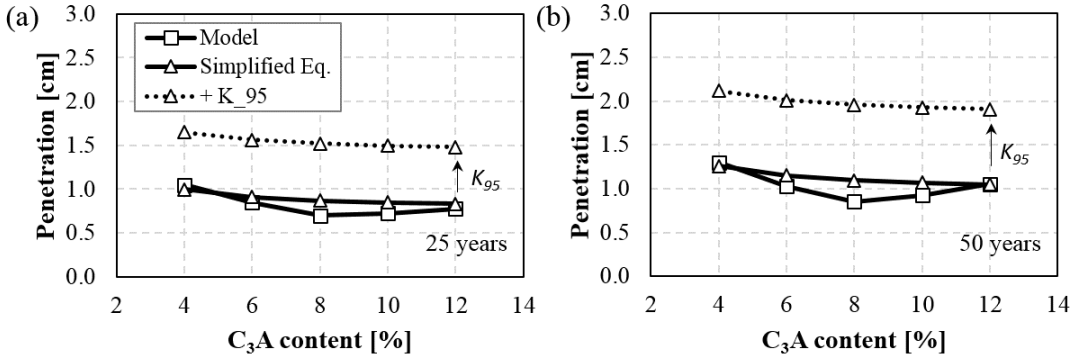

Fig. 10. Penetration depth for different aluminate contents

Figure 11 presents the stress/strength ratios for several C_3A contents in piles with 90 cm, 40 cm and 30 cm of diameter at 25 and 50 years. All curves present a similar trend, showing no failure for low contents of C_3A. Once a threshold content is reached, all stress/strength ratios increase abruptly, indicating a high risk of failure. This trend is in agreement with the criteria included in structural codes, which establish a limiting C_3A content for sulfate resistant cements (usually 5% to 6%). Below this limit it is assumed that no unacceptable damage will take place. The fact that this criterion has been successfully applied in many structural elements worldwide suggests that the simplified formulation proposed here is capable of reproducing the general behavior of concrete structures subjected to sulfate attack.

Results in piles with 90 cm of diameter indicate failure due to tangential stresses for C_3A contents above 12%. In piles with 40 cm and 30 cm of diameter, a tensile core failure is predicted for C_3A contents around 10%. It is evident that the C_3A threshold depends on the size of the element, the cement content and the mechanical properties of the concrete.

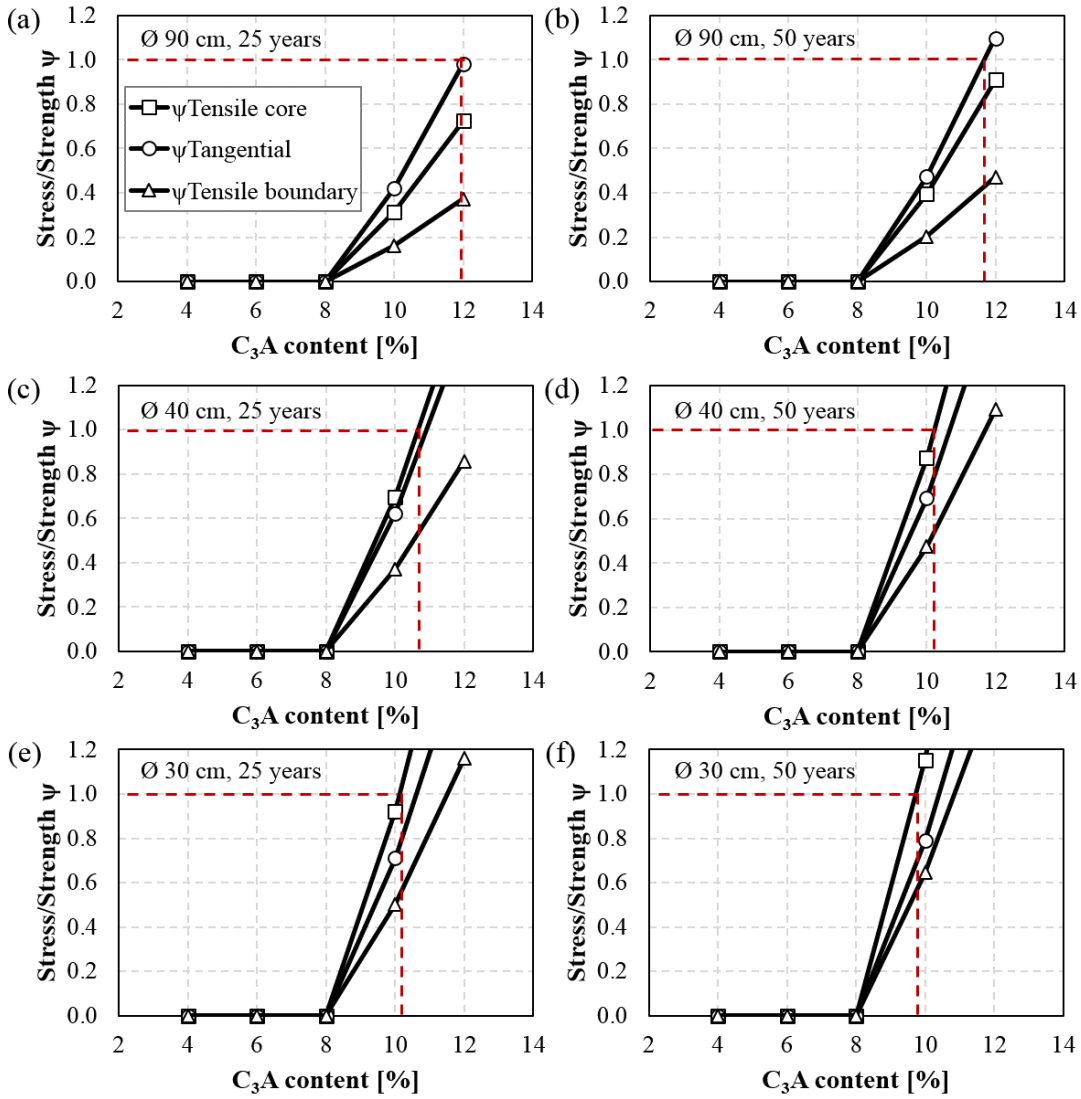

Fig. 11. Stress/strength ratio for different C_3A contents

4.3.- INFLUENCE OF THE BUFFER CAPACITY (*f*)

Figure 12 shows the thresholds obtained for different pile diameters, buffer coefficients and sulfate exposure conditions at 25 and 50 years. Values above 12% and below 4% are not depicted since are beyond the range used to deduct the simplified formulation.

The results show that the increase in the diameter of the pile leads to an increase of the C_3A threshold. Nevertheless, the main parameter governing the C_3A threshold is the buffer coefficient (*f*). According with Tixier and Mobasher [11], *f* may vary between 0.05 and 0.40. However, the results obtained suggest that values above 0.20 are not realistic, as the matrix is able to accommodate enough expansive products without any macro-structural damage for all exposure conditions considered. Therefore, a buffer capacity around 0.10 is proposed in the present study.

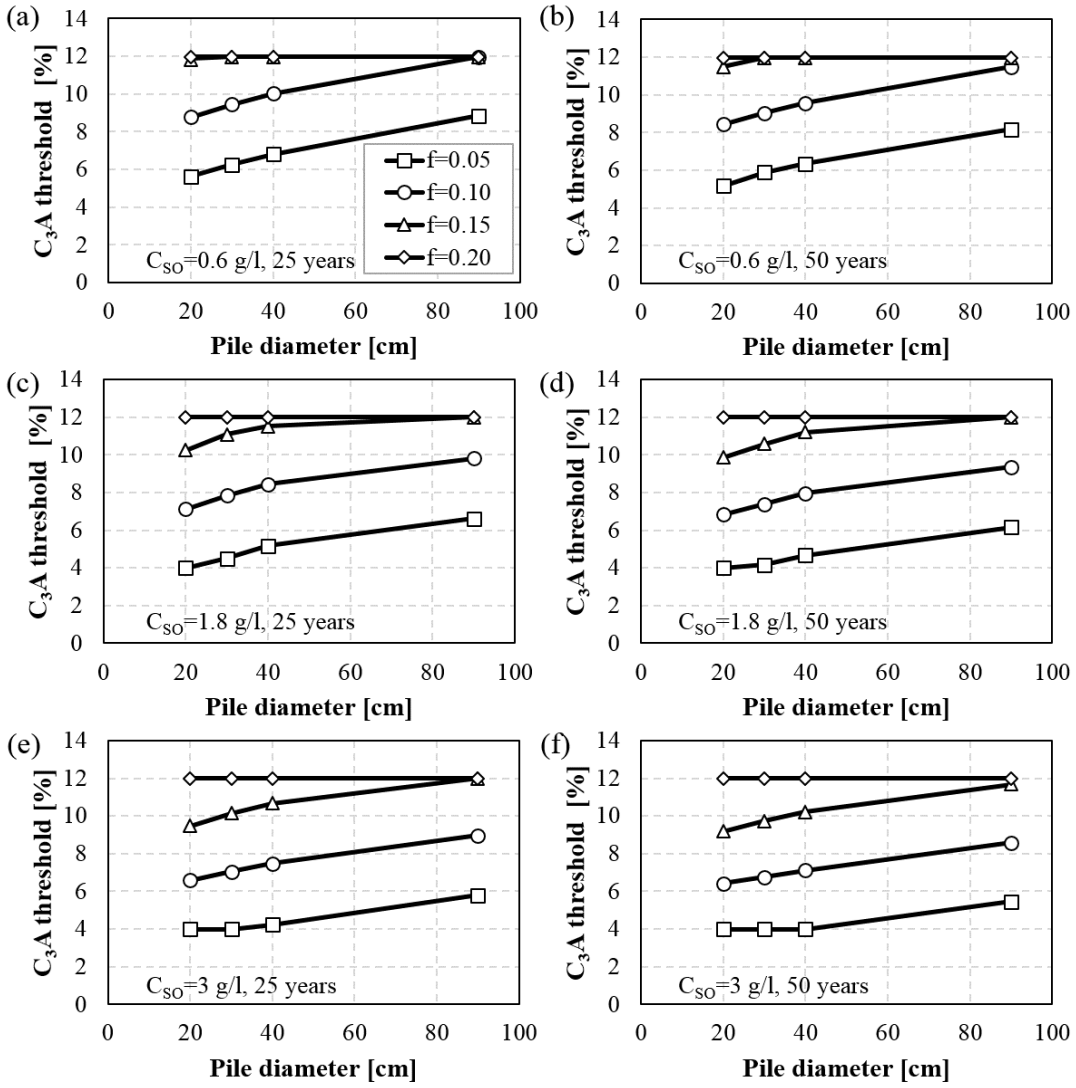

Fig. 12. C_3A threshold for different pile diameters and buffer coefficients

4.4.- PROPOSED C_3A THRESHOLD FOR PILES

Reference C_3A threshold values calculated with the simplified model are presented for different exposure conditions and dimensions for service lives of 25 and 50 years. Table 7 corresponds to radial elements –piles-, whereas Table 8 and Table 9 correspond to elements such as walls under full or partial exposure, respectively.

Table 7. Proposed % C_3A threshold for a service life of 25 years and 50 years (in brackets).

C_{SO} [g/l]	Pile diameter [cm]			
	20	30	40	90
0.6	8.8 (8.4)	9.4 (9.0)	10.0 (9.6)	≥12.00 (11.5)
1.8	7.1 (6.8)	7.8 (7.4)	8.4 (8.0)	9.8 (9.4)
3.0	6.6 (6.4)	7.0 (6.8)	7.5 (7.1)	8.9 (8.6)
4.2	6.3 (6.2)	6.7 (6.5)	7.0 (6.7)	8.5 (8.0)

Table 8. Proposed % C_3A threshold for a service life of 25 years and 50 years (in brackets) in surface elements with 2 faces exposed.

C_{SO} [g/l]	Surface element width [cm]			
	20	30	40	90
0.6	10.0 (9.6)	11.0 (10.4)	11.9 (11.2)	≥12.0 (≥12.0)
1.8	8.5 (7.9)	9.1 (8.7)	9.6 (9.2)	11.5 (10.9)
3.0	7.4 (7.1)	8.3 (7.8)	8.8 (8.5)	10.3 (9.8)
4.2	7.0 (6.7)	7.6 (7.2)	8.2 (7.7)	9.6 (9.2)

Table 9. Proposed % C_3A threshold for a service life of 25 years and 50 years (in brackets) in surface elements with 1 face exposed.

C_{SO} [g/l]	Surface element width [cm]			
	20	30	40	90
0.6	9.4 (8.6)	11.0 (10.1)	11.9 (11.2)	≥12.0 (≥12.0)
1.8	7.2 (6.9)	7.9 (7.5)	8.6 (8.0)	11.5 (10.9)
3.0	6.7 (6.5)	7.1 (6.8)	7.5 (7.2)	9.8 (9.0)
4.2	6.4 (6.3)	6.7 (6.5)	7.1 (6.8)	8.7 (8.1)

The values recommended in Tables 7 to 9 are applicable to concretes with 350 kg of cement per cubic meter, an *f* equal to 0.10, the sulfate diffusivity and concrete mechanical properties considered in the parametric study. Once more the values confirm that the C_3A threshold depends on the dimensions of the element and the exposure conditions. It is also observed that for equivalent conditions the threshold for piles tends be smaller than that obtained for walls or tunnels. This is the result of the bigger ratio between exposed surface and the total volume found in piles.

In case a different cement content is used, the values from all tables should be multiplied by 350 and divided by the actual content in kg per cubic meter of concrete. Moreover, in case an *f* equal to 0.05 should be considered, the values from Tables 7, 8 and 9 should be multiplied by 0.63, 0.66 and 0.60, respectively.

5.- CONCLUSIONS

A simplified methodology that considers the transport-reaction and the damage at a macro-structural level due to the ESA was proposed. This methodology allows a direct and simple assessment of the risk of failure for elements (piles, walls and tunnels) exposed to a sulfate rich environment, considering the conditions found in each application. The following conclusions may be derived from this study.

(1)- Flux intensification effect of the sulfate ions in radial elements plays a minor role in the maximum penetration depth for the typical size of real structures. Therefore, unidirectional flux is adopted for all structural typologies, thus avoiding the use of different formulations and the consideration of the element size in the simplified reactive-transport equations.

(2)- Sulfate and aluminate concentration, initial diffusivity and the buffer coefficient are the most influencing parameters for the estimation of the penetration front. Changes in the compressive strength and initial porosity display a smaller influence on the penetration depth.

(3)- According to the results obtained, buffer capacities above 0.20 of the initial porosity are not realistic. Therefore, buffer capacities between 0.05 and 0.20 should be used.

(4)- For lower sulfate concentrations and bigger pile diameters, failure is likely to occur due to tangential stresses that causes surface delamination. On the other hand, for bigger sulfate concentrations and lower pile diameters, failure is likely to occur due to the tensile stresses at the sound core that causes cracking at the cross-section.

(5)- The simplified methodology suggests the existence of a C_3A threshold above which a high risk of structural damage occurs. This trend is consistent with the philosophy used in structural codes and validated in practice. The C_3A threshold increases with the increase of the size of the element and with the reduction of the sulfate concentration.

(6)- Reference values are proposed for the C_3A threshold depending on the exposure conditions, type and dimensions of the structure. In case a more precise assessment is required, the equation included in the simplified methodology may be used to estimate the C_3A threshold. The procedure followed for this estimation requires the use of the formulation included in Tables 4 and 5, being compatible with the durability assessment found in building codes.

ACKNOWLEDGMENTS

Support from the Spanish Ministry of Economy and Competitiveness through research project BIA2013-49106-C2-1-R is greatly acknowledged. T. Ikumi is supported by the fellowship program FPI of the Spanish Ministry of Economy and Competitiveness.

REFERENCES.

[1] C. Ayora, S. Chinchón, A. Aguado, F. Guirado, Weathering of iron sulfides and concrete alteration: Thermodynamic model and observation in dams from central Pyrenees, Spain, Cem. Concr. Res. 28 (1998) 591–603.

[2] J.P. Skalny, I. Odler, J. Marchand, Sulfate Attack on Concrete, Spon, London, (2001).

[3] A. Neville, The confused world of sulfate attack on concrete, Cem. Concr. Res. 34 (2004) 1275–1296.

[4] J.S. Chinchón, C. Ayora, A. Aguado, F. Guirado, Influence of weathering of iron sulfides contained in aggregates on concrete durability. Cem. Concr. Res. 25 (1995) 1264-1272.

[5] S.T. Lee, R.D. Hooton, H. Jung, D. Park, C.S. Choi, Effect of limestone filler on the deterioration of mortars and pastes exposed to sulfate solutions at ambient temperature, Cem. Concr. Res. 38 (2008) 68–76.

[6] A. Atkinson, J.A. Hearne, An assessment of the long-term durability of concrete in radioactive waste repositories, MRS Proceedings 50 (1985) 239.

[7] A. Atkinson, J.A. Hearne, Mechanistic model for the durability of concrete barriers exposed to sulphate-bearing groundwaters, Mat. Res. Soc. Symp. Proc. 176 (1990) 149-156.

[8] K. E. Kurtis, P. J. Monteiro, Empirical models to predict concrete expansion caused by sulfate attack, ACI Materials J. 97 (2000) 156-161 (errata publ. 97:713).

[9] T. Ikumi, S.H.P. Cavalaro, I. Segura, A. Aguado, Alternative methodology to consider damage and expansions in external sulfate attack modeling, Cem. Concr. Res. 63 (2014) 105–116.

[10] C. Yu, K. Scrivener, Mechanism of expansion of mortars immersed in sodium sulphate solution, Cem. Concr. Res. 43 (2013) 105–111.

[11] R. Tixier, B. Mobasher, Modeling of Damage in Cement-Based Materials Subjected to External Sulfate Attack. I: Formulation, J. Mater. Civ. Eng. 15 (2003) 305–313.

[12] R. Tixier, B. Mobasher, Modeling of damage in cementbased materials subjected to external sulfate attack. II: Comparison with experiments, J. Mater. Civ. Eng. 15 (2003) 314–322.

[13] B. Bary, Simplified coupled chemo-mechanical modeling of cement pastes behavior subjected to combined leaching and external sulfate attack, Int. J. Numer. Anal. Meth. Geomech. 32 (2008) 1791–1816.

[14] S. Sarkar, S. Mahadevan, J.C.L. Meeussen, H. van der Sloot, D.S. Kosson, Numerical simulation of cementitious materials degradation under external sulfate attack, Cem. Concr. Compos. 32 (2010) 241–252.

[15] A.E. Idiart, C.M. López, I. Carol, Chemo-mechanical analysis of concrete cracking and degradation due to external sulfate attack: A meso-scale model,» Cem. Concr. Compos. 33 (2011) 411–423.

[16] X.B. Zuo, W. Sun, C. Yu, Numerical investigation on expansive volume strain in concrete subjected to sulfate attack, Constr. Build. Mater. 36 (2012) 404–410.

[17] N. Cefis, C. Comis, Damage modeling in concrete subject to sulfate attack, Frattura ed Integrità Strutturale vol.:8 núm:29 (2014) 222–229.

[18] B. Bary, N. Leterrier, E. Deville, P.L. Bescop, Coupled chemo-transport-mechanical modeling and numerical simulation of external sulfate attack in mortar, Cem. Concr. Comp. 49 (2014) 70–83.

[19] Q. Nie, C. Zhou, H. Li, X. Shu, H. Gong, B. Huang, Numerical simulation of fly ash concrete under sulfate attack, Constr. Build. Mater. 84 (2015) 261–268.

[20] W. Müllauer, R.E. Beddoe, D. Heinz, Sulfate attack expansion mechanisms, Cem. Concr. Res. 52 (2013) 208–215.

[21] J.R. Clifton, J.M. Pommersheim, Sulfate attack of cementitious materials: volumetric relations and expansions, NISTIR 5390, Building and Fire Research Laboratory, Gaithersburg (MD), 1994.

[22] G.W. Scherer, Stress from crystallization of salt, Cem. Concr. Res. 34 (2004) 1613–1624.

[23] R.J. Flatt, G.W. Scherer, Thermodynamics of crystallization stresses in DEF, Cem. Concr. Res. 38 (2008) 325–336.

[24] C.W. Correns, Growth and dissolution of crystals under linear pressure, Discuss Faraday Soc 5 (1949) 267–271.

[25] M. Steiger, Crystal growth in porous materials I: the crystallization pressure of large crystals, J. Cryst. Growth. 282 (2005) 455–469.

[26] W. Kunther, B. Lothenbach, K. Scrivener, Influence of bicarbonate ions on the deterioration of mortar bars under sulfate attack, Cem. Concr. Res. 44 (2013) 77–86.

[27] W. Kunther, B. Lothenbach, K. Scrivener, On the relevance of volume increase for the length changes of mortar bars in sulfate solutions, Cem. Concr. Res. 46 (2013) 23–29.

[28] M. Zhang, J. Chen, Y. lv, D. Wang, J. Ye, Study on the expansion of concrete under attack of sulfate and sulfate-chloride ions, Const. & Build. Mat. 39 (2013),26-32.

[29] B. Gérard, J. Marchand, Influence of cracking on the diffusion properties of cement-based materials. Part I: Influence of continuous cracks on the steady-state regime, Cem. Concr. Res. 30 (2000) 37–43.

[30] D.A. Hordijk, Local Approach to Fatigue of Concrete, Phd Thesis, Delft University of Technology, Delft, 1991.

[31] I. Oliveira, S.H.P. Cavalaro, A. Aguado, New kinetic model to quantify the internal sulfate attack in concrete, Cem. Concr. Res. 43 (2013) 95–104.

[32] R. Tixier, Microstructural development and sulphate attack modeling in blended cement-based materials, PhD Thesis, Arizona State University, Tempe, 2000.

[33] P.W. Brown, An evaluation of the sulfate resistance of cements in a controlled environment, Cem. Concr. Res. 11 (1981) 719–727.

[34] A. Chabrelie, Mechanisms of Degradation of Concrete by External Sulfate Ions under Laboratory and Field Conditions, PhD Thesis, ÉPFL, Lausanne, 2010.

[35] A. Kelly, Strong solids, Clarendon 1966.

[36] A. Jayatilaka, Fracture of engineering brittle materials, Applied Science Publishers, 1979.

[37] S. Oller, Simulación numérica del comportamiento mecánico de los materiales compuestos, CIMNE 74 (2003).

[38] Y. Kaneko, H. Mihashi and S. Ishihara, Shear failure of plain concrete in strain localized area, Proceeding of the Fifth International Conference on Fracture Mechanics of Concrete and Concrete Structures, Colorado, USA, V.C. Li, C.K.Y. Leung, K.J. Willam and S.L. Billington (ed.), 12-16 Vol.1 (2004) 383-390.

[39] B. Djazmati and J.A. Pincheira, Shear stiffness and strength of horizontal construction joints, ACI Structural J. 101 (2004) 484-493.

3.3. JOURNAL PAPER III. INFLUENCE OF EARLY SULFATE EXPOSURE ON THE PORE NETWORK DEVELOPMENT OF MORTARS

Published in Construction and Building Materials 143 (2017) 33-47.

Tai Ikumi[a,*], Ignacio Segura[a,b], Sergio H.P. Cavalaro[a,*]

[a] Department of Construction Engineering, Universitat Politècnica de Catalunya Barcelona Tech, Jordi Girona 1-3, C1, E-08034 Barcelona, Spain
[b] Smart Engineering, Jordi Girona 1-3 K2M 202c, Barcelona, Spain

* Corresponding authors at: Department of Civil and Environmental Engineering, Universitat Politècnica de Catalunya Barcelona Tech, Jordi Girona 1-3, C1, E-08034 Barcelona, Spain. Email addresses: tai.ikumi@upc.edu (T. Ikumi), sergio.pialarissi@upc.edu (S.H.P. Cavalaro), Tel: +34 93 401 6507 Fax: +34 93 401 1036

Abstract

The objective of this paper is to evaluate the influence of sulfate exposure on the pore network development of several Portland cement matrices. MIP, XRD and SEM analyses were performed at different ages in samples exposed to sulfates after 2 days of casting. Results suggest that patterns of precipitation of the expansive products are linked to the degree of refinement of the pore network. During early stages of exposure, large pores concentrate a higher proportion of the expansive product formed. At later stages, precipitation evolves towards finer pore sizes.

Keywords: Concrete; Durability; External sulfate attack; Pore structure; Ettringite; Precipitation pattern; Curing

1. INTRODUCTION

External sulfate attack (ESA) has been recognized as a complex degradation phenomenon that may cause severe damage in cement based materials [1,2]. The stresses generated by precipitation of expansive phases (ettringite and gypsum) in the pore network are reflected on the macro-scale in the form of expansions and cracking. After decades of extensive research, important aspects such as the precipitation pattern of expansive products are not fully understood. Because of that, codes have adopted simplified approaches to mitigate ESA in real structures. Moreover, numerical models to predict the damage include simplifications regarding the precipitation of expansive products, requiring several fitting parameters to correctly reproduce the effects of ESA [3,4].

The uncertainties in fundamental issues might be explained by the fact that most of the research conducted in this field is focused on the dimensional variation and cracking, which are the macro-scale response of the precipitation of expansive phases in the pore network. However, according to recent publications [5-7], to correctly assess the potential damage is key to understand the relationship between ettringite formation and pore network. When it comes to evaluate the damage generated, K. Tosun et al. [5] suggested that the location and morphology of the ettringite precipitation may be more relevant than the total quantity of ettringite formed. In fact, the crystallization pressure theory [6,7] states that only expansive products precipitated in small pores are likely to cause damage. Unfortunately, few experimental studies focusing on these aspects are found in the literature due to limitations in the techniques available to characterize the precipitation in the pore structure of the cement-based materials.

Another important issue hardly ever evaluated is the early sulfate exposure. In reality, the source of external sulfate ions is usually found in sulfate-rich soils and underground waters in contact with concrete. Therefore, ESA is especially significant in underground structures like foundations, tunnels or waste containers. Due to their massive size, these structures are usually built *in situ*, hence being exposed to sulfates since casting. However, most studies about the ESA in laboratory rely on testing of specimens cured several days in lime water prior immersion in the aggressive solution with sulfates.

To illustrate this, Table 1 summarizes some of the recent studies on the ESA performed in laboratory, including data on the mineral admixtures used and the age at which the specimens were exposed to the sulfate solution. Even though it only represents a small part of studies published, the table indicates that in most of them specimens are cured at least 28 days before sulfate exposure. If mineral admixtures are used, this non-aggressive curing may be extended to 90 days. This contrasts with the reality found in most structures, which are subjected to sulfates shortly after casting.

Despite the influence of pore characteristics on the precipitation of expansive phases and the importance of early sulfate exposure, there is little or no research focused on the combination of these aspects. The objective of this study is to assess the pore network development and estimate qualitatively the pore ranges at which the alterations might occur in specimens subjected to early sulfate exposure. Since these aspects are expected to vary depending on the initial pore size distribution of the material, five mortars with different pore systems were evaluated: one without any mineral admixture (reference), three with mineral admixtures (fly ash, silica fume or limestone filler) and one with air-entrainer. In addition to that, the influence of two different sulfate concentrations representative of field and laboratory conditions were evaluated.

Table 1. Age of sulfate exposure in a selection of recent publications

Authors	Year	Additions				Age of exposure [days]
		FA[a]	SF[b]	LF[c]	S[d]	
M.T. Bassuoni, M.L. Nehdi [8]	2009	x	x	x	x	56
T. Schmidt et al.[9]	2009			x		28
B. Lothenbach et al. [10]	2010					28
T. Aye, C.T. Oguchi [11]	2011	x	x			28
El-Hachem [12]	2012					3 and 28
W. Kunther et al. [13]	2012	x	x	x	x	28
J. Gao et al. [14]	2013	x			x	60
W. Müllauer [15]	2013					28
Zhang et al. [16]	2013					28
I. Sirisawat et al. [17]	2014	x		x		28
J. Stroh et al. [18]	2015	x			x	28
Yu et al. [19]	2015				x	90

a: Fly ash, b: Silica fume, c: Limestone filler and d: Slag

The evolution of the pore structure was assessed by mercury intrusion porosimetry (MIP). Although this technique may be affected by several experimental factors [20,21], it is one of the few that may provide an overview on the pore distribution. Moreover, a qualitative comparison should provide valuable information regarding the influence of early sulfate exposure and highlight possible differences on the precipitation patterns depending on the characteristics of the material. X-ray diffraction (XRD) combined with Rietveld analysis was performed to evaluate the presence of expansive phases at the end of the curing period. Scanning electron microscopy (SEM) was also performed to assess the influence of the external sulfate concentration and the degree of refinement of the matrix on the morphology and crystallinity of the ettringite formed.

The results obtained shed light on important issues related with the ESA. It provides a different view on the evolution of the attack, suggesting possible explanations for the alteration patterns observed in the porous network over time. The conclusions derived from this study may help to further understand the phenomenon behind the ESA, being useful for future development of prediction models and guidelines.

2. EXPERIMENTAL

2.1. MATERIALS AND MIXTURE CHARACTERISTICS

Table 2 shows the properties of the Portland cement and mineral admixtures used in this work. Chemical composition of Portland cement (CEM I 52.5 R) was determined by Xray fluorescence (XRF) and phase compositions were calculated using Bogue equations. Due to the presence of ferromagnetic particles, elemental compositions of the fly ash and silica fume were determined by ICP-MS. The fly ash used is equivalent to ASTM C618 class F. A low-calcium fly ash was chosen for its little or no self-cementing properties and to avoid a supplementary addition of the crystalline phases that may be present in high-calcium fly ashes, such as C_3A or C_4A_3S. Siliceous sand with maximum particle size of 2 mm was chosen for all binders.

Table 3 shows the composition of the 5 matrices included in the study, which intends to simulate the typical composition of the mortar that surrounds the coarse aggregate in a conventional concrete applied in foundations. In certain applications, mineral admixtures are used to replace a fraction of the cement, which reduces the C_3A content of the binder and its

expansive potential. However, in this work, the additional volume from the mineral admixtures was fully compensated by a reduction in the content of sand. This way, the content of cement remained the same for all mixtures, ensuring a constant amount of C_3A per unit of volume and similar potential expansion. Although the water/cement ratio remained constant for all compositions at 0.45, the addition of mineral admixtures caused changes to the water/binder ratio. This allows the assessment of the alterations introduced by early sulfate exposure in the pore system over a wide range of different pore size distributions. Values of water/binder ratio for each composition are included in Table 3.

Table 2. Properties of cement and mineral admixtures.

	PC[a]	LF[b]		FA[c]	SF[d]
Chemical comp. [%]			*Elemental comp. [%]*		
SiO_2	19.5	1.99	Si	23.56	46.26
Al_2O_3	5.9	1.05	Al	8.74	0.35
Fe_2O_3	1.7	0.46	Fe	6.92	1.26
CaO	63.1	54.16	Ca	3.70	0.32
MgO	2.1	0.63	Mg	0.50	0.07
SO_3	3.5	-	S	0.20	-
K_2O	0.78	0.10	K	0.55	0.21
Na_2O	0.35	0.02	Na	-	0.61
Cl^-	0.02	-	P	0.11	-
MnO	-	0.01	Mn	0.01	0.04
TiO_2	-	0.05	Ti	0.28	-
Ignition loss	2.96	42.39		1.68	3.35
Physical prop.					
Spec. surf. area (BET) [m^2/g]	1.10	3.74		1.56	19.84
Phase comp. [%]					
C_3S	65.4				
C_2S	10.6				
C_3A	12.3				
C_4AF	5.6				

a: Portland cement, b: Limestone filler, c: Fly ash and d: Silica fume

The mixing procedure defined in UNE-EN 196-1:2005 was adopted, assuming small modifications to cover the specificities of the admixtures added and the cylindrical molds used. In the case of compositions with mineral admixtures, the latter was first thoroughly mixed with cement prior to adding water. GLENIUM ACE 456 superplasticizer was added to all compositions mixed with the deionized water in contents to assure flow extents of 20 cm ± 0.5 cm. In the case of composition PC_A, air-entrainer admixture MasterAir 100 was added at the end of the mixing procedure and mixed at high speed for 60 s.

Table 3. Mortar composition.

	PC	PC_FA	PC_LF	PC_SF	PC_A
Cement [kg/m^3]	580	580	580	580	580
Sand [kg/m^3]	1325	1140	1210	1245	1325
Water [kg/m^3]	261	261	261	261	261
Fly ash [%[a]]	-	30	-	-	-
Limestone filler [%[a]]	-	-	20	-	-
Silica fume [%[a]]	-	-	-	10	-
Air-entrainer [%[a]]	-	-	-	-	0.3
Water/binder ratio	0.45	0.35	0.38	0.41	0.45
Superplasticizer [%[a]]	0.25	0.55	0.55	1.00	0.25

a: Percentage by cement weight

2.2. EXPERIMENTAL PROCEDURE

2.2.1. Specimen preparation

Mortars were cast into cylindrical molds of 2 cm of diameter and 16 cm of height. The specimen size was chosen according to the results of the size effect study by R. El Hachem et al. [22], who determined that 2x2x16 cm^3 prisms reached a good balance between test duration and representativeness. In the present study, cylindrical specimens were used to avoid the typical corner spalling experienced in rectangular prisms during the ESA. The specimens were cast individually to avoid presence of cut sand on the surface.

Figure 1a depicts a schematic representation of the molds used, which had a longitudinal opening to ease the demolding process. Prior to casting, this opening was sealed with a high strength duct tape. As shown in Figure 1b, the mortar was poured gradually in three steps. After each step, the material was manually compacted. Specimens were demolded 24 hours after casting and water sealed with epoxy resin at both ends to ensure radial penetration of the sulfate ions at the lateral surface (Figure 1c).

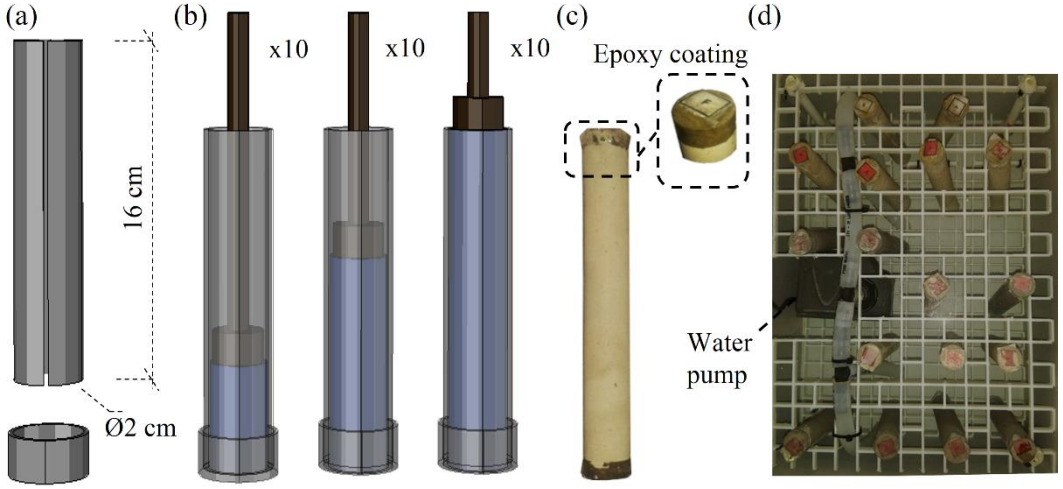

Fig. 1. Schematic representation of (a) cylindrical molds and (b) casting process, (c) specimen with epoxy coating and (d) specimen layout.

2.2.2. Exposure conditions

Once sealed, specimens were cured in water at 25 ºC ± 1 ºC for one day. Then, 2 days after mixing, they were placed vertically inside plastic containers and submerged in a sulfate rich water solution, as shown in Figure 1d. Sulfate concentrations of 3 and 30 g of Na_2SO_4/l were used to reproduce field and accelerated laboratory testing conditions (referred to as C3 and C30, respectively). The sulfate concentration of 3 g/l corresponds to the upper limit of the moderately aggressive class of exposure defined in EN 206-1. 30 g/l corresponds to 10 times the typical values found in the field [23]. The solution was renewed weekly during the first month and every other week until the end of the test. The volumetric ratio of sulfate solution to mortar was 12. This should be representative of field conditions where the material is exposed to continual supply of sulfate ions.

Water pumps were used at low speed to ensure a continuous flow from the bottom to the top of the container. The containers were filled up to the top and covered to reduce contact with the air, thus limiting CO_2 dissolution and further carbonation. Duration of exposure for all mortars with mineral (PC_FA, PC_LF and PC_SF) and an air-entrainer (PC_A)

admixtures was set to 90 days. In mortars without admixtures (PC) the period evaluated was shortened to 28 days. Test duration was set to cover typical curing periods before sulfate exposure reported in the literature (see Table 1). Reference samples of each composition were also exposed to non-aggressive curing with water without sulfates for comparative purposes.

2.2.3. Microstructural analysis methods

The pore characteristics of the mortars were examined by mercury intrusion porosimetry (MIP) with a Micrometrics AutoPore IV 9500 (contact angle 140º and Hg surface tension 485 dynes/cm) at 7, 28 and 90 days. Following the recommendations by [24,25], samples for MIP measurements were core drilled from original specimens (Figure 2a) using a column drill equipped with a diamond drill bit cooled with water, as this extraction method exhibited less sample–to–sample variation. Due to the symmetric radial sulfate exposure conditions, each sample was divided in two and analyzed separately (Figure 2b). Freeze-drying was applied to the samples to ensure full desaturation prior to mercury intrusion. The values presented in this study are the average of two specimens.

Quantitative results obtained by MIP may be prone to variations. Some studies found a shift towards finer pore sizes in intrusion curves by one or two orders of magnitude [20, 21]. Therefore, the pore sizes obtained do not necessarily correspond to the real pore sizes of the material. Nevertheless, a qualitative comparison should provide valuable information regarding the influence of early sulfate exposure and highlight possible differences on the precipitation patterns depending on the characteristics of the pore structure of the material.

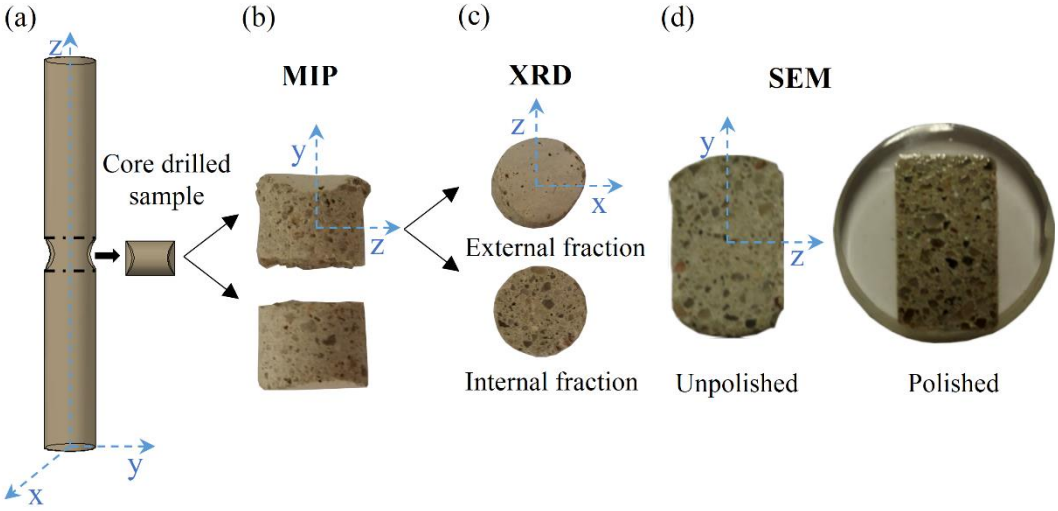

Fig. 2. (a) Core drilled sample and samples tested in (b) MIP, (c) XRD and (d) SEM.

Phase composition at the end of the curing period was investigated by X-ray diffraction (XRD). Samples for this test were core drilled as mentioned previously and depicted in Fig. 2a. Due to the symmetric exposure conditions, the sample was divided in two (Figure 2b). One half was considered for the XRD, the other half was discarded. In order to analyze separately the external (in contact with the sulfate solution) and internal fractions of the samples, the portion considered was further divided in half with a low speed diamond saw cooled with water (Figure 2c).

Samples for XRD were freeze-dried, grinded and mixed with 10 wt.% Al_2O_3 as an internal standard. The powder samples were sandwiched between polyester films of 3.6 µm and tested with a PANalytical X'Pert PRO MPD Θ/Θ diffractometer of 240 mm of radius in

a configuration of convergent beam with a focalizing mirror and transmission geometry. CuK_α radiation (λ=1.5418 Å) and PIXcel detector with active length of 3.347 º were used. Work power was set to 45 kV – 40 mA. 2Θ/Θ scans from 4 to 88 º2Θ with a step size of 0.026 º2Θ and a measuring time of 200 seconds per step were performed.

Rietveld analysis was performed with the XRD results for the quantitative study of the crystalline phases at the end of the curing period. All structures used in the refinement are listed in Table 4. The global variables refined were the background polynomial with 4 coefficients and the zero shift. For all phases detected, individual scale factors and lattice parameters were refined. A pseudo-Voigt function was chosen to model the peak shape. The phase profile width (*w*) was refined for all phases with wt.>2 %. For the main phases (wt.>10 %), the profile parameters *U*, *V* and the peak shape were also refined. Preferred orientation corrections were applied when necessary for alite (-1 0 1), gypsum (0 2 0) and quartz (1 0 1) as long as the phase content was above 2 %. Phase compositions in the whole sample were calculated by multiplying each phase content from the external and internal fractions of the sample by its corresponding thickness. This value was then divided by the sum of the thickness of both portions.

Table 4. Structures used for Rietveld refinement.

Phase	Chemical composition	ICSD Code	Reference
Alite	Ca_3SiO_5	94742	[26]
Belite_o	Ca_2SiO_4	81097	[27]
Portlandite	$Ca(OH)_2$	15471	[28]
Calcite	$CaCO_3$	79673	[29]
Ettringite	$Ca_6Al_2(SO_4)_3(OH)_{12}26H_2O$	155395	[30]
Gypsum	$CaSO_42H_2O$	15982	[31]
Ferrite	Ca_2AlFeO_5	9197	[32]
Quartz	SiO_2	200721	[33]
Monocarboaluminate	$3CaOAl_2O_3CaCO_311H_2O$	59327	[34]
Mullite	$Al_{4,74}Si_{1,25}O_{9,63}$	66448	[35]
Corundum	Al_2O_3	73725	[36]

Additional samples were extracted and examined by scanning electron microscopy using secondary and backscattered electrons as well as EDS X-ray analysis. The analysis was performed in a JEOL JSM 7100F microscope at the voltage of 20 kV. Sections were cut perpendicular to the exposed surfaces, freeze-dried, impregnated with epoxy resin, polished and coated with carbon (Figure 2d).

3. RESULTS AND DISCUSSION

3.1. PORE STRUCTURE DEVELOPMENT IN NON-AGGRESSIVE WATER

The pore structure development of the different mixtures in non-aggressive curing conditions (without sulfates) is initially assessed to distinguish the effects caused by the sulfate presence from the microstructure transformations due to normal cement hydration.

Figure 3 depicts the evolution of the cumulative intrusion curves in non-aggressive conditions for all dosages at 7 days, 28 days and 90 days. All dosages show a refinement of the pore structure due to the hydration process along the evaluated period. The mortars with mineral admixtures (PC_LF, PC_FA and PC_SF) show higher refinements due to the replacement of a fraction of sand by finer particles. Amongst these compositions, PC_FA and

PC_SF show the finest pore size distributions due to the additional refinement induced by the pozzolanic activity of the mineral admixtures used [37]. On the other hand, the addition of an air-entrainer produces a coarser pore structure due to the intrusion of air voids ranging from 0.1 µm to 2 µm. The total mercury intruded in PC_A is considerably higher than in any other composition studied. At 90 days, PC_SF offers the highest refinement of the pore structure, followed by PC_FA, PC_LF and PC_A.

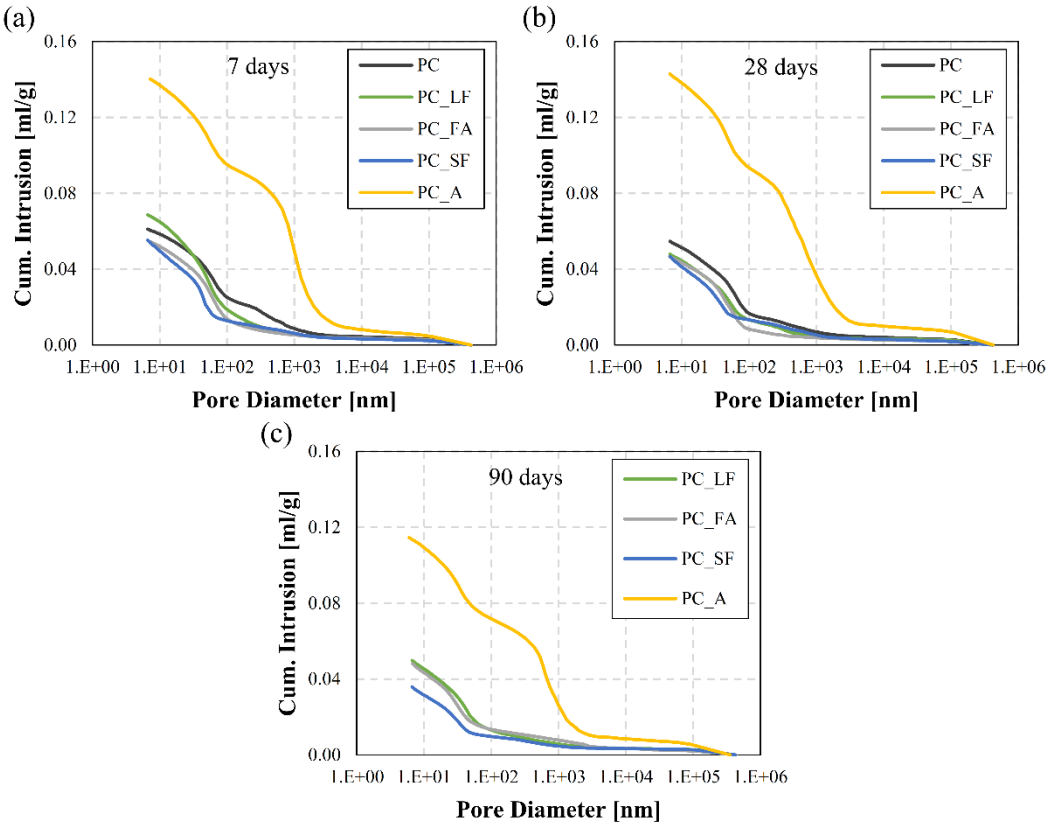

Fig. 3. Cumulative intrusion curves of PC, PC_SF, PC_LF, PC_FA and PC_A at (a) 7days, (b) 28 days and (c) 90 days.

Figure 4 shows the evolution of the critical pore diameter. This semi-quantitative parameter corresponds to the most frequently occurring diameter in the interconnected pores that allows maximum percolation. Therefore, it represents the maximum continuous pore size of the matrix and it can be related to the permeability of the specimens [38,39]. As expected from the cumulative intrusion curves, mortars with silica fume and fly ash present the smallest critical diameters at the end of the curing period. For those compositions, the reduction is produced gradually during the 90 days of curing due to the pozzolanic reaction [37]. For mortars with limestone filler, no further refinement of the pore structure is observed after 28 days, displaying a critical diameter similar to that of the reference mortar (PC). Notice that Figure 4 does not include PC_A series. The use of an air-entrainer generates micro air bubbles that distort the definition of the critical diameter.

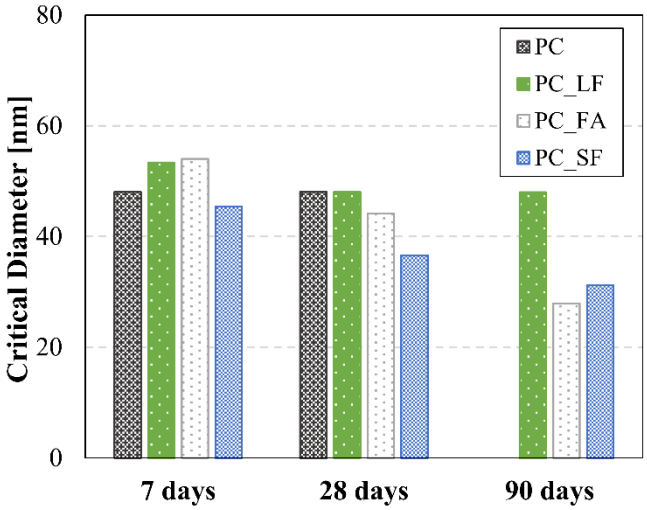

Fig. 4. Critical diameter evolution in lime water curing of PC, PC_SF, PC_LF and PC_FA.

3.2. PORE STRUCTURE DEVELOPMENT IN AGGRESSIVE CONDITIONS

3.2.1. MIP results

The evolution of the cumulative intrusion curves is evaluated separately for each of the five mortars studied. Results corresponding to the low aggressive solution representative of field conditions (C3) are available at the end of the curing period (28 days for PC and 90 days for the others). In order to ease the interpretation of the intrusion curves, the evolution of the critical diameter and the precipitation rates amongst 5 predefined pore ranges are evaluated.

Due to the known limitations associated to the MIP and the similar total mercury intruded by each composition at a specific age, results are presented as percentage of the cumulative volume intruded, not in absolute values. Variations in the intrusion curves between non-aggressive and aggressive curing conditions are assumed to be solely caused by the formation of expansive phases. The presence of anions (SO_4^{2-}) and cations (Na^+) in solution could also modify the solubility of the silicate phases. Changes on its solubility may cause different kinetics of hydration of the silicate compounds and morphology of the CSH gel between specimens exposed in aggressive and non-aggressive conditions [40,41]. Even though this could ultimately modify the pore characteristics of the matrices, to simplify the analysis the possible alterations in the pore network caused by the interaction of the sulfate salt with the silicate compounds are not taken into account. The results from the MIP tests are compared to XRD analysis in section 3.2.2, which should confirm the presence of expansive phases.

Reference mortar (PC)

Figure 5 shows the evolution of the cumulative intrusion curves for high (C30) and low (C3) aggressive curing conditions in PC. At 7 days of exposition (Figure 5a), the intrusion profile for specimens under high aggressive curing has already shifted towards a more refined pore structure. At 28 days (Figure 5b), this trend is even more evident, thus indicating the possible precipitation of expansive phases. Conversely, low aggressive curing does not affect significantly the pore network during the period evaluated.

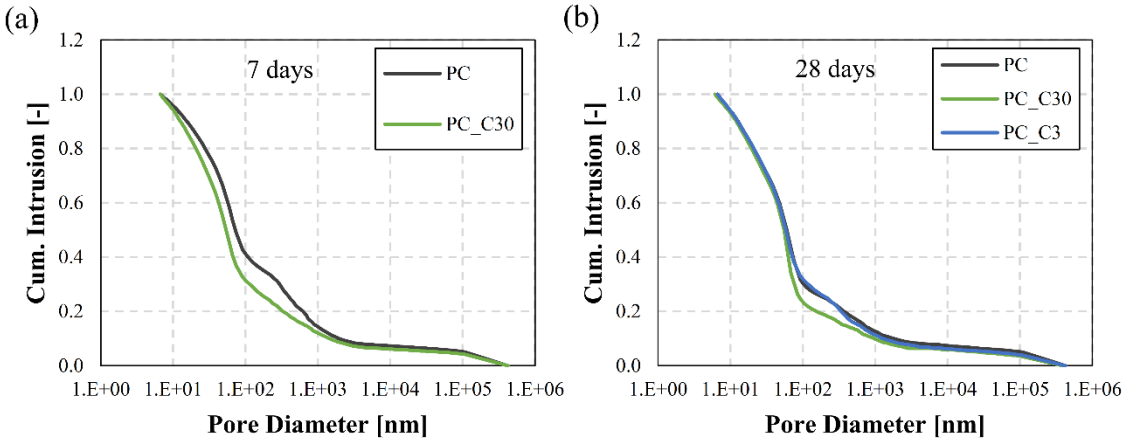

Fig. 5. Cumulative intrusion curves of PC at (a) 7 days and (b) 28 days.

In order to further analyze the MIP results, Figure 6a shows the evolution of the pore size distribution according to 5 predefined pore ranges (<10 nm, 10-50 nm, 50-100 nm, 100-500 nm and >500 nm) at different ages and curing conditions.

Figure 6a shows important modifications of the pore network at 7 days when C30 and non-aggressive curing are compared. A considerable reduction of the proportion of pores above 500 nm and 100-500 nm is observed. This is balanced by an increase of finer pores. At 28 days, the main difference on the pore size distribution between C30 and non-aggressive curing is found in the pore range 50-100 nm. An increase of the proportion of pores in this range indicates that the precipitation of expansive phases may be occurring preferentially in pores above 100 nm. Notice that larger pore ranges are affected at the initial ages of exposure. However, alterations evolve towards finer pore sizes as the exposition time increases. On the other hand, as expected from the cumulative intrusion curves presented in Figure 5b, mortars under C3 curing condition show similar pore size distributions to those of specimens subjected to non-aggressive curing both at 7 and 28 days of exposition.

Figure 6b shows the evolution of the critical diameter. No change in the critical diameter occurs at 7 or 28 days for specimens subjected to the aggressive curing in comparison to those under non-aggressive curing. Such outcome may be explained by the fact that modification in the pore network occurs in pores larger than the critical diameter presented in Figure 4 (around 50 nm).

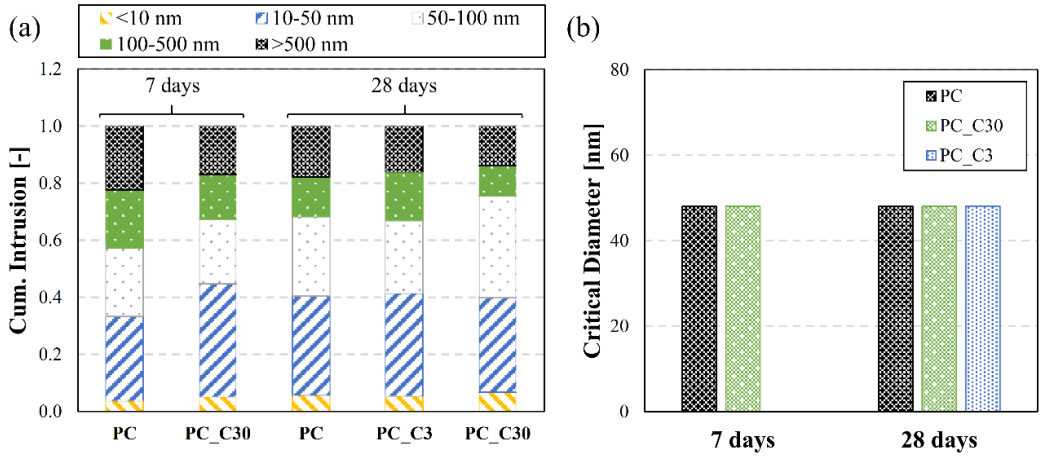

Fig. 6. Evolution of (a) pore size distribution and (b) critical diameter of PC.

Mortar with limestone filler (PC_LF)

Figure 7 presents the cumulative intrusion curves of PC_LF mortars at 7, 28 and 90 days of exposition to different curing conditions. At 7 days, no significant difference is observed between high (C30) and non-aggressive curing. However, from 28 days on, specimens submerged in the C30 solution displayed a more refined pore structure, which may indicate a precipitation of expansive phases such as ettringite or gypsum. At 90 days, specimens in the low sulfate concentration (C3) also showed a finer pore network compared to specimens under non-aggressive curing. This result suggests that the influence of an early sulfate exposure is not only significant in accelerated tests with high sulfate concentrations but also in concentrations representative of field conditions since alterations in the pore network are also observed.

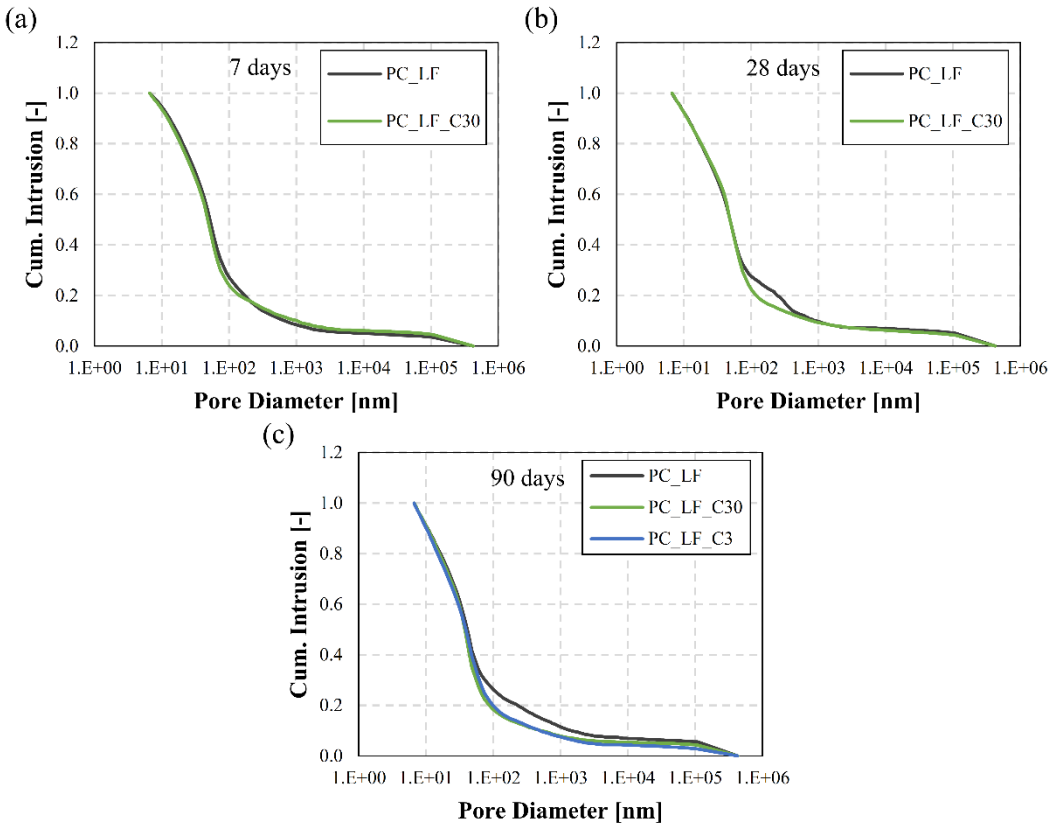

Fig. 7. Cumulative intrusion curves of PC_LF at (a) 7 days, (b) 28 days and (c) 90 days.

Figure 8a shows the evolution by pore range. At 28 days, results indicate a higher precipitation rate of expansive phases in pore sizes between 100-500 nm. Due to this precipitation, the proportion of pores between 50-100 nm increases. At 90 days, this trend is maintained, also leading to an increase in the proportion of pores between 10-50 nm. The results suggest that the evolution of pore refinement over time affects the additional deposition of expansive products, reaching smaller pore sizes. Like in the case of the reference PC mortar, a bigger refinement is achieved in samples exposed to C30 in comparison with those exposed to C3. Despite that, the critical diameter is not affected by the different curing conditions evaluated at 28 days and 90 days (see Figure 8b).

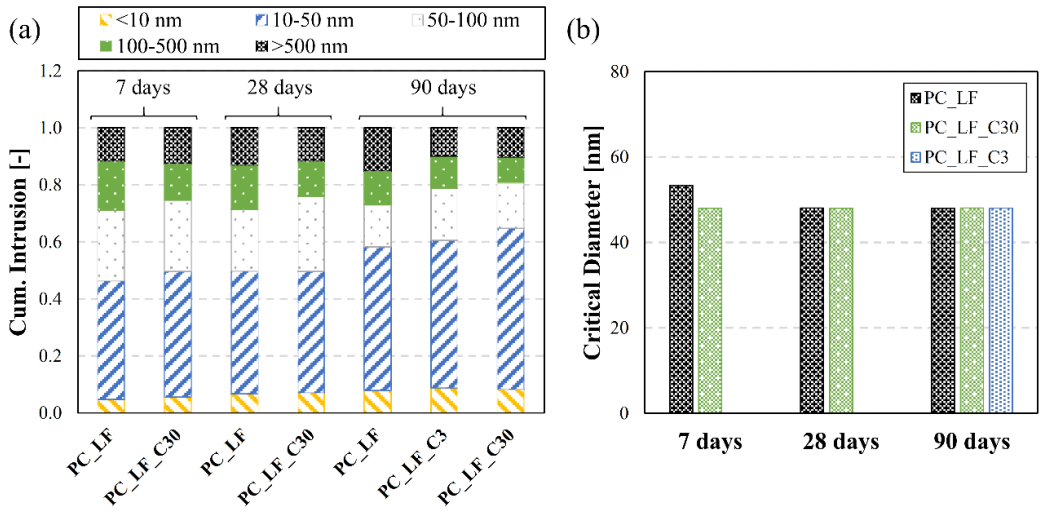

Fig. 8. Evolution of (a) pore size distribution and (b) critical diameter of PC_LF.

Mortar with fly ash (PC_FA)

Figure 9 depicts the cumulative intrusion curves of PC_FA mortars at 7, 28 and 90 days for the different curing conditions considered. Results at 7 days already show a slight refinement of the pore structure for the samples submerged in the high aggressive solution (PC_FA_C30). From 28 days on, this trend is confirmed and the shift towards a more refined pore structure becomes clearer. In the case of the specimens under low aggressive curing conditions (PC_FA_C3), at 90 days the cumulative intrusion curve also deviates towards a thinner pore network.

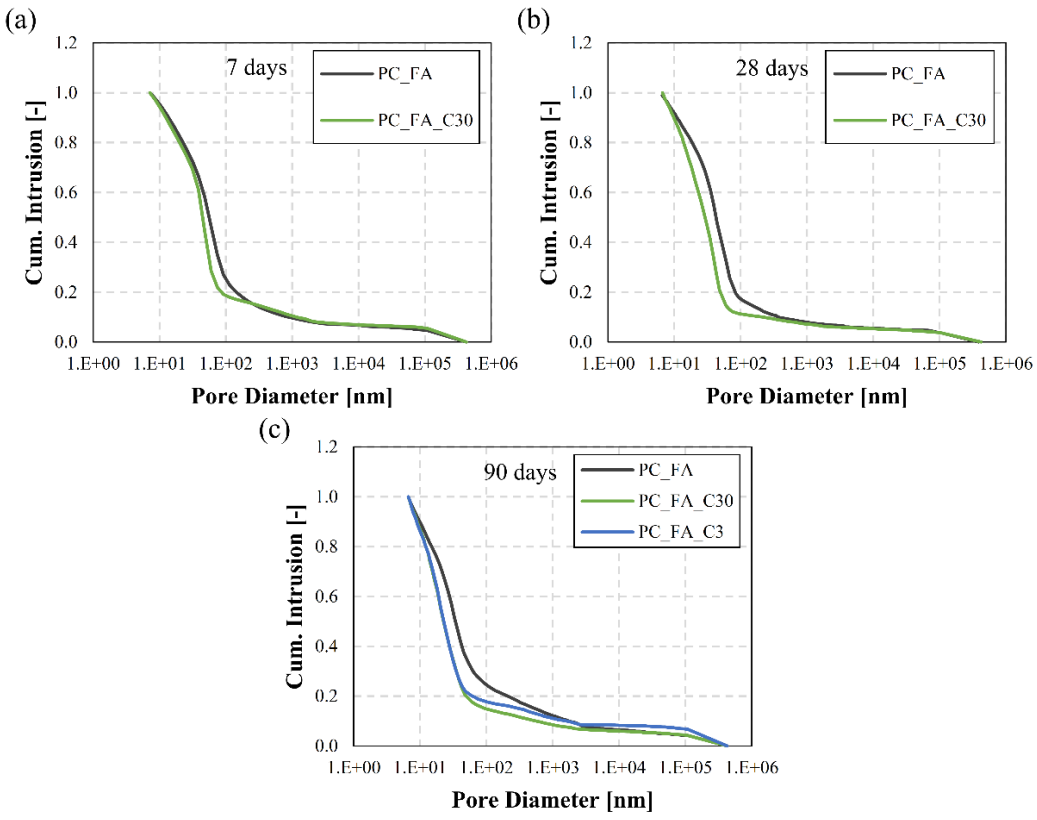

Fig. 9. Cumulative intrusion curves of PC_FA at (a) 7 days, (b) 28 days and (c) 90 days.

Figure 10a shows that specimens with fly ash submerged in high aggressive conditions present alterations in the pore network in low pore ranges as early as at 7 days of exposition. In fact, a significant increase in the relative volume of pores between 10-50 nm is observed. This trend is maintained for samples at 28 days and 90 days.

Interestingly, specimens submerged in low aggressive conditions reach similar pore size distribution to the ones under high aggressive conditions. This behavior of the PC_FA in the precipitation patterns is also reflected on the evolution of the critical diameter. Figure 10b illustrates how sulfate exposure decreases the critical diameter for all ages tested here. Results suggest that the finer pore system observed in samples with fly ash forces the deposition of expansive phases in smaller pores in comparison with equivalent composition without mineral admixtures and with limestone filler.

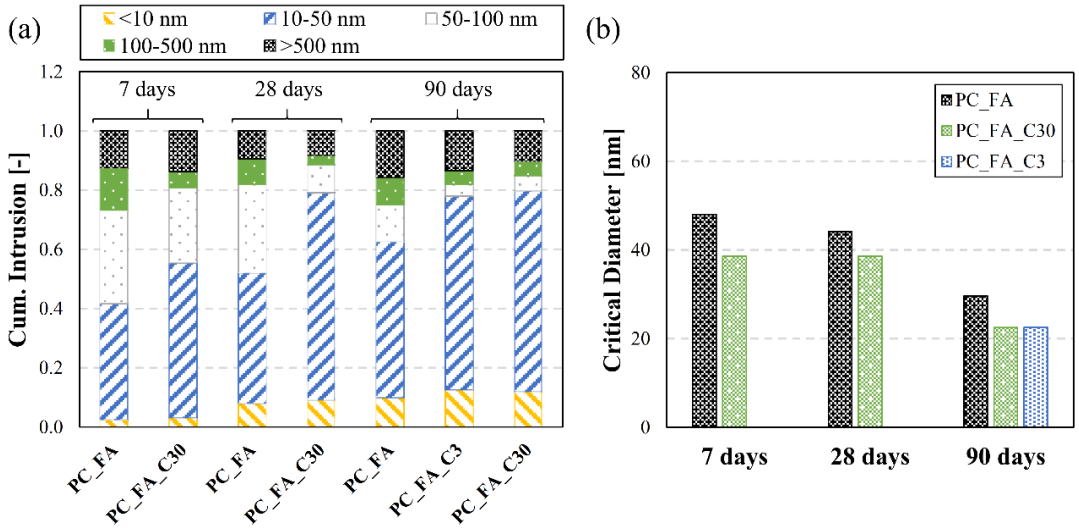

Fig. 10. Evolution of (a) pore size distribution and (b) critical diameter of PC_FA.

Mortar with silica fume (PC_SF)

According to the results presented in the section 3.1, silica fume addition leads to the most refined pore network during the period evaluated among the compositions studied. Figure 11 presents the evolution of cumulative intrusion curves for this series. As can be seen, differences observed between aggressive and non-aggressive curing are minor at all curing ages for both high and low aggressive conditions. This behavior seems to indicate that the amount of expansive phases precipitated during the first 90 days of curing in aggressive environments is less significant when the pore structure of the matrix is highly refined. The differences on the cumulative intrusion curve between 70-300 nm for PC_SF_30 at 28 days cannot be explained by normal hydration or deposition of expansive products. The fact that this behavior is consistent in all replicates might suggest that this deviation is caused by a differential damage generated during sample extraction.

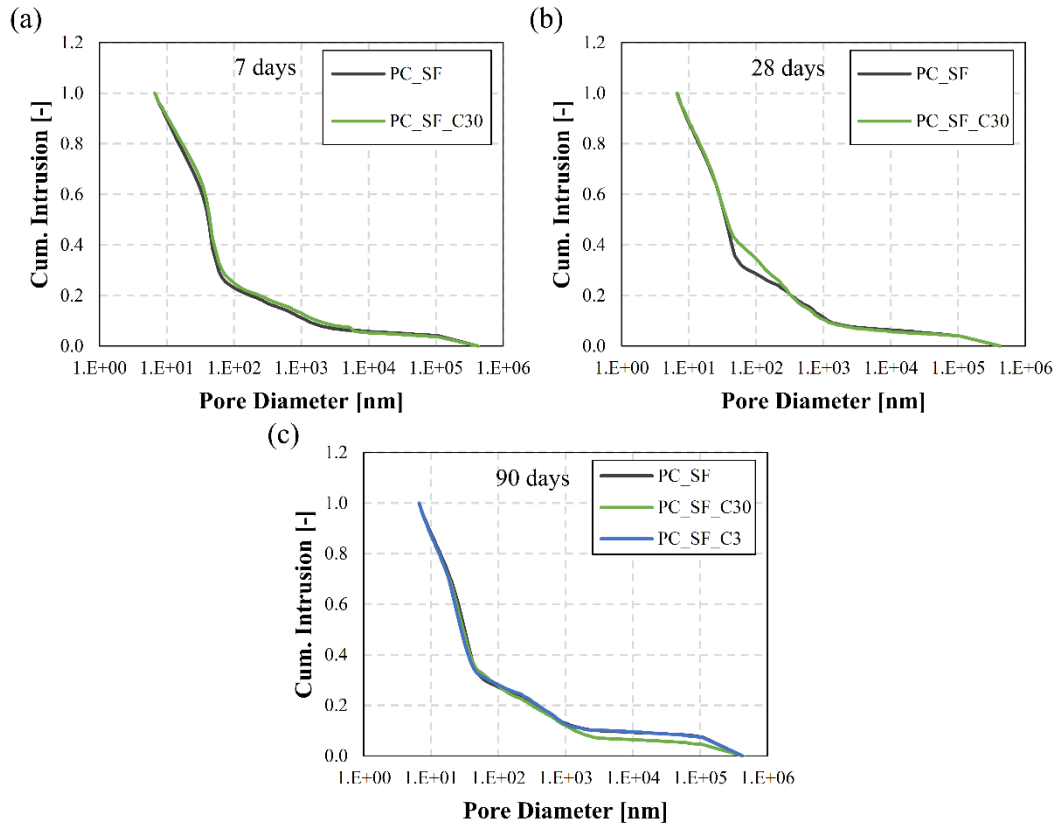

Fig. 11. Cumulative intrusion curves of PC_SF at (a) 7 days, (b) 28 days and (c) 90 days.

Figure 12a shows the evolution of the pore size distribution according to 5 predefined pore ranges. No evident deposition pattern is observed. Despite that, significant variations are identified in the critical diameter shown in Figure 12b. Even though the results presented in Figure 11 and Figure 12a indicate minor pore alterations for the different curing conditions considered, the evolution of the critical diameter captures slight variations (Figure 12b). Figure 12b highlights a reduction in the pore diameter that represents the maximum continuous pore size of the matrix in aggressive curing conditions. These results suggest a slight precipitation of expansive phases occurring in pores smaller than 40 nm.

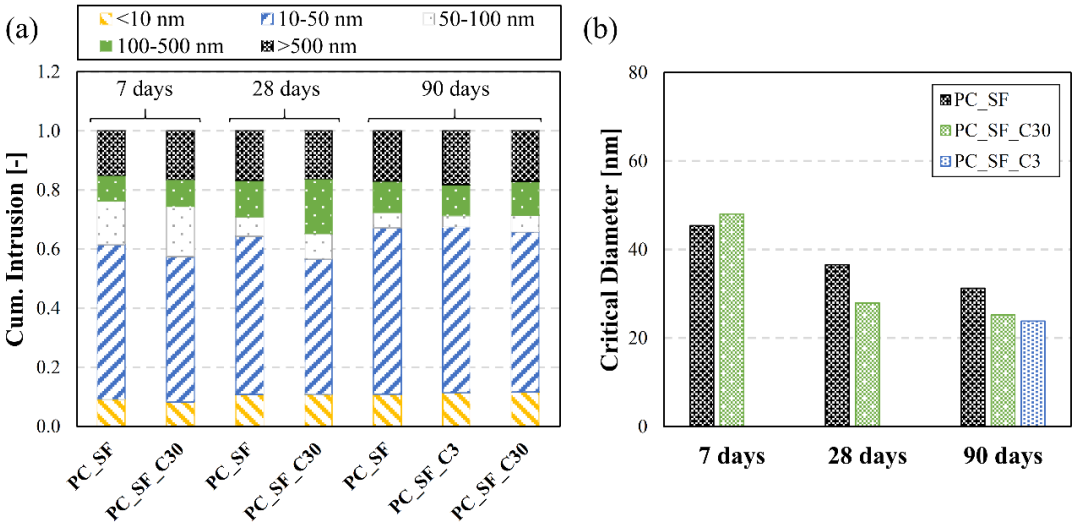

Fig. 12. Evolution of (a) pore size distribution and (b) critical diameter of PC_SF.

Mortar with air-entrainer (PC_A)

According to the analysis of the pore structure conducted in section 3.1, specimens with air-entrainer should have the most favorable conditions for ettringite and gypsum formation, as the high permeability might promote the penetration of sulfates. Figure 13 represents the evolution of cumulative intrusion curves for PC_A mortars. At 7 days, a slight refinement of the pore structure is already observed in samples exposed to C30 in comparison to equivalent ones exposed to non-aggressive environment. Differences between both curing conditions become more significant over time. At 28 days, the intrusion curve of the specimens in the high sulfate environment (C30) shows a shift towards thinner pores. At 90 days, the higher refinement of the pore structure is accentuated. Specimens submerged in low sulfate concentration solution (C3) also show a thinner pore network if compared with the one from samples under non-aggressive curing conditions, although differences are not as pronounced as in comparison with samples exposed to C30 solution.

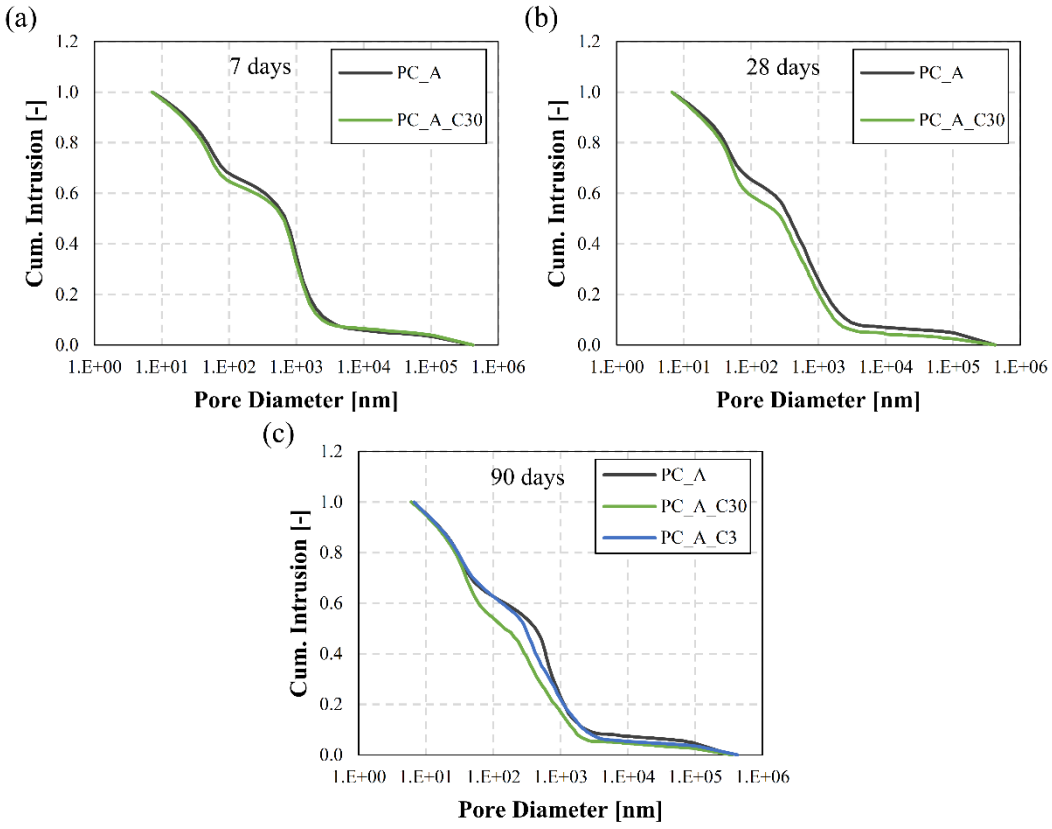

Fig. 13. Cumulative intrusion curves of PC_A at (a) 7 days, (b) 28 days and (c) 90 days.

The evolution of the pore size distribution depicted in Figure 14 suggests that these differences may be attributed to a significant reduction of the proportion of pores above 500 nm, increasing the ratio of pores between 50-100 nm and 100-500 nm. Even though compositions with air-entrainer might seem prone to penetration of sulfates and precipitation of expansive phases, results indicate that this precipitation occurs mainly in large pores, while smaller pore ranges remain unaltered.

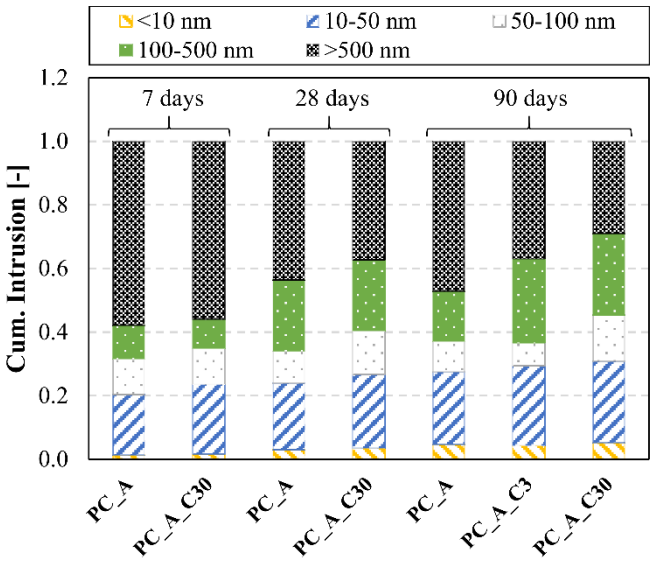

Fig. 14. Evolution of the pore size distribution of PC_A.

Discussion of MIP results

The results show significant differences between the cumulative intrusion curves of mortars cured in aggressive and non-aggressive conditions. The dosage that presents the greatest influence is the PC_A series. For this mortar, the presence of entrained air voids connected to the pore network may enhance the ingress of sulfate ions towards the inner layers of the material and promote ettringite and gypsum formation. On the other hand, the dosage that presents the lowest influence by early aggressive curing is the PC_SF series. In this case it seems that the high pore refinement leads to a matrix with lower permeability, which was barely penetrated by sulfates. Notice that the alterations in the pore network are observed not only in specimens submerged in the high aggressive solution (C30), but also in the solution representative of field conditions (C3) for PC_LF, PC_FA and PC_A.

In compositions PC, PC_FA and PC_A the alterations in the pore network due to early sulfate exposure are observed as early as at 7 days. Consequently, typical curing periods of 28 to 90 days (see Table 1) prior to sulfate exposure adopted in accelerated laboratory testing might not reproduce the behavior of the structures cast *in situ*, which will be affected by sulfate since casting. According to R. El Hachem et al. [12], the expansive product formed during early curing is less likely to cause damage due to the coarser pore network in which it is formed. Therefore, if the age of sulfate exposure in laboratory testing is not consistent with the field conditions, the damage predicted might not be realistic. A more realistic approach in accelerated tests would be to expose sample to sulfate at earlier ages.

Another relevant outcome derived from the analysis of the MIP results is related to how the pore size distribution of the matrix influences the precipitation pattern. Most models from the literature used to evaluate the ESA assume that all pores comprising the pore network are filled proportionally to their size [42,43]. By that, they are inherently assuming that the fraction filled of each pore size is the same at all times. If this assumption was true, the proportion of pores in samples exposed to aggressive and non-aggressive curing conditions should be similar. Conversely, results indicate that different pore ranges have different precipitation rates. In fact, the precipitation pattern depends strongly on the original pore size distribution of the material. As a general trend, it seems that initially larger pore

sizes are more affected by early sulfate exposure. At later ages, finer sizes are affected by the alterations.

Results also indicate that the pore size distribution of the material defines which is the lowest pore range affected. In more refined matrices, the precipitation of expansive phases reached the pore range of 50-100 nm (PC_FA). On the other hand, in coarser pore network of the mortar with air-entrainer (PC_A), the precipitation was mainly found in pores bigger than 500 nm.

The exact reasons for this differential alteration depending on the refinement of the pore system are not completely clear. However, it may be explained by the higher rate of penetration of the sulfates through paths that include coarser pore sizes, which exert smaller restriction to the diffusion and would also accommodate a bigger total sulfate content inside. This higher availability of sulfates would favor the formation of ettringite in the larger pores [44]. At the same time, the precipitation in coarser pores could act as a buffer that hinder the increase of concentration in smaller pores connected to them. Therefore, the concentration in smaller pores would not built up to allow ettringite precipitation. As time passes and the refinement of the system increases, the same phenomenon would extend to smaller pores.

The results also seem to indicate that mortars with air entrained bubbles (PC_A) and with silica fume (PC_SF) might be less affected by early aggressive curing conditions. Notice that each of these two mortars would reach this performance by two different reasons. In the case of PC_SF, the reduced permeability of the matrix would limit the sulfate ingress and, consequently, the extent of the ESA. In the case of PC_A, the large amount of big pores would act as a buffer that hinders the increase of the crystallization pressure in the system. The small levels of pressure generated in smaller pores would be unlikely to generate damage since the majority of the precipitation takes place in larger pores.

3.2.2. XRD results

This section presents the results from XRD tests in order to verify the presence of expansive phases (ettringite and gypsum) that could explain the alterations of the pore network observed in aggressive curing conditions. Figures 15a and 15b depict ettringite, gypsum and portlandite contents in the whole sample (average of external and internal) for high (C30) and low (C3) aggressive curing conditions, respectively. Due to the small size of the samples analyzed, the uniformity of the original dosage (sand/cement paste ratio) might not be guaranteed. For that, phase contents are expressed as a percentage by weight of the crystalline phases of the cement paste (wt. CPCP %). The XRD confirms a significant presence of expansive product that may explain the alterations presented in section 3.2.1.

Results obtained for high aggressive condition are also consistent with the cumulative intrusion curves since mortars with silica fume (PC_SF) show the lowest amount of expansive products whereas specimens with air entrained (PC_A) have the highest content of ettringite and gypsum. These compositions correspond to the matrices with the lowest and highest porosity, respectively. The high porosity of PC_A seems to promote sulfate penetration and the precipitation of expansive phases. On the other hand, the limited sulfate availability caused by the refined matrix of PC_SF limits the precipitation of ettringite and gypsum.

Figure 15b shows the results obtained for low aggressive curing conditions. In general, ettringite and gypsum contents are lower than in the high aggressive solution due to a more limited amount of sulfates that penetrate the sample. As expected, this reduction is

more remarkable in the compositions with high porosity (PC_A and PC_LF). In this case, the relation between porosity and amount of expansive phases formed is less evident than in samples subjected to C30 given the smaller sulfate content available in the solution.

In general, portlandite contents in PC_SF and PC_FA are lower than in PC_LF and PC_A for both curing conditions. These results can be explained by the pozzolanic activity of the silica fume and fly ash, which consumes reactive silica of the pozzolan and calcium hydroxide, producing calcium silicate hydrate [37].

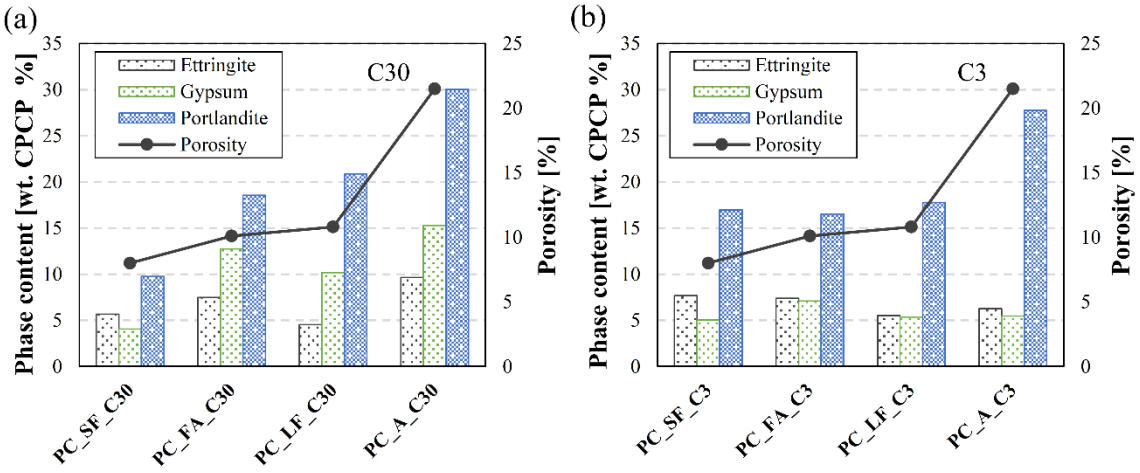

Fig. 15. XRD results of PC_SF, PC_LF, PC_FA and PC_A at 90 days for (a) C30 and (b) C3.

Figure 16 shows separately the ettringite, gypsum and portlandite contents obtained in the external (close to the surface) and the internal (close to the core) fractions of the sample, for high and low aggressive curing conditions. As expected, ettringite contents are higher in the external fraction of the samples for both aggressive curing conditions due to a higher sulfate concentration (Figures 16a and 16c). However, gypsum and portlandite contents exhibit an opposite trend, being higher in the internal fractions.

These results might be partially explained by a calcium leaching phenomenon from the soluble phases towards the aggressive solution. The solubility of [Ca^{2+}] of the phases of interest are listed in Table 5, along with their ion activity and solubility products. This table shows that the solubility of portlandite and gypsum is considerably bigger than the solubility of ettringite, which is thermodynamically more stable. In this context, the calcium leached may be provided by portlandite and, in a lesser extent, gypsum dissolution from the surface of the sample.

Another possible reason is that ettringite formation promoted by the high sulfate concentration in the external layer also consumes calcium ions from the pore solution. The combination of calcium leaching towards the external solution with high ettringite formation rates causes a reduction of calcium ions close to the external surface. To reach equilibrium, the dissolution of more soluble phases (portlandite and gypsum) might increase, thus explaining the differences in content between the surface and the inside of the sample.

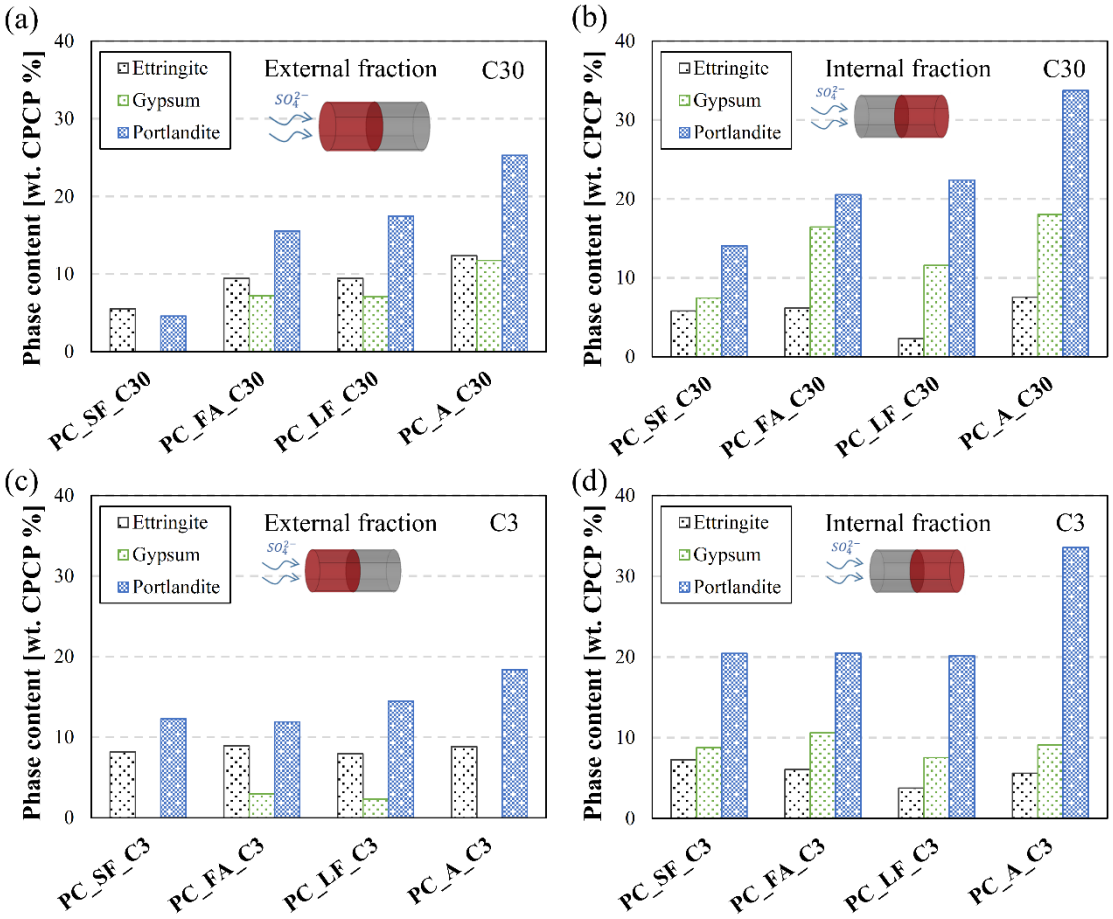

Fig. 16. XRD results of PC_SF, PC_LF, PC_FA and PC_A at 90 days for (a) the external and (b) internal fraction for C30, and (c) external and (d) internal for C3.

Table 5. $[Ca^{2+}]$ solubility of portlandite, gypsum and ettringite.

Phase	Ion activity product	log(k_{sp}) 25ºC	Solubility $[Ca^{2+}]$ [mmol/l]
Portlandite	$[Ca^{2+}][OH^-]^2$	-5.18 [45]	11.82
Gypsum	$[Ca^{2+}][SO_4^{2-}][H_2O]^2$	-4.58 [45]	5.13
Ettringite	$[Ca^{2+}]^6[Al(OH)_4^-]^2[SO_4^{2-}]^3[OH^-]^4[H_2O]^{26}$	-45 [46]	1.50

3.2.3. SEM results

The study of the microstructure and morphology was performed in samples that presented dissimilar trends in terms of initial pore system and alteration patterns after sulfate exposure in order to explain and justify previous results. For that reason, samples from mortars with air-entrainer (PC_A) and fly ash (PC_FA) after 90 days of exposition were selected.

Figure 17 shows SEM images of air voids and pores as well as the magnification of the hydrated products found in high (C30) and low (C3) aggressive curing conditions. Regions analyzed by EDS are indicated by a red circle. The Ca, S and Al ratios calculated from the counting are indicated in the upper right corner of each image. According to the EDS spectra, the needle-like hydrated product found in all cases should correspond to ettringite. However, evident differences are identified regarding the morphology and degree of crystallinity of the ettringite formed between the two mortars and between both aggressive solutions.

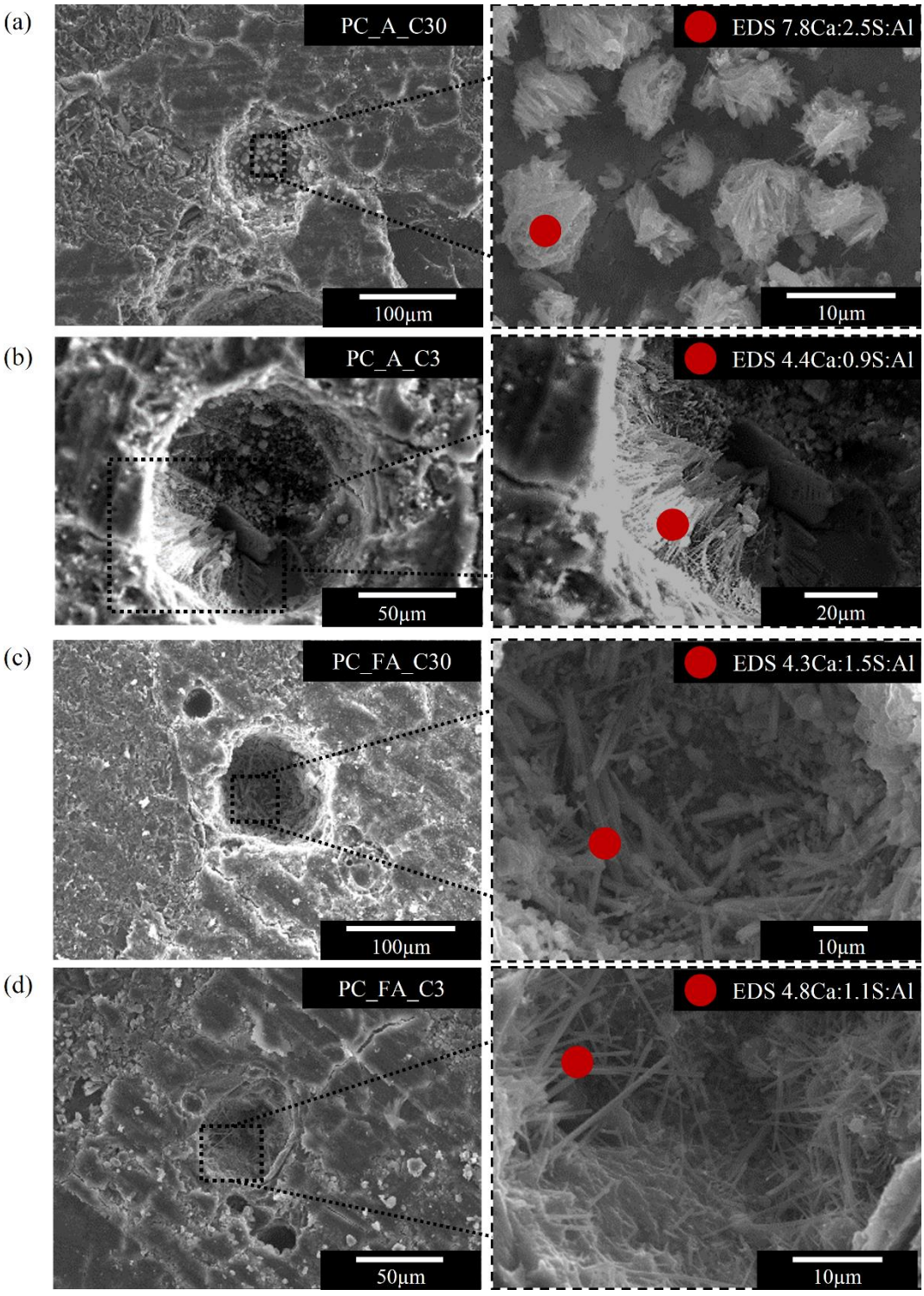

Figure 17. SEM images of air voids and its magnification for (a) PC_A_C30, (b) PC_A_C3, (c) PC_FA_C30 and (d) PC_FA_C3.

In the case of PC_A_C30 (Figure 17a), the air void is partially filled with clusters with less than 10 µm of diameter formed by ball-shaped ettringite crystals with lengths that go from 1 µm to 5 µm. On the other hand, the ettringite formed in PC_FA_C30 (Figure 17c) is more uniformly spread within the surface of the pore, with most crystals length over 15 µm. In the case of PC_A_C3 (Figure 17b), ettringite is observed in the form of well-defined crystals that grow perpendicular to the surface of the pore, indicating a slower formation.

Notice that the length of the crystals reach 20 μm. The same is also depicted in PC_FA_C3 (Figure 17d), where ettringite formed presents high crystallinity, with defined and separated crystals.

These results indicate that the degree of crystallinity of the ettringite formed increases with the refinement of the pore system and decreases with the aggressiveness of the media. Therefore, poorly crystallized ettringite is associated with formation under high supersaturation of the pore solution. The differences observed in the length of the crystals between the high and low aggressive curing conditions can be explained by the fact that the nucleus formation takes place far more rapidly than crystal growth, leading to the formation of a large number of small crystals in high supersaturated environments [47]. Moreover, small crystals formed in low aggressive curing conditions may dissolve because they are not stable with respect to larger crystals in equilibrium with lower concentrations [15].

4. CONCLUSIONS

The following conclusions may be derived from this study.

(1)- Results from cumulative intrusion curves indicate significant differences in the pore network between mortars cured in aggressive and non-aggressive conditions. The alterations are observed in both high and low aggressive solutions for most compositions. XRD tests indicate that these alterations may be attributed to the precipitation of ettringite and gypsum.

(2)- The modifications in the pore network are observed as early as at 7 days after early exposition to sulfates. Therefore, typical curing periods of 28 days or 90 days commonly adopted in accelerated laboratory tests prior to sulfate exposure might lead to imprecise damage estimations for structures cast *in situ*. In these cases, a more realistic approach would be to expose samples to sulfate at earlier ages.

(3)- MIP results indicate that the expansive products do not precipitate equally in all pores, as assumed in some models regarding the ESA. Initially, larger pores concentrate a higher proportion of the expansive product. As pore refinement increases with time, the precipitation evolves towards finer pore sizes.

(4)- Results also suggest that the degree of refinement of the pore network defines which is the lowest pore range affected by precipitation. In refined pore structures precipitation reaches smaller pore ranges than in coarser networks, where the precipitation is mainly produced in large pores.

(5)- SEM images of ettringite formed in air voids indicate that the morphology and degree of crystallinity varies depending on the availability of connected air voids and the external sulfate concentration. Crystallinity of ettringite increases with the degree of refinement of the pore system and decreases with the aggressiveness of the media.

ACKNOWLEDGMENTS

Support from the Spanish Ministry of Economy and Competitiveness through research project BIA2013-49106-C2-1-R is greatly acknowledged. T. Ikumi is supported by the fellowship program FPI BES-2014-068524 of the Spanish Ministry of Economy and Competitiveness.

REFERENCES

[1] J.P. Skalny, I. Odler, J. Marchand, Sulfate Attack on Concrete, Spon, London, 2001.

[2] A. Neville, The confused world of sulfate attack on concrete, Cem. Concr. Res. 34 (2004) 1275-1296.

[3] T. Ikumi, S.H.P. Cavalaro, I. Segura, A. Aguado, Alternative methodology to consider damage and expansions in external sulfate attack modeling, Cem. Concr. Res. 63 (2014) 105-116.

[4] T. Ikumi, S.H.P. Cavalaro, I. Segura, A. de la Fuente, A. Aguado, Simplified methodology to evaluate the external sulfate attack in concrete structures, Mater. Des. 89 (2016) 1147-1160.

[5] K. Tosun, B. Baradan, Effect of ettringite morphology on DEF-related expansion, Cem. Concr. Compos. 32 (2010) 271-280.

[6] G.W. Scherer, Stress from crystallization of salt, Cem. Concr. Res. 34 (2004) 1613-1624.

[7] R.J. Flatt, G.W. Scherer, Thermodynamics of crystallization stresses in DEF, Cem. Concr. Res. 38 (2008) 325-336.

[8] M.T. Bassuoni, M.L. Nehdi, Durability of self-consolidating concrete to different exposure regimes of sodium sulfate attack, Mater. Struct. (2009) 42 1039-1057.

[9] T. Schmidt, B. Lothenbach, M. Romer, J. Neuenschwander, K. Scrivener, Physical and microstructural aspects of sulfate attack on ordinary and limestone blended Portland cements, Cem. Concr. Res. 39 (2009) 1111-1121.

[10] B. Lothenbach, B. Bary, P.L. Bescop, T. Schmidt, N. Leterrier, Sulfate ingress in Portland cement, Cem. Concr. Res. 40 (2010) 1211-1225.

[11] T. Aye, C.T. Oguchi, Resistance of plain and blended cement mortars exposed to severe sulfate attacks, Constr. Build. Mater. 25 (2011) 2988-2996.

[12] R. El-Hachem, E. Rozière, F. Grondin, A. Loukili, Multi-criteria analysis of the mechanism of degradation of Portland cement based mortars exposed to external sulphate attack, Cem. Concr. Res. 42 (2012) 1327-1335.

[13] W. Kunther, Investigation of sulfate attack by experimental and thermodynamic means, PhD Thesis, ÉPFL, Lausanne, 2012.

[14] J. Gao, Z. Yu, L. Song, T. Wang, S. Wei, Durability of concrete exposed to sulfate attack under flexural loading and drying–wetting cycles, Constr. Build. Mater. 39 (2013) 33-38.

[15] W. Müllauer, R.E. Beddoe, D. Heinz, Sulfate attack expansion mechanisms, Cem. Concr. Res. 52 (2013) 208-215.

[16] M. Zhang, J. Chen, Y. Lv, D. Wang, J. Ye, Study on the expansion of concrete under attack of sulfate and sulfate–chloride ions, Constr. Build. Mater. 39 (2013) 26-32.

[17] I. Sirisawat, W. Saengsoy, L. Baingam, P. Krammart, S. Tangtermsirikul, Durability and testing of mortar with interground fly ash and limestone cements in sulfate solutions, Constr. Build. Mater. 64 (2014) 39-46.

[18] J. Stroh, B. Meng, F. Emmerling, Monitoring of sulphate attack on hardened cement paste studied by synchrotron XRD, Solid State Sci. 48 (2015) 278-285.

[19] C. Yu, W. Sun, K. Scrivener, Degradation mechanism of slag blended mortars immersed in sodium sulfate solution, Cem. Concr. Res. 72 (2015) 37-47.

[20] S. Diamond, Mercury porosimetry - An inappropriate method por measurement of pore size distributions in cement-based materials, Cem. Concr. Res. 30 (2000) 1517-1525.

[21] S. Wild, A discussion of the paper "Mercury porosimetry - An inappropriate method por measurement of pore size distributions in cement-based materials" by S. Diamond, Cem. Concr. Res. 31 (2001) 1653-1654.

[22] R. El-Hachem, E. Rozière, F. Grondin, A. Loukili, New procedure to investigate external sulphate attack on cementitious materials, Cem. Concr. Compos. 34 (2012) 357-364.

[23] A. Chabrelie, Mechanisms of degradation of concrete by external sulfate ions under laboratory and field conditions, PhD Thesis, ÉPFL, Lausanne, 2010.

[24] R. Kumar, B. Bhattacharjee, Study on some factors affecting the results in the use of MIP method in concrete research, Cem. Concr. Res. 33 (2003) 417-424.

[25] I. Segura, M. Molero, S. Aparicio, J.J. Anaya, A. Moragues, Decalcification of cement mortars: Characterisation and modeling, Cem. Concr. Comp. 35 (2013) 136-150.

[26] A.G. de la Torre, S. Bruque, J. Campo, M.A.G. Aranda, The superstructure of C_3S from synchrotron and neutron powder diffraction and its role in quantitative analysis, Cem. Conc. Res. 32 (2002) 1347-1356.

[27] W.G. Mumme, R.J. Hill, G.W. Bushnell, E.R. Segnite, Rietveld crystal structure refinements, crystal chemistry and calculated powder diffraction data for the polymorphs of dicalcium silicate and related phases, N. Jb. Miner. Abh. (J. Min. Geochem.) 169 (1995) 35-68.

[28] H.E. Petch, The hydrogen positions in portlandite, $Ca(OH)_2$, as indicated by the electron distribution, Acta Crystallogr. 14 (1961) 950-957.

[29] R. Wartchow, Datensammlung nach der ''learnt profile"-methode(LP) für calcit und vergleich mit der ''background peak background"-methode (BPB), Z. Kristallogr. 186 (1989) 300-302.

[30] F. Goetz-Neunhoeffer, J. Neubauer, Refined ettringite structure for quantitative X-ray diffraction analysis, Powder Diffr. 21 (2006) 4-11.

[31] W.A. Wooster, On the crystal structure of gypsum $CaSO_4(H_2O)_2$, Z. Kristallogr. 94 (1936) 375-396.

[32] A.A. Colville, S. Geller, The crystal structure of brownmillerite, Ca_2FeAlO_5, Acta Crystallogr. B 27 (1971) 2311-2315.

[33] L. Levien, C.T. Prewitt, D.J. Weidner, Structure and elastic properties of quarz at pressure, Am. Mineral. 65 (1980) 920-930.

[34] M. François, G. Renaudin, O. Evrard, A cementitious compound with composition $3CaO{\cdot}Al_2O_3\ CaCO_3{\cdot}11H_2O$, Acta Crystallogr. C 54 (1998) 1214-1217.

[35] T. Ban, K. Okada, Structure refinement of mullite by the Rietveld method and a new method for estimation of chemical composition, J. Am. Ceram. Soc. 75 (1992) 227-230.

[36] E.N. Maslen, V.A. Streltsov, N.R. Streltsova, N. Ishizawa, Y. Satow, Synchrotron X-ray study of the electron density in alpha-Al_2O_3, Acta Crystallogr. B 49 (1993) 973-980.

[37] A.A. Ramezanianpour, Cement Replacement Materials: Properties, Durability, Sustainability, Springer, Berlin, Germany, 2014.

[38] I. Segura, Caracterización del proceso de descalcificación en morteros, mediante ensayos destructivos y no destructivos, PhD Thesis, ETSICCP, Madrid, 2008.

[39] K.K. Aligizaki, Pore Structure of Cement-based Materials—Testing, Interpretation and Requirement, Taylor & Francis, New York (2006).

[40] S. Kumar and C.V.S. K. Rao, Effect of sulfates on the setting time of cement and strength of concrete, Cem. Concr. Res. 24-7 (1994) 1237-1244.

[41] B. Mota, T. Matschei, K. Scrivener, The influence of sodium salts and gypsum on alite hydration, Cem. Concr. Res. 75 (2015) 53-65.

[42] R. Tixier, B. Mobasher, Modeling of damage in cement-based materials subjected to external sulfate attack. I: formulation, J. Mater. Civ. Eng. 15 (2003) 305–313.

[43] S. Sarkar, S. Mahadevan, J.C.L. Meeussen, H. van der Sloot, D.S. Kosson, Numerical simulation of cementitious materials degradation under external sulfate attack, Cem. Concr. Compos. 32 (2010) 241–252.

[44] S. Emmanuel, L.M. Anovitz, R.J. Day-Stirrat, Effects of coupled chemo-mechanical processes on the evolution of pore-seize distribution in geological media, Rev. Mineral. Geochem. 80 (2015) 45-60.

[45] D.L. Parkhurst, User's Guide to PHREEQC—A Computer Program for Speciation, Reaction-Path, Advective-Transport, and Inverse Geochemical Calculations, Water-Resources Investigations Report 95-4227, United States Geological Survey, Lakewood, Colorado, 1995.

[46] R.B. Perkins, C.D. Palmer, Solubility of ettringite ($Ca_6[Al(OH)_6]_2$ $(SO_4)_3$ 26 H_2O) at 5 – 75 ºC, Geochim. Cosmochim. Acta 63 (1999) 1969-1980.

[47] RILEM PRO 35, Proceedings of the International RILEM TC 186-ISA on Internal Sulfate Attack and Delayed Ettringite Formation (Eds. K. Scrivener and J. Skalny), RILEM publications, Bagneux, France, 2002.

3.4. CONFERENCE PAPER I. SIMPLIFIED MODEL TO ASSESS THE DURABILITY OF ELEMENTS SUBJECTED TO EXTERNAL SULFATE ATTACK: INFLUENCE OF SHAPE AND SIZE OF THE ELEMENTS

Published in: Proceedings of the workshop External sulfate attack. RILEM - LNEC, Baroghel-Bouny V., Martins I., Menéndez E. (eds), (2017) 131-142.

Tai Ikumi[a,*], Sergio Cavalaro[a,*], Ignacio Segura[b], Albert de la Fuente[a], Antonio Aguado[a]

[a]Department of Civil and Environmental Engineering, Universitat Politècnica de Catalunya, Barcelona Tech, Jordi Girona 1-3, C1, E-08034 Barcelona, Spain, email: tai.ikumi@upc.edu, sergio.pialarissi@upc.edu
[b]Smart Engineering Ltd., C/Jordi Girona 1-3, Parc UPC – K2M, 08034, Barcelona, Spain.

Abstract

The mitigation of the external sulfate attack from the standpoint of the design of concrete structures is usually based on the use of cement with limited content of aluminates. Nevertheless, other parameters may affect the final durability, such as the cement content, the geometry and size of the structure. The consideration of these factors is highly complex. Few straightforward methods are available to verify the durability of structures subjected to sulfate ingress. The objective of this paper is to present a simplified model for the verification of the durability, considering variables related with the composition, the exposure and the geometry of the structure. First, a model to simulate the chemical-physical- mechanical phenomenon is proposed and validated. Then, this model is simplified to make it easy to apply. Finally, a parametric study is performed to evaluate the influence of the shape and size of the element on the durability

1. INTRODUCTION

External sulfate attack (ESA) is one of the most complex degradation process affecting underground concrete structures. This phenomenon is defined by multiple variables related to the penetration process of sulfate ions (sulfate content and pore network characteristics), material reactivity (concrete composition) and mechanical and geometrical properties of the element under attack. Moreover, since ESA normally only affects a fraction of the whole section of the specimen, the processes acting at the micro-scale have to be reflected at the macro-scale by complex mechanical calculations.

Despite the complexity of this phenomenon, most design codes only consider a limitation of the aluminate content by the use of sulfate resistant cements where the sulfate concentration in the groundwater surpass a predefined limit. The limitation of aluminate content in aggressive environments is equal regardless of the cement content in the concrete and the size or structure typology of the element under attack. Indeed, according to current structural codes it seems that the only way to obtain durable materials against the ESA is by the use of a sulfate resistant cement. However, since this phenomenon is defined by multiple parameters, there should be multiple ways to obtain durable materials.

One of the key aspects that might define the final durability of structures exposed to sulfates is the geometrical characteristics of the specimen. Precisely, the ratio between the affected and sound region of the section. It seems common sense that a large pile of 2 m of diameter should resist better the deleterious effects related to ESA than a micro-pile of 30 cm of diameter. Unfortunately, the current approach adopted in the structural codes do not allow any differentiation between these two cases. Despite building codes must contain simplified approaches, the application of the current guidelines might lead to very penalizing measures in some situations.

This paper presents a simplified methodology that allows a direct assessment of the ESA by considering parameters related to the aggressiveness of the media, the reactivity of the material and the geometrical characteristics of the element under attack. Moreover, a case study is presented to highlight the contribution of the shape and size of the specimen on the durability against the ESA.

2. SIMPLIFIED METHODOLOGY

The methodology proposed is based on the application of a set of simplified equations to assess the extent of the reactive-transport process and the possible mechanical structural failure at a given service life (25 or 50 years). Figure 1 represents a schematic diagram of the methodology.

As can be seen, the assessment proposed takes into account the aggressiveness of the external media, the reactivity of the material and the geometric characteristics of the element under attack. After the definition of the input parameters, the second phase consists on the estimation of the strain profile at a given service life (penetration of the sulfate ions and magnitude of expansions). Since this methodology consider the geometrical characteristics of the element under attack, it allows the verification of three of the most typical failure modes associated to the ESA. If no mechanical failure occurs and the serviceability is not compromised, it is considered that the structure will comply with the required service life. In this section, the fundamentals and final equations of the simplified methodology are

presented. An in-depth description of the derivation process of the simplified equations is available in [1].

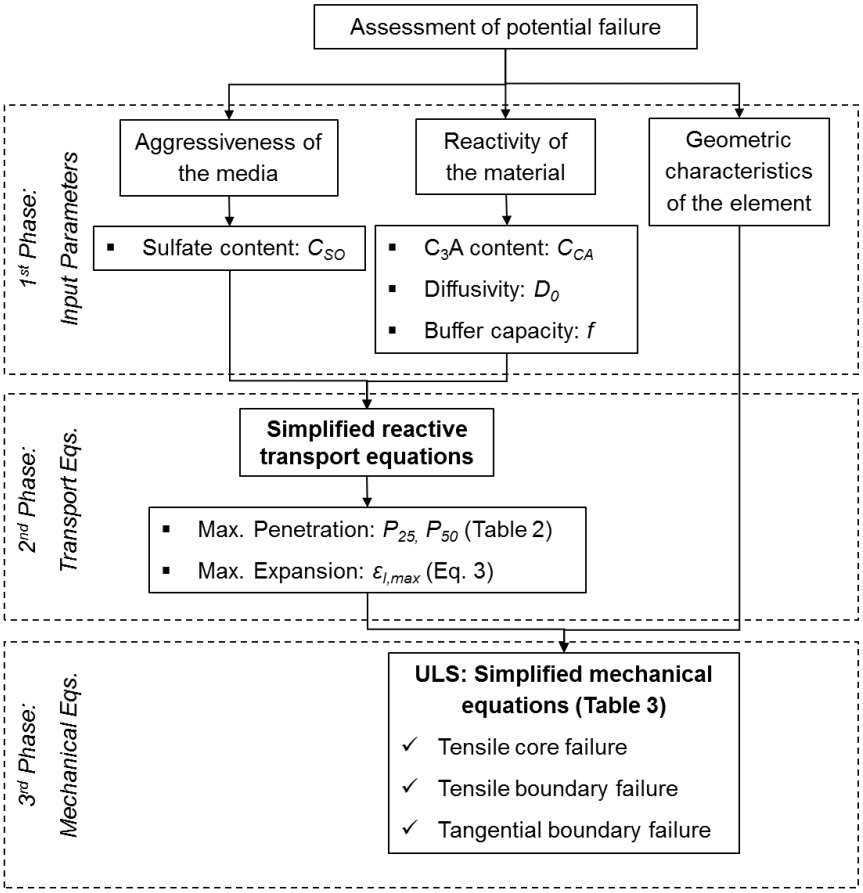

Fig. 1. Outline of the simplified methodology for the durability assessment of the ESA [1].

2.1 SIMPLIFIED TRANSPORT EQUATIONS

The simplified equations to quantify the maximum penetration of the sulfate front at 25 and 50 years were deduced from a series of simulations performed in the model presented by T. Ikumi et al. [2] with multiple combinations of the most influencing parameters. Table 1 describes the ranges of the parameters considered. More than 2000 simulations were completed at 25 and 50 years. Once a sufficiently big database of penetration depths was obtained, a nonlinear numerical regression was applied to derive the simplified equations that yield the best fit with the numerical results. Prior description of the transport equations obtained, the general hypothesis adopted during the simulations performed in the comprehensive numerical model [2] are explained below.

Table 1. Ranges of parameters.

Parameter	Description	Minimum	Maximum
C_{SO}	Sulfate Concentration in the media [mol/m^3 water] ([g/l])	6.25 (0.6)	62.5 (6.0)
D_0	Initial diffusivity of sulfates [m^2/s]	10-12	10-11
f	Buffer coefficient	0.0	0.4
C_{CA}	Aluminate content in the concrete [mol/m^3 concrete] ([%C_3A])	41 (4)	124 (12)
φ_o	Initial porosity	0.08	0.14
f_{cm}	Compressive strength [MPa]	20	40

2.1.1. Chemical reactions

Sulfate ions (SO_4^{2-}) penetrate the structure and react with calcium hydroxide (CH) to form gypsum ($C\bar{S}H_2$) according with Eq. 1.

$$CH + SO_4^{2-} \rightarrow C\bar{S}H_2 + 2OH^- \quad (1)$$

Gypsum is considered as an intermediate phase that may later react with the aluminate phases to form secondary ettringite ($C_6A\bar{S}_3H_{32}$). Even though several aluminate phases may react with gypsum, to simplify the model it is assumed that all aluminates are in the form of monosulfate ($C_4A\bar{S}H_{12}$) since this should be the predominant phase in the hydrated cement paste at long ages. It is also assumed that the expansions are only caused by the formation of secondary ettringite. The expansive nature of gypsum is not taken into account, as there is still controversy regarding its contribution. By this way, only one single chemical reaction defines the kinetics of the expansive process (Eq. 2).

$$C_4A\bar{S}H_{12} + 2C\bar{S}H_2 + 16H \rightarrow C_6A\bar{S}_3H_{32} \quad (2)$$

2.1.2. Transport process

To simplify the mathematical representation of the transport process, only the penetration of sulfate ions by a concentration gradient and its depletion due to ettringite formation is considered in the model. It is assumed that the system is saturated and all pores are accessible.

The effective diffusivity of the sulfate ions takes into account the pore filling effect and local damage caused by ettringite precipitation. The hyperbolic function proposed by Idiart et al. [3] was adopted to simulate the pore filling process. The value of the diffusivity when the porosity is totally filled by expansive product is set at a tenth of the initial diffusivity and the shape factor β_D is set to 1.5 in accordance with the recommendation from Idiart [3]. On the other hand, the increase of diffusivity due to the local damage generated by ettringite formation is considered through the approach presented by Ikumi et al. [2]. The latter considers that the increase of diffusivity is related with the expansions that may be estimated from a stress-strain curve. Such curve is defined by the uniaxial tensile strength of the material and the strain at which the crack becomes stress-free.

For the simulations performed, the upper bound of the diffusivity reached when the material is completely damaged is set to 10^{-10} m^2/s. This value is slightly below the diffusivity of sulfates in free solution, which Gerard and Marchand [4] quantified as 10^{-9} m^2/s for ions able to move freely within cracks. The value of c_1 and c_2 described in [2] were defined respectively as 3 and 6.93, in accordance with the recommendation from [5]. The characteristic cracking length (l_{ch}) is fixed at 26 mm, following the validation by [2].

2.1.3. Expansion mechanism at the micro-scale

It is assumed that the expansion mechanism associated to the ESA is based on the additional volume generated by the ettringite formation. The increase of volume ($\Delta V/V$) is calculated by the stoichiometric constant of the reaction. This calculation gives a 55% volume increase when monosulfate is converted into ettringite. According to this hypothesis, the linear strain (ε_l) is obtained by multiplying the expansion factor by the amount of monosulfate reacted ($C_{C_4A\bar{S}H_{12}}^{react}$), as described in Eq. 3. The term M/ρ corresponds to the molar volume of

monosulfate and $C_{C_4A\bar{S}H_{12}}^{react}$ (expressed as a molar concentration). Notice that maximum expansive strain ($\varepsilon_{l,max}$) may be calculated with Eq. 3 by assuming that all monosulfate reacts to form ettringite.

$$\varepsilon_l = \left(1 + \frac{\Delta V}{V}\frac{M}{\rho} C_{C_4A\bar{S}H_{12}}^{react} - f\varphi_0\right)^{1/3} - 1 \quad (3)$$

Since ettringite precipitates within the pore network, the matrix is able to accommodate a certain amount of expansive product without exerting any pressure to the pore walls. The expression presented by Tixier & Mobasher [6] is used to estimate the buffered expansion. This is represented in the second term of Eq. 3, in which φ_0 is the initial porosity of the matrix and f is the fraction of this porosity that may be filled by expansive products before expansions occur. According with Tixier & Mobasher [6], f usually ranges between 0.05 and 0.40.

2.1.4. Simplified reactive - transport equations

Final formulations obtained to estimate the penetration depth at 25 and 50 years (P_{25} and P_{50}) are presented in Table 2. Both equations are applicable as long as the input parameters remain within the ranges defined in Table 1.

Table 2. Simplified reactive-transport equations.

Service Life [years]	Simplified reactive transport formulation [cm]	K_{95} [cm]
25	$P_{25} = (7e10D_0 + 0.035C_{SO}) \exp\left(\frac{6.65e11D_0+10.737}{C_{CA}} - \frac{1e-10}{35D_o}f\right)$ (4)	0.65
50	$P_{50} = 1.26P_{25}$ (5)	0.86

The initial diffusivity (D_0) is introduced in m^2/s, whereas the aluminate content (C_{CA}) is expressed in mol per cubic meter of concrete. The sulfate content (C_{SO}) is expressed in mol of sulfate per cubic meter of water. As these equations are deduced from the model described by Ikumi et al. [2], sulfate consumption, acceleration of the penetration due to cracking and decrease of diffusivity due to pore filling are indirectly considered.

The simplified transport equations provide a fair approximation of the model [2] with correlation coefficients of 0.91 and 0.90 for 25 and 50 years, respectively. For estimations on the safe side, a statistical analysis was performed in order to assess the error of prediction. A Gumbel distribution of the error estimation was used to assess the minimum penetration depth that had to be summed to the obtained penetration to assure a 95% of probability of achieving values above the calculated with the integrated model by [2]. This additional value (K_{95}) is shown in Table 2 and should be directly added to Eq. 4 and Eq. 5 in case a safer estimation is required.

2.2. STRAIN PROFILE

Typical strain distributions have complex profiles, as they are defined by the aluminates reacted at each depth. Figure 2 shows in continuous lines a typical strain profile caused by ESA.

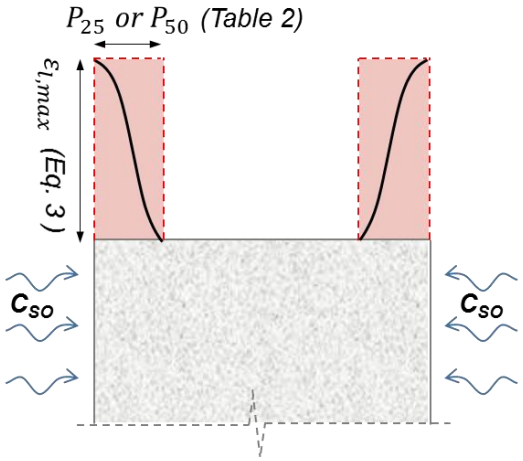

Fig. 2. Strain profile for symmetric sulfate exposure

To simplify the structural consideration, the strain profile depicted with the red discontinuous line is used instead. It assumes that the whole penetrated region estimated by Eq. 4 and Eq. 5 is affected by the same expansions. The magnitude of this expansions is calculated by Eq. 3 assuming that all monosulfate has reacted to form ettringite, which is a hypothesis on the safe side.

2.3. SIMPLIFIED MECHANICAL EQUATIONS

Although expansion due to ettringite formation is concentrated in the superficial layers, strains also appear in the sound core of the element to ensure compatibility. In fact, the sound core acts as a restriction that reduces the expansion calculated with Eq. 3. An auto-balanced tension state is generated, leading to possible mechanical failures outside the zone directly affected by the sulfate penetration. Three failures modes are distinguished; tensile failure of the sound core (Figure 2a), tangential failure (Figure 2b) and tensile failure in the boundary between the surficial layers and the sound core (Figure 2c). The compressive stresses generated in the external layers are not considered as a failure mode. However, these are considered indirectly in the simplified transport equations by a degradation of the elastic modulus in the affected region.

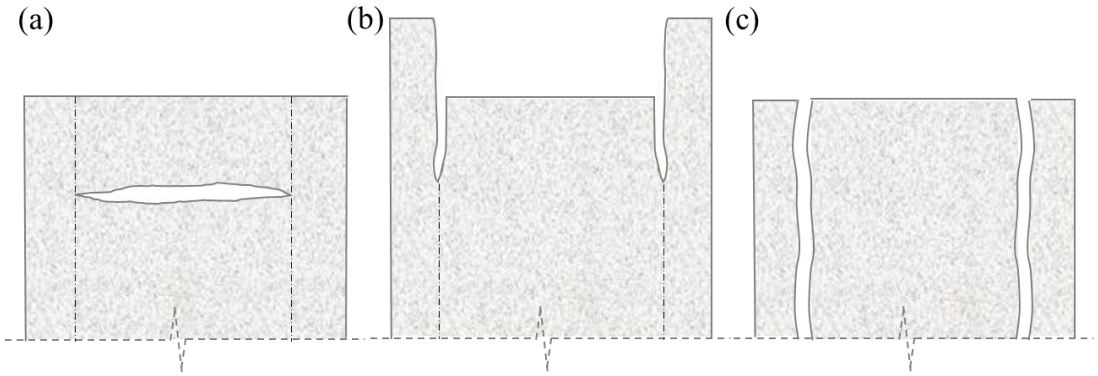

Fig. 2. (a) Tensile core (b) Tangential boundary and (c) Tensile boundary failure mode.

Table 3 includes the final expressions for the assessment of the three failure modes in linear and surface elements under different exposure conditions. This section presents a brief description of the derivation process, a detailed explanation can be found in [1].

2.3.1. Tensile failure of the sound core

Expansions generated by ettringite formation in the external layers are constrained by the sound region of the element. As a result of the interaction, normal compressive stresses (σ_c) rise at the surficial layers, while normal tensile stresses (σ_{tc}) appear at the sound inner core. If σ_{tc} reaches the tensile strength of concrete, the inner core might crack. This might produce a release of the restricted strains and an abrupt displacement of the structure. Figures 3a and 3b depict the stress distribution for symmetric and 1 face sulfate exposure conditions. By assuming equilibrium and compatibility of strains, Eqs. 6-8 are obtained to predict the maximum tensile stresses acting at a certain time in the cross-section (see Table 3).

In the case of piles, R represents the total radius of the cross-section and R_i is the radius of the sound core given by the difference between R and the penetration depth *P* calculated with Eq. 4 or 5. In the case of diaphragm walls or tunnels, b represent the half thickness of the element.

Table 3. Simplified equations to predict the maximum stresses due to ESA

Struct. typology	Sulfate exp.	Tensile failure of the sound core	Tangential boundary failure	Tensile boundary failure
Piles (linear elements)	Full	$\sigma_{tc} = \frac{E_0 E_e \varepsilon_l (R^2 - R_i^2)}{E_e (R^2 - R_i^2) + E_0 {R_i}^2}$ (6)	$\tau_b = \frac{E_0 E_e \varepsilon_l (R^2 - R_i^2) R_i \beta_r}{2(E_e (R^2 - R_i^2) + E_0 {R_i}^2)} tanh\left(\frac{\beta_r l}{2}\right)$ (9) $\beta_r = \sqrt{\frac{2G}{E_0 R_i^2 ln\left(\frac{R}{R_i}\right)}}$ (10)	$\sigma_{tb} = \frac{\varepsilon_l E_e P}{R_i}$ (13)
Diaphragm walls or tunnels (surface elements)	2 faces	$\sigma_{tc} = \frac{E_0 E_e \varepsilon_l P}{E_e P + E_0 (\mathrm{b-P})}$ (7)	$\tau_b = \frac{E_0 E_e \varepsilon_l P b_i \beta}{E_e P + E_0 (\mathrm{b-P})} tanh\left(\frac{\beta l}{2}\right)$ (11) $\beta = \sqrt{\frac{G}{E_0 (b-P) P}}$ (12)	--
	1 face	$\sigma_{tc} = \frac{E_0 \varepsilon_l P (3P^2 - 9Pb + 8b^2)}{4b^3}$ (8)		

2.3.2. Tangential boundary failure

Elements attacked by ESA commonly present a layered spalling of the external surface [7]. Such failure mode might be explained by the tangential stresses that appear at the top and bottom edge of the specimen due to the difference in terms of vertical displacement between the attacked and sound region of the section. These stresses should guarantee the compatibility of displacements at the extremities of the element as the normal stresses do not act at these locations. If the tangential stresses reach the tangential strength of the material, cracks might appear leading to delamination of the structure. Figures 3c and 3d depict the tangential stress distribution for symmetric and 1 face sulfate exposure. Final equations of maximum tangential stresses (τ_b) for symmetric exposure conditions derived from the classical Mixing Theory for short fibers [8-9] are listed in Table 3.

The same formulation is also adopted when elements are exposed to the sulfate ingress only in one face. The curvature introduced by the asymmetric load increases the macroscopic strain in the external damaged layer and reduces the compressive stresses in this region. Therefore, the tangential stresses transmitted to the sound core are reduced, leading

to an assessment on the safe side. It is important to remark that the length of the element (l) only affects the assessment of the tangential stresses if it is below a critical value (around 1 m for most structures). For bigger values of l, the maximum tangential stress at the extremities of the element will remain approximately constant.

2.3.3. Tensile boundary failure

In linear structures fully exposed to sulfates, the spalling of the external layers might be also caused by a tensile stress failure at the boundary between the sound and damage regions. As shown in Figure 3e, tensile stresses (σ_{tb}) are induced by the restrictions of the sound core to the expansions experienced by the affected layers in the cross-sectional plane.

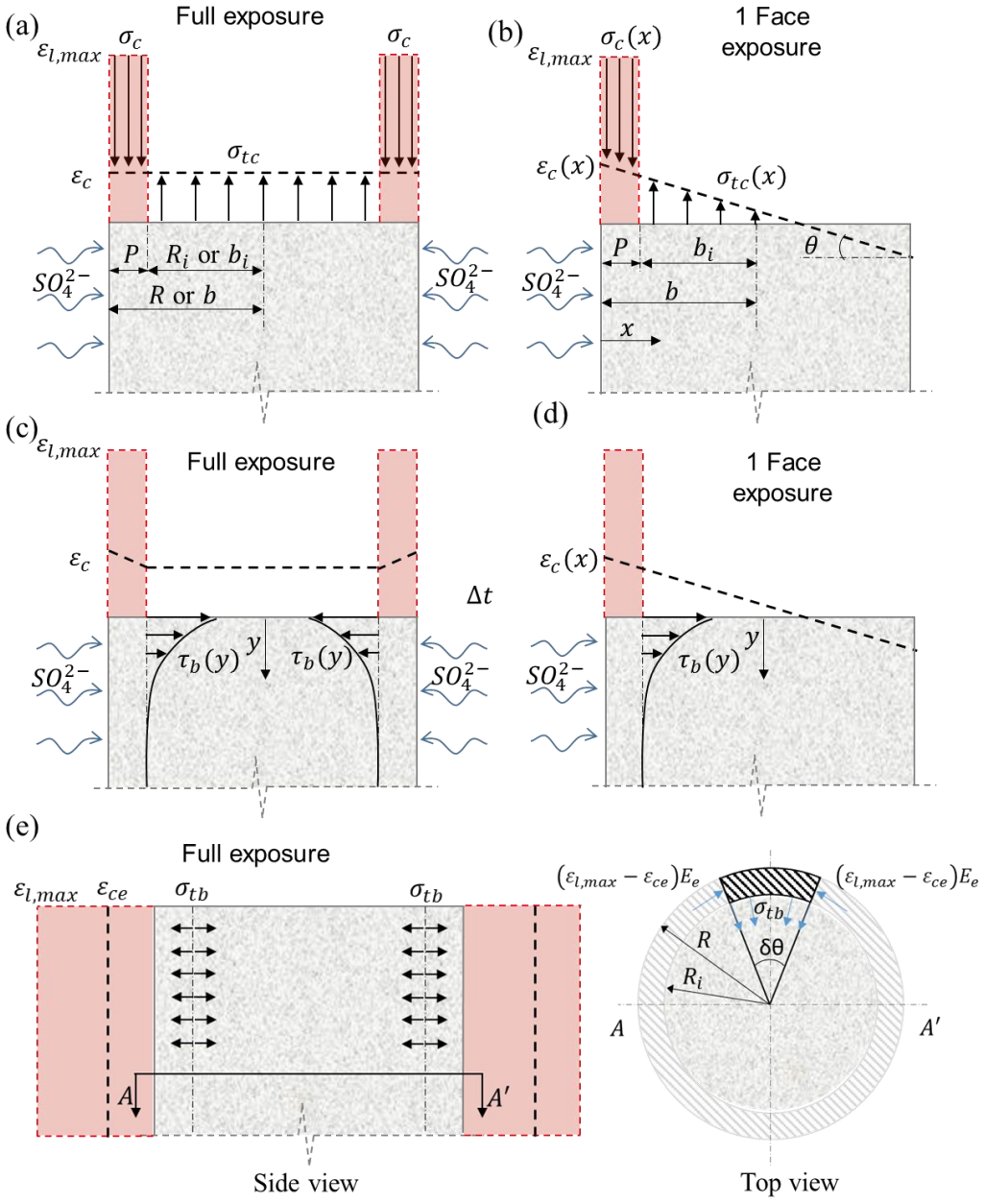

Fig. 3. Stress distribution for (a) Tensile core (b) Tangential boundary and (c) Tensile boundary failure modes under symmetric or 1 face sulfate exposure.

The simplified expression to assess this phenomenon is obtained by an analogy with the thin-walled cylinders subjected to internal pressure (penetration depth tends to be significantly smaller than the radius of the element). In order to obtain the maximum tensile stress, it is assumed that the sound core restrains all the expansions in the cross sectional plane, that is, ε_{ce} equals 0. This gives Eq. 13, which should be used for the assessment of σ_{tb} (see Table 3).

3. CASE STUDY: INFLUENCE OF SHAPE AND SIZE OF THE ELEMENT

One of the main features of the simplified methodology is that it allows the consideration of the geometrical characteristics of the specimen under attack. By this way, it is possible to take into account the positive contribution of the sound region of the element. In this section, the C_3A limit content prior failure is evaluated for piles and diaphragm walls of different sizes at 25 and 50 years. The results obtained are compared to the criteria from current structural codes.

The sulfate concentration (C_{SO}) was fixed at 3 g/l, which corresponds to a highly aggressive exposure class according to UNE EN 206-1. Initial diffusivity and the buffer capacity of the matrix are fixed at 10^{-12} m^2/s and 0.10, respectively. The length (l) of the structural element is fixed at 5 m, which is above the critical length for the assessment of the tangential stresses. This means that the results derived from the parametric study also apply to elements with bigger values of l.

To ease the interpretation of the graphs, the different failure modes are represented as the ratio between the stress and its corresponding strength (Ψ). The compressive strength and the elastic modulus of concrete are fixed at 30 MPa and 28000 MPa, respectively. The elastic modulus was considered the same at the sound core and at the superficial layer affected by ESA. This consideration is on the safe side since it provides higher internal stresses in the equations from Table 3. The tensile strength of the material is approximated through the formulation included in the Model Code. The formulation proposed by Kaneko et al. [10] is used to estimate the shear strength, which gives a τ_{max} of 7.1 MPa. This value is in agreement with experimental tests performed by Djazmati [11]. The aluminate content depicted in Figures 4-6 correspond to concretes with 350 kg/m^3 of cement with 80% of clinker. In these figures, the first failure mode is depicted with a discontinuous red line.

Figure 4 depicts the stress/strength ratio for different C_3A contents in piles with 90, 60 and 30 cm of diameter at 25 and 50 years. All curves present similar trends, showing minimum degrees of damage for low contents of C_3A. However, once a threshold content is reached, all stress/strength ratios increase abruptly, indicating a high risk of failure. Notice that this behavior is in agreement with the criteria included in structural codes, which establish a limiting C_3A content for sulfate resistant cements. Below this limit it is assumed that no significant damage occurs.

Results suggests that the size of the element play a very important role on the limit aluminate content. Failure is predicted to occur at C_3A contents around 9%, 8% and 7% for pile diameters of 90, 60 and 30 cm, respectively. Therefore, the limit content of aluminate prior failure decreases along the decrease of size. The failure modes predicted also depend on the size of the element. Large diameters seems to promote the delamination of the external layers due to the tangential stresses in the boundary of the sound and affected regions. On the

other hand, for smaller diameters tensile failure in the core might be the predominant failure mode.

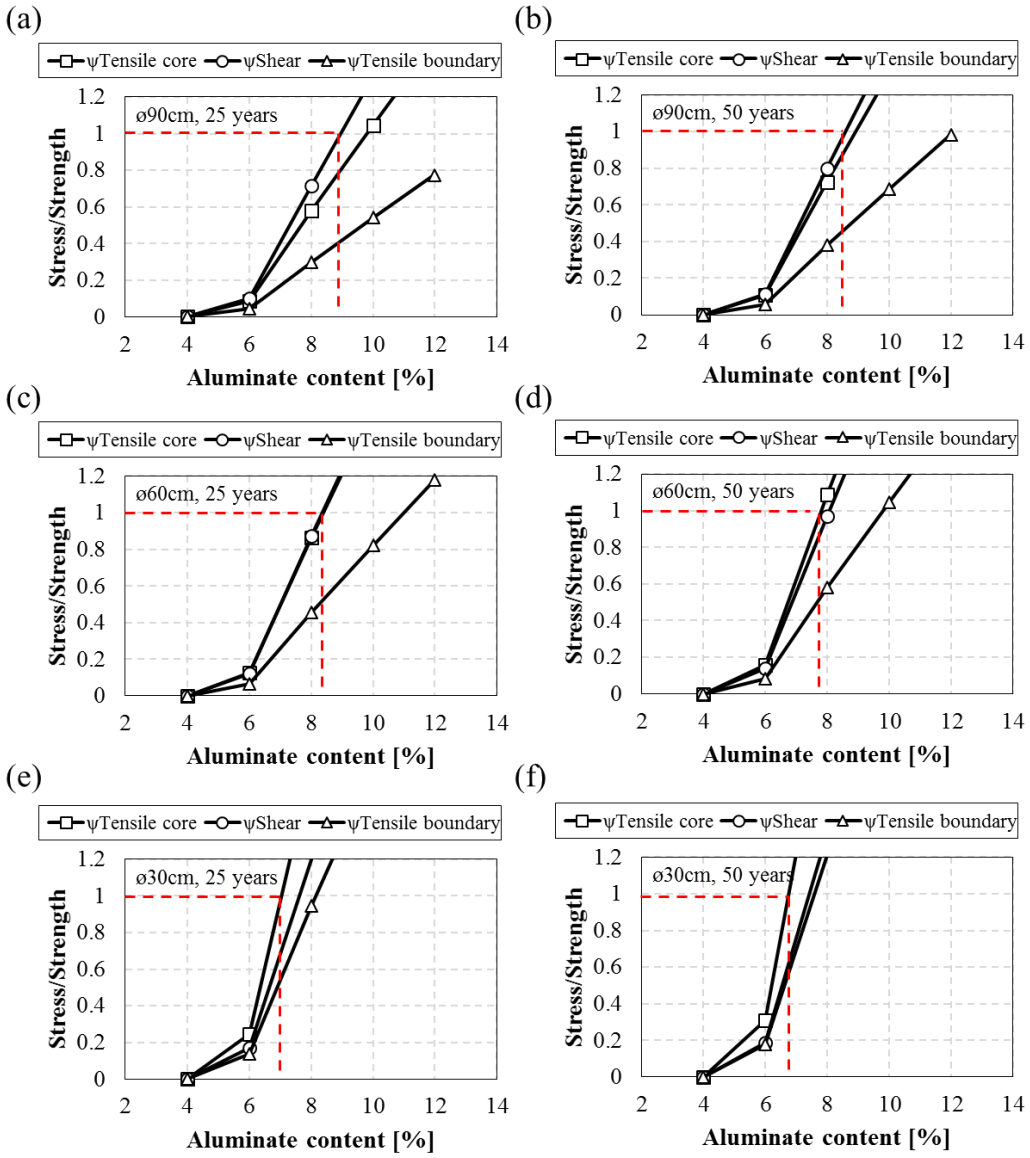

Fig. 4. Stress/strength ratio for piles under full exposure.

Figure 5 shows the stress/strength ratio for different C_3A contents in diaphragm walls of 90, 60 and 30 cm of thickness exposed on the two faces at 25 and 50 years. In this case, only two failure modes are displayed as the tensile boundary failure cannot occur. All curves follow the same trend as the one depicted for the piles. However, in this case the aluminate content at failure is slightly bigger, with allowed contents around 10%, 9% and 8% for 90, 60 and 30 cm of thickness, respectively. Spalling of the external layers is predicted for walls of 90 and 60 cm. In the case of walls of 30 cm, tensile failure in the sound core might be the predominant failure mode.

Notice that according to most design codes, a maximum aluminate content of around 5% should be used for all cases, as the exposure class defined by the sulfate concentration demands the use of a sulfate resistant cement regardless of the size or shape of the element under attack.

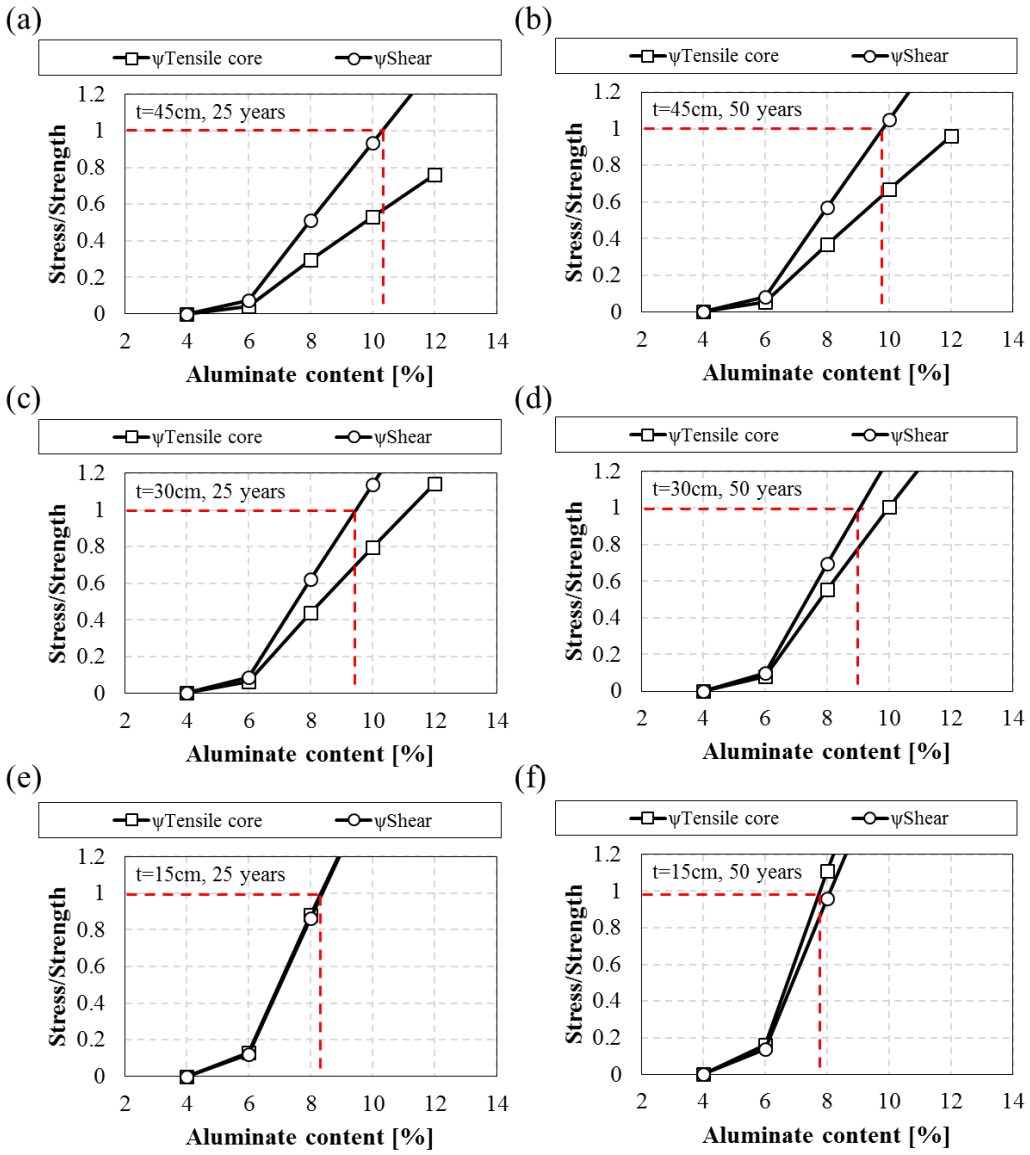

Fig. 5. Stress/strength ratio for diaphragm walls exposed to 2 faces.

4. CONCLUSIONS

A direct and straightforward methodology is developed for the evaluation of the durability of structures exposed to the ESA. This methodology allows a more detailed evaluation of this phenomenon since the specific conditions and expected service life are considered. As a result, an optimized definition of precautionary measures may be obtained for each application.

(1)- Results highlight the influence of the dimensions and structural typology of the element under attack for the assessment of the durability.

(2)- The simplified methodology suggests the existence of a C_3A threshold above which a high risk of structural damage occurs. This threshold increases with the increase of the size of the element and decreases with the desired service life.

(3)- Results indicate that spalling of the external layers due to the tangential stresses might be the predominant failure mode in large elements. However, for slender elements, tensile failure in the core might occur prior delamination.

(4)- Results suggest that the application of the prescriptions described in current design codes might lead to unnecessary penalizing measures in some situations.

ACKNOWLEDGMENTS

Support from the Spanish Ministry of Economy and Competitiveness through research project BIA2013-49106-C2-1-R is greatly acknowledged. T. Ikumi is supported by the fellowship program FPI of the Spanish Ministry of Economy and Competitiveness.

REFERENCES

[1] T. Ikumi,, S.H.P. Cavalaro, I. Segura, A. de la Fuente, A. Aguado, Simplified methodology to evaluate the external sulfate attack in concrete structures, Mat. Des. 89 (2016), 1147-1160.

[2] T. Ikumi, S.H.P. Cavalaro, I. Segura, A. Aguado, Alternative methodology to consider damage and expansions in external sulfate attack modeling, Cem. Concr. Res. 63 (2014), 105–116.

[3] A.E. Idiart, C.M. López, I. Carol, Chemo-mechanical analysis of concrete cracking and degradation due to external sulfate attack: A meso-scale model,» Cem. Concr. Compos. 33 (2011), 411–423.

[4] B. Gérard, J. Marchand, Influence of cracking on the diffusion properties of cement-based materials. Part I: Influence of continuous cracks on the steady-state regime, Cem. Concr. Res. 30 (2000), 37–43.

[5] D.A. Hordijk, Local Approach to Fatigue of Concrete, Phd Thesis, Delft University of Technology (1991).

[6] R. Tixier, B. Mobasher, Modeling of Damage in Cement-Based Materials Subjected to External Sulfate Attack. I: Formulation, J. Mater. Civ. Eng. 15 (2003), 305–313.

[7] S.T. Lee, R.D. Hooton, H. Jung, D. Park, C.S. Choi, Effect of limestone filler on the deterioration of mortars and pastes exposed to sulfate solutions at ambient temperature, Cem. Concr. Res. 38 (2008) 68–76.

[8] A. Jayatilaka, Fracture of engineering brittle materials, Applied Science Publishers (1979).

[9] S. Oller, Simulación numérica del comportamiento mecánico de los materiales compuestos, CIMNE 74 (2003).

[10] Y. Kaneko, H. Mihashi and S. Ishihara, Shear failure of plain concrete in strain localized area, Proceeding of the Fifth International Conference on Fracture Mechanics of Concrete and Concrete Structures, Colorado, USA, V.C. Li, C.K.Y. Leung, K.J. Willam and S.L. Billington (ed.), 12-16 Vol.1 (2004), 383-390.

[11] B. Djazmati and J.A. Pincheira, Shear stiffness and strength of horizontal construction joints, ACI Structural J. 101 (2004), 484-493.

4. ANNEX: SUBMITTED PAPERS

This chapter reproduces the journal papers derived from this thesis that are currently under revision in different journals. Since these are still not published, the papers presented in this chapter cannot be considered as part of the official compendium of publications. However, the outcomes of these works answer important aspects discussed in the previous chapters. Consequently, these are reproduced before the general discussion of the results. Each paper follows its own numbering of sections, figures, equations and references.

Contents

4.1. JOURNAL PAPER IV. THE ROLE OF POROSITY IN EXTERNAL SULFATE ATTACK

Submitted to Cement and Concrete Research in Nov. 2016.

Tai Ikumi[a,*], Sergio H.P. Cavalaro[a,*], Ignacio Segura[b]

[a] Department of Construction Engineering, Universitat Politècnica de Catalunya Barcelona Tech, Jordi Girona 1-3, C1, E-08034 Barcelona, Spain
[b] Smart Engineering, Jordi Girona 1-3 K2M 202c, Barcelona, Spain

* Corresponding authors at: Department of Civil and Environmental Engineering, Universitat Politècnica de Catalunya Barcelona Tech, Jordi Girona 1-3, C1, E-08034 Barcelona, Spain. Email addresses: tai.ikumi@upc.edu (T. Ikumi), sergio.pialarissi@upc.edu (S.H.P. Cavalaro), Tel: +34 93 401 6507 Fax: +34 93 401 1036

Abstract

Design codes promote a limitation of permeability (indirectly of porosity) to reduce the sulfate ingress and improve the resistance of concrete and mortar to the external sulfate attack (ESA). However, porosity could also have a positive effect on the durability by generating additional space to accommodate the expansive phases. The objective of this study is to evaluate the role of porosity in ESA. For that, changes at the macro-scale, phase composition and pore network are monitored for mortar compositions with different pore size distribution. Results indicate the existence of two mechanisms: the capacity to accommodate expansive phases controls the durability during the initial stages of the attack, while at later stages durability is defined by the permeability. Results from specimens with air-entrainer suggest that the intentional increase of the porosity towards maximizing the capacity to accommodate expansive products might be a valid approach to protect elements against the ESA.

Keywords: Sulfate Attack (C); Ettringite (D); X-Ray Diffraction (B); Mercury Porosimetry (B);Pore structure

1. INTRODUCTION

External sulfate attack (ESA) is a complex degradation process that might compromise the long-term durability of cement-based materials in contact with sulfate rich environments. Despite ESA is influenced by a wide variety of factors, the intensity and rate of the attack are mainly related to the exposure conditions, material properties and mixture proportioning. Building and structural codes specify precautionary measures to obtain sulfate-resisting concrete. These measures consist of limiting the aluminate content in the cement, using low water/cement ratios to reduce the permeability and increasing of compressive strengths to resist the internal stresses caused by the expansions (e.g. Model Code 2010, BS 8500-1:2006, ACI 201.2R-08, UNE EN 206-1:2008).

The recommendation of low permeability aims to reduce the penetration of external aggressive ions into the inner layers of the material. Several studies support this recommendation. Nowadays, it is accepted that cement-based materials with low permeability show a better durability against sulfates than the corresponding samples with higher permeability (e.g. [1-7]). Although permeability and porosity are not synonyms, in general the decrease of permeability is accompanied by a consequent decrease in the porosity of the matrix. Therefore, the limitation of permeability usually indirectly implies a reduction of the porosity provided by the pore network.

The role of the pore network during the attack is not only related to the transport of sulfate ions. Since pores are basically empty spaces within a rigid matrix, they have a certain capacity to accommodate expansive phases before creating damage. In this context, pores might act as deposits or containers of the expansive products precipitated during the ESA. This phenomenon has been described by other authors [8-11] as the buffer or damping capacity of the matrix.

A few studies report trends that may suggest the positive consequence of a highly porous material in comparison with a dense matrix with low permeability and porosity. Naik et al. [12] found that a reduction of water/cement ratio caused more severe physical damage in samples exposed to a sodium sulfate solution. The authors attributed the earlier damage and the more rapid failure of the samples to the reduced extensibility of the material and to the low capacity of the dense pore network to accommodate expansive phases [12]. M. Santhanam et al. [13,14] assessed the behavior of mortars with a presumably high capacity to accommodate expansive phases by the use of an air-entrainer admixture. The authors obtained lower and delayed levels of deterioration in such mortars. They suggested that entrained air might provide sites for nucleation of expansive phases, which might lead to a reduced damage in the paste. Another hypothesis formulated was that air might help arresting the growth of cracks due to their spherical shape.

Despite that, solid evidences and explanations regarding the contribution of a highly porous matrix are rare and inconclusive. Consequently, the maximization of the buffer capacity of the matrix by increasing the porosity has not been recognized as a possible approach to obtain durable materials against the ESA.

The objective of this study is to assess the influence of the pore network on the durability against the ESA. For that, mortar compositions with different porosities (from 8.1 % to 18.8 %) are subjected to accelerated sulfate attack. In order to isolate the effects of porosity, the C_3A content, external sulfate concentration and geometrical characteristics of samples are kept constant for all compositions. Characterization of the macro-scale behavior

is performed by monitoring the dimensional, mass and ultrasonic velocity variation over time. Changes in phase composition are investigated by X-ray diffraction (XRD) and evolution of the pore characteristics of the mortars are examined by mercury intrusion porosimetry (MIP).

This study provides evidences and explanations that help understanding the role of porosity in samples subjected to the ESA. The findings might open up alternative strategies for the future design of durable cementitious materials against the attack.

2. EXPERIMENTAL PROGRAM

2.1 MATERIALS AND MORTAR COMPOSITIONS

Portland cement (CEM I 52.5R) with high C_3A content was used in order to promote ettringite formation and the potential damage during ESA. Table 1 shows the chemical (determined by XRF spectrometry) and mineralogical (estimated using Bogue equations) composition and summarizes the physical properties of the cement. Data provided by Bogue equations is only used to classify the cement as highly reactive under sulfate exposure. Deionized water and siliceous sand following the specifications of UNE-EN 196-1:2005 were used in all mortars. Commercial superplasticizer GLENIUM ACE 456 and air-entrainer MasterAir 100 were added to the mixtures.

Table 1. Chemical and mineralogical composition of the Portland cement.

Chemical composition [% bcw*]	
SiO_2	19.5
Al_2O_3	5.9
Fe_2O_3	1.7
CaO	63.1
MgO	2.1
SO_3	3.5
K_2O	0.8
Na_2O	0.4
Cl^-	-
LOI	3.0
Phase composition [% bcw*]	
C_3S	65.4
C_2S	10.6
C_3A	12.3
C_4AF	5.6
Physical properties	
Spec. surf. area (BET) [m^2/g]	1.10
d_{10} [µm]	0.58
d_{50} [µm]	6.88
d_{90} [µm]	31.84

*bcw: By cement weight

Table 2 shows the composition of the 4 matrices included in this study. Different degrees of refinement of the pore network were obtained by varying the water/cement ratio from 0.38 to 0.55 and by using an air-entrainer. Initial reference porosities obtained by MIP test at 14 days after sulfate exposure are included in Table 2. The different compositions considered cover a wide range of porosities (from 8.1 % to 18.8 %). The nomenclature adopted for each composition follows the pattern 'water/cement ratio'_'initial porosity'. Mortars with air entrained have the term 'AE' prior to the water/cement ratio. Notice that the cement content remained constant for all compositions, ensuring similar amount of C_3A and

potential expansion. Therefore, the macro-scale response of mortars after sulfate exposure can be associated mainly to differences in the pore system.

The mixing procedure defined in UNE-EN 196-1:2005 was adopted, introducing small modifications to cover the specificities of the admixtures added. The air-entrainer was added at the end of the mixing procedure and mixed at high speed for 60 s. The superplasticizer was mixed with the deionized water in contents to assure flow extents of 20 cm ± 0.5 cm. This flow extent was defined to favor similar workability and surface finish amongst all mortar compositions.

Table 2. Compositions and mass attenuation coefficient (MAC) of the mortars.

Material	0.38_8.1%	0.45_12.4%	0.55_13.7%	AE0.45__18.8%
Cement [kg/m^3]	580	580	580	580
Sand [kg/m^3]	1425	1325	1180	1325
Water [kg/m^3]	220	261	319	261
Air-entrainer [% bcw]	-	-	-	0.3
Superplasticizer [% bcw]	1.00	0.50	-	0.25
Water/cement ratio	0.38	0.45	0.55	0.45
Porosity [%]	8.1	12.4	13.7	18.8
MAC [cm^2/g]	48.11	48.01	47.84	48.01

2.2 EXPERIMENTAL PROCEDURE

2.2.1 Specimen preparation

Mortars specimens of Ø78 mm x 17 mm were cast to conduct this study. Such geometry was chosen to avoid the typical corner spalling observed in rectangular samples that might alter the macro-scale response during the attack [15]. The dimensions selected maintain similar exposed surface-volume ratio than other studies that showed good balance between test duration and representativeness [16]. Due to the importance of the surface finish in transport-related degradation processes, specimens were cast in individual molds to obtain external surfaces representative of field conditions and to avoid the presence of cut aggregates on the exposed surfaces.

Figure 1 depicts a schematic representation of the molds and the casting process adopted. The molds were composed by a PE rigid base with 4 fixed PVC pipes and a moving PE rigid cover. Top and side views of these components are presented in Figure 1a. 5 Ø12 mm x160 mm bolts were used to guide the cover into the base during assembly (Figure 1b). 12 PE bars were used to fix the PVC pipes and block the cover at a specific height to obtain a sample thickness of 17 mm. To relieve the excess of mortar, purge exits were introduced in the cover. Before assemblage, the mortar (represented in light hatching) was first poured inside the PVC pipes and compacted with 15 jolts in the flow table (ASTM C1437) at a rate of 1 jolt per second to eliminate air pockets. After that, the cover was placed and tightened to the base. In order to ensure adequate surface finish quality, the molds were then vibrated during 10 seconds at the vibration table. Finally, the hex nuts were further tightened until the cover reached the PE bumpers that control the height of the specimens.

Specimens were demolded 24 hours after casting and the lateral surface was water sealed with the flexible epoxy coating MasterSeal M 338 to ensure linear penetration of the sulfate ions through the two main surfaces of the specimen. Figure 2a shows a final specimen obtained after applying the coating. Once sealed, all specimens were cured in water at 25 ºC

± 1 ºC for one day. Then, they were placed laterally inside plastic containers and submerged in a sulfate-rich water solution (Figure 2b).

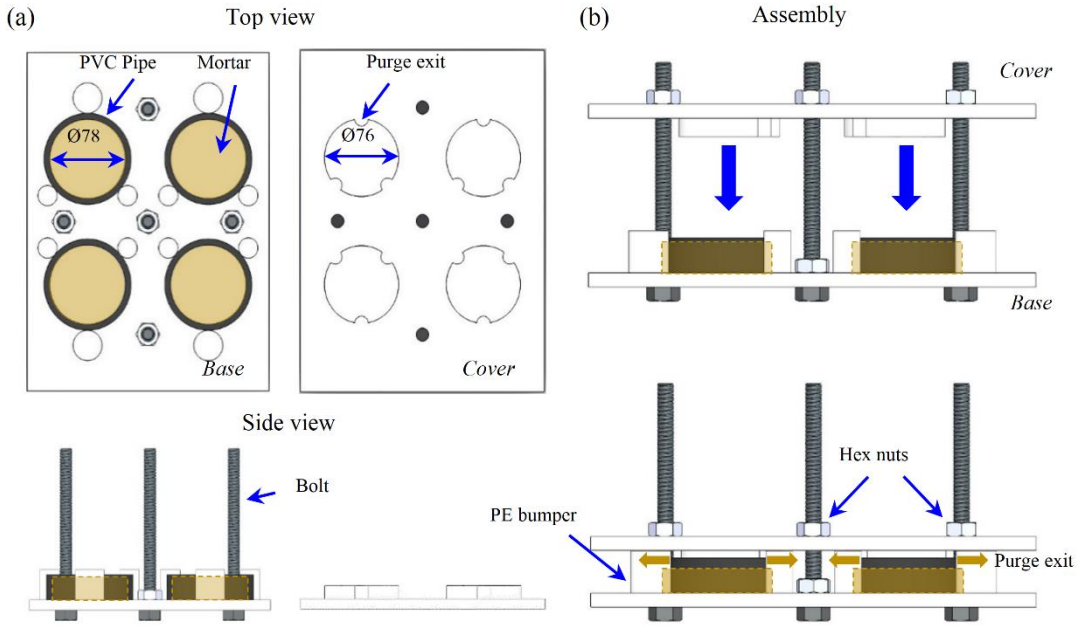

Fig. 1. Schematic representation of (a) top and side view of the molds and (b) assembly and casting process (Dimensions in mm).

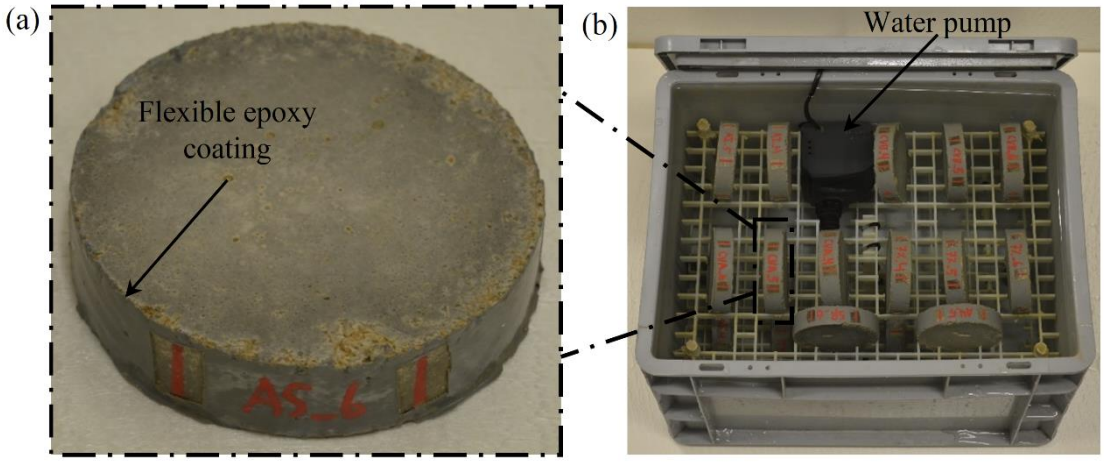

Fig. 2. Detail of (a) final specimen and (b) layout of specimens.

2.2.2 Exposure conditions

Specimens were exposed to the sulfate solution shortly after casting to reproduce the real exposure conditions of most structures subjected to the ESA, which are usually built in situ. A sulfate concentration of 30 g of Na_2SO_4/l was used to accelerate the degradation process. The solution was renewed weekly during the first month and every other week until the end of the test at 365 days. The volumetric ratio of sulfate solution to mortar was 12. This should be representative of field conditions where the material is exposed to continual supply of sulfate ions.

Water pumps were placed inside the plastic containers to ensure a continuous flow from the bottom to the top in order to minimize concentration gradients (Figure 2b). The containers were filled up to the top and covered to reduce contact with the air, thus limiting CO_2 dissolution and carbonation. Reference samples of each composition were also exposed to non-aggressive curing with water without sulfates for comparative purposes.

2.2.3 Test methods

-Macrostructural monitoring

Characterization of the macro-scale behavior relies upon measurements of expansion, mass and ultrasonic velocity and visual inspection of the specimens. All measurements were taken weekly during the first month and every other week until the end of the study. The values presented in this study are the average of three specimens.

Due to the singular shape of the specimens, a device was designed to measure the radial free expansions of the mortars (Figure 3a), which consisted in a MICROMASTER electronic micrometer with a precision of ± 0.001 mm and a metallic platform to fix the measured points. Several vertical strips were introduced to facilitate the measuring and to guarantee a similar position of the specimens (Figure 2a). Prior to the start of the experimental program, the precision of the equipment was evaluated during a series of over 500 measurements on mortar specimens with and without gage studs. Specimens with gage studs obtained higher variability of the measurements (± 0.008 mm with studs and ± 0.002 mm without studs). Consequently, the use of studs was discarded. For each specimen, 3 radial directions were measured at each time to cover all the sample (Figure 3b). Therefore, each expansion value presented in this study is the average of 9 measurements.

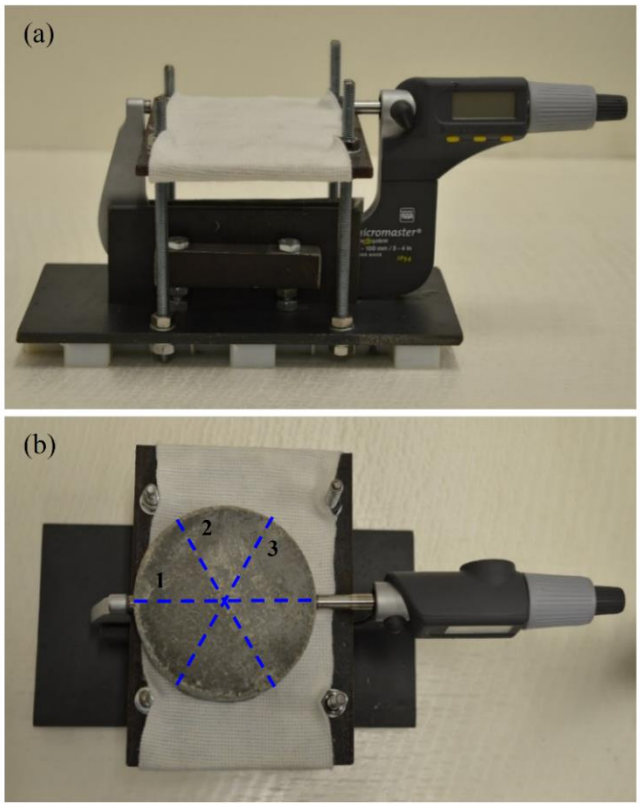

Fig. 3. (a) Length measurement device and (b) directions measured.

The ultrasonic pulse velocity between the two exposed faces was measured at 500 kHz sampling frequency with a PUNDIT PL-200. A zero-crossing algorithm was used to calculate the travelling time of the ultrasonic wave. Mass evolution was controlled with a precision balance of ±0.01 g. Surface water of the samples was dried up before weighting.

-Phase composition evolution

Changes in phase composition were investigated by X-ray diffraction (XRD) at 28, 90, 180, 270 and 365 days. Samples for XRD were core drilled from original specimens using a column drill equipped with a diamond drill bit cooled with water [17]. For each composition, samples were extracted from the same specimens to reduce the variability of the results. Due to the symmetric sulfate exposure conditions, each sample was divided in two. One half was crushed and the powder was pressed in cylindrical standard sample holders of 16 mm of diameter and 2.5 mm of height. The other half was discarded. XRD measurements were made using a PANalytical X'Pert PRO MPD Alpha1 Θ/2Θ diffractometer in reflection Bragg Brentano geometry of 240 mm of radius. CuKα1 radiation (λ=1.5406 Å) and X'Celerator detector with active length of 2.122 º were used. Work power was set to 45 kV – 40 mA. Θ/2Θ scans from 4 to 80 º2Θ with a step size of 0.017 º2Θ and a measuring time of 50 seconds per step were performed. Sample holders were spun at 2 revolutions per second.

Rietveld analysis using external standard method was performed with the XRD results for the quantitative study of the crystalline phases. The external standard method was used for quantification instead of the more common internal standard method to avoid homogenisation problems and further dilution of the cement paste in the analyzed sample [18-20]. The adopted methodology is similar to earlier works [18-20]. Phase weight fractions were calculated from phase scale factors by comparison to the scale factor of the external standard (Al_2O_3), measured under identical diffractometer conditions. The values of density and volume of the unit cell of each phase were obtained from data sets from ICSD. Mass attenuation coefficients (MAC) of the different compositions used were calculated from the MAC of each component, including the water content and taking into account the weight fraction of each one. Final MAC of the different mortars used are listed in Table 2.

All Rietveld refinements were done with X'Pert High Score Plus software package by PANalytical using the structures listed in Table 3. Small peaks of Fe-substituted ettringite formed as a result of the reaction between sulfate ions and the Ferro aluminate phases were detected in some mortars at late stages of the attack. Since its crystalline structure for Rietveld refinement was not available it was not considered during quantification. The global variables refined were the background polynomial with 4 coefficients (1st, 2nd, 3rd and 5th) and the zero shift. For all phases detected, individual scale factors and lattice parameters were refined. A pseudo-Voigt function was chosen to model the peak shape. The phase profile width (w) was refined for quartz, ettringite, portlandite and gypsum. For quartz and portlandite, the profile parameters U, V and the peak shape were also refined. Preferred orientation corrections were applied when necessary for gypsum (0 2 0), portlandite (0 0 1), ettringite (1 0 0) and quartz (1 0 1) as long as the phase content was above 2 %.

Table 3. Phase structures used for Rietveld refinement.

Phase	Chemical composition	ICSD Code	Reference
Alite	Ca_3SiO_5	94742	[21]
Belite_o	Ca_2SiO_4	81097	[22]
Portlandite	$Ca(OH)_2$	15471	[23]
Calcite	$CaCO_3$	79673	[24]
Ettringite	$Ca_6Al_2(SO_4)_3(OH)_{12}26H_2O$	155395	[25]
Gypsum	$CaSO_42H_2O$	15982	[26]
Ferrite	Ca_2AlFeO_5	9197	[27]
Quartz	SiO_2	200721	[28]
Corundum	Al_2O_3	73725	[29]

-Pore system evolution

Evolution of the pore system of the mortars were examined through mercury intrusion porosimetry (MIP) with a Micrometrics AutoPore IV 9500 (contact angle 140º and Hg surface tension 485 dynes/cm) at 14, 28, 91, 180 and 270 days. Tests after 270 days were not performed due to the spalling of the external layer of the sample during drilling. Samples were extracted following the same procedure as described in the previous section. Due to the symmetric sulfate exposure conditions, each sample was divided in two and analyzed separately. Freeze-drying was applied to the samples to ensure full desaturation prior to mercury intrusion.

3. RESULTS AND DISCUSSION

3.1 MACROSTRUCTURAL CHARACTERIZATION

3.1.1 Visual aspect of samples

Visual appearance during the attack indicates no major failure in any composition in the form of generalized spalling of the external surface or tensile splitting of the sample. Therefore, the geometrical characteristics and specimen preparation adopted in this study prevented the development of failure modes that might compromise the interpretation of the macro-structural response of the material.

Figure 4 depicts the visual appearance of the external surface of the 4 compositions at the end of the test. In 0.38_8.1%, 0.45_12.4% and 0.55_13.7%, a thin dense layer covering most of the surface is observed. This layer appeared in small localized regions approximately in the second month of exposure and spread at different rates until the end of the test. Samples with lower water/cement ratio (0.38_8.1% and 0.45_12.4%) showed the higher formation rates. As a result, these samples experienced localized spalling in locations within the region covered by the layer. In Figure 4, these locations are highlighted with a red circle.

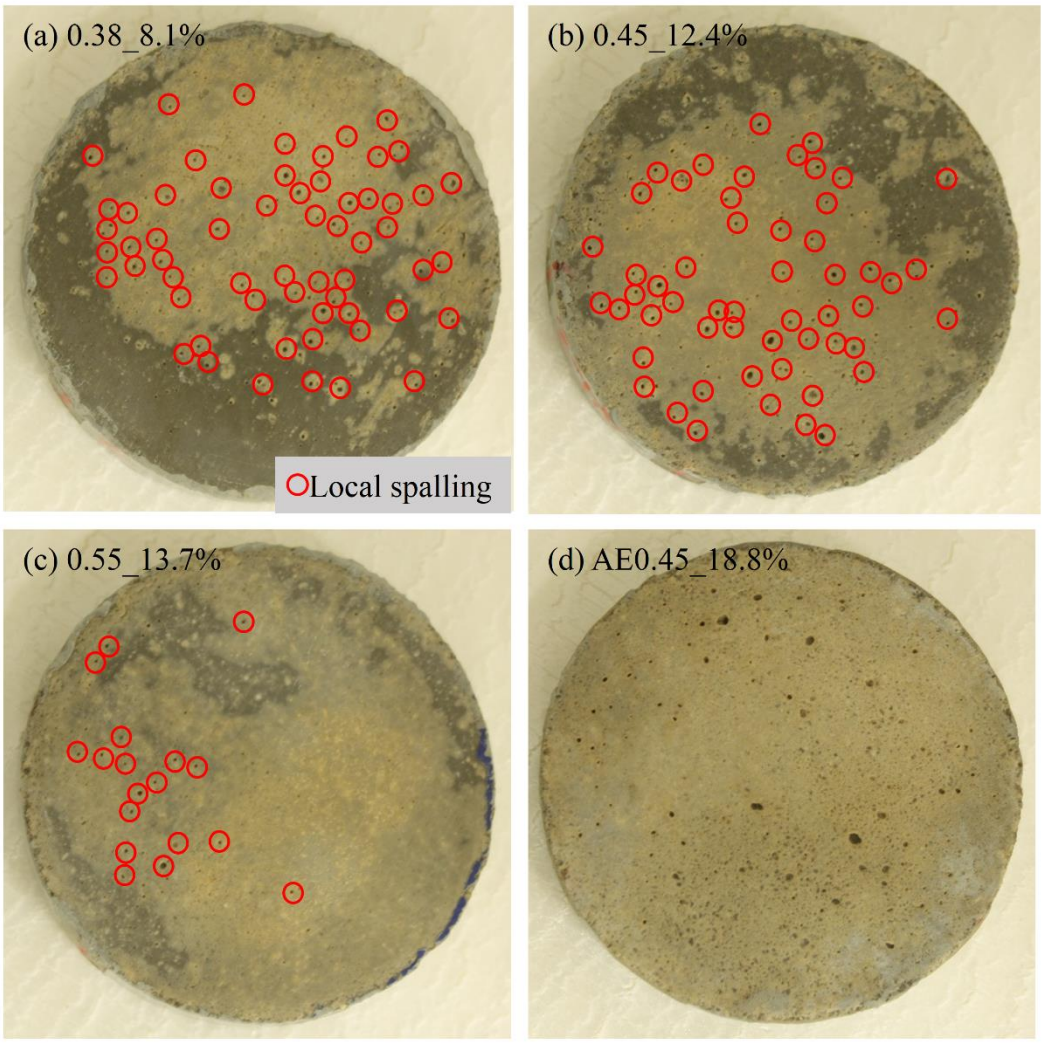

Fig. 4. Visual aspect of the mortars at 365 days.

A comparison of the amount of red circles between Figure 4a, 4b and 4c clearly indicates that the physical damage in the form of local spalling increases with the decrease of the porosity of the samples. This observation is in agreement with the results presented by Naik et al. [12]. On the other hand, in mortars with air entrained (Figure 4d) this dense layer is not visible at any stage of the attack.

3.1.2 Expansions

Figure 5 depicts the radial expansion of the mortars during the 365 days of sulfate exposure. In order to distinguish the effects of sulfate exposure from the normal hydration process, data presented in Figure 5 corresponds to the difference between exposed and control specimens. Results for 0.38_8.1%, 0.45_12.4% and 0.55_13.7% series show a first stage of rapid expansions followed by a second stage characterized by a decrease in the expansion rate. In the case of 0.55_13.7%, this decrease is considerably less pronounced than in the other compositions. The duration of the first stage is approximately 77, 63 and 25 days respectively for 0.38_8.1%, 0.45_12.4% and 0.55_13.7%, as indicated by the vertical lines on each expansion curve (duration estimated by the first consecutive measure where the expansion increase is below 5%).

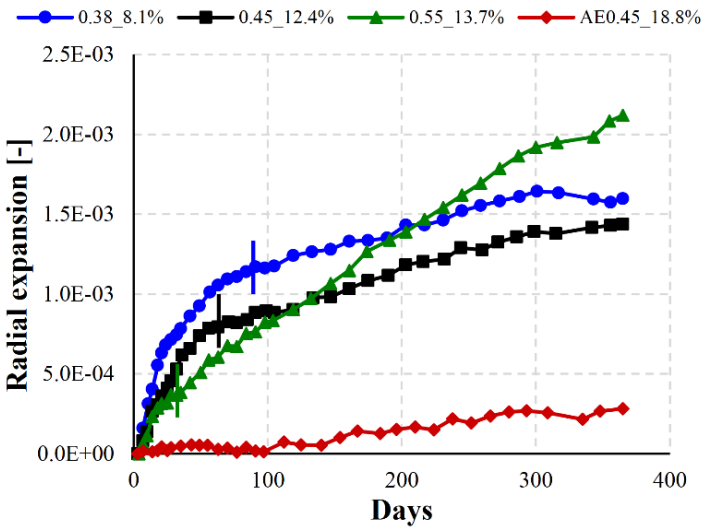

Fig. 5. Radial expansion of mortars.

The first stage may be caused by the high initial sulfate concentration gradient between the solution outside and inside the specimen. Moreover, the early exposure (2 days after casting) also facilitates sulfate ingress due to low hydration degree and consequent low densification of the matrix at this moment. Therefore, a sudden sulfate concentration boost in the pore solution of the matrix close to the surface should be observed. This may cause ettringite precipitation and crystallization pressure uprise at locations where calcium, aluminum and sulfates meet.

According to the prescriptions included in codes, the magnitude of the expansions should be more evident in the compositions with higher porosity, as the penetration is presumably enhanced. However, Figure 5 shows the opposite trend for the first stage of the expansion curve. In this stage the expansions seems to be defined by the capacity of the matrix to accommodate expansive products. In refined pore networks, the initial sulfate concentration boost might cause sudden ettringite precipitation in small pores, as the dense matrix force the sulfate flux through small capillary pores before reaching larger pores. On the contrary, due to the large availability of large pores in coarse pore networks, the precipitation could mainly occur in locations with a high capacity to accommodate expansive phases without creating expansions [13,14].

The decrease of expansion rates observed in the second stage for series 0.38_8.1%, 0.45_12.4% and 0.55_13.7% might be related to the kinetics of diffusion (reduction of concentration gradient) and the influence of pore filling effect in the diffusion coefficient of the external layers of the samples. Interestingly, the reduction of the expansion rate is also related to the porosity of the mortars. In this case, mortars with lower porosity (0.38_8.1% and 0.45_12.4%) show bigger reductions in the expansion rate in comparison with mortars with higher porosity (0.55_13.7%), which present lower decrease. A possible explanation is that in refined pore systems, the precipitation produced during the first stage severely hinders the sulfate penetration at later ages, thus decreasing the expansion rates. In porous matrices, the precipitation achieved is not enough to fill a significant fraction of the capillary pores. Consequently, the penetration rate should not be significantly altered and expansions would only be slightly reduced. This hypothesis explains the steady expansion of samples 0.55_13.7%.

The mortar with air-entraining agent presents a particular evolution over time. For this series, no initial expansion is observed in the first stage. Expansion onset is produced only after 100 days of exposure. However, the expansion rates observed are still smaller than in other compositions. The absence of expansions during the first 100 days could be related to the high capacity of the matrix to accommodate expansive product. Due to the extensive availability of large pores, the pore filling effect that hinders sulfate penetration described for the other compositions does not apply. As a result, instead of a reduction of expansions in the late stages of the attack, for this composition the expansion rate increases. In terms of the absolute values reached at the end of the accelerated test, the total expansion of the composition with air-entrainer is 7.5 times smaller than the composition with 0.55 water-cement ratio.

The profiles depicted in Figure 5 reflect the double role of porosity in the ESA. To highlight this, Figure 6 shows the incremental radial expansion at different periods of exposure. During the first 28 days, results indicate that the capacity of the matrix to accommodate expansive product constitutes the main resistance mechanism against the ESA, as expansions decreases with the increment of porosity. However, from 90 days of exposure this trend is reversed for the mortars without air-entrainer, as expansions decrease with the decrease of porosity. Therefore, at this stage the permeability of the matrix is the main factor that define the behavior against the attack. Notice that the mortar with air-entrainer shows the smallest increments of expansions almost in all periods evaluated. This result may indicate that the first stage where the buffer capacity of the matrix controls the overall resistance against the attack can be extended over time if sufficient amount of large pores are available.

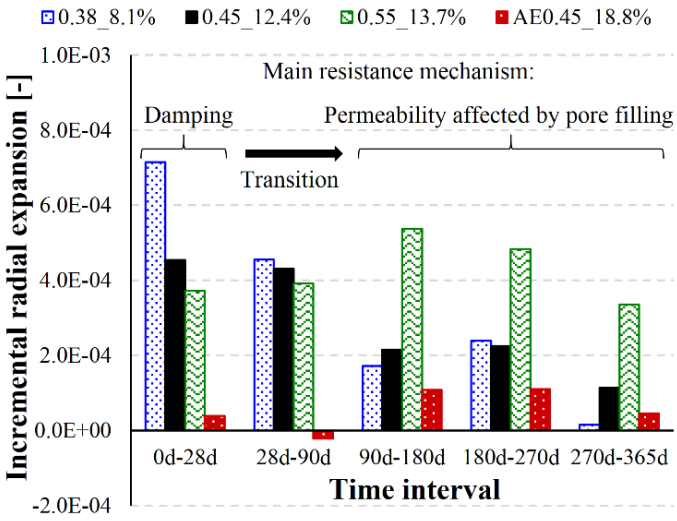

Fig. 6. Incremental radial expansion of mortars.

Figure 6 also sheds light on the reasons for the differences in behavior found between mixes 0.38_8.1% and 0.45_12.4%. The higher final expansion of the former is justified by a significantly higher expansion in the period 0d-28d, which is approximately 57% bigger than the observed in 0.45_12.4% at the same period. In later periods, both compositions show similar increments in radial expansion. Therefore, the bigger final expansion of 0.38_8.1% in comparison with that from 0.45_12.4% is possibly the consequence of a lower damping capacity in the initial stages due to the more refined porosity.

3.1.3 Ultrasonic pulse velocity

Figure 7 shows the evolution of the ultrasonic pulse velocity for the different compositions considered (difference between specimens stored in sulfate solution and control at a certain time divided by the difference at the beginning of the accelerated attack). Changes in velocity can be related to the change in the density and integrity of the specimens. Positive values suggest denser matrices while negative values are indicative of damage. Samples from series 0.38_8.1%, 0.45_12.4% and 0.55_13.7% show similar trends with a decrease in ultrasonic velocity with the exposure time. As described in Figure 5 for the expansion, the relative velocity change also depicts 2 stages. The first stage presents a rapid decrease of relative velocity indicating high degradation rates. After that, a deceleration of the degradation is observed, probably caused by the reduction of the penetration rate of sulfates due to the pore filling effect and the decrease of the sulfate concentration gradient, as described in section 3.1.2.

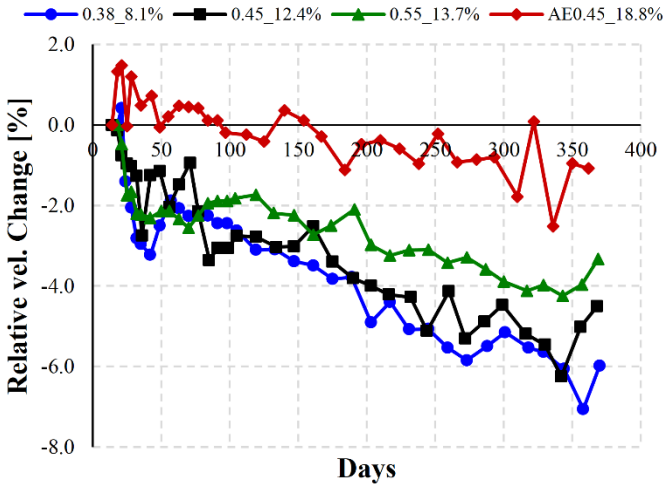

Fig. 7 Evolution of ultrasonic velocity variation of mortars.

The evaluation of the velocity change at the end of the test shows that the degree of damage increased inversely with the porosity. In fact, the composition with the denser matrix and smaller porosity (0.38_8.1%) presents the higher velocity reduction amongst all the compositions studied, indicating relatively higher damage caused by the attack. This result is in agreement with the visual inspection performed in section 3.1.1, but is not consistent with the expansion profiles presented in 3.1.2 (at the end of the test, 0.38_8.1% did not show the highest dimensional variation). Such results could be explained by the reduced extensibility of the material due to higher stiffness of the denser matrix [12]. Therefore, even though a relatively higher damage occurs, the higher elastic modulus restrains the deformation, leading to the assessment of smaller expansion.

On the other hand, mortars with air-entrainer (AE0.45_18.8%) maintained similar velocities than the control specimens throughout the accelerated attack, indicating low levels of damage. These results are in agreement with the expansion curves presented in Figure 5, where AE0.45_18.8% mortars exhibited the lowest expansions amongst all compositions.

3.1.4 Mass evolution

Figure 8 depicts the relative mass variation over time for all mortars studied. In order to isolate the effects of sulfate exposure from the phenomena of absorption, hydration and leaching

experienced by all samples, this figure represents the differences between exposed and control specimens. Despite all samples presented a slight positive mass change, mortars under sulfate exposure showed a much lower mass increase. Therefore, Figure 8 shows negative mass variations for all compositions. Up to 200 days, sulfate exposure causes higher mass reduction as porosity increases. Then, the mass of 0.38_8.1%, 0.45_12.4% and AE0.45_18.8% mortars continues to decrease over time. However, 0.55_13.7% series presents a change in tendency, showing a mass increase after 200 days.

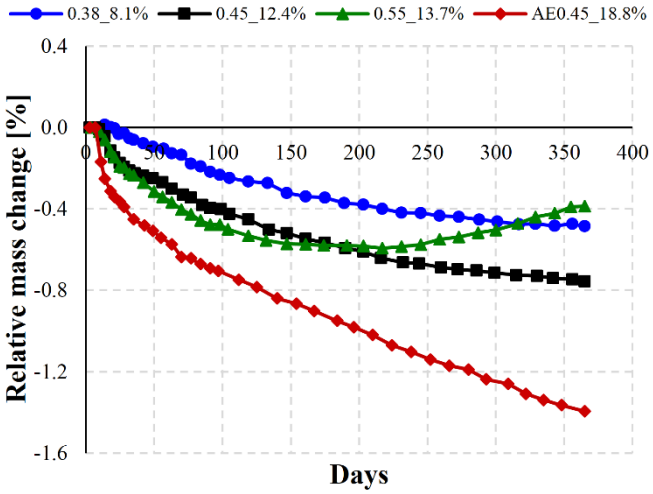

Fig. 8. Evolution of mass variation of mortars.

The mass reduction due to sulfate exposure could be explained by several processes occurring after sample immersion. Mortars in the aggressive media experience sulfate uptake from the external solution, which causes an increment of mass. However, sulfate ingress triggers a series of chemical reactions that involves dissolution of soluble calcium bearing phases for ettringite and gypsum precipitation. To maintain the equilibrium of the system, hydroxide ions released from portlandite dissolution diffuse towards the external solution, causing mass reduction. Measures of pH at the end of the test confirm higher leaching rates in the mortars submerged in the Na_2SO_4 solution compared to control (9.46 and 8.73, respectively). Measures of calcium contents by ICP-OES at the end of the test also indicate that calcium leaching phenomenon is more pronounced in the aggressive solutions (88.37 ppm over 56.06 ppm). These phenomena should be intensified as porosity and permeability of the specimen increases, thus being in agreement with the initial trends depicted in Figure 8.

The slope reduction depicted by mortars without air-entrainer at later stages of the attack indicates a deceleration of the leaching process. The deceleration could be explained by lower concentration gradients between external and internal solutions and the pore filling effect caused by the precipitation of phases in the superficial pores of the specimens. As described in Figure 4, mortars without air-entrainer present a thin dense external layer that might slow down the leaching process. On the other hand, this dense layer is not visible in AE0.45_18.8% series, which could explain why in this composition the leaching phenomenon seems to progress at a similar rate until the end of the test. The particularly high mass gain experienced by 0.55_13.7% from 200 days on could be explained by a macroscopic swelling caused by the large expansions measured. Notice that this age corresponds to the age when the expansion of this series becomes the highest amongst all compositions studied (see Figure 5).

The physical changes observed here suggest that the role of the pore network during the ESA is not only related to the transport process and the amount of expansive phases formed. According to the results obtained, the buffer capacity of the matrix to accommodate the product precipitated might be more relevant than the permeability itself when it comes to define the durability of the specimens at early stages of the attack.

3.2 MICROSTRUCTURAL ANALYSIS

3.2.1 XRD analysis

This section presents the evolution of phase composition measured by quantitative XRD analysis for the different compositions during sulfate exposure. To simplify the interpretation of the results, only crystalline phases interacting with the sulfate ions are presented and phase contents are expressed as a percentage of the cement content.

Figure 9 depicts ettringite, gypsum and portlandite contents for all compositions at the end of the test. The sum of expansive phases (ettringite and gypsum) range between 14.3 %, in the composition with 0.38 water/cement ratio, and 29.9 % in the mortars with air-entrainer. On the other hand, Portlandite contents only present a slight variation, with values between 14.0 % and 17.6 % for 0.38_8.1% and AE0.45_18.8%, respectively. As expected, Rietveld quantification reveals increasing amounts of expansive phases with the increase of porosity of the composition. These results suggest that the pore system affects the sulfate penetration rate of each composition, causing precipitation of different amounts of expansive products.

Figure 9 also includes the radial expansions measured at 365 days. Results indicate no clear relationship between the amounts of expansive phases and the final radial expansions measured. Although the amount of expansive phases in AE0.45_18.8% is 2.1 times bigger than in 0.38_8.1%, the final radial free expansion obtained decreases by a factor of 5.7.

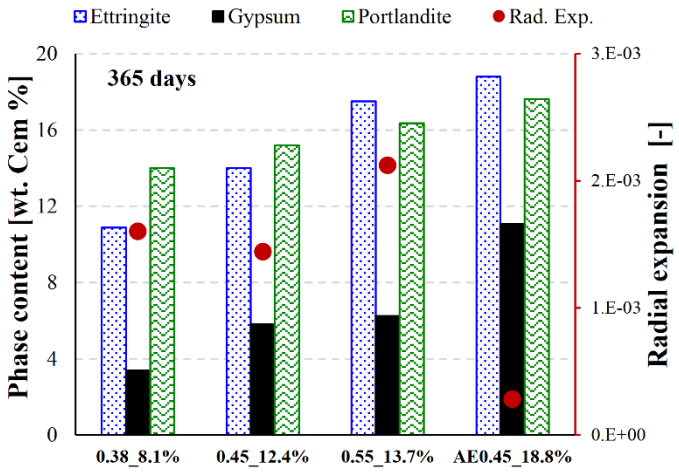

Fig. 9. XRD results and final radial expansions at 365 days.

In order to further evaluate the relationship between expansive phases and expansions at different stages of the attack, Figure 10 shows the evolution of ettringite, gypsum and portlandite contents combined with the radial expansions for 0.45_12.4% and AE0.45_18.8% mortars at 28, 90, 180, 270 and 365 days. These compositions were selected for presenting the same water/cement ratio and aggregate content. Therefore, the main difference is the

presence of air voids intruded by the air-entraining agent. Both compositions already exhibit high ettringite and gypsum contents after 28 days of exposure.

After that, 0.45_12.4% depicts similar contents until the end of the test (-0.1 % between 28 and 365 days) while AE0.45_18.8% shows a moderate increase (+8.9 % between 28 and 365 days). In both cases, the increments of expansion and the amount of expansive phases formed during the same period do not seem to present any direct relationship at any stage of the attack. Series 0.45_12.4% clearly illustrates this statement. Even though expansions increase by $9.8 \cdot 10^{-4}$ between 28 and 365 days, the amount of expansive phases remains almost unaltered. Again, this suggests that the progressive precipitation of expansive phases consumes part of the buffering capacity of the pore system. Once the buffering capacity is reduced, precipitations of even small amounts of expansive phases lead to significant expansions.

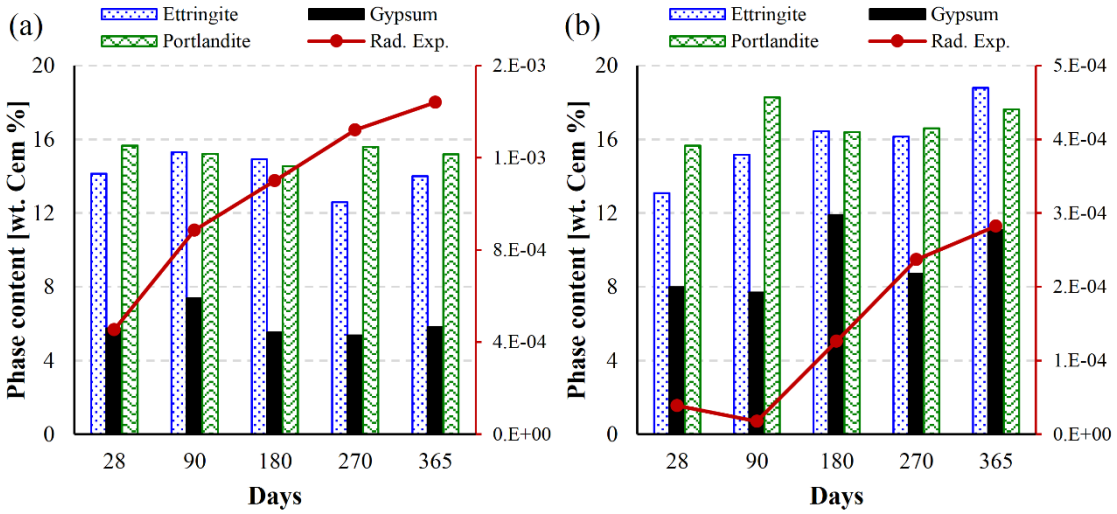

Fig. 10. Evolution of XRD results and radial expansions for (a) 0.45_12.4% and (b) AE0.45_18.8%.

ESA-related expansions have been traditionally attributed to the additional volume generated by ettringite formation. Therefore, dimensional variations should imply the precipitation of expansive phases. However, the results obtained depicts no clear link between these two variables. This is in agreement with other studies of the literature [30-32] that did not find any clear correlation between the amount of ettringite formed and the expansions observed. Amongst the other possible ESA expansion mechanisms that have been suggested in the literature [33], the crystallization pressure theory might be the only one that could explain the results obtained.

This theory states that expansions are originated from the crystallization pressure developed by ettringite formation in a supersaturated pore solution [34-36]. According to this theory, only ettringite formed in small pores is likely to generate enough pressure to cause damage [31]. During the initial stages of exposure, there is rapid increase of sulfate content in the pore network causing the early precipitation of expansive phases. Due to the extremely high concentration of sulfates and the inability to generate enough ettringite to reduce the degree of supersaturation in regions with a very refined matrix, there is a crystallization pressure boost at these locations. This pressure is responsible for the degradation and damage observed during the first stage of the attack (Figures 5 and 7). At later stages, due to a lower penetration rate caused by the pore filling effect, this excess of sulfate ions can be allocated

to other locations, more thermodynamically stable. Consequently, the crystallization pressure decreases. This phenomenon is reflected on the macro-scale by a reduction of the expansions and degradation rates, as observed in Figures 5 and 7.

In the case of AE0.45_18.8%, the absence of expansions during the initial stage might be explained by the large availability of locations to accommodate the initial ettringite precipitated and sulfate excess without developing high crystallization pressures. Unlike more refined matrices, the mortars with air-entrainer do not experience a significant reduction of sulfate penetration due to the pore filling effect (Figure 1). Consequently, sulfate content keep increasing at a steady rate until crystallization pressures start to develop at some locations of the matrix. This phenomenon might explain the slight expansion and degradation observed after 150 days of exposure (Figures 5 and 7).

3.2.2 Characterization of the pore structure

This section presents the results of a comprehensive analysis of the pore size distribution performed by MIP tests at 14, 28, 90, 180 and 270 days to obtain a qualitative picture of the evolution of the pore network throughout the attack. Figure 11 shows the evolution of the total volume of mercury intruded and MIP porosity for all mortars under sulfate exposure. As expected, the volume intruded and porosity increase with increasing water/cement ratio and addition of air-entrainer. Initial porosities at 14 days range between 8.1 % and 13.7 % for mortars with water/cement ratio between 0.38 and 0.55. In mortars with air-entrainer, porosities of 18.8 % are observed as consequence of the inclusion air bubbles.

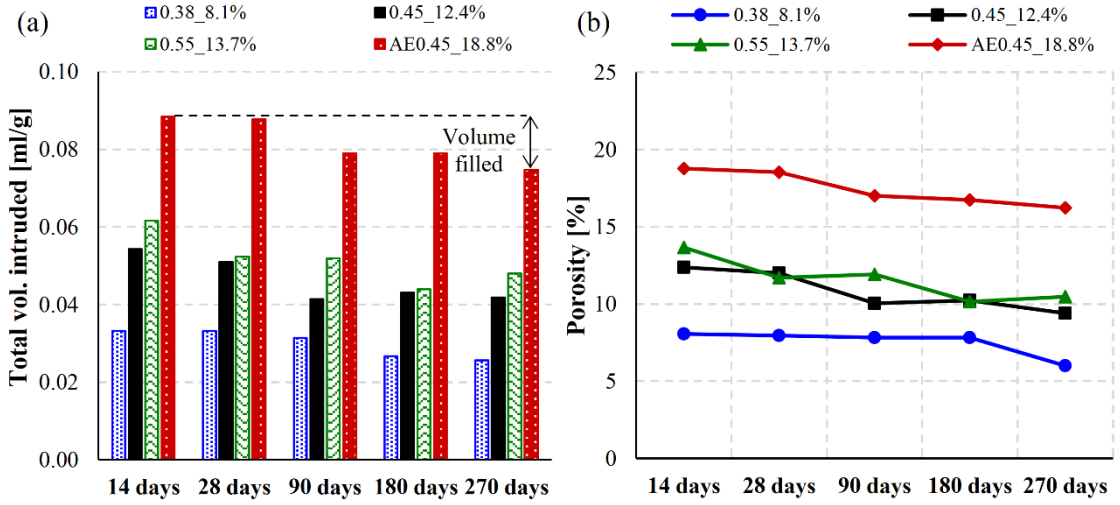

Fig. 11. (a) Total volume of mercury intruded and (b) MIP porosity for all compositions.

As the attack proceeds, mercury intruded and porosity decrease as a result of normal cement hydration processes and the precipitation of expansive phases in the pore network. The difference between the total volume intruded at 14 and 270 days allows the assessment of the pore volume filled by these two phenomena in each composition. Mortars with higher porosity (0.55_13.7% or AE0.45_18.8%) display 1.8 times more pore volume filled than the composition 0.38_8.1%. This result suggests that both cement hydration and precipitation of expansive phases are more significant in compositions with higher porosities, which is in agreement with the XRD results described in Figure 9.

However, the assessment of the fraction of volume filled from the initial total pore volume depicts different trends. In this case, 0.38_8.1% mortars show 1.5 times more ratio of

volume filled than AE0.45_18.8% between 14 and 270 days. This result suggests that despite mortars with refined pore networks present lower precipitation of expansive phases and slower cement hydration, the volume filled represents a higher fraction of the total volume available. Therefore, in these compositions the pore filling effect is more significant. These trends are in agreement with the visual inspection of the specimens described in section 3.1.1.

Figure 12 shows the evolution of the critical pore diameter for 0.38_8.1%, 0.45_12.4% and 0.55_13.7% under sulfate exposure at 14, 28, 90, 180 and 270 days. This semi quantitative parameter can be usually related to the permeability of the material [17]. Results for AE0.45_18.8% series are not included as the air bubbles produce high increments of intrusion in large diameters which distort the assessment and hinder comparison with the other compositions.

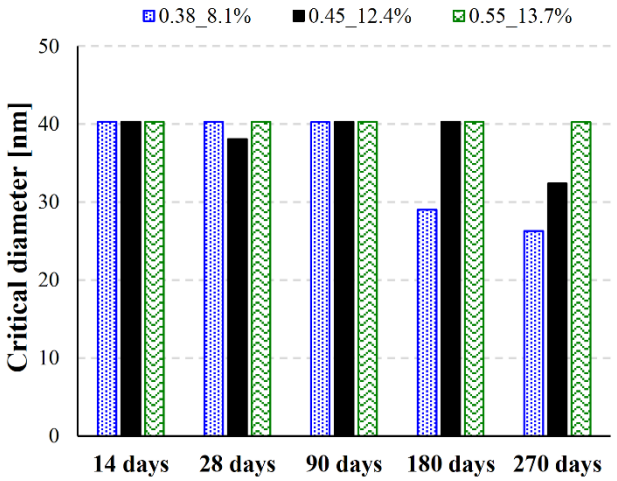

Fig. 12. Critical diameter evolution.

Despite the differences in porosity, mortars without air-entrainer present similar critical diameters until 90 days of exposure. After that, mortars with low water/cement ratios display an important reduction of critical diameter. At the end of the period evaluated, this trend becomes even more evident. The inability of the critical diameter to capture differences in the permeability during the early stages of the attack might be explained by the fact that this parameter does not account for the most accessible path for fluid transport in the cement paste but the mean pore size that allows maximum percolation. Results suggest that these pores might only be affected at late stages of the attack, when the most accessible paths are reduced due to the pore filling effect and the formation of the thin layer described in section 3.1.1.

Figure 13 shows the evolution of the pore size distribution of all mortars according to 5 predefined pore ranges (<10 nm, 10-50 nm, 50-100 nm, 100-500 nm and >500 nm). This figure depicts how sulfate exposure alters the pore size distribution of the material and allows a qualitative assessment of the precipitation patterns amongst the different compositions. The evolution of the different pore ranges between 14 and 270 days shows similar trends for the mortars without air-entrainer. For these compositions, the refinement of the pore network during the attack is mainly caused by the reduction of pores between 50 – 100 nm. This pore range accumulates the 63.0 %, 66.4 % and 58.2 % of the total volume filled by the combined action of cement hydration and precipitation of expansive phases in 0.38_8.1%, 0.45_12.4% and 0.55_13.7%, respectively. However, AE0.45_18.8% series only accumulates the 31.1 %

of the volume filled in this pore range. In this case, the main reduction of intrusion is observed in pores of 100 - 500 nm, which concentrate the 60.4 % of the reduction.

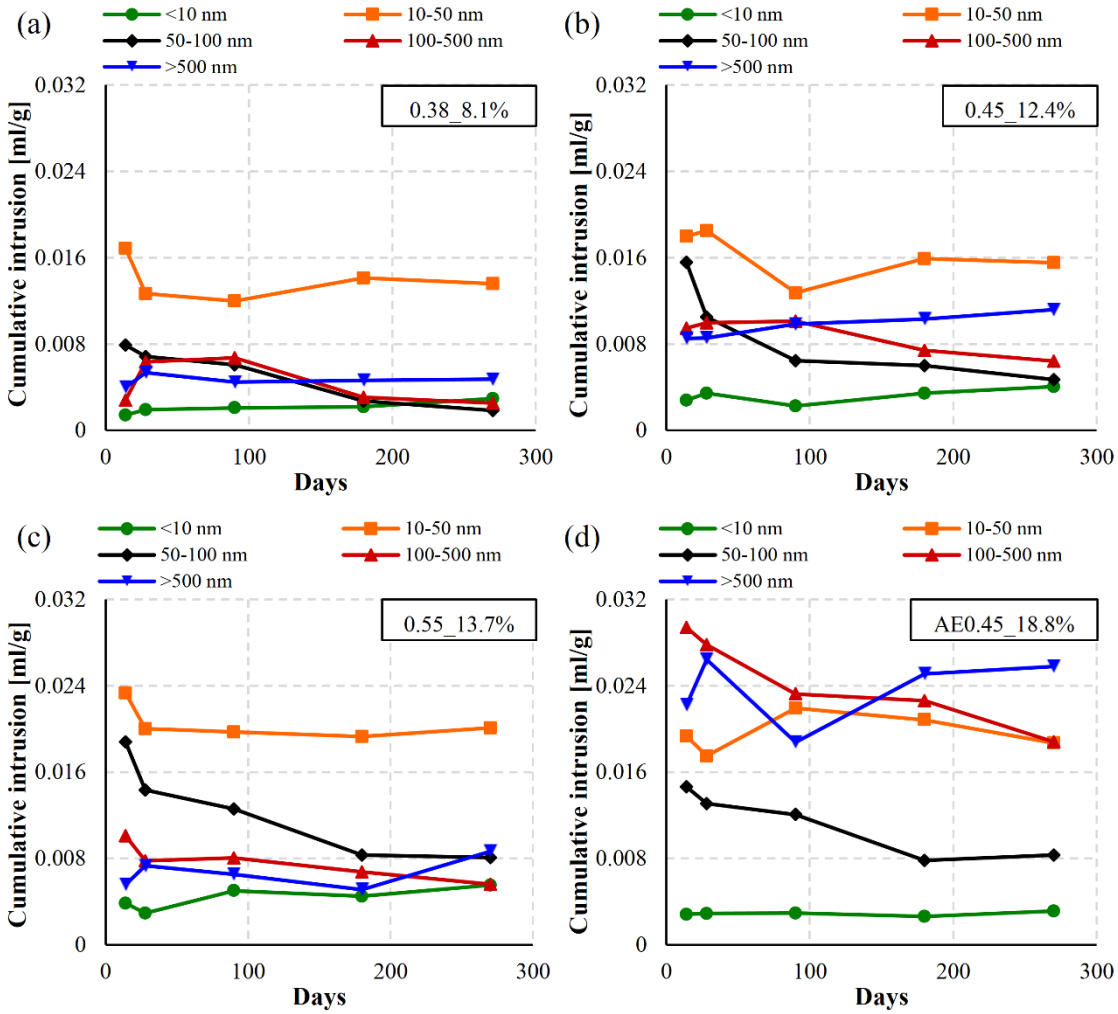

Fig. 13. Evolution of pore size distribution for (a) 0.38_8.1%, (b) 0.45_12.4%, (c) 0.55_13.7% and (d) AE0.45_18.8%.

Although the pore sizes measured in the MIP technique do not necessarily match the real pore sizes of the material, the qualitative analysis of the results highlights that the pore sizes affected during ESA vary depending on the characteristics of the pore system of the matrix. Results indicate that in mortars with air-entrainer, the alterations in the pore network are produced in bigger pore ranges than the observed in other compositions. The bigger pores of AE0.45_18.8 act as pressure releases that limit the pressure increase of the system, especially in smaller pores. This pressure release effect combined with the capacity to accommodate expansive phases might explain the lower degrees of damage observed in AE0.45_18.8.

4. CONCEPTUAL MODEL OF THE ROLE OF POROSITY

The approach adopted in the codes to obtain durable materials against the ESA is based on a fairly simple perception of the role of the porosity. It assumes that the amount of ettringite precipitated defines the damage generated in the material. Therefore, codes prescribe materials with low permeability to reduce the penetration of sulfate ions. However, this study

shows that the amount of expansive phases itself is not always a good indicator of the level of deterioration. Sometimes, other aspects such as the location of the precipitation and the presence of pressure release pores might play a more significant role in the outcome of the attack.

The results obtained in this study highlight two mechanisms defined by the pore network that contribute to the resistance against the ESA: the permeability, which is related to the amount of expansive phases potentially generated, and the damping capacity, which might define the preferential location of the precipitation of expansive products. The overall ESA resistance defined by the pore network is the result of the contribution of these two mechanisms. Since the pore network characteristics do not remain constant over time (due to cement hydration and pore filling effect), the contribution of these two mechanisms also varies during the attack.

Figure 14 represents this phenomenon in a schematic way. A material with low porosity achieve high durability by the low permeability of the matrix, which hinder sulfate ingress and potential ettringite precipitation. As porosity increases, sulfate penetration is promoted, thus reducing the durability of the material. On the other hand, the damping curve shows an opposite trend. In this case, ESA resistance increases for high values of porosity due to a preferential precipitation in large pores and decreases along the refinement of the pore network.

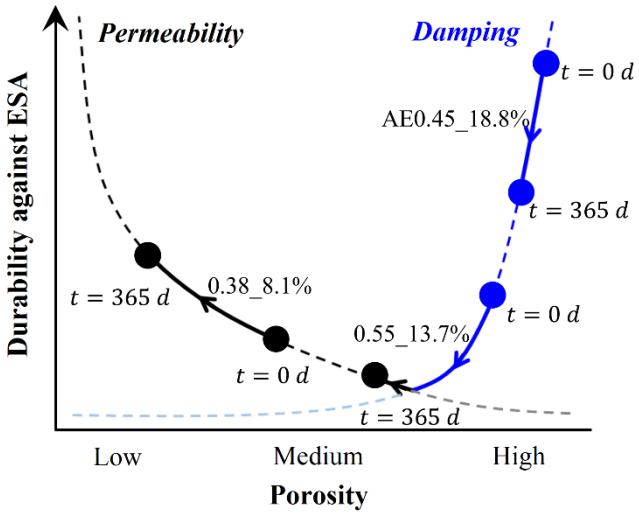

Fig. 14. Contribution of permeability and damping in the ESA durability.

Figure 14 includes a qualitative location of 0.38_8.1%, 0.55_13.7% and AE0.45_18.8% based on the porosity of these compositions. 0.45_12.4% is not depicted for clarity in the interpretation of the graph. At early stages of the attack, 0.38_8.1% presents the lowest durability, which is reflected by displaying the largest expansions amongst the compositions evaluated (Figure 5). As time proceeds, the durability of this composition improves due to a reduction of porosity, which results in a decrease of the expansion rate.

On the other hand, the mortar with air-entrainer initially presents the highest durability due to the large damping capacity of the matrix (no expansions measured). Despite durability decreases over time as the precipitation of expansive phases reduces the buffer capacity, this composition keeps displaying the highest potential durability against ESA at the end of the test. Conversely, 0.55_13.7% mortars display a half-way behavior with an initial stage characterized by a pore system that is capable of accommodating part of the

expansive phases. A decrease of the durability is caused by the precipitation of expansive phases that reduces the damping effect of the porosity.

5. CONCLUSIONS

This study assess the mechanisms defined by the pore network that determine the resistance against the ESA. The following specific findings may be derived from this study.

(1)- The evolution of expansion over time is characterized by an initial stage in which the damping capacity of the pore structure defines the damage developed by the ESA. After that, the transport process affected by the precipitation of expansive phases controls the durability. Results indicate that the duration of the first stage can be extended if sufficient amount of large pores is available in the material.

(2)- The analysis of the ultrasonic pulse velocity shows lower relative damage levels as the porosity of the matrices increases. Mortars with air-entrainer displayed the lowest variation in the ultrasonic pulse velocity over time being possibly characterized by the smallest damage level amongst all compositions tested here.

(3)- Quantitative XRD analyses show no direct relationship between the measured expansions and the amount of expansive product formed during any stage of the attack. In fact, the biggest precipitation of expansive phases was found in the composition with air-entrainer that presents the smallest expansions.

(4)- The pore system might influence the precipitation patterns of the expansive phases. MIP results suggest that the low expansion and damage in mortars with air-entrainer is explained by a preferential precipitation of expansive phases in large pores, which dumps the pressure increase of the pore system and accommodates expansive phases without causing damage.

(5)- Results indicate that it might be possible to obtain a durable material against ESA by solely increasing the capacity of the matrix to accommodate expansive product. The design of durable materials against the ESA based on high damping capacities should be made with caution. In these cases, the durability tends to decrease with time since the pore filling effect has a negative impact on the damping capacity of the matrix. On the other hand, the approach based on low permeability is safer as the pore filling effect developed over time has a positive impact on the permeability.

ACKNOWLEDGMENTS

Support from the Spanish Ministry of Economy and Competitiveness through research project BIA2013-49106-C2-1-R is greatly acknowledged. T. Ikumi is supported by the fellowship program FPI BES-2014-068524 of the Spanish Ministry of Economy and Competitiveness.

REFERENCES

[1] P.K. Mehta, Sulfate attack on concrete—a critical review, Mater. Sci. Concr. III, Am. Ceram. Soc., Westerville, (1992) 105-130.

[2] J.P. Skalny, I. Odler, J. Marchand, Sulfate Attack on Concrete, Spon, London, 2001.

[3] P.J.M. Monteiro, K.E. Kurtis, Time to failure for concrete exposed to severe sulfate attack, Cem. Concr. Res. 33 (2003) 987-993.

[4] F.P. Glasser, J. Marchand, E. Samson, Durability of concrete — Degradation phenomena involving detrimental chemical reactions, Cem. Concr. Res. 38 (2008) 226-246.

[5] A. Çavdar, S. Yetgin, Investigation of mechanical and mineralogical properties of mortars subjected to sulfate, Constr. Build. Mater. 24 (2010) 2231-2242.

[6] R. El-Hachem, E. Rozière, F. Grondin, A. Loukili, Multi-criteria analysis of the mechanism of degradation of Portland cement based mortars exposed to external sulphate attack, Cem. Concr. Res. 42 (2012) 1327-1335.

[7] W. Piasta, J. Marczewska, M. Jaworska, Durability of air entrained cement mortars under combined sulphate and freeze-thaw attack, Procedia Eng. 108 (2015) 55-62.

[8] R. Tixier, B. Mobasher, Modeling of Damage in Cement-Based Materials Subjected to External Sulfate Attack. I: Formulation, J. Mater. Civ. Eng. 15 (2003) 305–313.

[9] T. Ikumi, S.H.P. Cavalaro, I. Segura, A. de la Fuente, A. Aguado, Simplified methodology to evaluate the external sulfate attack in concrete structures, Mater. Des. 89 (2016) 1147-1160.

[10] I. Oliveira, S.H.P. Cavalaro, A. Aguado, New kinetic model to quantify the internal sulfate attack in concrete, Cem. Concr. Res. 43 (2013) 95–104.

[11] T. Ikumi, S.H.P. Cavalaro, I. Segura, A. Aguado, Alternative methodology to consider damage and expansions in external sulfate attack modeling, Cem. Concr. Res. 63 (2014) 105-116.

[12] N.N. Naik, A.C. Jupe, S.R. Stock, A.P. Wilkinson, P.L. Lee, K.E. Kurtis, Sulfate attack monitored by microCT and EDXRD: Influence of cement type, water-to-cement ratio, and aggregate, Cem. Concr. Res. 36 (2006) 144-159.

[13] M. Santhanam, M.D. Cohen, J. Olek, Mechanism of sulfate attack: A fresh look Part 1: Summary of experimental results, Cem. Concr. Res. 32 (2002) 915-921.

[14] M. Santhanam, M.D. Cohen, J. Olek, Mechanism of sulfate attack: a fresh look Part 2. Proposed mechanisms, Cem. Concr. Res. 33 (2003) 341-346.

[15] A.E. Idiart, C.M. López, I. Carol, Chemo-mechanical analysis of concrete cracking and degradation due to external sulfate attack: A meso-scale model, Cem. Concr. Compos. 33 (2011) 411-423.

[16] R. El-Hachem, E. Rozière, F. Grondin, A. Loukili, New procedure to investigate external sulphate attack on cementitious materials, Cem. Concr. Compos. 34 (2012) 357-364.

[17] I. Segura, Caracterización del proceso de descalcificación en morteros, mediante ensayos destructivos y no destructivos, PhD Thesis, ETSICCP, Madrid, 2008.

[18] D. Jansen, F. Goetz-Neunhoeffer, C. Stabler, J. Neubauer, A remastered external standard method applied to the quantification of early OPC hydration, Cem. Concr. Res. 41 (2011) 602-608.

[19] D. Jansen, C. Stabler, F. Goetz-Neunhoeffer, S. Dittrich, J. Neubauer, Does Ordinary Portland Cement contain amorphous phase? A quantitative study using an external standard method, Powder Diffract. 26 (2011) 31-38.

[20] R. Snellings, A. Bazzoni, K. Scrivener, The existence of amorphous phase in Portland cements: Physical factors affecting Rietveld quantitative phase analysis, Cem. Concr. Res. 59 (2014) 139-146.

[21] A.G. de la Torre, S. Bruque, J. Campo, M.A.G. Aranda, The superstructure of C3S from synchrotron and neutron powder diffraction and its role in quantitative analysis, Cem. Conc. Res. 32 (2002) 1347-1356.

[22] W.G. Mumme, R.J. Hill, G.W. Bushnell, E.R. Segnite, Rietveld crystal structure refinements, crystal chemistry and calculated powder diffraction data for the polymorphs of dicalcium silicate and related phases, N. Jb. Miner. Abh. (J. Min. Geochem.) 169 (1995) 35-68.

[23] H.E. Petch, The hydrogen positions in portlandite, Ca(OH)2, as indicated by the electron distribution, Acta Crystallogr. 14 (1961) 950-957.

[24] R. Wartchow, Datensammlung nach der ‘‘learnt profile”-methode(LP) für calcit und vergleich mit der ‘‘background peak background”-methode (BPB), Z. Kristallogr. 186 (1989) 300-302.

[25] F. Goetz-Neunhoeffer, J. Neubauer, Refined ettringite structure for quantitative X-ray diffraction analysis, Powder Diffr. 21 (2006) 4-11.

[26] W.A. Wooster, On the crystal structure of gypsum CaSO4(H2O)2, Z. Kristallogr. 94 (1936) 375-396.

[27] A.A. Colville, S. Geller, The crystal structure of brownmillerite, Ca2FeAlO5, Acta Crystallogr. B 27 (1971) 2311-2315.

[28] L. Levien, C.T. Prewitt, D.J. Weidner, Structure and elastic properties of quarz at pressure, Am. Mineral. 65 (1980) 920-930.

[29] E.N. Maslen, V.A. Streltsov, N.R. Streltsova, N. Ishizawa, Y. Satow, Synchrotron X-ray study of the electron density in alpha-Al2O3, Acta Crystallogr. B 49 (1993) 973-980.

[30] R.S. Gollop and H.F.W. Taylor, Microstructural and microanalytical studies of sulfate attack III. Sulfate-Resisting Portland cement: Reactions with sodium and magnesium sulfate solutions, Cem. Concr. Res. 25-7 (1995) 1581-1590.

[31] W. Müllauer, R.E. Beddoe, D. Heinz, Sulfate attack expansion mechanisms, Cem. Concr. Res. 52 (2013) 208-215.

[32] W. Kunther, B. Lothenbach, K. Scrivener, On the relevance of volume increase for the length changes of mortar bars in sulfate solutions, Cem. Concr. Res. 46 (2013) 23-29.

[33] P. Brown, H. Taylor, The role of ettringite in external sulfate attack, in: J. Marchand, J. Skalny (Eds.), Materials Science of Concrete Special Volume: Sulfate Attack Mechanisms, The American Ceramic Society, 1999, 73-98.

[34] G.W. Scherer, Stress from crystallization of salt, Cem. Concr. Res. 34 (2004) 1613-1624.

[35] R.J. Flatt, G.W. Scherer, Thermodynamics of crystallization stresses in DEF, Cem. Concr. Res. 38 (2008) 325-336.

[36] C. Yu, W. Sun, K. Scrivener, Degradation mechanism of slag blended mortars immersed in sodium sulfate solution, Cem. Concr. Res. 72 (2015) 37-47.

4.2. JOURNAL PAPER V. EFFECTS OF CONFINEMENT IN MORTARS EXPOSED TO EXTERNAL SULFATE ATTACK

Submitted to Cement and Concrete Research in Jan. 2017.

Tai Ikumi[a,*], Ignacio Segura[a,b], Sergio H.P. Cavalaro[a,*]

[a] Department of Civil and Environmental Engineering, Universitat Politècnica de Catalunya Barcelona Tech, Jordi Girona 1-3, C1, E-08034 Barcelona, Spain
[b] Smart Engineering, Jordi Girona 1-3 K2M 202c, Barcelona, Spain

* Corresponding authors: Department of Civil and Environmental Engineering, Universitat Politècnica de Catalunya Barcelona Tech, Jordi Girona 1-3, C1, E-08034 Barcelona, Spain. Email addresses: tai.ikumi@upc.edu (T. Ikumi), sergio.pialarissi@upc.edu (S.H.P. Cavalaro), Tel: +34 93 401 6507 Fax: +34 93 401 1036.

Abstract

Research on external sulfate attack (ESA) is usually performed on small scale specimens under free expanding conditions. However, most field structures cannot expand freely due to confinement induced by the ground or other elements from the structure. As a result, ESA usually develops in confined conditions. This work aims to assess the interaction of stresses generated by confinement with the ESA. Visual appearance, mass and ultrasonic velocity were monitored to characterize the macro-scale behavior of free and restrained mortar samples. Changes on phase composition and crystal morphology induced by confinement were evaluated by X-Ray diffraction and scanning electron microscopy. The confining stresses generated were estimated during the attack. Results indicate that confinement reduces the degradation caused by the ESA by delaying or reducing micro-cracking, which limits sulfate penetration and reduces ettringite formation. Moreover, SEM images and a conceptual framework developed on supersaturation suggest that confinement may reduce the amount of crystals growing in confined conditions.

Keywords: Concrete (E); Durability (C); Sulfate attack (C); Ettringite (D); Confinement

1. INTRODUCTION

External sulfate attack (ESA) is a degradation process that affects concrete structures. It is caused by the interaction between the reactive phases of the cement paste and sulfate ions from an external source. The continuous sulfate exposure may lead to cracking, spalling, softening and disintegration. Fortunately, in typical service conditions the attack usually develops during decades before causing high degrees of damage.

The majority of common methods to investigate the resistance of cement-based materials exposed to sulfates are based on accelerated tests to obtain representative results in a reasonable time (e.g. ASTM C1012 or ASTM C452). These test methods assess the sulfate resistance by length change measurements of unconfined specimens submerged in sulfate rich solutions. As a result, most research carried out in this field use free expansions as the main degradation parameter. However, typical elements exposed to ESA, such as foundations or retaining walls, can rarely expand freely during sulfate exposure. Instead, these elements are subjected to a wide variety of external loads and to different degrees of confinement due to interactions with other elements of the structure and the soil.

Most studies dealing with the coupled action of external loads and ESA apply a constant flexural or compressive load since sulfate exposure [1-9]. In general, flexural loading applied together with the sulfate exposure resulted in negative effects on the durability against the attack, especially when the loading exceeded 40-60 % of the maximum flexural load [7,8]. R. Gao et. al [7] reported more serious deterioration of the face subjected to tensile stresses than the one subjected to compressive stresses. According to the authors [7], the tensile stresses might accelerate the sulfate attack due to micro-cracks that promote sulfate penetration.

Fewer studies are available in the literature dealing with the combined action of sulfate attack and compressive loading [1-3,9]. This is probably caused by the higher complexity of the experimental set up. In general, studies report favorable effects on the durability against the attack for low stress levels, as it might slow down the sulfate ingress into concrete. However, compressive stresses seems to accelerate the sulfate attack when the stress is set above a certain threshold value, estimated between the 30-60 % of the ultimate compressive strength. This acceleration is attributed to the generation of micro-cracks that promotes sulfate penetration [1-3,9].

In all studies presented above, the load was applied from exposure and remained constant until the end of the test. Although this configuration might simulate the effects of underground water, rocks, overlaying soil or dead loads from the superstructure, it does not represent the effects of confinement that might appear in indeterminate structures. In this case, the load rises as a consequence of the expansions generated by the ESA, thus increasing gradually along the attack. Figure 1 illustrates this situation with a group of end bearing piles joined at the top by a pile cap. Due to the heterogenic characteristics of the groundwater level and the distribution of gypsum veins in the soil, the expansions generated by the attack (ε_{ESA}) evolve at different rates at each pile. However, highly indeterminate structures act as a single entity prior to failure. Consequently, the least affected elements (pile 2 and 3) restraint the expansions and confine the concrete of pile 1 by applying a gradual compressive load (F_c) in the whole section.

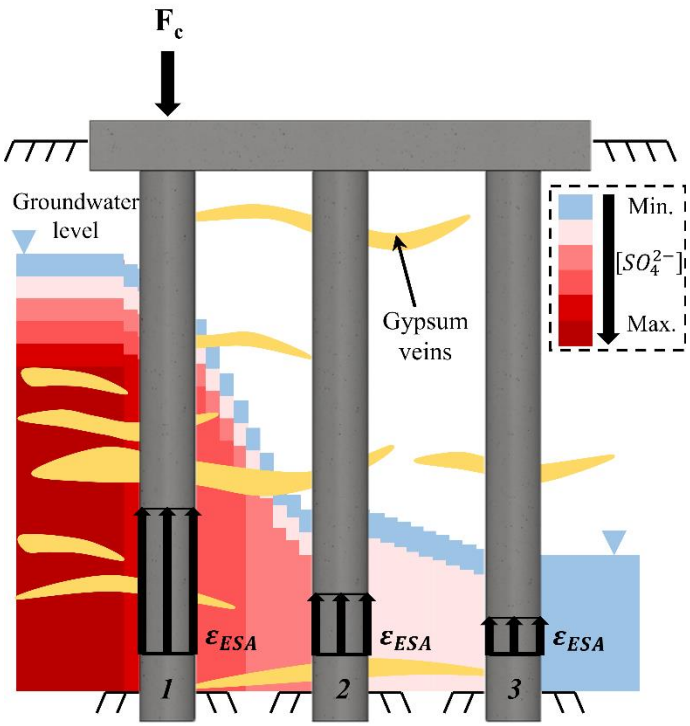

Fig. 1. Schematic representation of a group of end bearing piles under ESA.

Previous research on the interaction between constant compressive loads and ESA [1-3,9] suggests that the effects of confinement will probably depend on the stress level. Therefore, for a precise assessment of this phenomenon, it is necessary to link the different behavior of confined and free specimens with the stress level applied. The monitoring of the confining stresses generated during the attack requires complex experimental set ups. Only one study was found in the literature able to capture this phenomenon [10]. Mullauer et. al [10] applied different degrees of confinement to thin-walled mortar cylinders exposed to sulfates by a specially constructed stress cell. Even though the main objective was to estimate the stresses generated during the attack, it indirectly pointed some possible positive effects of confinement on the durability. Evolution of the phase composition with and without confinement showed that both ettringite and gypsum were partially suppressed at late stages of the attack by increasing the degree of confinement.

Understanding how stresses generated by confinement interact with ESA is not only relevant in highly indeterminate structures such as the one represented in Figure 1. ESA frequently only affects the external layers of the cross section. The sound core of the element restraints the expansions and confines the external layers in order to ensure equilibrium and compatibility of strains in the section. As a result, almost all elements exposed to the ESA are under a certain degree of confinement. Unfortunately, the potential effects of stresses generated by confinement remain practically unexplored and are usually ignored during the assessment of the ESA. The present work aims to shed light on this phenomenon and identify which processes (ionic transport, phase composition or crystal morphology) might be altered by the confining stresses.

One of the key aspects to study this phenomenon is the experimental set up adopted to generate the confinement. In this work, the confinement is achieved by casting mortar specimens in the shape of flattened cylinders within metallic rings. To increase the

representativeness of this study, 6 mortar compositions with different expansive potentials are considered to induce varying magnitudes of confining stresses. Stresses are estimated by the monitoring of expansions in restrained specimens throughout the attack. Visual appearance, mass and ultrasonic velocity variations are used to characterize the macro-scale behavior of free and restrained samples. Changes on phase composition and crystal morphology are evaluated by X-Ray diffraction with Rietveld refinement and scanning electron microscopy with energy dispersive X-ray analysis, respectively.

This study describes how the confined conditions in which ESA usually develops reduce the deleterious effects associated to the attack. The understanding of the positive effects of confinement could lead to more realistic assessments of the ESA and contribute to explain the large difference between the damage developed in small-scale free-expanding laboratory specimens and the one observed in real structures.

2. EXPERIMENTAL PROGRAM

2.1 MATERIALS AND MIXTURE CHARACTERISTICS

Materials and mixture characteristics were defined to obtain mortars with different expansion rates to assess the effects of confinement over a wide range of confining stresses. Two different Portland cements were used as binders: ordinary CEM I 52.5R (OPC) and sulfate-resisting CEM I 42.5 R-SR5 (SRPC). Moreover, a low-calcium fly ash (ASTM C618 class F) and the air-entrainer MasterAir 100 were incorporated in some dosages. Table 1 shows the chemical and mineralogical composition of the binders and summarizes the physical properties. Chemical composition was determined by XRF spectrometry and mineralogical composition was estimated by Bogue equations. Data provided by Bogue equations is only used qualitatively to classify the cements. Due to the presence of ferromagnetic particles, the elemental composition of the fly ash was determined by ICP-MS. Deionized water and siliceous sand following the specifications of UNE-EN 196-1:2005 were used in all mortars. Commercial superplasticizer GLENIUM ACE 456 was added to the mixtures.

The composition of the 6 matrices used in this study are listed in Table 2. Mortars with high expansive potentials were produced by using OPC with varying water/cement ratios (from 0.38 to 0.55) and the use of an air-entrainer to promote sulfate penetration. Fly ash was incorporated in one composition to obtain a highly refined pore network. Volumetric variations caused by the different water/cement ratios considered and the use of fly ash were fully compensated by a reduction of sand, maintaining a constant amount of cement in all compositions. The slight increase of volume produced by the air-entrainer was not taken into account. On the other hand, a dosage with SRPC was designed to assess the behavior of low expansive mortars under confined conditions. The nomenclature adopted for each composition follows the pattern ‘cement type’_‘water/cement ratio’. Mortars with air-entrainer or fly ash have the term ‘AE’ or ‘FA’ after the cement type, respectively.

The mixing procedure defined in UNE-EN 196-1:2005 was adopted. In the case of the composition with fly ash, the latter was first thoroughly mixed with cement prior to water addition. The air-entrainer was added at the end of the mixing procedure and mixed at high speed for 60 s. To assure similar surface finish qualities and workability amongst the different compositions, superplasticizer was mixed with the deionized water to obtain flow extents of 20 cm ± 0.5 cm.

Table 1. Properties of binders.

	OPC[a]	SRPC[b]		FA[c]
Chemical comp. [% bcw[d]]			*Elemental comp. [%]*	
SiO_2	19.50	20.80	Si	23.56
Al_2O_3	5.90	4.00	Al	8.74
Fe_2O_3	1.70	4.00	Fe	6.92
CaO	63.10	62.70	Ca	3.70
MgO	2.10	1.70	Mg	0.50
SO_3	3.50	3.02	S	0.20
K_2O	0.78	0.55	K	0.55
Na_2O	0.35	0.24	Na	-
Cl^-	0.02	0.01	P	0.11
MnO	-		Mn	0.01
TiO_2	-		Ti	0.28
Physical prop.				
Spec. surf. area (BET) [m^2/g]	1.10	1.16		1.56
d_{10} [µm]	0.58	0.57		2.08
d_{50} [µm]	6.88	7.29		8.97
d_{90} [µm]	31.84	34.92		29.21
Phase comp. [% bcw[d]]				
C_3S	65.4	62.1		
C_2S	10.6	15.6		
C_3A	12.3	4.1		
C_4AF	5.6	13.6		

[a]: Ordinary Portland cement, [b]: Sulfate-resisting Portland cement, [c]: Fly ash and [d]:By cement weight.

Table 2. Compositions and mass attenuation coefficient (MAC) of the mortars.

Material	OPC_0.38	OPC_0.45	OPC_0.55	OPC+AE_0.45	OPC+FA_0.45	SRPC_0.45
Cement [kg/m^3]	580	580	580	580	580	580
Sand [kg/m^3]	1425	1325	1180	1325	1140	1330
Water [kg/m^3]	220	261	319	261	261	261
Water/cement ratio	0.38	0.45	0.55	0.45	0.45	0.45
Air-entrainer [% bcw]	-	-	-	0.3	-	-
Fly ash [% bcw]					30	
Superplasticizer [% bcw]	1.00	0.35	-	0.25	0.55	0.20
MAC [cm^2/g]	48.11	48.01	47.84	48.01	49.15	48.98

2.2 EXPERIMENTAL PROCEDURE

2.2.1 Specimen preparation

Specimens traditionally used for the assessment of the ESA consist of slender prisms with low volume to surface ratios to maximize sulfate ingress and facilitate measurement of expansions. However, the generation of confinement in samples with such geometric characteristics submerged in aggressive solutions requires complex devices with limited accuracy and replicability [1-3,9].

In this work, mortars specimens of 78 mm of diameter and 17 mm of height were used. This configuration allows easier expansion restraint by casting the sample within a metallic ring. The dimensions of the mortar specimens were defined to maintain similar exposed surface-volume ratio than other studies that showed good balance between test

duration and representativeness [11]. Steel rings were laser cut from a duplex stainless steel 2205 (EN 1.4462) seamless pipe of 3" SCH. 40s. This material was used for its high strength and resistance to local and uniform corrosion in aggressive environments. Thickness and material properties of the steel ring were chosen to obtain high degrees of restraint in order to maximize the confining stresses applied to the mortar and to avoid onset of inelastic deformations on the steel.

Figure 2a and 2b depicts a schematic representation of the molds and the casting process adopted. The molds were composed by a PE rigid base with 4 fixed PVC or steel molds with the same inner diameter and a moving PE rigid cover. The mortar (represented in light hatching) was poured inside the PVC or steel molds and compacted with 15 jolts in the flow table (ASTM C1437) at a rate of 1 jolt per second to eliminate air pockets. 5 bolts were used to guide the cover into the base during assembly (Figure 2b). In order to ensure adequate surface finish quality, the molds were then vibrated during 10 seconds at the vibration table. Notice that these molds allowed the casting of both free and restrained specimens by following the same procedure. By that, mortars in both configurations reached similar initial mixture properties and surface finish qualities.

Specimens were demolded 24 hours after casting. Specimens in free conditions were extracted from the PVC molds and their lateral faces were water sealed with the flexible epoxy coating MasterSeal M 338 to ensure similar penetration of the sulfate ions than in restrained specimens and to avoid corner spalling (Figure 2c). Specimens in restrained conditions were not coated since the steel ring surrounding the mortar prevents the sulfate ingress from the lateral faces of the specimen (Figure 2d).

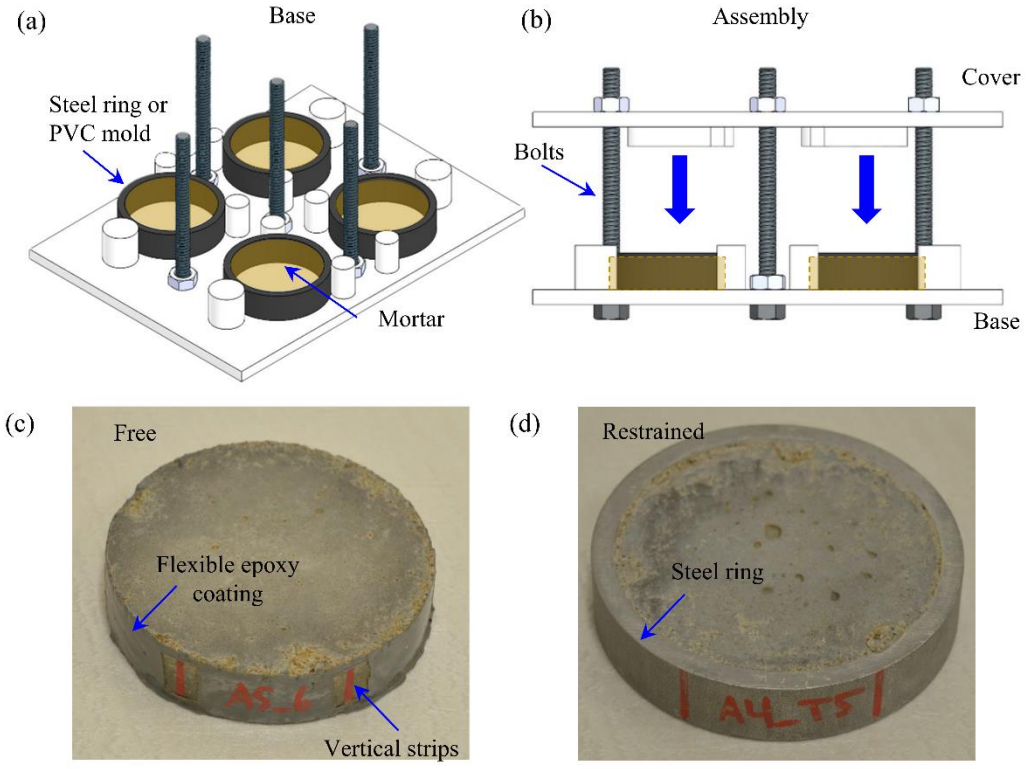

Fig. 2. Schematic representation of (a) the molds and (b) the casting process. Detail of (c) free and (d) restrained specimens.

2.2.2 Exposure conditions

All specimens were cured in water at 25 ºC ± 1 ºC for one day to ensure full saturation of the samples prior to sulfate exposure. Two days after casting, specimens were exposed to two different sodium sulfate solutions (3 and 30 g of Na_2SO_4/l). The sulfate concentration of 3 g/l corresponds to the upper limit of the moderately aggressive class of exposure defined in EN 206-1, whereas 30 g/l corresponds to 10 times the typical values found in the field conditions [12]. The early exposure was adopted to reproduce the conditions of structures build *in situ* and to accelerate the attack [12]. The age of sulfate exposure is considered as day 0 in the analysis of the results. The solution was renewed weekly during the first month and every other week until the end of the test at 365 days. The volumetric ratio of sulfate solution to mortar was 12.

Water pumps were used at low speed to ensure a continuous flow from the bottom to the top of the container in order to minimize concentration gradients. The containers were filled up to the top and covered to reduce contact with the air, thus limiting CO_2 dissolution and carbonation. Reference samples of each composition with and without confinement rings were exposed to non-aggressive curing with water without sulfates for comparative purposes.

2.2.3 Confining stresses provided by the steel ring

In free expanding conditions, stresses generated by ESA are released in the form of strains. However, when the strains are restrained due to the steel ring only a fraction of the stresses generated by the attack are released in the form of expansions, while the other fraction confines the mortar with compressive stresses (σ_c). This situation is depicted in Figure 3a, where free, restrained and steel expansions are denoted as ε_f, ε_r and ε_s, respectively. The term D corresponds to the diameter of the specimen.

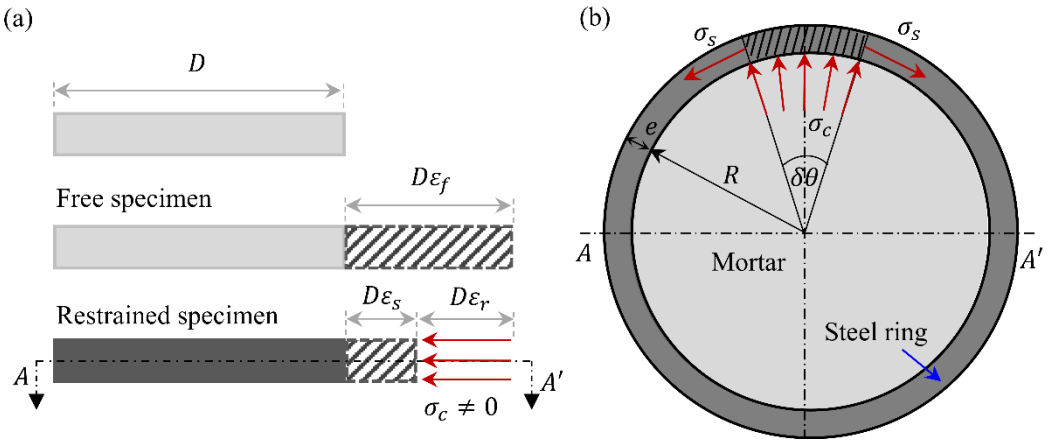

Fig 3. (a) Macroscopic strains in free and restrained specimens and (b) Ideal stress distribution in the steel ring.

Figure 3b shows the ideal stress distribution assumed to estimate the confining stresses (σ_c). As depicted, compressive stresses are balanced by tensile stresses in the steel ring (σ_s). By imposing equilibrium in the steel ring, it is possible to relate the confining stresses applied to the mortar and the strains measured in the steel ring (Eq. 1). In Eq. 1, E_s and e refers to the elastic modulus and the thickness of the steel ring, while R represents the radium of the mortar specimen (Figure 6b).

$$\sigma_c = \frac{\varepsilon_s E_s e}{R} \quad \text{(Eq. 1)}$$

The degree of confinement (DC) provided by the steel ring is defined as the ratio between the strains restrained and the free strains. It can be estimated by imposing that free expansions are the sum of the expansions measured in the steel ring and the ones restrained (Eq. 2). Final expression for the DC, expressed in %, is described in Eq. 3. In this equation E_c represents the elastic modulus of the mortar.

$$\varepsilon_f = \varepsilon_s + \varepsilon_r \quad \text{(Eq. 2)}$$

$$DC = 100\frac{\varepsilon_r}{\varepsilon_f} = 100\left(1 - \frac{E_c R}{(E_s e + E_c R)}\right) \quad \text{(Eq. 3)}$$

According to Eqs. 1 and 3, the confining stresses and DC of the restrained specimens can be estimated taking into account the geometric characteristics and the stiffness of the steel ring and mortar. Due to the importance of the Young Modulus of the steel rings for the assessment of the confining stresses generated, two tensile coupon tests were performed to precisely determine this parameter. Coupon dimensions and loading configuration are depicted in Figure 4. Strain gauges were placed on each face of the coupon specimen to measure the longitudinal tensile strains. The amplitude of the cycles depicted in Figure 4 was defined to cover the expected stress levels reached during the attack. The Young Modulus (E_s) was calculated from the slope of the strain-stress curves obtained during the 10 loading cycles. The average value obtained considering both strain gauges was 178769 MPa with a standard deviation of 10294 MPa.

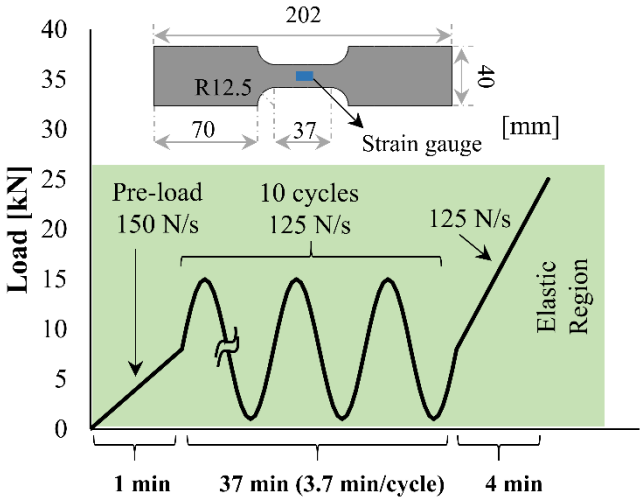

Fig 4. Loading history of tensile coupon test and coupon dimensions.

The Young Modulus of the mortar was indirectly estimated from ultrasonic pulse velocity measurements. The dynamic modulus of elasticity was calculated according to ASTM C 597-02 for the average pulse velocity measured in all restrained specimens during the attack (3328 m/s). Density and dynamic Poisson's ratio of 2150 kg/m^3 and 0.2 were assumed, respectively. The Static modulus of elasticity was estimated by considering that the dynamic modulus is 1.2 times the static modulus [13]. The final value obtained was 11906 MPa. Based on the assumptions described, the DC provided by the steel ring is 68 %. In other

words, the steel ring should restraint 68 % of the free expansions generated. Notice that the formulation presented does not consider second order effects of structurally indeterminate specimens. Creep, potential cracking and plastic effects might significantly vary the real value of the DC at the late stages of the attack. However, to simplify the calculations it is assumed that this value remains constant over the duration of the test.

2.2.4 Test methods

- Expansions and confining stresses

In this work, free and restrained expansions were used to estimate the theoretical and real confining stresses generated during the attack based on the mechanical equations described in section 2.2.3. A MICROMASTER electronic micrometer with a precision of ± 0.001 mm was used to measure the expansions (Figure 5). A metallic platform braced with the micrometer was used to fix the specimen and measured points. Several vertical strips were introduced to facilitate the measuring and to guarantee a similar position of the specimens (Figures 2c and 2d). Prior to the start of the experimental program, the precision of the equipment was evaluated on free and restrained specimens during a series of over 500 measurements. Both free and restrained specimens showed a variability of the measurements of ± 0.002 mm. This variability corresponds to ± 0.6 MPa in terms of stresses generated by confinement. Measurements were taken weekly during the first month and every other week until the end of the study. For each specimen, 3 radial directions were measured at each time (Figure 5a and 5b). Since 3 replicas were considered, each expansion value presented in this study is the average of 9 measurements.

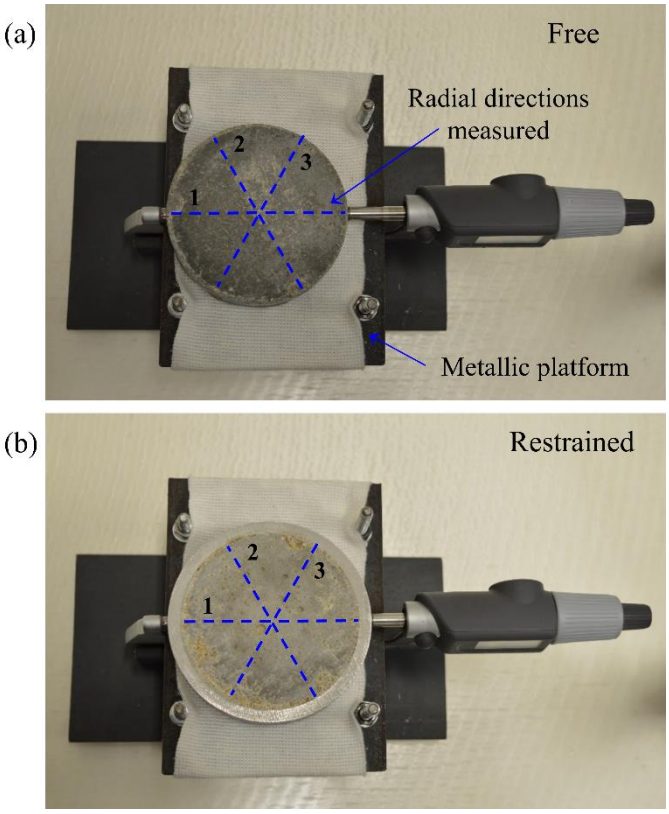

Fig. 5. Expansion measurements in (a) free and (b) restrained specimens.

- Macrostructural monitoring

Characterization of the macro-scale behavior relies upon measurements of ultrasonic velocity and mass variation and visual inspection of the specimens. Ultrasonic pulse velocity between the two exposed faces was measured at 500 kHz sampling frequency with a PUNDIT PL-200. A high frequency transducer was selected due to the low thickness of the specimens (17 mm). A zero-crossing algorithm was used to calculate the travelling time of the ultrasonic signal. The measurements were performed immediately after extraction from the solution tanks to ensure similar saturation conditions. A sample holder was used to fix the position of the measured location (the center of the specimen). Mass evolution was controlled with a precision balance of ± 0.01 g. In this case, surface water of the samples was dried before weighting. Measurements were taken weekly during the first month and every other week until the end of the study. The values of ultrasonic pulse velocity and mass presented in this study represent the average of three specimens.

- X-ray diffraction (XRD)

Differences on phase composition between free and restrained specimens were investigated by XRD at 90, 180 and 365 days. Samples for XRD were core drilled from original specimens using a column drill equipped with a diamond drill bit cooled with water (14 mm of diameter). For each dosage, samples were extracted from the same specimen to reduce the variability of the results. Due to the symmetric sulfate exposure conditions, each sample was divided in two. One half was crushed and the powder was pressed in cylindrical standard sample holders of 16 mm of diameter and 2.5 mm of height. The other half was discarted. XRD measurements were made using a PANalytical X'Pert PRO MPD Alpha1 Θ/2Θ diffractometer in reflection Bragg Brentano geometry of 240 mm of radius. $CuK_{\alpha 1}$ radiation (λ=1.5406 Å) and X'Celerator detector with active length of 2.122 º were used. Work power was set to 45 kV – 40 mA. Θ/2Θ scans from 4 to 80 º2Θ with a step size of 0.017 º2Θ and a measuring time of 50 seconds per step were performed. Sample holders were spun at 2 revolutions per second.

Rietveld analysis using external standard method was performed with the XRD results for the quantitative study of the crystalline phases. The external standard method was used for quantification instead of the more common internal standard method to avoid homogenisation problems and further dilution of the cement paste in the analyzed sample [14-16]. The adopted methodology is similar to earlier works [14-16]. Phase weight fractions were calculated from phase scale factors by comparison to the scale factor of the external standard (Al_2O_3), measured under identical diffractometer conditions. The values of density and volume of the unit cell of each phase were obtained from data sets from ICSD. Mass attenuation coefficients (MAC) of the different compositions used were calculated from the MAC of each component, including the water content and considering the weight fraction of all components. Final MAC of the different mortars used are listed in Table 2.

All Rietveld refinements were done with X'Pert High Score Plus software package by PANalytical using the structures listed in Table 3. Small peaks of Fe-substituted ettringite formed as a result of the reaction between sulfate ions and the ferroaluminate phases were detected in some mortars at late stages of the attack. Since its crystalline structure for Rietveld refinement was not available it was not considered during quantification. The global variables refined were the background polynomial with 4 coefficients (1^{st}, 2^{nd}, 3^{rd} and 5^{th}) and the zero shift. For all phases detected, individual scale factors and lattice parameters were refined. A pseudo-Voigt function was chosen to model the peak shape. The phase profile width (*w*) was

refined for quarz, ettringite, portlandite and gypsum. For quarz and portlandite, the profile parameters *U*, *V* and the peak shape were also refined. Preferred orientation corrections were applied when necessary for gypsum (0 2 0), portlandite (0 0 1), ettringite (1 0 0) and quartz (1 0 1) as long as the phase content was above 2 %.

Table 3. Phase structures used for Rietveld refinement.

Phase	Chemical composition	ICSD Code	Reference
Alite	Ca_3SiO_5	94742	[17]
Belite_o	Ca_2SiO_4	81097	[18]
Portlandite	$Ca(OH)_2$	15471	[19]
Calcite	$CaCO_3$	79673	[20]
Ettringite	$Ca_6Al_2(SO_4)_3(OH)_{12}26H_2O$	155395	[21]
Gypsum	$CaSO_42H_2O$	15982	[22]
Ferrite	Ca_2AlFeO_5	9197	[23]
Quartz	SiO_2	200721	[24]
Mullite	$Al_{4,74}Si_{1,25}O_{9,63}$	66448	[25]
Corundum	Al_2O_3	73725	[26]

- *Scanning electron microscopy (SEM)*

Morphology of the hydrates precipitated during sulfate exposure at the end of the test were examined by SEM (Jeol J-6510) using backscattered and secondary electrons at the voltage of 20 kV. Chemical composition was determined by energy disperse X-ray spectroscopy (EDS). Sections of the samples extracted were cut with an end-cutting plier perpendicular to the exposed surfaces. Fractured samples were frozen in liquid nitrogen, dried in vacuum during 48 hours and coated with carbon.

3. RESULTS AND DISCUSSION

3.1 EXPANSIONS AND CONFINING STRESSES

Figure 6 depicts the evolution of free and restrained expansions for specimens stored in 30 and 3 g/l. Traditionally, the expansions presented by most researchers correspond to the difference between the expansions measured in aggressive and non-aggressive conditions to isolate the effects of sulfates from dimensional variations caused by normal cement hydration processes. However, in this work expansions are used to assess the theoretical and actual confining stresses generated in the restrained specimens. For that, the discrimination of the contribution of sulfates and normal cement hydration on the expansions measured is not appropriate since all expansions contribute to generate stresses, regardless of its origin.

Free specimens under high aggressive conditions reach a wide variety of expansions depending on the mixture composition (Figure 6a). The expansions obtained at the end of the period assessed varies between $2.8 \cdot 10^{-3}$ and $6.6 \cdot 10^{-4}$. Mortars with fly ash and water/cement ratio of 0.55 (OPC+FA_0.45 and OPC_0.55) present the highest expansions while mortars with air-entrainer and sulfate-resisting cement (OPC+AE_0.45 and SRPC_0.45) show the lowest expansions throughout the attack. On the other hand, in low aggressive curing conditions the expansions developed by free specimens presented maximum values below $5.0 \cdot 10^{-4}$ at 365 days (Figure 6c).

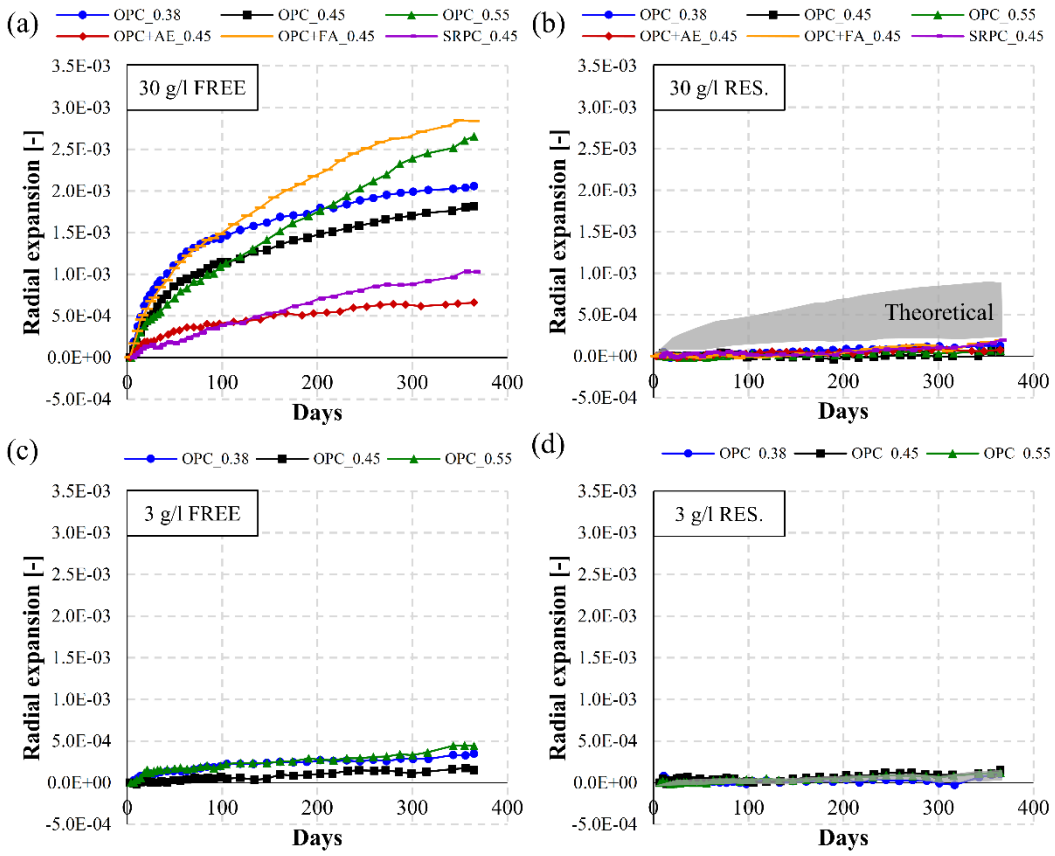

Fig. 6. Evolution of free and restrained expansions for high and low aggressive conditions.

Results obtained for restrained specimens (Figures 6b and 6d) show expansions below $2 \cdot 10^{-4}$ for all compositions in both aggressive environments. The results corresponding to the high aggressive environment were not expected according to the estimation of the mechanical effects produced by the steel rings described in section 2.2.3. Figure 6b and 6d include the envelop domains of the expected restrained expansions, considering that steel rings restraint 68 % of the free expansions. For high aggressive conditions, final expansions measured at 365 days are between 2 and 12 times lower than the theoretical expansions. For low aggressive conditions, measured and theoretical expansions are similar.

Figure 7 presents the real and theoretical evolution of confining stresses in restrained specimens for high and low aggressive conditions. Stresses are estimated by Eq. 1 based on the expected and measured restrained expansions depicted in Figure 6b and 6d. Real and theoretical stresses for each composition are represented with solid lines with markers and dotted lines, respectively, following the same color pattern. The envelop domain covered by the theoretical stresses is depicted in grey. Based on the mechanical contribution of the steel rings, the confining stresses applied to the restrained specimens should reach values between 5 and 23 MPa at the end of the test. However, the actual confining stresses generated for high and low aggressive conditions increase with the exposed period but always remain below 5 MPa. Even though this was the expected behavior for 3 g/l, the actual stresses generated in specimens under the high aggressive solution are significantly lower than the theoretical stresses.

The large difference between theoretical and measured stresses are observed in all mortars. Therefore, it seems that the composition of the different matrices considered had

minor effects on the confining stresses generated. Due to the low values measured, the influence of water/cement ratio, cement, air-entrainer or fly ash is not clear. In most cases, the differences observed amongst these compositions are relatively close to the precision of the equipment (± 0.6 MPa).

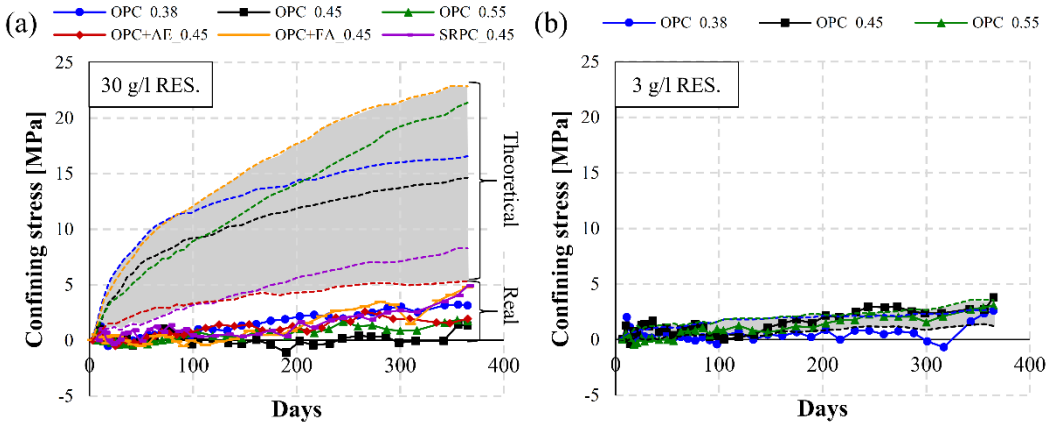

Fig. 7. Evolution of confining stress in restrained specimens for high and low aggressive conditions.

These results might be partially influenced by several factors. As indicated in section 2.2.3, the formulation used to estimate theoretical stresses does not take into account second order effects such as cracking or creep, which may overestimate the confining stresses generated, especially at the late stages of the attack. On the other hand, the presence of the steel ring might promote the release of strains in the non-restrained plane. However, special considerations were taken during the design stage of the samples to minimize this phenomenon. Due to the geometric characteristics of the specimens, strains developed in the horizontal plane are about 4 times the strains in the vertical plane. Therefore, it is unlikely that the large difference between the theoretical and measured stresses depicted in Figure 7a is entirely explained by a transfer of strains from the restrained plane to the free direction.

The results obtained indicate that only a small fraction of the expansions restrained by the steel ring are translated into stresses. This unexpected behavior suggests the presence of an additional phenomenon: There might be an interaction between the confining stresses caused by restraint and processes associated with the ESA that define the expansive forces generated during the attack.

3.2 MACROSTRUCTURAL EFFECTS OF EXPANSION RESTRAINT

3.2.1 Visual aspect of samples

Figure 8 allows the comparison of the external surface of free and restrained specimens for OPC+FA_0.45, OPC_0.45, SRPC_0.45 and OPC+AE_0.45 in high aggressive conditions (30 g/l) at the end of the test. These mixtures are selected to cover different free expansions depicted in Figure 6a. No major failure in the form of generalized spalling of the external surface, cracking due to compressive stresses or tensile splitting is observed in any composition. Restrained and free OPC+FA_0.45 and OPC_0.45 specimens present a thin dense layer covering most of the surface. In both cases, samples experienced similar degrees of localized spalling (highlighted with a red circle) in locations within the region covered by the dense layer. This layer is not observed in SRPC_0.45 or OPC+AE_0.45. The similar

visual appearance between free and restrained specimens of each composition may be caused by the low confining stresses developed during the attack (below 5 MPa). Compressive stresses of this magnitude should not cause additional damage.

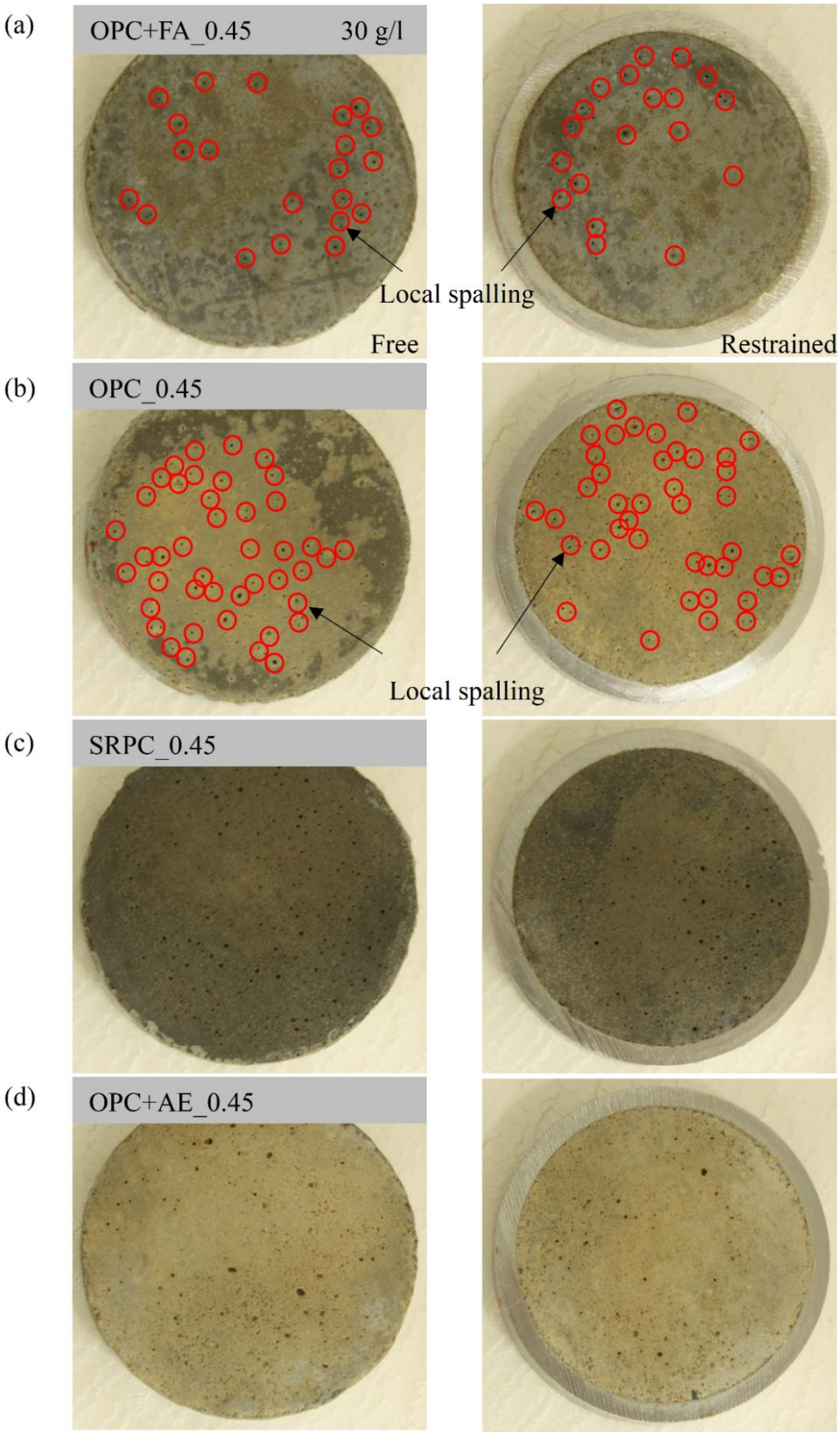

Fig. 8. Visual aspect of free and restrained mortars in 30 g/l at 365 days.

Figure 9 presents the visual aspect of OPC_0.45 in the low aggressive solution (3 g/l) at 365 days. As described for 30 g/l, the external surface of free and restrained mortars are in similar conditions and do not present any form of major failure. As expected, specimens show lower levels of degradation than the same composition stored in 30 g/l (Figure 8b). Figure 9 depicts the beginning of the formation of a thin layer of precipitated product covering a small fraction of the exposed surface. At the end of the test, no local spalling is detected in any configuration.

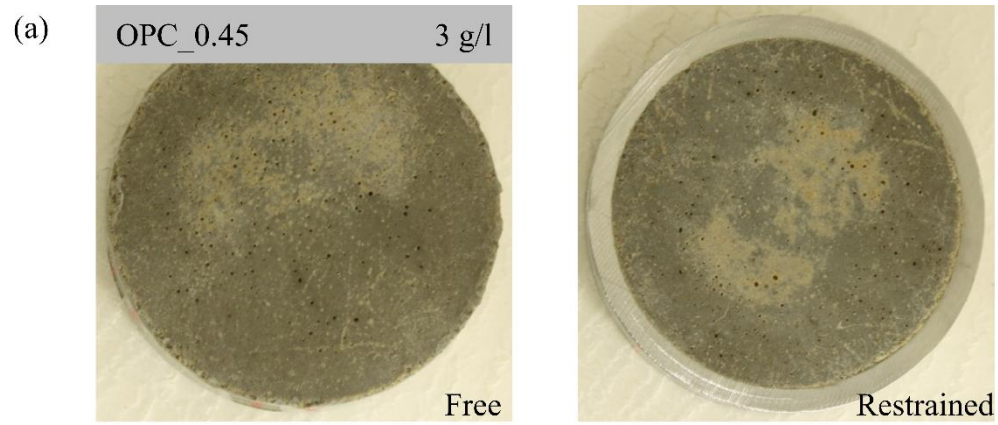

Fig. 9. Visual aspect of free and restrained OPC_0.45 mortars in 3 g/l at 365 days.

3.2.2 Mass variation

Figure 10 shows the influence of confinement on the evolution of the relative mass variation over time for all mortars stored in 30 and 3 g/l. The relative mass variation is calculated as the ratio between the mass variation and initial mass for each composition. The envelops covered by the relative mass variation curves measured in all compositions considered for free and restrained specimens (without considering the weight of the steel ring) are represented with green and grey domains, respectively. To isolate and highlight the effects of confinement, Figure 10 includes relative mass variation curves corresponding to the difference between restrained and free specimens for each composition (represented in solid lines with markers). Curves with positive values indicate that confinement reduces the relative mass loss whereas negative values suggest that confined conditions promote mass loss.

Prior to cracking, mass variation in saturated conditions can be related to the mobility of ions between the pore and the external solution. On one hand, mortars exposed to ESA might experience positive mass changes caused by sulfate uptake from the external solution. On the other hand, negative mass changes are associated to leaching. The domains depicted in Figure 10 depict negative relative mass variations for free and restrained specimens during sulfate exposure. These results indicate that leaching overrides the sulfate uptake phenomenon in both aggressive conditions evaluated.

The curves corresponding to the difference between relative mass variation of restrained and free specimens shows positive values for most compositions. Based on the assumption of full saturation and the similar cracking state between free and restrained mortars (Figure 8 and 9), these results indicate lower leaching rates in confined specimens. This phenomenon might be explained by the mechanical action of the steel rings over the mortar sample. Confinement could potentially limit the appearance of micro-cracks and

partially close or reduce pore channels connecting the inner layers of the matrix with the external media. Consequently, the ionic movement between the pore and external solution is indirectly reduced. This observation is in agreement with several studies that report that low or moderate compressive stresses reduce the availability of sulfates [1-3,9].

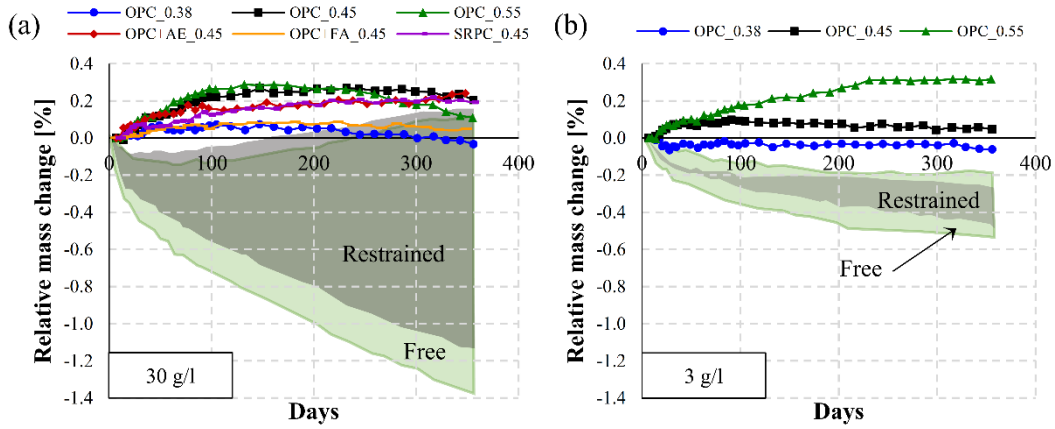

Fig. 10. Effects of confinement on the evolution of mass for (a) 30 g/l and (b) 3 g/l.

Mortars OPC_0.55, OPC_0.45, SRPC_0.45 and OPC+AE_0.45 show the highest influence of restrained conditions on the mass variation. The restrained configuration of these compositions presents on average between 2.6 to 6 times less mass reduction than mortars OPC_0.38 and OPC+FA_0.45 throughout the attack. According to these results, the lower ionic movement between internal and external solutions in restrained conditions is more significant in matrices with high water/cement ratios and the presence of air bubbles. This trend can be explained by the expectedly higher ionic flux between internal and external solutions present in those matrices due to a coarser pore network.

3.2.3 Ultrasonic velocity variation

Figure 11 depicts the effects of expansion restraint on the ultrasonic velocity for the different compositions stored in 30 and 3 g/l. The relative velocity change corresponds to the ratio between the velocity variation and initial velocity. The envelops covered by the measurements of relative ultrasonic velocity change in all compositions for free and restrained specimens are represented with green and grey domains, respectively. To facilitate the analysis, the effects of confinement are isolated in Figure 11 by including the relative velocity variation curves corresponding to the difference between restrained and free specimens for each composition (solid lines with markers).

For high aggressive conditions (Figure 11a), shaded regions depict negative relative velocity changes for free and restrained specimens. The decrease on the ultrasonic velocity indicates that ESA has caused physical damage in both configurations. Domains depicted in low aggressive conditions (Figure 11a) show either null or positive velocity variations throughout the attack. These results suggest that ESA did not generate significant physical damage to the matrices in this exposure condition.

Most curves that illustrate the effects of confinement depict positive variations of ultrasonic velocity. In this case, positive values indicate that confinement causes denser matrices and lower levels of physical damage. The series OPC_0.38 and OPC_0.45 describe the most significant reduction of damage caused by confinement in high aggressive

conditions (Figure 11a). For these compositions, restrained conditions prevented almost completely the formation of physical damage. The effects of confinement for the other compositions are less significant, with differences ranging from -2 to +2 %. For low aggressive conditions, the 3 series evaluated present slight positive values, indicating that confinement also causes denser matrices.

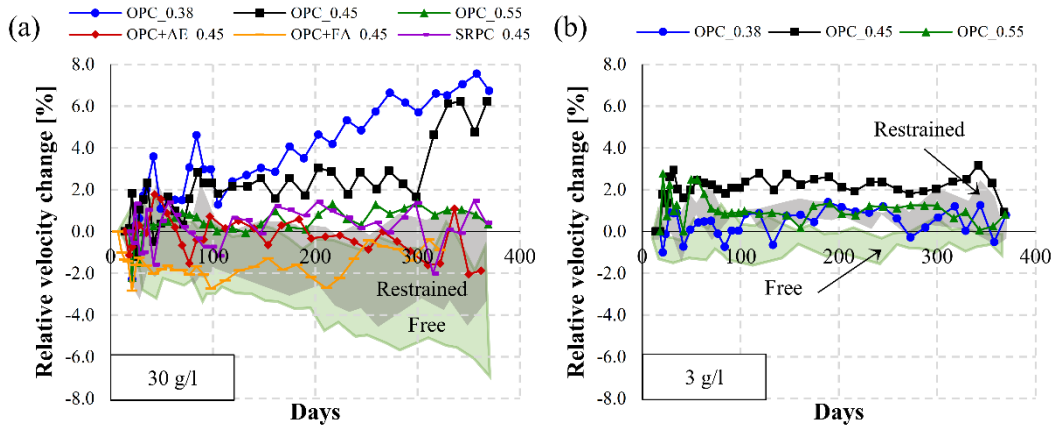

Fig. 11. Effects of confinement on the evolution of ultrasonic velocity for (a) 30 g/l and (b) 3 g/l.

The higher integrity and density of confined matrices can be explained by the confining stresses generated by the steel rings. The compressive stresses acting in the opposite direction of the expansive forces caused by the ESA should reduce or delay the appearance of micro-cracks in the matrix. As a consequence, sulfate ingress in confined specimens might be slower than in free specimens (as suggested in section 3.2.2). A limited sulfate availability in the pore solution should cause a decrease on the amount of expansive phases precipitated and thus, reduce the damage generated. This hypothesis is verified in section 3.3.1. by the quantification of the expansive phases in free and restrained specimens.

3.3 MICROSTRUCTURAL EFFECTS OF EXPANSION RESTRAINT

3.3.1 X-Ray diffraction

This section presents a comprehensive analysis of the evolution of phase composition for free and restrained specimens by quantitative XRD. To simplify the interpretation of the results, only the main crystalline phases interacting with the sulfate ions are presented. Phase contents are expressed as a percentage of the cement content defined by the initial dosage of each composition.

Figure 12 shows ettringite, gypsum and portlandite contents for all compositions submerged in the high aggressive solution (30 g/l) at 365 days. Values corresponding to free and restrained conditions are represented as circles and triangles, respectively. Ettringite and gypsum contents vary between 11-19 % and 3-11 %, respectively. Higher ettringite over gypsum contents were expected due to the lower solubility of ettringite [27]. The composition with the least amount of expansive phases correspond to OPC_0.38, followed by the mortar with sulfate-resisting cement. Increasing amounts of expansive phases are measured for the compositions OPC_0.55 and OPC+AE_0.45. These trends might be explained by an increase of sulfate availability in the pore solution caused by the increase of water/cement ratio and the presence of air bubbles. Portlandite contents evolve similarly to ettringite contents. In this

case, the increase of water/cement ratio and the presence of air bubbles seems to promote hydration of the silicate phases. The only composition that does not follow this trend is OPC+FA_0.45, which presents the lowest portlandite content amongst all mortars evaluated. This result can be explained by the pozzolanic activity of the fly ash, which consumes reactive silica and calcium hydroxide, producing calcium silicate hydrate [28].

The differences on phase content between restrained and free specimens are presented in clustered columns for each composition. Positive values indicate that restrained conditions promote phase precipitation while negative values suggest that the confining stresses from the steel ring hinder its formation. For most compositions, expansion restraint causes a slight decrease on ettringite content. The reduction seems to increase with the amount of ettringite measured in free conditions. Series OPC+AE_0.45 presents the highest influence, with a relative decrease of 22 % between free and restrained specimens. These results might be explained by the reduced mobility of ions between external and internal solutions in restrained conditions. As described in section 3.2.2, the decrease of ionic mobility and sulfate availability is more significant in compositions with high water/cement ratio and air-entrainer, which is consistent with the XRD results presented here. The effects of confinement on gypsum formation is unclear as confinement causes significant variations on gypsum content without any recognizable pattern.

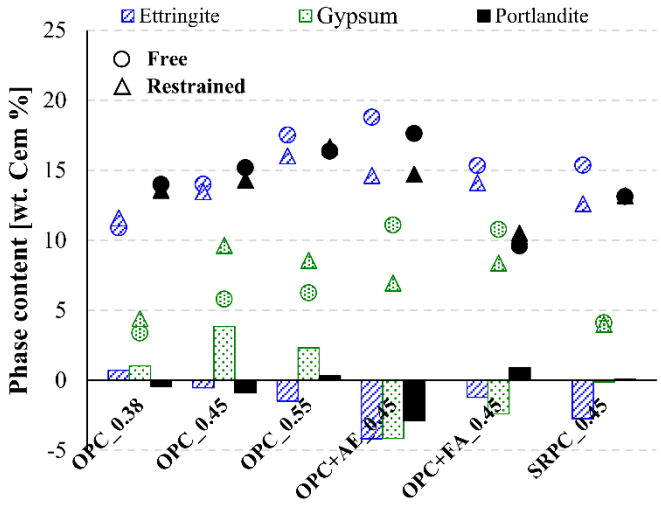

Fig. 12. XRD results at 365 days in 30 g/l.

Phase composition analysis at different ages are performed to investigate the effects of confinement throughout the attack. Figure 13 shows the evolution of ettringite, gypsum and portlandite content for free and restrained OPC_0.45, OPC+AE_0.45, SRPC_0.45 and OPC_FA samples stored in 30 g/l at 90, 180 and 365 days. These mixtures are selected to cover different magnitudes of free expansions (Figure 6a). Rietveld quantification reveals only slight variations on the total phase content within each composition from 90 days of exposure. Even though the amount of ettringite remains approximately constant, ultrasonic velocity measurements indicate that physical damage increases with time. This could suggest that the amount of ettringite is not an accurate indicator of the damage generated. Instead, the increasing levels of damage measured might be explained by variations in the location of the precipitation promoted by the continuous refinement of the pore network [29].

The phase contents depicted with clustered columns in Figure 13 (difference between restrained and free specimens) indicate that confined conditions cause a progressive reduction on the amount of expansive phases over time for series OPC+AE_0.45, SRPC_0.45 and OPC+FA_0.45. The composition OPC_0.45 do not follow the same trend due to an unexpected increase on the gypsum content at 180 and 365 days in restrained condition.

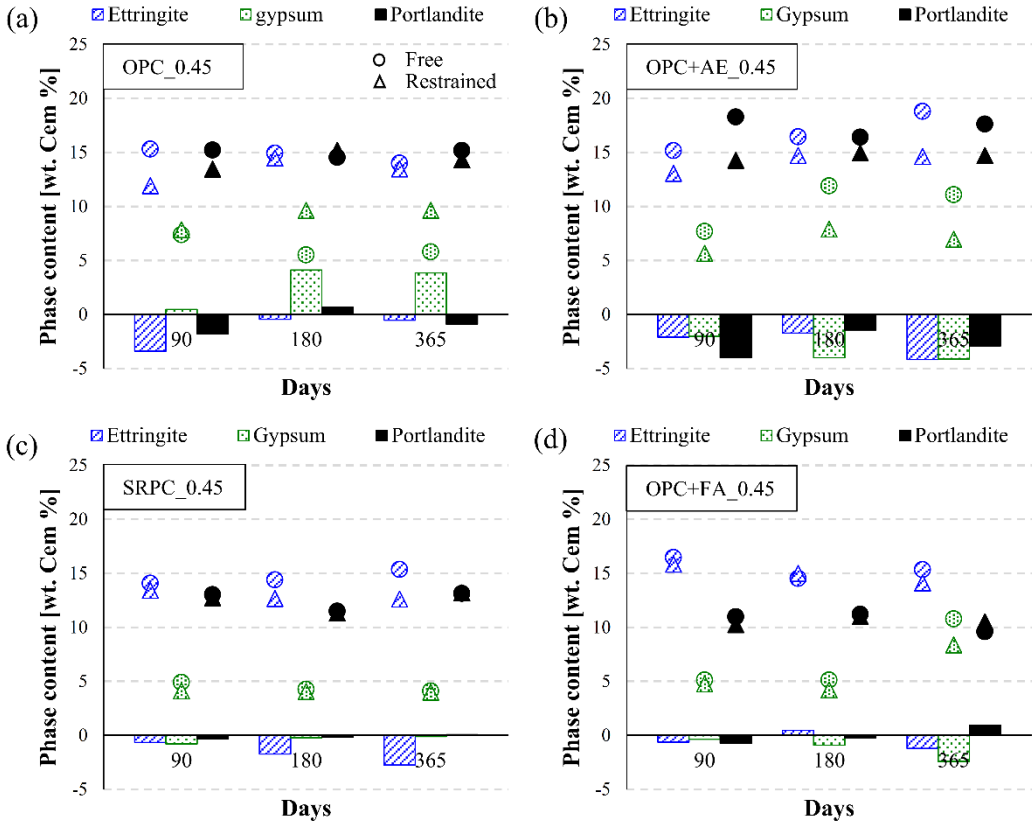

Fig. 13. Evolution of XRD results for (a) OPC_0.45, (b) OPC+AE_0.45, (c) SRPC_0.45 and (d) OPC+FA_0.45 in 30 g/l.

Figure 14a shows ettringite, gypsum and portlandite contents for all compositions stored in low aggressive conditions (3 g/l) at 365 days. The phase content of all phases increases with the water/cement ratio of the composition. However, in this case the amount of expansive phases is considerably reduced due to the lower external sulfate concentration. By lowering the sulfate concentration from 30 g/l to 3 g/l, the average ettringite contents are reduced by 8.1 and 19.2 % in free and restrained specimens, respectively. In the case of gypsum, this reduction increases to 36.6 and 48.4 % for free and restrained specimens. The clustered columns indicate that confinement causes a significant reduction of the ettringite content for the series OPC_0.55. However, the other compositions do not show any clear trend, with slight positive and negative variations of the ettringite and gypsum contents. Figure 14b illustrates the evolution of phase composition at 90, 180 and 365 days for series OPC_0.45 stored in 3 g/l. Similarly to the results obtained for this composition in 30 g/l, absolute values of phase content remain approximately constant since 90 days of exposure and the results do not show any clear trend regarding the influence of expansion restraint.

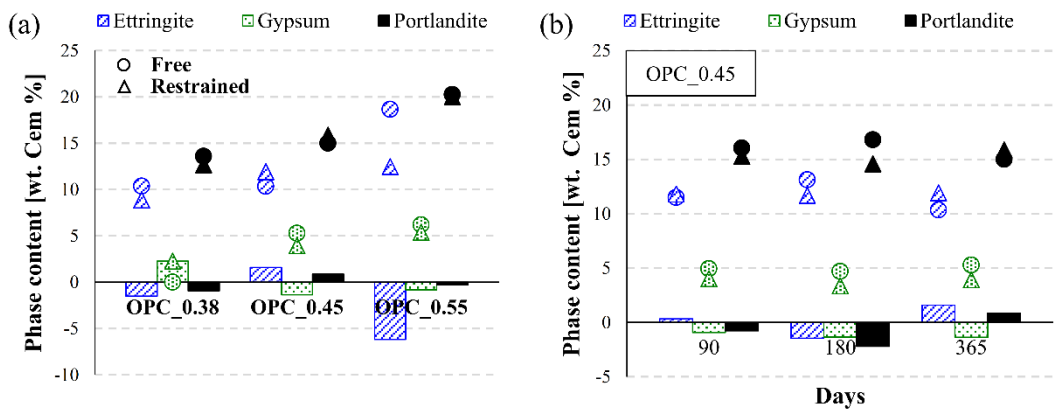

Fig. 14. (a) XRD results at 365 days and (b) Evolution of XRD results for OPC_0.45 in 3 g/l.

In general, XRD results indicate that expansion restraint causes a reduction on the amount of ettringite in most of the compositions evaluated. This reduction is more significant in the mortars with high water/cement ratio and air-entrainer (OPC_0.55 and OPC+AE_0.45). However, this trend is unclear for the compositions with lower water/cement ratios (OPC_0.38 and OPC_0.45). Notice that both OPC_0.38 and OPC_0.45 showed the highest influence of confinement according to ultrasonic velocity measurements at 30 g/l (section 3.2.3). For these series, the presence of confining stresses caused a significant increase of ultrasonic velocity and a reduction of physical damage. This behavior was initially attributed to a limited sulfate availability and a lower precipitation of expansive phases in confined conditions. However, the results obtained in this section indicate that the lower damage measured cannot be attributed to a lower precipitation of ettringite and gypsum. Therefore, results suggest that there might be an additional phenomenon acting in restrained specimens that causes the lower levels of deterioration observed.

3.3.2 SEM and EDS microanalysis

Free and restrained samples of mortar compositions OPC+AE_0.45, OPC_0.55 and OPC_0.38 submerged in the high aggressive solution (30 g/l) were evaluated at 365 days. The regions analyzed by EDS are indicated by a red circle in the corresponding image. The relative intensities of each element calculated from the counting are placed on the upper right corner. The peaks considered to measure the intensity of Ca, Si, S and Al correspond to the energies of 3.73, 1.78, 2.33 and 1.52 keV, respectively.

Figure 15 shows the microstructure of porous regions observed in OPC+AE_0.45 for free and restrained configurations. In free expanding conditions, a significant fraction of the visible pores is partially or completely filled with large needle-like ettringite crystals (Figure 15a). The length of those crystals is approximately 10 µm. In restrained conditions, the majority of pores are not filled with any large crystalline structure, giving the appearance of emptiness. However, most pores present a thin layer of poorly crystalline phases covering the pore walls (Figure 15b). EDS analysis in the pore walls reveals the presence of Ca, Si, S and Al, which suggests that small AFt crystals are spread over the pore walls instead of growing into larger structures.

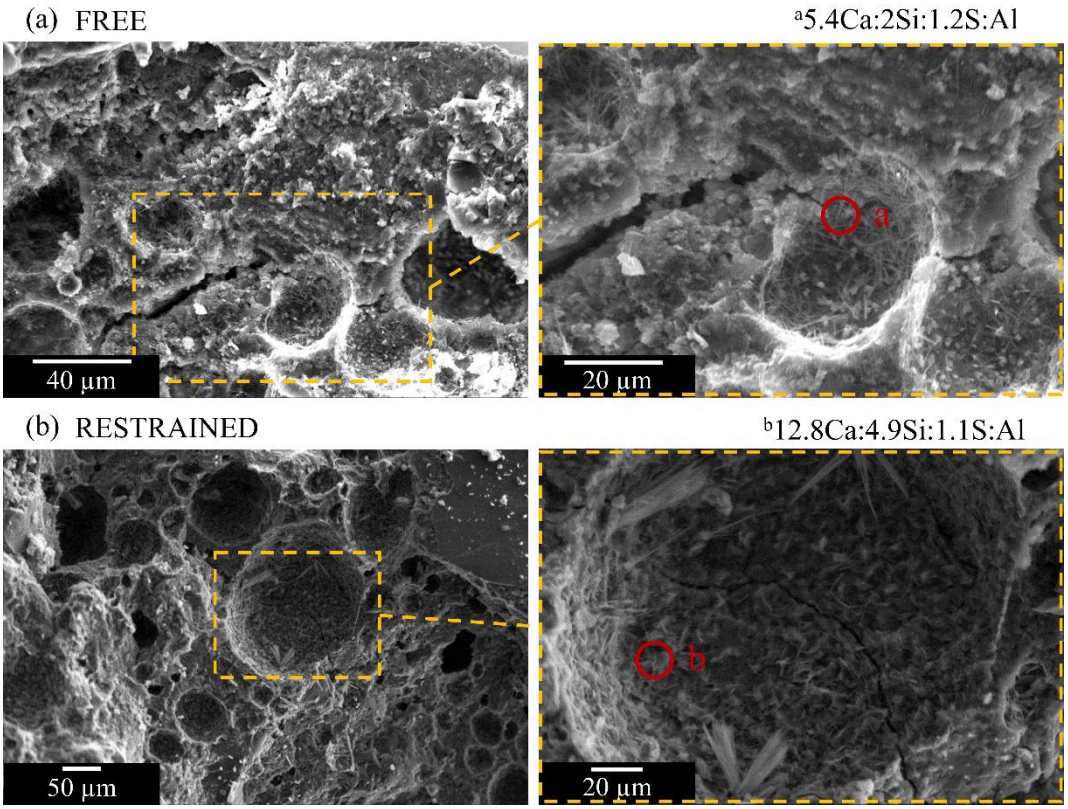

Fig. 15. SEM images and EDS spectrum of (a) Free and (b) Restrained OPC+AE_0.45.

A comparison between the microstructure of free and restrained OPC_0.55 samples also reveals significant differences on the morphology of the crystals formed (Figure 16). In free conditions, large portlandite plates and ettringite clusters are easily observed inside pores (Figures 16a and 16b). The arrangement of these phases suggest a simultaneous growth, probably due to the early age when specimens were exposed to sulfates. However, such crystalline formations are not observed in restrained conditions. In this configuration, pores are either empty or filled with a highly amorphous phase covering the pore walls (Figures 16c and 16d). EDS analysis performed in this phase identify mostly calcium. Large ettringite crystals were not found. Highly dispersed needle-like crystals were found mixed with the CSH gel in some regions outside the pores. EDS detected the presence of S and Al at these locations, which might suggest that ettringite is precipitating within the CSH gel.

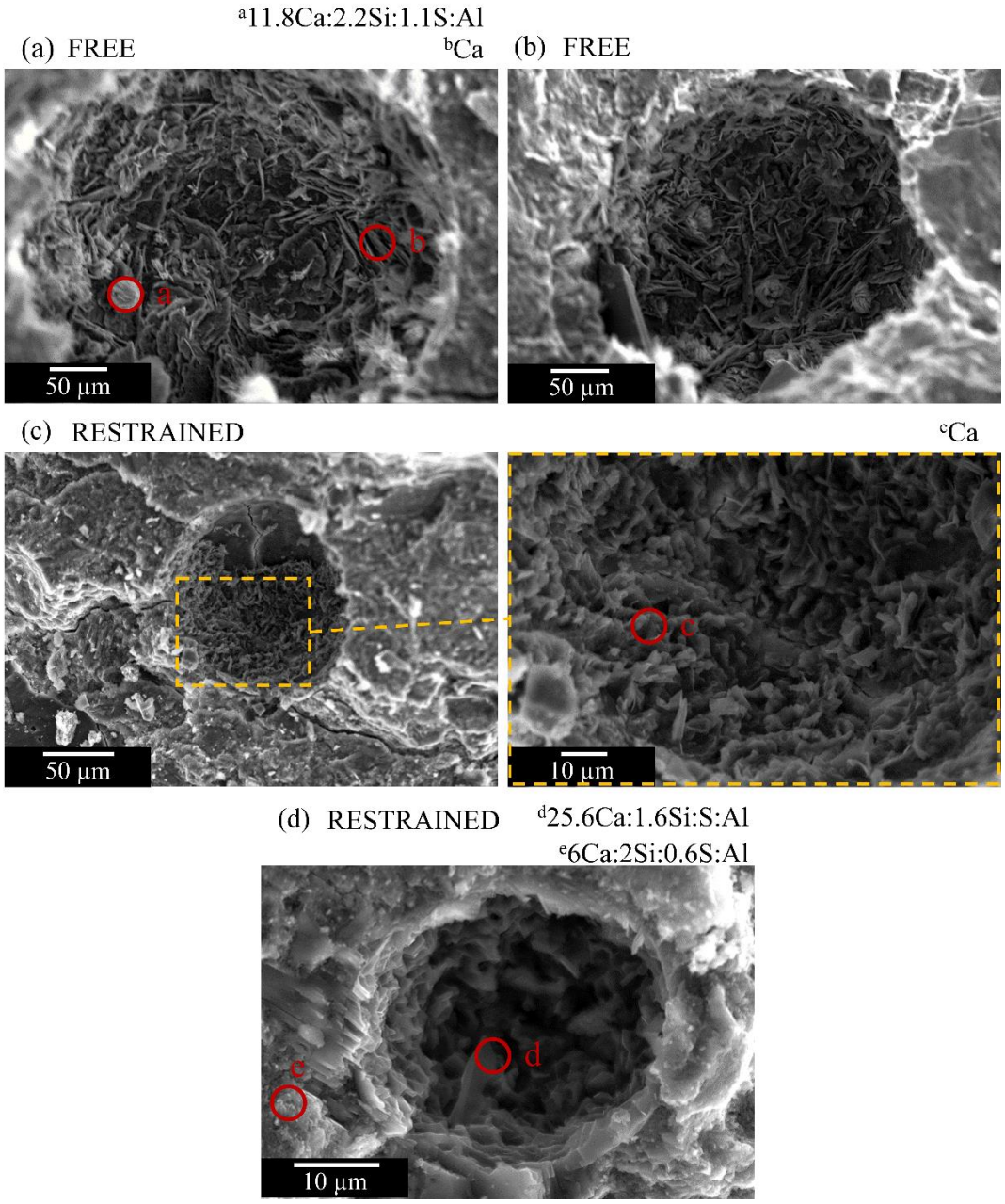

Fig. 16. SEM images and EDS spectrum of (a), (b) Free and (c), (d) Restrained OPC_0.55.

Similar trends are observed in the composition with lower water/cement ratio (OPC_0.38). Figures 17a and 17b show large amounts of ettringite and portlandite covering the pore walls of the samples in free expanding conditions. As observed in OPC_0.55, both phases present well-defined structures and seem to be growing simultaneously (Figure 17b). For this composition, some pores with similar hydration products were also found in restrained conditions (Figure 17c). However, a magnification of the crystals covering the pore walls depicts smaller structures with lower degrees of crystallinity than the ones observed in free conditions (Figure 17b).

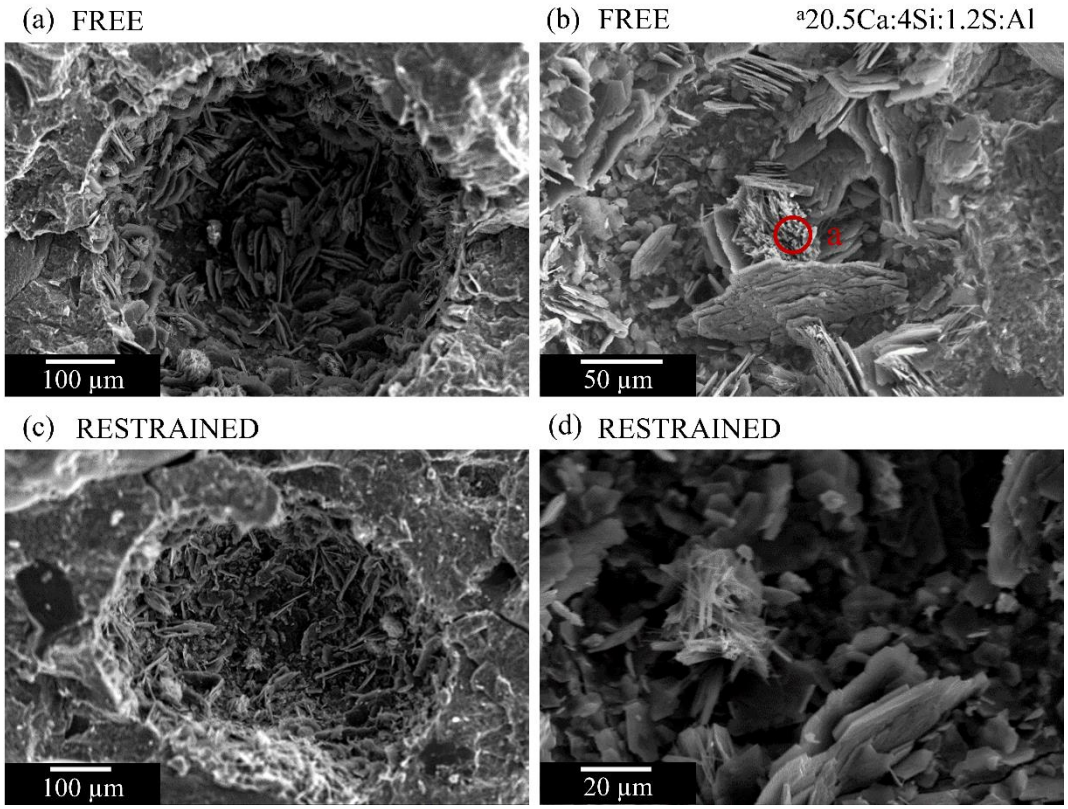

Fig. 17. SEM images and EDS spectrum of (a), (b) Free and (c), (d) Restrained OPC_0.38.

3.3.3 Discussion of SEM results

Results of the SEM analysis suggest that size and degree of crystallinity of phases formed during ESA might be significantly affected by expansion restraint. In the same way a structure element deforms after the application of an external stress, when a crystal is subjected to stresses it might change its dimensional configuration by precipitation and dissolution mechanisms until equilibrium is reached with the surrounding media. Some authors studied different aspects related to the effects of pressure on crystal growth caused by salt crystallization between pore walls [30-33]. The theoretical framework developed by M. Steiger [31,32] is used here to assess the influence of externally generated confining stresses due to expansion restraint on crystal development.

When a crystal grows in directions in which growth is opposed by external forces, free and loaded faces of the crystal present different values of chemical potential. According to [34], the chemical potential of a crystal face under pressure p (μ_p) can be expressed as indicated in Eq. 4 when elastic behavior is assumed. The contribution of the molar strain energy of a deformed crystal is neglected since the pressure difference between free and confined specimens is below 100 MPa [31,34].

$$\mu_p = \mu_0 + pV_m \quad \text{(Eq. 4)}$$

In this equation, μ_0 is the chemical potential of the solid in the unstressed reference state and V_m is the molar volume of the solid in the stressed state. This equation shows that the loaded faces of a crystal have higher chemical potentials than unloaded faces. On the other hand, the chemical potential of the salt in the solution (μ_l) increases with the ion activity of

the solute (K) in the pore solution (Eq. 5). The term μ_l^0 refers to the chemical potential in the standard state.

$$\mu_l = \mu_l^0 + RTln(K) \quad \text{(Eq. 5)}$$

Both loaded and unloaded faces of a crystal seek equilibrium with the surrounding pore solution. Therefore, as indicated in Eq. 6, the chemical potential of the solute must be equal to the chemical potential of the respective crystal face.

$$\mu_0 + pV_m = \mu_l^0 + RTln(K) \quad \text{(Eq. 6)}$$

Eq. 6 shows that when a pressure is introduced to the crystal, the solubility of that crystal increases to balance the increase on chemical potential produced by the pressure. This phenomenon is sometimes referred to as "Riecke's principle". It states that the crystal solubility increases with the pressure applied. According to this principle and assuming that the pressure caused by the steel rings is transferred to the crystals growing in confined conditions, crystals formed in restrained samples should exhibit higher solubility than those in free expanding conditions. If the pressure is anisotropic, the dissolved material may then be redeposited on those parts of the crystal exposed to lower pressures. This phenomenon should cause crystals with smaller sizes and lower degrees of crystallinity in restrained specimens.

However, as indicated in section 3.1, the confining stresses generated by the steel rings are below 5 MPa. Such low stresses may not be able to cause significant effects on the solubility of the phases precipitated, as stresses in the order of 20 MPa are necessary to increase 20 % the solubility of NaCl crystals at 25 ºC [31]. According to M. Steiger [31], the increase of solubility due to an increase of pressure (Δp) can be estimated by Eq. 7. In this equation, the term K_0 corresponds to the ion activity product of the saturated solution.

$$\ln\left(\frac{K}{K_0}\right) = \frac{\Delta p V_m}{RT} \quad \text{(Eq. 7)}$$

Figure 18 presents the equilibrium curve of the solubility increase produced by pressures between 0 – 5 MPa in ettringite, gypsum and portlandite crystals at 25 ºC. The molar volumes considered for those phases are 707, 75 and 33 cm^3/mol, respectively [27]. Ettringite depicts a significant increase of solubility within the pressures evaluated. The solubility at 5 MPa of pressure is 4.2 times the reference solubility in the absence of load, which indicates that ettringite is very sensitive to the range of pressures applied. This phenomenon could explain the absence of large ettringite crystals in restrained conditions. For the other phases considered, the influence of stresses up to 5 MPa on the solubility is minimum.

The high supersaturation needed to counteract the effects of pressure might alter the balance between crystal growth and nucleation rate of the ettringite crystals. According to [35], the rate of nucleation (I) can be expressed as indicated in Eq. 8. This equation has been simplified by grouping all the parameters other than supersaturation into the positive coefficients A and B. Large K/K_0 leads to rapid nucleation of ettringite. Therefore, an increase of solubility should promote ettringite nucleation over crystal growth, ultimately resulting in smaller crystals distributed over a large surface.

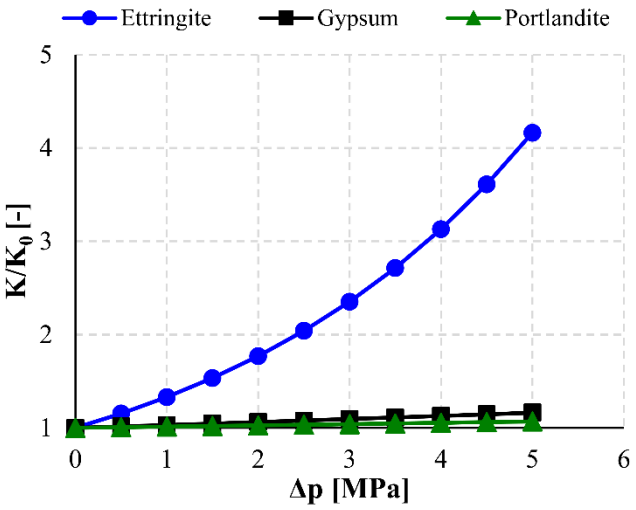

Fig. 18. Solubility increase of a loaded surface of ettringite, gypsum and portlandite crystal.

$$I = A\exp\left[\frac{-B}{(\ln(K/K_0))^2}\right] \quad \text{(Eq. 8)}$$

The crystallization pressure theory states that the crystals must be confined in order to exert pressure. Therefore, the expansive stress generated in a specimen depends on the volume fraction of crystals growing in confined conditions [33]. The smaller crystal size distribution of ettringite caused by its increased solubility in the restrained specimens might reduce the fraction of crystals growing in confined conditions and thus, the amount of crystals exerting pressure. This phenomenon, together with the lower presence of ettringite, could explain the low confining stresses measured and the reduced damage observed in specimens under restrained conditions. However, further experimental research is needed to validate this statement since it was not possible to compare by SEM imaging the morphology of ettringite growing in confined conditions for free and restrained specimens.

4. CONCLUSIONS

The results presented in this paper indicate that the confining stresses alter the normal development of the ESA by reducing the potential damage generated. The following specific conclusions may be derived from this study.

(1)- The level of stress generated by the attack in confined samples exposed to accelerated ESA is significantly smaller than the stresses predicted considering the free expansions of equivalent unconfined samples. Such difference confirms the important role of the confinement in the outcome of the attack and raises questions about the representativeness of the accelerated laboratory tests conducted under unconfined conditions. The numerical simulation of the structural repercussion of the ESA obtained by applying free expansion in structural models should also be questioned since it is likely to bring higher stresses than expected in reality in case confinement exists.

(2)- Results of mass variation suggest that the ionic transport process between external and pore solutions is reduced in confined conditions. This behavior might be

explained by the lower micro-cracking generated, which decreases the penetration paths and reduces the sulfate concentration in the pore network.

(3)- The evolution of the ultrasonic velocity confirms that confined specimens present denser matrices and lower presence of micro-cracks than equivalent unconfined specimens.

(4)- In general, XRD results indicate that the confinement causes a reduction on the amount of expansive phases precipitated, especially in compositions with high water/cement ratios and air-entrainer. The lower precipitation observed might be explained by the reduced availability of sulfates in confined conditions.

(4)- The theoretical framework formulated to explain the effects of confinement on the morphology and arrangement of the crystals formed suggests that confinement might increase the solubility of ettringite and promote a spread nucleation of small crystals within the pore network. These phenomena might reduce the amount of crystals growing in confined conditions and thus generating pressure, which may contribute to explain the lower stresses generated by the attack in the confined specimens. Further experimental evidences are needed to validate this hypothesis.

ACKNOWLEDGMENTS

Support from the Spanish Ministry of Economy and Competitiveness through research project BIA2013-49106-C2-1-R is greatly acknowledged. T. Ikumi is supported by the fellowship program FPI BES-2014-068524 of the Spanish Ministry of Economy and Competitiveness.

REFERENCES

[1] W. Piasta, Z. Sawicz, J. Piasta, Sulfate durability of concretes under constant sustained load, Cem. Concr. Res. 19 (1989) 216-227.

[2] U. Schneider, W. Piasta, The behaviour of concrete under Na_2SO_4 solution attack and sustained compression or bending, Mag. Concr. Res. 43 (157) (1991) 281-289.

[3] V. Zivica, V. Szabo, The behavior of cement composite under compression load at sulphate attack, Cem. Concr. Res. 24 (8) (1994) 1475-1484.

[4] K. Werner, Y. Chen, I. Odler, Investigations on stress corrosion of hardened cement pastes, Cem. Concr. Res. 30 (2000) 1443-1451.

[5] M.T. Bassuoni, M.L. Nehdi, Durability of self-consolidating concrete to sulfate attack under combined cyclic environments and flexural loading, Cem. Concr. Res. 39 (2009) 206-226.

[6] D. Yang, J. Luo, The damage of concrete under flexural loading and salt solution, Constr. Build. Mater. 36 (2012) 129-134.

[7] R. Gao, Q. Li, S. Zhao, Concrete Deterioration Mechanisms under Combined Sulfate Attack and Flexural Loading, J. Mater. Civ. Eng. 25 (1) (2013) 39-44.

[8] J. Gao, Z. Yu, L. Song, T. Wang, S. Wei, Durability of concrete exposed to sulfate attack under flexural loading and drying–wetting cycles, Constr. Build. Mater. 39 (2013) 33-38.

[9] H. Xu, Y. Zhao, L. Cui, B. Xu, Sulphate attack resistance of high-performance concrete under compressive loading, J Zhejiang Univ-Sci A (Appl Phys & Eng) 14 (7) (2013) 459-468.

[10] W. Müllauer, R.E. Beddoe, D. Heinz, Sulfate attack expansion mechanisms, Cem. Concr. Res. 52 (2013) 208-215.

[11] R. El-Hachem, E. Rozière, F. Grondin, A. Loukili, New procedure to investigate external sulphate attack on cementitious materials, Cem. Concr. Compos. 34 (2012) 357-364.

[12] A. Chabrelie, Mechanisms of degradation of concrete by external sulfate ions under laboratory and field conditions, PhD Thesis, ÉPFL, Lausanne, 2010.

[13] F.D. Lydon, R.V. Balendran, Some observations on elastic properties of plain concrete, Cem. Concr. Res. 16 (1986) 314-324.

[14] D. Jansen, F. Goetz-Neunhoeffer, C. Stabler, J. Neubauer, A remastered external standard method applied to the quantification of early OPC hydration, Cem. Concr. Res. 41 (2011) 602-608.

[15] D. Jansen, C. Stabler, F. Goetz-Neunhoeffer, S. Dittrich, J. Neubauer, Does Ordinary Portland Cement contain amorphous phase? A quantitative study using an external standard method, Powder Diffract. 26 (2011) 31-38.

[16] R. Snellings, A. Bazzoni, K. Scrivener, The existence of amorphous phase in Portland cements: Physical factors affecting Rietveld quantitative phase analysis, Cem. Concr. Res. 59 (2014) 139-146.

[17] A.G. de la Torre, S. Bruque, J. Campo, M.A.G. Aranda, The superstructure of C_3S from synchrotron and neutron powder diffraction and its role in quantitative analysis, Cem. Conc. Res. 32 (2002) 1347-1356.

[18] W.G. Mumme, R.J. Hill, G.W. Bushnell, E.R. Segnite, Rietveld crystal structure refinements, crystal chemistry and calculated powder diffraction data for the polymorphs of dicalcium silicate and related phases, N. Jb. Miner. Abh. (J. Min. Geochem.) 169 (1995) 35-68.

[19] H.E. Petch, The hydrogen positions in portlandite, Ca(OH)2, as indicated by the electron distribution, Acta Crystallogr. 14 (1961) 950-957.

[20] R. Wartchow, Datensammlung nach der ‘‘learnt profile”-methode(LP) für calcit und vergleich mit der ‘‘background peak background”-methode (BPB), Z. Kristallogr. 186 (1989) 300-302.

[21] F. Goetz-Neunhoeffer, J. Neubauer, Refined ettringite structure for quantitative X-ray diffraction analysis, Powder Diffr. 21 (2006) 4-11.

[22] W.A. Wooster, On the crystal structure of gypsum CaSO4(H2O)2, Z. Kristallogr. 94 (1936) 375-396.

[23] A.A. Colville, S. Geller, The crystal structure of brownmillerite, Ca2FeAlO5, Acta Crystallogr. B 27 (1971) 2311-2315.

[24] L. Levien, C.T. Prewitt, D.J. Weidner, Structure and elastic properties of quarz at pressure, Am. Mineral. 65 (1980) 920-930.

[25] T. Ban, K. Okada, Structure refinement of mullite by the Rietveld method and a new method for estimation of chemical composition, J. Am. Ceram. Soc. 75 (1992) 227-230.

[26] E.N. Maslen, V.A. Streltsov, N.R. Streltsova, N. Ishizawa, Y. Satow, Synchrotron X-ray study of the electron density in alpha-Al2O3, Acta Crystallogr. B 49 (1993) 973-980.

[27] B. Lothenbach, T. Matschei, G. Möschner, F.P. Glasser, Thermodynamic modelling of the effect of temperature on the hydration and porosity of Portland cement, Cem. Concr. Res. 38 (2008) 1-18.

[28] A.A. Ramezanianpour, Cement Replacement Materials: Properties, Durability, Sustainability, Springer, Berlin, Germany, 2014.

[29] T. Ikumi, I. Segura, S.H.P. Cavalaro, Influence of early sulfate exposure on the pore network development of mortars, Constr. Build. Mater. 143 (2017) 33-47.

[30] G.W. Scherer, Stress from crystallization of salt, Cem. Concr. Res. 34 (2004) 1613-1624.

[31] M. Steiger, Crystal growth in porous materials—I: The crystallization pressure of large crystals, J. Cryst. Growth 282 (2005) 455-469.

[32] M. Steiger, Crystal growth in porous materials—II: Influence of crystal size on the crystallization pressure, J. Cryst. Growth 282 (2005) 470-481.

[33] R.J. Flatt, G.W. Scherer, Thermodynamics of crystallization stresses in DEF, Cem. Concr. Res. 38 (2008) 325-336.

[34] R.B. de Boer, On the thermodynamics of pressure solution-interaction between chemical and mechanical forces, Geochim. Cosmochim. Ac. 41 (1977) 246-256.

[35] D. Min, T. Mingshu, Formation and expansion of ettringite crystals, Cem. Concr. Res. 24 (1994) 119-126.

5. GENERAL DISCUSSION AND CONCLUSIONS

The main purpose of this chapter is to discuss the relevance and limitations of the main contributions derived from the thesis based on a general perspective, which results from the combination of papers written. Additionally, opinions on future research lines are integrated in the discussion. It is important to highlight that the present chapter does not aim to summarize the work done or replace the specific discussion of the results included in each paper.

The critical discussion is structured in three main topics, based on the areas of contribution defined in chapter 2: Numerical modeling of the ESA, the role of porosity in the ESA and the effects of field-like conditions on ESA assessment. New insights derived from the discussion of each topic are gradually introduced into the discussion of the next topic to reproduce the real timeline of the research done during the thesis. Finally, general and specific conclusions are summarized.

Contents

5.1. NUMERICAL MODELING OF THE ESA

The contributions of this thesis in the field of the numerical modeling of the ESA aim to address limitations regarding comprehensive models and simplified assessment procedures. The former are reproduced in Journal Paper I (pages 24-47) while the latter are described in detail in Journal Paper II (pages 48-71).

5.1.1. Comprehensive model for ESA assessment

The critical review on advanced models for ESA assessment presented in section 1.2.2 describes several important limitations associated to the approach usually adopted to reproduce expansive stresses. One of the main criticism is related to its inability to capture expansive forces generated during the early stages of the attack. This limitation is addressed in Journal Paper I by the development of a comprehensive ESA model with a new methodology to compute the expansions based on a more realistic representation of the pore network. Additionally, this model incorporates a direct and intuitive approach to compute damage and reflect the effects of cracking on the ionic transport process. A schematic representation of the model developed is depicted in Figure 5.1 with the purpose of identifying the main features of the model and easily locate the main areas of contribution, which are highlighted by green hatching.

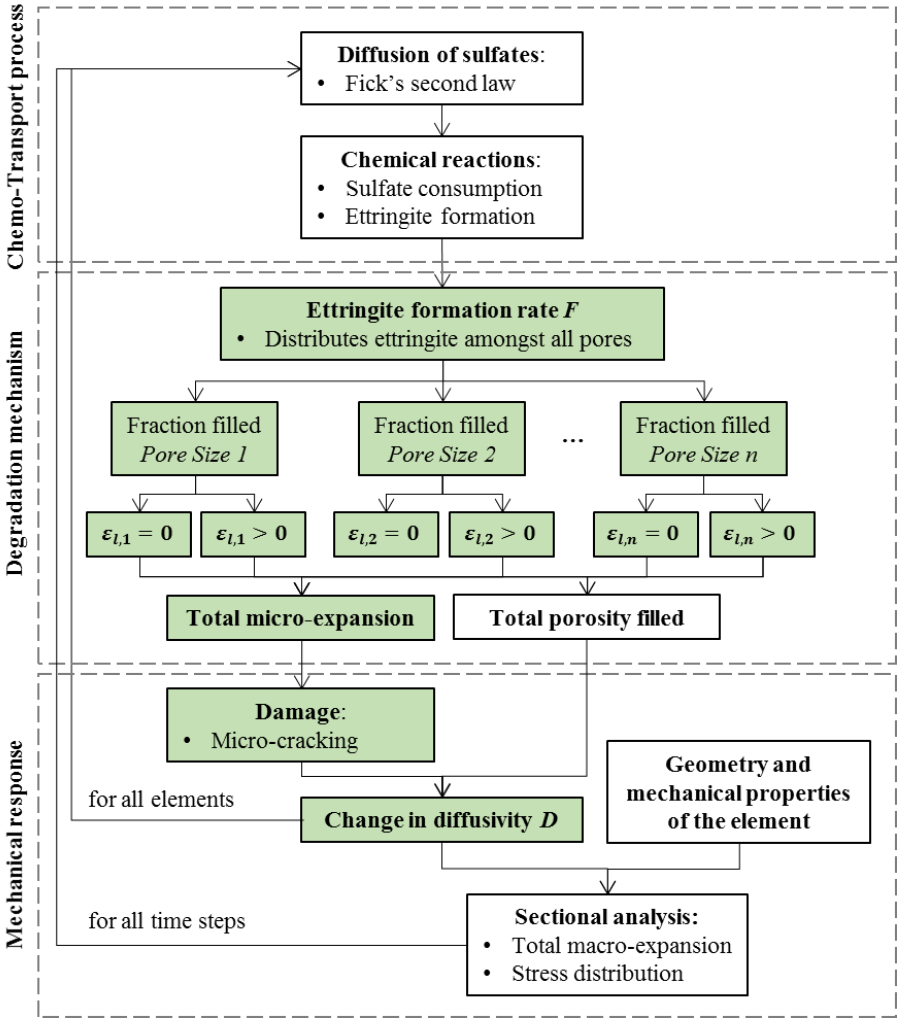

Fig. 5.1. Schematic representation of the model described in Journal Paper I.

The main idea behind the new methodology to compute expansions is to discretize the real pore size distribution of the material into a finite number of pores, each one representing a volume fraction of the total porosity. Then, a parameter referred to as ettringite formation rate ($\mathcal{F}$) is used to quantify and distribute the ettringite formed within the pores considered. The contribution to the total local expansion of each pore size ($\varepsilon_{l,i}$) is estimated based on its volume ratio filled by ettringite and its individual capacity to accommodate expansive phases. This methodology acknowledges that not all ettringite precipitated during the attack contributes with the same weight into the expansive forces generated. Instead, ettringite precipitated in small pores is likely to generate higher and earlier pressures than ettringite growing in larger pores due to a faster filling rate and a smaller capacity to accommodate expansive products.

Table 5.1 summarizes the main approaches adopted by the most relevant numerical models developed during the last decades to simulate the expansive forces generated during the ESA. This table demonstrates the singularity of the methodology presented here, as the model developed (highlighted by green hatching) stands as the only that does not reduce all the complexity of the pore network into a single pore where all ettringite precipitates in. This feature, combined with the possibility to attribute different buffer capacities to different pore sizes, place the model developed as the only capable of capturing the importance of both the amount and location of the ettringite formed to estimate the local pressures generated by the attack. The noteworthy models proposed by F. Schmidt-Döhl & F.S. Rostásy [1,2] and P. Feng et al. [3] could not be included in Table 5.1 due to the lack of clarity in some aspects related to the mechanical considerations adopted and the absence of a transport module to account for the ionic transport process, respectively.

Table 5.1. Main features of the modeling approaches to simulate ESA expansive forces.

Authors	Year	Expansion mechanism		Pore network		Buffer capacity
		Volume Increase	Crystallization pressure	1 pore	N pores	
R. Tixier & B. Mobasher [4,5]	2003	x		x		$f\phi_0$
B. Bary [6]	2008		x	x		
M. Basista & W. Weglewski [7]	2009	x		x		$f\phi_0$
S. Sarkar et al. [8]	2010	x		x		$f\phi_0$
A. Idiart et al. [9]	2011	x		x		$f\phi_0$
X.-B. Zuo et al. [10]	2012	x		x		$f\phi_0$
B. Bary et al. [11]	2014	x	x	x		$f\phi_0$
T. Ikumi et al. [12]	2014	x			x	$f_i\phi_i$
Y. Yu et al. [13]	2015	x		x		$f\phi_0$
N. Cefis & C. Comi [14]	2017	x		x		
J. Zhang et al. [15]	2017	x		x		$f\phi_0$

Notice that even models based on the crystallization pressure theory adopt a unified approach to simulate the pore network and precipitation patterns of ettringite. Such limited framework does not allow to reproduce one of the main features of this theory, the influence of the location of ettringite on the pressures exerted. Several researchers have used Eq. (5.1) to assess the influence of crystal size and shape on the potential crystallization pressure (p) developed during ettringite growth in confined conditions [16–18].

$$p = \kappa_{CL}\gamma_{CL} = \frac{RT}{V_{Et}}\ln\left(\frac{Q_{Et}}{K_{Et}}\right) \quad (5.1)$$

$$Q_{Et} = (C_{Ca^{2+}}\gamma_{Ca^{2+}})^6\left(C_{Al(OH)_4^-}\gamma_{Al(OH)_4^-}\right)^2(C_{OH^-}\gamma_{OH^-})^4\left(C_{SO_4^{2-}}\gamma_{SO_4^{2-}}\right)^3\left(C_{H_2O}\gamma_{H_2O}\right)^{26} \quad (5.2)$$

The terms γ_{CL}, κ_{CL} K_{Et} and V_{Et} correspond to the interfacial free energy, the crystal curvature, the equilibrium constant and the molar volume of an ettringite crystal. R corresponds to the gas constant and T is the absolute temperature. The ionic activity product of ettringite (Q_{Et}) might be calculated as indicated in Eq. (5.2). Eq. (5.1) shows that small crystals with high curvatures are in equilibrium with a higher concentration than larger macroscopic crystals. Consequently, small crystals can potentially generate higher crystallization pressures as long as sulfate supply is not restricted. On the other hand, large crystals are unable to exert significant pressures and therefore, are unlikely to be the origin of damage [16]. Accordingly, this theory states that the expansive force developed during sulfate attack is mainly determined by the locations of ettringite growth in the microstructure rather than the total volume of ettringite formed.

The first requirement to capture this phenomenon is to consider a more realistic representation of the pore network, able to account for ettringite growth in different locations within the pore structure. The flexible framework presented here could be used in this regard. However, in order to fully reproduce the crystallization pressure theory, important modifications should be made in the chemical and transport module to account for different saturation conditions (Q_{Et}/K_{Et}) in each pore size considered. The feasibility of this last step is currently uncertain. In the near future, numerical models might have to rely on combined approaches to simulate some complex features of the crystallization pressure theory from the more accessible volume increase theory. The model proposed here is conceived in this direction and establish the foundations to couple both approaches by relating the buffer capacity assigned to each pore size to the different saturation conditions reached.

Table 5.1 also highlights a concerning fact. The new methodology to compute expansions is one of the few innovations in the modelization of the degradation mechanisms and the estimation of the expansive forces since the early 2000s. During the last two decades, the scientific community has been more focused on improving the simulation of the reactive-transport phenomenon and the mechanical response of the structure. One might wonder whether it is of the best interest to keep improving the simulation of the macro-structural response of the element when it is still not possible to reliable quantify the expansive forces generated at the pore-scale, which are the origin of all damage developed. One of the major achievements of the thesis was the early recognition of this subject as key to provide reliable and solid models in the near future.

Two main limitations associated to the new methodology are identified. First, the model still relies on a correct quantification of the buffer capacities of the different pore sizes present in the matrix. As discussed in section 1.2.2, the only way to address this topic is by increasing the knowledge on fundamental aspects related to the role of porosity during the ESA. Contributions on this field are included in Journal Paper IV and discussed in section 5.2. The other main controversy refers to the procedure adopted to distribute the ettringite formed within the different pore sizes considered. The model assumes that the location of ettringite is defined by the area covered by each pore size. Therefore, pores covering a bigger surface would receive a larger portion of the ettringite precipitated. Even though this simplified approach might seem logic, currently few experimental studies are focused on the

assessment of the ettringite precipitation patterns during the ESA. Further experimental investigations should be performed to assess its validity. Insights on the precipitation patterns are presented in Journal Papers III and IV and discussed in section 5.2.

5.1.2. Simplified methodology for ESA assessment

Currently, practitioners facing the need to evaluate or design durable structures against the ESA through simplified procedures can mainly resort to prescriptive approaches included in standards or building codes and simplified analytical relations. Section 1.2.1 examines and highlights the advantages and limitations associated to the use of these methodologies. The main criticism is that both approaches systematically neglect or overlook the mechanical aspect of the attack. Due to the large size of typical structures affected by ESA (tunnel linings, piles, retaining walls) and the slow progress of sulfate penetration, the mechanical contribution into the overall sulfate resistance of the structure cannot be ignored. To address this limitation, a new simplified methodology for ESA assessment is presented in Journal Paper II (pages 48-71) that explicitly accounts for the specific conditions found in each application.

The methodology proposed in this paper is based on the application of a set of simplified equations to assess the extent of the reactive-transport process and the possible mechanical structural failure at a given service life. The simplified equations to estimate the penetration depth of sulfate ions are derived from a nonlinear numerical regression analysis of over 2000 simulations performed with the comprehensive model described in Journal Paper I. Equations are proposed to verify the failure modes usually associated to the ESA: tensile failure at the sound core and spalling of the superficial layers. If no mechanical failure occurs and the serviceability is not compromised, it is considered that the structure will comply with the required service life.

Beyond the specific contributions related to the sets of simplified equations presented, the main novelty of the new methodology with respect to other simplified assessment procedures is reflected in Table 5.2. This table describes the input parameters considered by the most relevant guidelines and simplified models to evaluate the ESA. As can be seen, the methodology developed (highlighted by green hatching) stands as the only that accounts for the aggressiveness of the media, reactivity and mechanical properties of the material and geometrical characteristics of the element under attack.

The parametric analyses performed in the Journal Paper II and in the Conference Paper I show how the consideration of the shape and size of the element, the required service life and the cement content of the material might influence the sulfate resistance of a structure in realistic scenarios. The results obtained in the parametric analyses are compared with the criteria from structural codes to highlight the deficiencies of the current approaches. An example of this situation might be reflected in Figure 9 of Journal Paper II (page 64). This figure predicts the sulfate concentration causing failure in concrete piles of different diameters with a 10 % C_3A cement. Results show no failure for sulfate concentrations below 4.2 g/l in piles with 90 cm of diameter at 50 years. For piles with 30 cm of diameter, the threshold sulfate concentration decreases until 2.6 g/l. However, according to EN 206–1, the 10% C_3A cement used in this study is not allowed for sulfate concentrations above 0.6 g/l, leading to penalizing measures and cost overruns due to the unnecessary use of sulfate resistant cement.

Table 5.2. Characteristics of the simplified procedures to assess the ESA.

	Name / Authors	Year	Aggressiveness of the media				Material reactivity		Transport properties			Mechanical response		Time
			Sulfate content	Type of soil	Mobility of water	Acidity (pH)	Cement comp.	Cement content	w/c ratio	Porosity	Diffusion coefficient	Mechanical properties	Size	
Standards	ACI 318-08 [19]	2008	x											
	EN 206:2013+A1:2016 [20]	2016	x											
	BS 8500-1:2015+A1:2016 [21] BRE Special Digest 1 [22]	2016	x	x	x	x							x	x
Simplified empirical and mechanistic relations	A. Atkinson & J.A. Hearne [23]	1984	x				x							x
	R. Shuman et al. [24]	1989	x				x				x			x
	A. Atkinson & J.A. Hearne [25]	1990	x								x	x		x
	J.R. Clifton & J.M. Ponnersheim [26]	1994					x	x	x	x				x
	K.E. Kurtis & P.J. Monteiro [27]	2000					x		x					x
	P.J. Monteiro & K.E. Kurtis [28]	2008					x		x					x
	T. Ikumi et al. [29]	2016	x				x	x		x	x	x	x	x

The influence of size in ESA resistance is also clearly shown in Figure 4 of Conference Paper I (page 105). This figure shows that the same material under the same exposure conditions might increase its maximum C_3A content in the cement from around 7 % to 9 % without compromising the safety of the structure if the pile diameter increases from 30 to 90 cm. Notice that standards would prescribe the same measures for both piles solely based on the aggressiveness of the media, ignoring the mechanical contribution of the size on the sulfate resistance.

Another important feature of the methodology developed is its capability to predict the most probable failure mode according to the specific conditions found. This distinction is relevant since delamination of exterior layers may be acceptable as long as it does not compromise the safety of the structure or the protection of the steel rebar. On the contrary, cracking of the cross-section should be taken with care especially in piles subjected to moments or to tensile forces. The combination of all the measures introduced in the methodology developed here allows a detailed evaluation of the durability without resorting to complex numerical tools. Additionally, it represents a step forward on how to assess the ESA explicitly in the design of concrete structures as it allows the definition of a flexible set of precautionary measures for each application.

Despite the obvious potential benefits of full performance-based methodologies such as the one developed here, building codes are still far from embracing this approach. The prescriptive guidelines included in building codes have traditionally been implemented to provide simple assessments, which is understandable considering that an important fraction of practitioners consider these documents as rulebooks to be followed more or less blindly. The natural process to follow might be the gradual incorporation of reliable performance-based test methods in combination with the existing prescriptive frameworks. This step is already adopted for the classification of cements and currently the RILEM TC 251-SRT is working on the development of representative test methods applicable to concrete mixtures to assess the resistance against the ESA. In any case, methodologies such as the one developed here can always be used as a competent source of advice for qualified engineers.

The simplified procedure proposed here also presents limitations that should be understood in order to use it safely. The accuracy of the assessments relies on a correct estimation of the expansive forces generated during the attack. These are quantified based on the same hypothesis adopted in the comprehensive numerical model discussed in section 5.1.1. Consequently, practitioners still need to estimate the capacity of the matrix to accommodate expansive phases, which might not be an intuitive task. This limitation is partly addressed in the Journal Paper II by proposing realistic values for the buffer coefficient based on the outcomes of a full parametric analysis and assuming safety approaches during the mechanical analysis. However, as indicated in section 5.1.1, fundamental research on aspects related to the role of porosity during the ESA is still needed. Contributions on this field are included in Journal Papers III and IV and discussed in following section.

Moreover, before considering the methodology presented as fully operational, the set of simplified mechanical equations proposed should be validated. The most convenient approach to perform the validations involves the use of advanced mechanical simulations methods such as the FEM. Future advances on the quantification of the expansive forces generated during the attack and possible modifications on the mechanical equations proposed could be easily implemented without modifying the overall philosophy of the methodology.

5.2. ROLE OF POROSITY IN THE ESA

Journal Papers III (pages 72-95) and IV (pages 110-133) present the findings derived from two experimental campaigns performed to shed light on the ESA expansion mechanism and the role of the pore network during the attack. It is widely accepted by the scientific community that matrices with low permeability show higher durability against the ESA than the corresponding matrices with high permeability. The reasoning is simple, by limiting the penetration of external aggressive ions both the final penetration depth and the amount of expansive product precipitated are reduced. Consequently, the expansive forces generated during the attack are applied within a smaller region and develop lower stresses. Several studies published during the last decades support this recommendation (e.g. [31–36]) and now this approach is adopted in all standards.

However, Journal Paper I reports that the vast majority of advanced numerical models incorporate one more mechanism that contributes to ESA resistance, the capacity of the matrix to accommodate expansive phases. Unlike what occurs with permeability, the mere existence of a buffer mechanism has been barely documented and structural codes do not acknowledge its positive contribution towards ESA durability. Due to the key weight attributed to the buffer capacity of the pore network in current advanced numerical assessment tools and in the simplified procedure developed here, an extensive experimental program was performed to assess the role of permeability and damping during the attack.

The specimens with air-entrainer presented the highest porosity, the highest amount of expansive phases but the lowest expansions and damage amongst the wide range of compositions evaluated throughout the attack. In fact, the expansions reached at the end of the test are more than 5 times lower than the ones experienced by the same composition without air-entrainer. Such behavior cannot be explained based on the approach adopted in the codes, as the largest presence of ettringite caused by an increased sulfate penetration should result in the generation of the highest expansive forces. Indeed, a comprehensive comparison of the Rietveld quantifications of expansive phases with the radial expansions developed refuted the belief that solely the amount of ettringite determines the magnitude of the expansive forces generated during the attack (Figures 9 and 10 in Journal Paper IV, pages 123-124).

These results provide evidence of another mechanism defined by the pore network that contributes into the ESA resistance, referred to as damping capacity in Journal Paper IV. Precipitation patterns of the expansive phases during the attack for different compositions are evaluated through mercury intrusion porosimetry (MIP) tests. Results indicate that initially, a significant portion of the ettringite precipitated is concentrated in large pores. Then, the precipitation evolves towards finer pore sizes. In refined matrices, ettringite precipitation reached smaller pore ranges than in coarser pore networks, where the precipitation was mainly found to occur in larger pores. Results from matrices with air-entrainer indicate that if sufficient large pores are provided, ettringite precipitation might never reach smaller pores. Notice that according to the crystallization pressure theory only ettringite growing in small pores are likely to generate damage, which is in agreement with the low levels of degradation observed in mortars with air-entrainer.

The wide range of compositions assessed, each with different pore characteristics, allowed the understanding of the complex balance between the contributions of permeability and damping into ESA resistance. This led to the development of a conceptual model, which is included in Journal Paper IV and constitutes one of the most relevant contributions derived

from the thesis since might open up alternative strategies for the future design of durable cementitious materials against the ESA. The damping capacity of a matrix is determined by two phenomena defined by the pore characteristics: the probability of an ettringite crystal to precipitate in a certain location and the capacity of this location to accommodate expansive phases in unconfined conditions.

The numerical model presented in Journal Paper I is able to capture most of the outcomes derived from the experimental campaign. Unlike the traditional approach to compute local expansions, the mathematical framework developed introduces the required flexibility to acknowledge the importance of the location of the ettringite formed during the attack to estimate the expansive forces generated. The algorithms adopted in the numerical model to distribute ettringite and to quantify the capacity of the pores to accommodate expansive phases reproduce the main trends observed in the experimental campaign and are fully defined from the pore characteristics of the matrix, as formulated in the conceptual model. The validations performed in Journal Paper I indicate that through a correct calibration of the damping parameters attributed to each pore size, the model is not only capable to capture the main processes related to the expansion mechanism but also to provide a fair quantification.

Unfortunately, one of the objectives of the experimental phase could not be attained. Originally, it was thought to be possible to quantify buffer coefficients associated to different pore sizes by an inverse analysis using the advance numerical model and the large pool of experimental data regarding precipitation patterns and expansions. However, the MIP did not quantify the precipitation patterns with the precision needed to conduct such analysis. Consequently, results obtained through this technique could only be used qualitatively to examine general trends. Although the combination of experimental and numerical methods to assess the buffer capacity might be valid, precise techniques to characterize the pore network throughout the attack are still required. The selection of alternative methods is not simple as MIP currently stands as one of the few techniques able to provide the pore size distribution over a wide range of pores.

Increased knowledge on the precipitation patterns of expansive phases during the attack could also lead to more precise algorithms to distribute the reactions products throughout the pore network. Even though the current approach is able to reproduce qualitatively the general trends observed by MIP tests, it does not consider the possibility that ettringite formed in a certain location might dissolve and recrystallize in a different location where the thermodynamic conditions are more favorable. This “movement” of ettringite crystals over time could play a relevant role in the damage developed during the early stages of the attack by introducing transient stresses in certain locations.

5.3. EFFECTS OF FIELD-LIKE CONDITIONS ON ESA ASSESSMENT

The slow progress of the deleterious effects associated to the ESA encourages the use of accelerated test methods in performance-based assessment methodologies and in most experimental studies. The acceleration of the attack often involves the use of certain testing conditions that greatly differ from the conditions found in the field. The assessment of the alterations introduced by accelerated testing has drawn a lot of attention in the scientific community, which led to a fair understanding of how most of these practices may modify the attack. Journal Papers III (pages 72-95) and V (pages 134-162) address the potential effects associated to two testing conditions that have been barely evaluated: the effects of early sulfate exposure and confining stresses.

Most field structures affected by the ESA are exposed to sulfates since casting. However, the majority of test methods adopt pre-curing periods in non-aggressive conditions prior to sulfate exposure. In general, the typical durations of pre-curing periods represent a small fraction of the total span of the attack. Consequently, the potential alterations introduced by a few weeks of different curing conditions are often perceived as negligible. Journal Paper III evaluates the validity of this assumption by comparing the pore size distribution obtained from MIP tests in mortars cured in aggressive and non-aggressive conditions during the first 90 days of curing.

MIP results show that mortars cured in aggressive conditions since casting present more refined pore networks than the corresponding mortars under non-aggressive curing conditions. XRD tests suggest that the refinement may be attributed to a significant precipitation of expansive phases. The differences on the pore network are observed after only 7 days of curing for sulfate concentrations representative of both laboratory (30 g/l) and field (3 g/l) conditions in most compositions. As discussed in section 5.2, the pore characteristics play a major role in determining the location and subsequent damage developed by ettringite precipitation. The different pore characteristics in specimens exposed to sulfates since casting or after non-aggressive pre-curing periods might lead to imprecise damage estimations for structures cast in situ. In these cases, a more realistic approach would be to expose samples to sulfate at earlier ages. Unfortunately, the short duration of this study (90 days) does not allow to verify trends related to the behavior at late stages of the attack.

The effects of confining stresses on the development of the ESA are analyzed in Journal Paper V. Although most field structures cannot expand freely due to confinement induced by the ground or other elements from the structure, all experimental assessment methods and most general research on ESA are performed on specimens in free-expanding conditions. The objective defined in the present study is to examine whether this common practice might alter the representativeness of the results obtained and identify and understand the alterations caused by the stresses.

The processes involved during the ESA that might be potentially affected by confining stresses are ionic transport, chemical reactions, degradation mechanisms and the mechanical response of the element. Beforehand, it seems clear that confining stresses acting in the opposite direction of the expansive pressure generated by the attack should reduce the expansions developed and thus, alter the mechanical response of the specimen. The mechanical analysis included in Journal Paper V estimates that confined specimens should develop around 65-70 % less expansions than the corresponding samples in free conditions, based on purely mechanical considerations. Consequently, a comparison between the expansions measured in free and confined conditions should highlight whether the effects of

confinement are limited to the mechanical response of the element or also alter other processes involved during the attack.

If confinement only alters the mechanical response, the experimental studies or test methods focused on chemical, transport and/or degradation mechanisms of ESA (i.e. test methods designed for the classification of cements) could be performed in specimens in free-expanding conditions without compromising the representativeness of the results. Moreover, current advanced ESA models that include comprehensive mechanical modules would be already capable to fully account for the effects of confinement. However, the lower damage levels observed in confined conditions by expansion and ultrasonic velocity measurements cannot be solely explained from the mechanical contribution of the steel rings. These results indicate that internal processes of the ESA are not developed equally in free and confined specimens. Therefore, degradation measured in free-expanding conditions might not be realistic when the attack is developed in confined conditions.

Results suggest that the compressive stresses generated by confinement modify the normal development of the attack by two mechanisms that might act simultaneously. On one hand, confinement might limit or delay the appearance of microcracks. This causes a reduction of pore channels connecting the inner layers of the matrix with the external media and reduces the effective sulfate concentration in the pores. Mass evolution and XRD results between free and confined specimens confirm these phenomena.

On the other hand, the compressive stresses generated might be transferred to ettringite crystals growing in confined conditions. These crystals react to the external stresses applied by increasing its solubility to reach equilibrium, which promotes a spread nucleation of small crystals instead of large ettringite formations. By that, the amount of ettringite growing in confined conditions and generating damage might be reduced. In general, SEM micrographs show that crystals precipitated in pores corresponding to specimens in restrained conditions present lower sizes and degrees of crystallinity compared with the ones formed in free specimens, which is in line with the hypothesis formulated. However, a thorough verification of this theory would require the comparison of the morphology of ettringite growing in confined conditions for free and restrained specimens. Unfortunately, it was not possible to locate and clearly visualize the morphology of ettringite growing under such conditions due to the small scale at which this phenomenon occurs.

Even though the outcomes of this study may raise more questions than answers, the idea that stresses induced by restraint might reduce the amount of ettringite crystals growing in confined conditions during the ESA has not been formulated before and might have huge implications if proved true. The understanding of the positive effects of confinement could lead to more realistic assessments and contribute to explain the large difference between the damage developed in laboratory specimens and the one observed in real structures. For that, it is essential to keep advancing knowledge on the interactions of loads and the expansive forces generated to validate the mechanisms proposed. Additionally, it is imperative to improve the simplistic mechanical model used by incorporating second order effects such as creep and potential cracking.

The current state of knowledge is not enough to propose quantitative approaches to incorporate the effects of confinement in ESA assessment tools. However, the results obtained indicate that confinement should always contribute positively into the durability against sulfates. Therefore, neglecting its effects might lead to unnecessary precautionary measures but would not compromise the safety of the assessment.

5.4. CONCLUSIONS

5.4.1. General conclusions

This thesis presents important contributions on three different research lines to improve and advance knowledge on ESA assessment tools: numerical modeling, role of porosity during the attack and the relevance of field-like conditions on ESA assessment.

The advances on the numerical modelization led to the development of a chemo-transport-mechanical model and a simplified assessment methodology. The main novelty of the comprehensive model is the approach proposed to compute expansions, which is based on a more realistic representation of the concrete porosimetry. The parametric analyses and validations performed prove that this approach is able to distinguish the contributions from ettringite growing in different pore sizes into the overall expansions. By that, it captures the early expansions observed in practice and reproduces certain effects associated to the crystallization pressure theory through the simplified volume increase approach.

The simplified assessment methodology proposed currently stands as the only procedure that evaluates the risk of failure during ESA based on the aggressiveness of the media, the reactivity and mechanical properties of the material, the geometric characteristics and the service life of the element under attack, without resorting to complex iterative algorithms. Several parametric analyses on realistic scenarios highlight the deficiencies of current approaches and recommend the use of performance-based methodologies like the one presented here to define flexible and optimized precautionary measures for each application.

The outcomes derived from the experimental study on the role of porosity together with the conceptual model formulated prove the existence of two opposing mechanisms defined by the pore network that might contribute into the ESA resistance, referred in this work as permeability and damping. The role of permeability on the durability of external attacks is well established and is already acknowledged by building codes and standards. However, the results obtained in this thesis constitutes one of the few clear proofs that damping phenomenon exists and might contribute to the durability of ESA by promoting the precipitation of ettringite in locations where it can grow without generating expansive forces.

These results break with the traditional idea that high porosities are always negative for ESA durability and suggest the possibility to obtain a durable material by solely increasing the capacity of the matrix to accommodate expansive products. The design of durable materials against the ESA based on high damping capacities should be made with caution. In these cases, the durability tends to decrease with time since the pore filling effect has a negative impact on the damping capacity of the matrix. On the other hand, the approach based on low permeability is safer as the pore filling effect developed over time has a positive impact on the permeability.

The third research line of this thesis evaluates the influence of early sulfate exposure and the effects of confinement on the ESA. The former study suggests that the late exposition to aggressive curing commonly adopted in accelerated laboratory tests might lead to imprecise damage estimations for structures cast in situ. In these cases, it is recommended to expose the samples to sulfates at earlier ages.

The comprehensive study performed to assess the effects of confinement indicates that the confining stresses commonly generated in real-scale structures alter the normal development of the ESA and reduce the potential damage generated. The important influence

observed raises questions about the representativeness of the accelerated laboratory tests conducted under unconfined conditions. The numerical simulation of the structural repercussion of the ESA obtained by applying free expansion in structural models should also be questioned since it might predict higher stresses than expected in reality in case confinement exists.

5.4.2. Specific conclusions

A selection of the main specific conclusions are listed below grouped within the three main areas of contribution of this thesis.

iv. Numerical modeling of the ESA

Advanced ESA model

(1)- The new expression implemented for the consideration of the diffusion in a cracked porous media does not require the definition of any damage parameter such as the one used by isotropic damage models based on continuum damage mechanics. In this case, the damage is considered indirectly, thus allowing more direct and intuitive estimations.

(2)- The model is able to reproduce the general trends of ettringite precipitation patterns as described by the crystallization pressure theory. Large pores locate most of the ettringite precipitated. However, small pores are filled faster and thus, constitute the main contribution to the total strain observed in the simulations.

(3)- The parametric analysis identifies the sulfate concentration in the aggressive soil and the lumped rate of sulfates take-up as the most influencing parameters on the reaction front. On the other hand, changes in the initial diffusivity and calcium aluminates concentration do not affect significantly the reaction front.

(4)- Two independent validations of the model indicate that the proposed model is able to predict expansions with good accuracy providing a good estimation of the buffer capacity and the reaction rate.

Simplified ESA assessment methodology

(1)- The preliminar parametric analysis indicates that the flux intensification effect of the sulfate ions in radial elements plays a minor role in the maximum penetration depth for the typical size of real structures. Therefore, unidirectional flux might be adopted for all structural typologies without compromising the accuracy of the penetration profiles.

(2)- The parametric study indicates that sulfate and aluminate concentration, initial diffusivity and the buffer coefficient are between 2.7 to 8 times more influencing on the penetration depth reached than the compressive strength and initial porosity of the material.

(3)- Results suggest that buffer capacities above 0.20 of the initial porosity are not realistic if aluminates are in the form of monosulfate. Buffer capacities between 0.05 and 0.20 are recommended, which considerably narrow the typical ranges suggested in the literature for this parameter.

(4)- Results highlight the influence of the pile diameter and sulfate concentration on the assessment of the damage induced by ESA and the predominant failure mode expected. Results indicate that spalling of the external layers might be the main failure mode in large

elements exposed to low sulfate concentrations. However, for slender elements and high sulfate concentrations, tensile failure in the core might occur prior to delamination.

(5)- The simplified methodology suggests the existence of a C_3A threshold above which a high risk of structural damage occurs. This trend is consistent with the philosophy used in structural codes and validated in practice. The C_3A threshold increases with the increase of the size of the element and with the reduction of the sulfate concentration.

(6)- The parametric analyses performed indicate that the limitation of the C_3A content in the cement included in most structural codes may lead to different degradation levels depending on the cement content considered. The limitation on the C_3A content should not be referred to the cement but to a unit volume of concrete.

(7)- Reference values are proposed for the C_3A threshold depending on the exposure conditions, type and dimensions of the structure. In case a more precise assessment is required, the equation included in the simplified methodology may be used to estimate the C_3A threshold. The procedure followed for this estimation requires the use of the formulation included in Tables 4 and 5 of Journal paper II, being compatible with the durability assessment found in building codes.

v. Role of porosity in the ESA

(1)- The damping capacity of the pore structure determines the expansions generated during the initial stage of the attack. After that, the transport process (permeability) affected by the precipitation of expansive phases controls the durability. Results indicate that the duration of the first stage can be extended depending on the amount of large pores available in the material.

(2)- Expansion monitoring and ultrasonic pulse velocity test show that mortars with air-entrainer displayed the lowest expansions and variations in the ultrasonic velocity during the attack. These results suggest that this composition developed the smallest damage levels amongst all dosages tested despite presenting the highest porosity. These results were not expected according to the established knowledge on the ESA.

(3)- Quantitative XRD analysis shows no direct relationship between the measured expansions and the amount of expansive product formed during any stage of the attack. In fact, the biggest precipitation of expansive phases was found in the composition with air-entrainer that presents the smallest expansions.

(4)- Results obtained indicate that the pore characteristics of the matrix might determine a preferential location of precipitation for the expansive phases. Initially, larger pores concentrate a higher proportion of the expansive product. As pore refinement increases with time, the precipitation evolves towards finer pore sizes.

(5)- MIP results suggest that the low expansion and damage observed in mortars with air-entrainer might be explained by a preferential precipitation of expansive phases in large pores, which dump the pressure increase of the pore system and accommodate expansive phases without causing damage.

(6)- Results obtained prove that the typical approach used to estimate local expansions based on a unified consideration of the porosity is not able to reproduce the main features of the real expansion mechanism, which is mainly defined by the location of precipitation rather than for the amount of ettringite formed.

vi. Effects of field-like conditions on ESA assessment

Influence of early sulfate exposure on the pore network development

(1)- Early sulfate exposure causes alterations on the pore network after 7 days of curing for most compositions.

(2)- The alterations on the pore network are observed in high (30 g/l) and low (3 g/l) aggressive solutions for most compositions. XRD tests indicate that these alterations may be attributed to the precipitation of ettringite and gypsum.

(3)- SEM images of ettringite formed in air voids indicate that the morphology and degree of crystallinity varies depending on the availability of connected air voids and the external sulfate concentration. Crystallinity of ettringite increases with the degree of refinement of the pore system and decreases with the aggressiveness of the media.

Influence of confinement

(1)- The level of stress generated by the attack in confined samples exposed to accelerated ESA is significantly smaller than the stresses predicted considering the free expansions of equivalent unconfined samples.

(2)- Results of mass variation suggest that the ionic transport process between external and pore solutions is more limited in confined specimens than in free-expanding conditions. This behavior might be explained by the reduced microcracking generated in confined conditions, which decreases the number of penetration paths and reduce the sulfate concentration in the material.

(3)- In general, XRD results indicate that the confinement causes a reduction on the amount of expansive phases precipitated, especially in compositions with high water/cement ratios and air-entrainer. This behavior might also be related to the lower penetration of aggressive ions in confined conditions caused by the reduced microcracking of the matrix.

(4)- The theoretical framework formulated to explain the effects of confinement on the crystals formed suggests that confinement might alter the solubility of ettringite and promote a spread nucleation of small crystals within the pore network. These phenomena might reduce the amount of crystals growing in confined conditions and contribute to explain the lower stresses generated by the attack in the confined specimens.

(5)- The images obtained by SEM analysis show that crystals precipitated in restrained samples present lower size and degree of crystallinity compared with the ones formed in free-expanding specimens. Unfortunately, this behavior is always observed in crystals growing in large pores and therefore, presumably in unconfined conditions. Consequently, SEM analysis is not able to confirm the hypothesis formulated in point (4) as it is not possible to locate ettringite growing in confined conditions for both configurations.

REFERENCES

[1] F. Schmidt-Döhl, F.S. Rostásy, A model for the calculation of combined chemical reactions and transport processes and its application to the corrosion of mineral-building materials Part I. Simulation model, Cem. Concr. Res. 29 (1999) 1039–1045. doi:10.1016/S0008-8846(99)00087-3.

[2] F. Schmidt-Döhl, F.S. Rostásy, A model for the calculation of combined chemical

reactions and transport processes and its application to the corrosion of mineral-building materials Part II. Experimental verification, Cem. Concr. Res. 29 (1999) 1047–1053. doi:10.1016/S0008-8846(99)00094-0.

[3] P. Feng, E.J. Garboczi, C. Miao, J.W. Bullard, Microstructural origins of cement paste degradation by external sulfate attack, Constr. Build. Mater. 96 (2015) 391–403. doi:10.1016/j.conbuildmat.2015.07.186.

[4] R. Tixier, B. Mobasher, Modeling of Damage in Cement-Based Materials Subjected to External Sulfate Attack. I: Formulation, J. Mater. Civ. Eng. 15 (2003) 305–313. doi:10.1061/(ASCE)0899-1561(2003)15:4(305).

[5] R. Tixier, B. Mobasher, Modeling of damage in cement-based materials subjected to external sulfate attack. II: Comparison with experiments, J. Mater. Civ. Eng. 15 (2003) 314–322. doi:10.1061/(ASCE)0899-1561(2003)15:4(314).

[6] B. Bary, Simplified coupled chemo-mechanical modeling of cement pastes behavior subjected to combined leaching and external sulfate attack, Int. J. Numer. Anal. Methods Geomech. 32 (2008) 1791–1816. doi:10.1002/nag.696.

[7] M. Basista, W. Weglewski, Chemically Assisted Damage of Concrete: A Model of Expansion Under External Sulfate Attack, Int. J. Damage Mech. 18 (2009) 155–175. doi:10.1177/1056789508097540.

[8] S. Sarkar, S. Mahadevan, J.C.L. Meeussen, H. van der Sloot, D.S. Kosson, Numerical simulation of cementitious materials degradation under external sulfate attack, Cem. Concr. Compos. 32 (2010) 241–252. doi:10.1016/j.cemconcomp.2009.12.005.

[9] A.E. Idiart, C.M. López, I. Carol, Chemo-mechanical analysis of concrete cracking and degradation due to external sulfate attack: A meso-scale model, Cem. Concr. Compos. 33 (2011) 411–423. doi:10.1016/j.cemconcomp.2010.12.001.

[10] X.B. Zuo, W. Sun, C. Yu, Numerical investigation on expansive volume strain in concrete subjected to sulfate attack, Constr. Build. Mater. 36 (2012) 404–410. doi:10.1016/j.conbuildmat.2012.05.020.

[11] B. Bary, N. Leterrier, E. Deville, P. Le Bescop, Coupled chemo-transport-mechanical modeling and numerical simulation of external sulfate attack in mortar, Cem. Concr. Compos. 49 (2014) 70–83. doi:10.1016/j.cemconcomp.2013.12.010.

[12] T. Ikumi, S.H.P. Cavalaro, I. Segura, A. Aguado, Alternative methodology to consider damage and expansions in external sulfate attack modeling, Cem. Concr. Res. 63 (2014). doi:10.1016/j.cemconres.2014.05.011.

[13] Y. Yu, Y.X. Zhang, A. Khennane, Numerical modeling of degradation of cement-based materials under leaching and external sulfate attack, Comput. Struct. 158 (2015) 1–14. doi:10.1016/j.compstruc.2015.05.030.

[14] N. Cefis, C. Comi, Chemo-mechanical modeling of the external sulfate attack in concrete, Cem. Concr. Res. 93 (2017) 57–70. doi:10.1016/j.cemconres.2016.12.003.

[15] J. Zhang, M. Sun, D. Hou, Z. Li, External sulfate attack to reinforced concrete under drying-wetting cycles and loading condition: Numerical simulation and experimental validation by ultrasonic array method, Constr. Build. Mater. 139 (2017) 365–373. doi:10.1016/j.conbuildmat.2017.02.064.

[16] W. Müllauer, R.E. Beddoe, D. Heinz, Sulfate attack expansion mechanisms, Cem. Concr. Res. 52 (2013) 208–215. doi:10.1016/j.cemconres.2013.07.005.

[17] G.W. Scherer, Stress from crystallization of salt, Cem. Concr. Res. 34 (2004) 1613–1624. doi:10.1016/j.cemconres.2003.12.034.

[18] G.W. Scherer, Crystallization in pores, Cem. Concr. Res. 29 (1999) 1347–1358. doi:10.1016/S0008-8846(99)00002-2.

[19] ACI Committee 318, Building Code Requirements for Structural Concrete (ACI 318-08) and Commentary, 2008. doi:10.1016/0262-5075(85)90032-6.

[20] BS EN 206, BSI Standards Publication Concrete — Specification , performance , production and conformity, 2013.

[21] BS 8500-1:2015 Complementary British Standard to BS EN 206 Part 1 : Method of specifying and guidance for the specifier, 2015.

[22] BRE construction Division Special Digest 1, Concrete in aggressive ground, 2005.

[23] A. Atkinson, D.J. Goult, J.A. Hearne, The influence of wasteform permeability on the release of radionuclides from a repository, Nucl. Chem. Waste Manag. 5 (1985) 203–214. doi:10.1016/0191-815X(85)90079-8.

[24] R. Shuman, V.C. Rogers, R.A. Shaw, The barrier code for predicting long-term concrete performance, Waste Manag. 89 (1989) 701–705.

[25] A. Atkinson, J.A. Hearne, Mechanistic Model for the Durability of Concrete Barriers Exposed to Sulphate-Bearing Groundwaters, MRS Proc. 176 (1989) 149. doi:10.1557/PROC-176-149.

[26] J.R. Clifton, J.M. Pommersheim, Sulfate attack of cementitious materials: Volumetric relations and expansions, NISTIR 5390, Natl. Inst. Stand. Technol. (1994) 22.

[27] K.E. Kurtis, P.J.M. Monteiro, S.M. Madanat, Empirical Models to Predict Concrete Expansion Caused by Sulfate Attack, ACI Mater. J. 97 (2000) 156–161. doi:10.14359/818.

[28] P.J.M. Monteiro, K.E. Kurtis, Experimental asymptotic analysis of expansion of concrete exposed to sulfate attack, ACI Mater. J. 105 (2008) 62–71.

[29] T. Ikumi, S.H.P. Cavalaro, I. Segura, A. de la Fuente, A. Aguado, Simplified methodology to evaluate the external sulfate attack in concrete structures, Mater. Des. 89 (2016). doi:10.1016/j.matdes.2015.10.084.

[30] A. Neville, The confused world of sulfate attack on concrete, Cem. Concr. Res. 34 (2004) 1275–1296. doi:10.1016/j.cemconres.2004.04.004.

[31] J. Marchand, I. Odler, J.P. and Skalny, Sulfate attack on concrete, Spon Press, Taylor & Francis Group, New York, 2002.

[32] P.J.M. Monteiro, K.E. Kurtis, Time to failure for concrete exposed to severe sulfate attack, Cem. Concr. Res. 33 (2003) 987–993. doi:10.1016/S0008-8846(02)01097-9.

[33] F.P. Glasser, J. Marchand, E. Samson, Durability of concrete - Degradation phenomena involving detrimental chemical reactions, Cem. Concr. Res. 38 (2008) 226–246. doi:10.1016/j.cemconres.2007.09.015.

[34] A. Çavdar, Ş. Yetgin, Investigation of mechanical and mineralogical properties of mortars subjected to sulfate, Constr. Build. Mater. 24 (2010) 2231–2242. doi:10.1016/j.conbuildmat.2010.04.033.

[35] R. El-Hachem, E. Rozière, F. Grondin, A. Loukili, Multi-criteria analysis of the

mechanism of degradation of Portland cement based mortars exposed to external sulphate attack, Cem. Concr. Res. 42 (2012) 1327–1335. doi:10.1016/j.cemconres.2012.06.005.

[36] W. Piasta, J. Marczewska, M. Jaworska, Durability of Air Entrained Cement Mortars Under Combined Sulphate and Freeze-thaw Attack, Procedia Eng. 108 (2015) 55–62. doi:10.1016/j.proeng.2015.06.119.